# SOFT X-RAYS
# FROM COMPACT PLASMA FOCUS

A THESIS SUBMITTED BY

LIU MAHE

FOR THE DEGREE OF DOCTOR OF PHILOSOPHY

SCHOOL OF SCIENCE

NANYANG TECHNOLOGICAL UNIVERSITY

DECEMBER 1996

# Acknowledgments

I wish to express my deepest gratitude and indebtedness to my supervisor Prof. Lee Sing, Head of Division of Physics, School of Science, National Institute of Education, Nanyang Technological University, for his constant help, inspiring guidance, stimulating and invaluable advice throughout the entire course of this project and the writing of this thesis, without which it would not have been possible for me to complete this work.

I express my gratitude to Dr. Stuart Springham for his help, useful suggestions and discussions during the first period of this work.

I would like to take this opportunity to express my sincere gratitude to Dr. Feng Xianping for his invaluable suggestions and advice during the experimental work of this project. He joined and helped me with the experiments on some occasions.

I am thankful to National Institute of Education, Nanyang Technological University, for hosting my research and providing me with the necessary facilities. I would like to acknowledge Prof. Leo Tan Wee Hin, Director of National Institute of Education, and Dean of School of Science for his support, encouragement and confidence in me.

I am also thankful to the following members of the plasma research group for their help and friendship, in particular: Mr. Suresh Kumar, Dr. Paul Lee, Mr. Zhang Guixin, Dr. Adrian Serban and Miss Cecelia M .N. Selvam.

The cooperation from the General Workshop, in particular from Mr. Michael Ng Yiow Piow and Mr. Lee is acknowledged.

Finally, I wish to dedicate this thesis to all members of my family: my father, my mother, all my sisters and brothers for their moral support from afar in China, and especially, my wife, Du Dongmei, and our child Liu Chang, for their continuous loving support, encouragement and forbearance during my long hours of work and study.

## Abstract

This thesis reports investigations of soft x-ray emission from a compact plasma focus. Experiments were carried out under various operational conditions with (a) three different working gases, neon, argon or deuterium, and (b) with the central electrode operating at initial positive and negative charging voltages.

A current transformer, a Rogowski current derivative coil, a resistive voltage divider, a PIN optical speed detector and magnetic probe arrays were used to study the evolution, gross dynamics, and discharge characteristics of this plasma focus device.

Soft x-rays (SXR) in the spectral regime 3 - 30 Å from the neon plasma focus have been investigated in detail. An x-ray pinhole camera, a pinhole transmission grating spectrograph, a flat crystal spectrograph, a filtered 5-channel PIN soft x-ray detector, a photoelectric effect x-ray detector and an x-ray calorimeter were the diagnostics viewing the x-ray output of the pinched plasma region. The pinhole camera, the pinhole transmission grating spectrograph and the spatially resolved flat crystal spectrograph observed a non-uniform column-like x-ray source with ~ 300 μm diameter and ~ 7 mm length centred at the axis under optimum operational conditions. The x-ray spectrum with high resolution from this neon plasma source is obtained by the flat crystal spectrograph. The x-ray emission is mainly within the wavelength range from 8 Å to 14 Å. The hydrogenlike alpha line (He-α) at 13.447 Å and the helium alpha line (Ly-α) at 12.132 Å are observed to be the most intense features of the neon spectrum, contributing 53 ~ 67% of the total spectrum emission. The x-ray spectrum deduced from the 5-channel PIN detector shows that 44% of the total soft x-ray energy is at 13.447 Å, 20% at 12.132 Å and 36% in the wavelength range of 8 ~ 11.568 Å, which is consistent with the results obtained by the flat crystal spectrograph. The calorimeter is used to measure the total SXR yield. At optimum condition (14 kV, 4 mbar) a total SXR yield of 6 J/shot at source into $4\pi$ steradians is observed from this plasma source.

A radiative plasma focus model was developed. Reflected shock phase and radiative phase are added to the earlier model to simulate the x-ray emission from the plasma focus. Electron temperature of 360 eV and electron density of $10^{26}$ $m^{-3}$ were computed for the uniform radiative compression. Radiation from this compression was also computed. Line radiation comprises 70% of the total x-ray emission. These results show good agreement with the experimentally measured values. The radiative plasma focus model also shows that for a good SXR yield from neon plasma a temperature range of 300 ~ 500 eV is optimum. Computations also indicate the need to reduce circuit inductance. Reduction of stray inductance from 110 nH to 10 nH will result in a 10-fold increase in proportion of stored energy converted into focused plasma energy. SXR yield will rise correspondingly. The results of this thesis form a data base for the development of a high performance, high repetition rate SXR source for lithography applications which is now in progress in our laboratory.

# Table of Contents

# List of Figures

# List of Tables

# Chapter 1

# Introduction

## 1.1 Introduction

Since the original experiments of Roentgen, x-rays have become a most versatile tool for fundamental research and applications spanning physical, chemical and life sciences as well as materials technology, engineering and medicine. X-rays, including x-ray sources, their measurements and applications, have been extensively investigated. The stream of technological innovations using information derived from x-ray investigation includes semiconductor materials and devices, catalysts, magnetic storage media, drugs and enzyme analysis, micromachined components, chemical and mechanical sensors.

Some modern uses and applications of x-rays cover [1]:

- digital subtraction angiography
- x-ray diffraction
- EXAFS (Extended X-ray Absorption Fine Structure)
- x-ray microscopy

- x-ray astronomy
- x-ray tomography
- x-ray used for plasma diagnostics
- x-ray lithography and
- medical and dental radiography, etc.

The studies of x-ray radiation from plasmas began to play an important role from 1930 [2], when x-ray emission from plasmas was first observed by Edle`n and Erikon [3], Ekefors [4] and others in high voltage vacuum sparks. Spectrometers, e.g. grazing incidence spectrometer, were used to identify line spectra of highly ionized atoms during that period of time. Much more attention has been concentrated on this subject since 1960, when several plasma devices developed for nuclear fusion research were observed to emit strong x-ray spectra. A great deal of work has been done showing that x-rays radiated from plasmas (laboratory produced or solar plasmas) cover a wide range of spectra, intensities, and temporal profiles (continuous and pulsed) and thus are capable of being widely used in various applications.

It can be seen that laboratory plasma devices, including those built for nuclear fusion research, have enriched our knowledge of x-rays, their diagnostics and various kinds of applications. Dense (Compact) Plasma Focus (DPF or CPF) is one type of these plasma facilities.

## 1.2 X-ray Sources

### 1.2.1 X-ray Emission Process

An important component in connection with x-ray studies is the source. Demand for higher energy, more powerful sources for industrial applications has increased recently.

X-rays are produced in two main types of process: acceleration of charged particles (usually electrons) and when an electron changes from an atomic or ionic energy level to a lower one. Examples of the first type are synchrotron radiation (from relativistic charged particles caused to travel in curved paths by magnetic fields) and Bremsstrahlung (from electrons decelerated by collisions with heavy nuclei). These normally give continuous spectra, although it is possible to obtain quasi-monochromatic lines from insertion devices (undulators) in storage rings (synchrotron sources). The second type of process, which occurs when electrons bombard a low atomic number target or when a plasma is formed from a low atomic number material, gives discrete line spectra. Highly ionized plasmas can be made to behave as x-ray lasers. Other processes [5] such as transition radiation (which occurs when a particle crosses an interface between two materials) and channeling radiation (which occurs when a particle moves along channels formed by planes in a crystal) can give rise to x-rays, but as yet no sources using them have been built.

Generally, x-ray sources can be divided into four main groups, i.e.: 1) Solid target sources, 2) Synchrotron radiation, 3) Plasmas and 4) X-ray lasers. A comparison of different sources concerning their applications on x-ray lithography is given in Ref. [6].

### 1.2.2 X-rays from Plasma Focus

Pinch plasmas are promising as emitters of soft x-ray pulses with duration from nanoseconds to hundreds of nanoseconds. In general they enjoy growing interest for the following applications:

(1) production of soft x-rays in the energy range from 1 Å to beyond 200 Å ($h\nu$<12.3keV) for (a) x-ray microscopy [7-10] and x-ray lithography [6,11,12];

(2) basic research in spectroscopy and plasma physics [13-15];

(3) measurement of the population dynamics of transient plasma producing data for comparison of experimental with plasma modelling in order to predict soft x-ray laser action [16,17].

The emitted x-ray energy per pulse from z-pinch devices is higher than the one produced by other available sources. The Plasma Focus (PF) is a special z-pinch-like device capable of producing plasma electron density $N_e > 10^{20}$ cm$^{-3}$ and temperature $T_e > 500$eV. Because of its simple construction, cost-effectiveness and easy maintenance, the plasma focus appears to be a promising device for x-rays. Experiments show that the radiation spectrum of the plasma focus in the x-ray region covers a large range from below 1 keV up to 500 keV in a time span ranging from a few nanoseconds to a few hundred nanoseconds [18].

Since early 1960's the plasma focus has been studied as a nuclear fusion facility. The research has been more concentrated on improving neutron yield usually using deuterium as the working gas, although argon plasma (or other noble gas seeded deuterium plasma) has been used to produce more intense bursts of x-rays.

The emission of x-rays from DPF is characterized by high intensity and wide spectral range. The pinched plasma is column-like and viewed end-on appears like a point. Because of these distinct characteristics DPFs are suitable to be used as a pulsed point source for some special applications such as microscopy, x-ray lithography, etc. One of the promising applications is x-ray lithography. The present project studies a small plasma focus for its characteristics in the context of lithography.

## 1.3 Plasma Focus: Candidate of Soft X-ray (SXR) Source for X-ray Lithography

### 1.3.1 X-ray Lithography

X-ray lithography is an advanced technology for ULSI (ultra large scale integrated) manufacturing. Since R. Kilby and R.Noyce invented the first integrated circuit (IC) in 1961, the number of devices that can be fabricated on semiconductor substrates, typically silicon wafers, has steadily increased [19]. Simultaneous fabrication of millions of electronic devices on a single silicon wafer reduces the cost and improves the performance and reliability of electrical circuits. The impetus comes from both the increased memory requirements of DRAM (dynamic random access memory) and also from the speed needs of SRAM (static RAM).

The "size" of each element , the so called critical dimension (CD), has decreased from >20μm in early 60s to ~ 0.35μm in today's state of art 64 Mbits DRAMs. Miniaturization of electronic devices gives high density, high speed and low threshold voltage - all beneficial properties. DRAMs have the largest production volume among the IC devices. In the past 20 years, they have been the technology driver. The general trends of DRAM evolution are given by Moore's law, which predicts 4X increase of bits in A DRAM chip every 3 years. Table 1.1 shows such a evolution chart [20].

***Table 1.1.*** IC product evolution

| DRAM generation | First Mfg. Year | Chip Size ($mm^2$) | CD (μm) | LW Control (nm) | Overlay Accuracy (nm) |
|---|---|---|---|---|---|
| 4 Mb | 1989 | 80-90 | 0.7 | 70 | 240 |
| 16 Mb | 1991 | 120-140 | 0.5 | 50 | 170 |
| 64 Mb | 1994 | 170-200 | 0.35 | 35 | 120 |
| 256 Mb | 1997 | 250-300 | 0.25 | 25 | 80 |
| 1 Gb | 2000 | 350-400 | 0.18 | 18 | 60 |

note: CD is critical dimension, LW is line width

Silicon, a semiconductor, forms the basic starting material for a large class of integrated circuits. In the six processing steps lithography is the technique to print patterns onto the silicon wafer [21,22] for subsequent etching, deposition, or implanting. It is one of the key elements of semiconductor (microelectronics) manufacturing. The development of new IC devices relies on the evolution of processing technologies, especially lithography. Lithography determines the minimal feature size on a IC chip. It is the single most expensive processing step in today's IC fabrication, accounting for more than 30% of the manufacturing cost.

The use of soft x-rays (~ 10 Å wavelength) for lithography has several advantages. The diffraction effect that limits optical proximity lithography is greatly reduced by the short wavelength. X-ray proximity lithography can be used at larger gaps (10 - 50 μm) whilst retaining a very high resolution. Particles such as skin flakes are transparent to x-rays at this wavelength range.

### 1.3.2 Plasma Focus as a Source of Choice for X-ray Lithography

To develop x-ray lithography for industrial applications, a bright soft x-ray source has become important. The two main approaches being pursued for such sources are: the multi-beam synchrotron orbital radiation source (SOR), and single-beam point sources of various types. Point sources are generally less complex and much cheaper than the SOR source, however issues of SXR flux and exposure field uniformity are critical for point sources if they are to match the performance of the SOR source. The point source concepts which have been investigated are plasma sources such as laser-plasma, z-pinch device, dense plasma focus device, etc. Among these sources, it is known that plasma focus is very compact, cost-effective and easy to maintain.

Recent investigations with plasma focus sources designed specifically for SXR proximity lithography appear promising [11,23-25]. X-ray output of up to several hundred watts, in the wavelength range from 8 to

14 Å has been achieved [11,25]. There are still a lot of question marks in this area. Work has to be done on this so as to meet the requirements by industry. But before approaching the stage of application, some fundamental investigations must be conducted, which leads to the necessity of this project work.

## 1.4 Scope of Research

Studies on neon plasma focus are still very limited thus far. This project is mainly intended for studying the characteristics of x-ray emission from a compact plasma focus operated in neon both experimentally and by theoretical modelling. The studies include:

(a) diagnostic methods for measuring x-ray radiation from plasma focus (spectral, spatial, temporal and total fluence characteristics of x-ray emission, mainly from neon plasmas);

(b) mechanisms of plasma focus x-ray emission (origins of the emission and their contributions to the total yield);

(c) dependence of the x-ray emission on operating parameters (working gas, its filling pressure, charging voltage and its polarity, etc.) and regimes;

(d) characteristics of the x-ray emission from neon plasma focus;

(e) using the information from x-ray radiation to reveal relevant plasma phenomena;

(f) comparison of dynamic characteristics among neon, argon and deuterium plasmas by using magnetic probing, optical probing and using the help of physical model.

To study the gross dynamics of plasma focus in neon, a speed detector made of photodiodes was built to detect the optical luminous front to get the maximum axial speed. Magnetic probes were used to obtain the current shedding factor as well as the current profile in the axial run down phase.

Several diagnostics were developed and employed to perform detailed measurements on x-ray emission as well as basic parameters from the small plasma focus. A pinhole camera was used to obtain the side-on and end-on time-integrated x-ray source image. A pinhole transmission grating spectrograph was set up to survey the gross spatially resolved x-ray spectrum. A flat crystal spectrograph was developed to measure spatially resolved x-ray spectrum with high resolution. A 5-channel PIN detector was used to obtain the time-resolved x-ray signal and also to estimate the total x-ray yield. A SXR detector based on the photoelectric effect was fabricated and used to measure the time-resolved x-ray signal. A calorimeter detector for absolute flux measurement was employed.

With the help of x-ray spectrum information we obtained 1) the electron temperature by means of relative line or continuum intensity; 2) the electron density by comparing with the density-sensitive satellite lines.

A model concerning x-ray emission based on Lee's model [26] was developed to theoretically simulate the procedure. The model has included the finite small disturbance speed between the shock front and the magnetic piston to solve some problems encountered by the previous model. More realistic results are obtained. The model has also shown its possibility for optimizing neon plasma focus for larger x-ray output.

The theoretical results were compared with experimental results. Some general conclusions about x-radiations from plasma focus were obtained providing a better understanding for both the experiments and the model itself.

The experimental results were obtained in the small NIE-SSC-PFF (National Institute of Education - School of Science - Plasma Focus

Facility) plasma focus. With the help of modelling, however, it is possible to extract the common points for DPF and some of the features can be generalized enabling us to check and design other devices which are dedicated for effective x-ray production.

## 1.5 Layout of this Thesis

The thesis is organized as follows:

Chapter 2 (Plasma Focus and X-ray Emission) describes general aspects of the plasma focus device and gives an overview of its dynamics. Following that is a short review of works done by other researchers on the area of x-ray emission from plasmas, especially from DPF.

In Chapter 3 (Radiative Plasma Focus Model), radiative plasma focus model is introduced in detail. A part of the results is discussed. This mainly includes some general conclusions of the x-rays from plasma focus device operated in neon. Some of the numerical results are left to be discussed in Chapter 5 for comparison with the experimental results.

Chapter 4 (Apparatus and Diagnostic Techniques) describes in detail the NIE-SSC-PFF plasma focus facility, the diagnostic techniques and experimental set-up to be used for this project. The first section introduces the details of the plasma focus facility. The conventional monitors like voltage, current and current derivative probes are in the second section followed by a description of the magnetic probe, and the speed detector. In the final part the x-ray diagnostics (pinhole imaging, pinhole transmission grating, flat crystal spectrograph, 5-channel PIN detector, flux calorimeter) are described.

Chapter 5 presents the experimental results. Some basic measurements, e.g. current, tube voltage, optical and magnetic probings on neon plasma focus are shown. Then results from various x-ray diagnostics such as the pinhole imaging, pinhole transmission grating spectrograph, crystal spectrograph and absolute x-ray yield determination, etc. are presented. Plasma parameters are evaluated from these measurements. A discussion of optimizing plasma focus for soft x-ray radiation is followed.

Chapter 6 (Conclusions and Suggested Future Work) contains the summary of the results and interpretations, the conclusions and suggested future research work.

# Chapter 2

# Plasma Focus and X-ray Emission

## 2.1 Introduction

The plasma focus was discovered independently by Mather (USA) [27] and Filippov (USSR) [28] in 1965, although the devices investigated by these two pioneers had significantly different geometries. Many plasma focus devices have since been built by other investigators, but all broadly conform to one of the two original geometries, and can be classified as being either of the Mather or Filippov type. These devices have been built with stored bank energy ranging from 1 kJ to 1 MJ with consequent variation in the physical sizes of the device. The plasma focus is well known as both a source of fusion neutrons and a source of x-rays (Mather 1965 [90]). Since 1965 a large range of investigations has been performed on both types.

The early work on the plasma focus has shown that in this device a hot (~1 keV) and dense (~$10^{19}$ $cm^{-3}$) plasma is created with a lifetime ~ 50 ns. Considerable interest was directed on this device because of the high $n\tau$ ($n$: number density, $\tau$: energy confined time) value of the plasma and the readily detected bursts of fusion neutrons when operated in deuterium. Besides being a ready source of hot dense plasma and fusion neutrons the focus also emits copious amounts of soft x-rays, especially when operated with high $Z$ gases rather than deuterium. This distinctive feature of the plasma focus sets it apart from other devices as a prime candidate for the application of x-ray lithography.

It is known that the plasma focus is a very complex and rich source of phenomena. The details for these will not be reviewed in this thesis. Excellent review works can be found in Refs. [29-33]. In this thesis only the x-ray related characteristics are introduced.

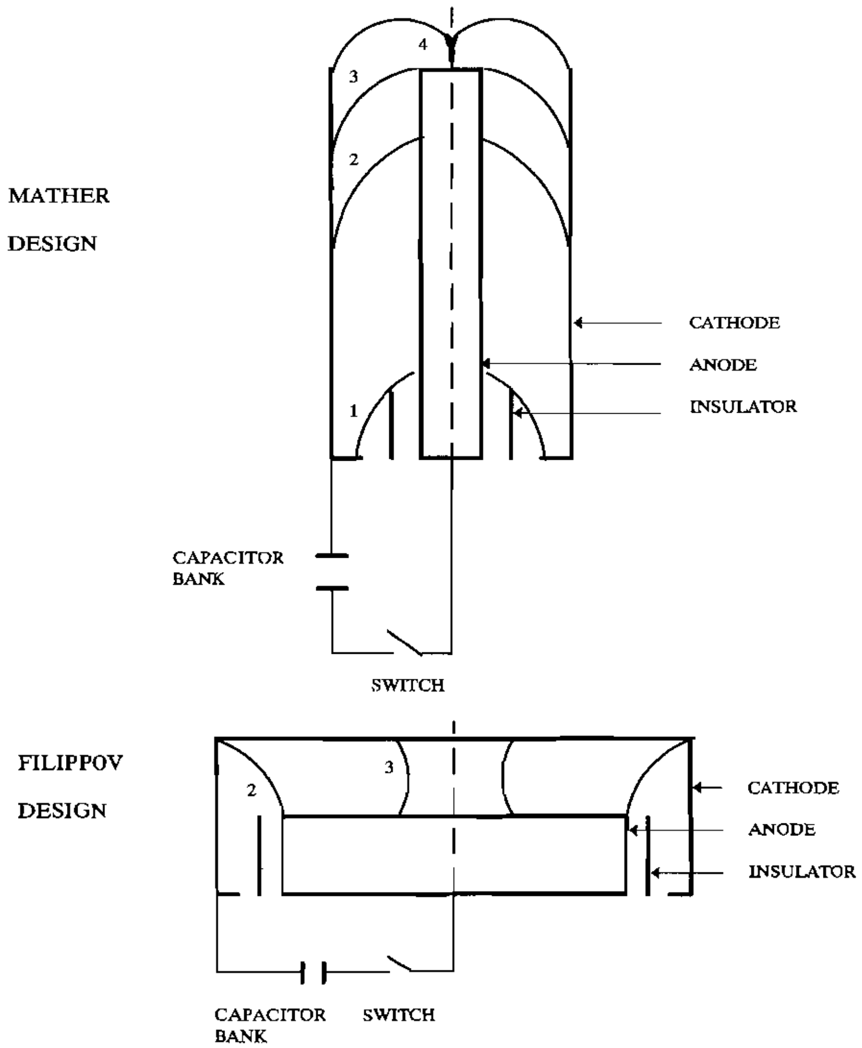


**FIGURE 2.1**
Schematic drawings of Mather-type and Filippov-type Dense Plasma Focus devices

The Plasma Focus is a two-dimensional Z-pinch formed on or near the axis at the end of a coaxial plasma accelerator. Basic details of the Mather-type and Filippov-type plasma focus electrode geometries are illustrated in Fig.2.1.

The Filippov machine was developed as a modification of the straight Z-pinch to "hide" the insulator zone from the pinch region and prevent restrikes caused by radiation from the hot plasma. The Mather-type device was modified from the coaxial plasma gun operated at higher fill pressure.

The operating principle of the DPF is simple: the energy stored electrically in a capacitor bank is rapidly transferred to the electrodes by means of a fast switch. In both geometries the current discharge initiates along the surface of cylindrical insulator in a coaxial electrode region (see 1 in Fig.2.1). By the Lorentz force action the conducting plasma sheath accelerates from position 1 through position 2 to position 3 (same figure). In 4 the sheath reaches the axis of symmetry of the electrodes. In the figure of the Filippov-type geometry, positions 1 and 4 are not shown.

To optimize the machine one chooses the dimensions of the electrodes (length and diameters) and the operational pressure in relationship with the characteristics of the energy source so that the current is maximum when the sheath reaches the axis. At this instant a filament of hot and dense plasma (pinch) is formed in front of the inner electrode (usually the anode). After a very short time due to instabilities the plasma column breaks up and decays. Details of the time scale and other plasma parameters will be given later.

The obvious differences between the two configurations lie in the electrode dimensions and the aspect ratio (diameter/length) of the inner electrode. The Filippov-type device has a large aspect ratio, usually greater than 5 with the inner electrode diameter of 50 ~ 200 cm. The Mather-type device has a small aspect ratio of typically below 0.25, with an inner electrode diameter of 2 ~ 22 cm. The electrodes are usually made of copper or stainless steel. The anode may be a solid cylinder or a cylindrical tube in order to avoid excessive hard x-ray emission due to electron bombardment. The cathode is in the form of a squirrel cage consisting of 6 ~ 24 rods arranged eccentrically around the anode. The insulator may be made of Pyrex, glass, alumina or ceramic.

Similarities between these devices are in (i) the dynamics of the current sheath, (ii) the scaling laws [34-39] for neutron emission and (iii) the emission of energetic ion and electron beams, x- rays, microwaves etc.

## 2.2 Dynamics of Plasma Focus

Our interest in this project work is on the Mather-type plasma focus device as the electrode assembly in our DPF facility is of that kind.

The study of plasma focus dynamics can be divided into three distinct phases: the breakdown phase, the axial acceleration phase (or axial rundown phase) and the radial phase (or radial collapse phase).

### 2.2.1 The Breakdown Phase

When the high voltage pulse is applied between the electrodes of the DPF device filled up with the working gas under an appropriate pressure (usually several mbar Hydrogen or Deuterium, Neon, Argon), an azimuthal symmetric electrical discharge will be initiated. This discharge is preceded by an electrical breakdown phase which generates an initial plasma configuration through which the discharge current can flow. According to Paschen's law [40] the values of the static breakdown voltage in any DPF operating with 1 ~ 10 mbar deuterium are lower than 1 kV (for DC voltage), which is one order of magnitude smaller than the usual (10 ~ 60 kV) capacitor bank voltage. Therefore the breakdown is always a highly overvolted phenomenon.

The development of the high current discharge in a DPF depends substantially on the initial gas conditions [41,42], the parameters of the electrodes [43,44] and insulator [41,42,45,46] and the polarity. The initial rate of current rise which depends on the inductance and charging voltage of the electrical circuit also play significant roles. For optimized conditions a sliding discharge (or gliding discharge) will develop along the insulator.

The process can be explained by the effect of a surface capacitance. Before applying the high voltage, free charged particles drift towards the surface of the electrodes as well as towards the insulator because of the image forces. Free electrons in the vicinity of the insulator tend to create a negative potential at the insulator surface because of the dielectric constant of the material (usually $\varepsilon_r>1$) and high surface resistivity. On applying high voltage to the electrodes a time delay of some tens of nanosecond is observed [41] before breakdown along the insulator surface. During this time further electrons are created by field emission from metallic edges and ionization of the ambient gas. These electrons are accelerated along the field lines of mainly radially directed electric field towards the inner electrode and the insulator surface, or the outer electrode, depending upon the polarity of the applied voltage. As the discharge develops the surface capacitance is charged gradually while the highest electric field remains at the front of the discharge. This effect assists the propagation of the ionization front along the insulator. When the sliding discharge reaches the end of the insulator it connects both electrodes. Due to the $\boldsymbol{j}\times\boldsymbol{B}$ force the current is lifted off in an inverse pinch manner. After some time (50 ~ 500 ns) the conductance of the sliding discharge becomes high enough and the discharge converts into a plasma sheath, in fact a double-layer structure consisting of the ionization front and the magnetic piston [29,47,48]. This is the end of the breakdown phase and the focus formation process will enter into the second phase, the axial rundown phase.

Monitoring the voltage across the electrodes of a DPF machine, usually, an initial voltage rise is noticed, followed by a voltage drop determined by the breakdown development and parameters of the electrical circuit, as shown in Fig.2.2.

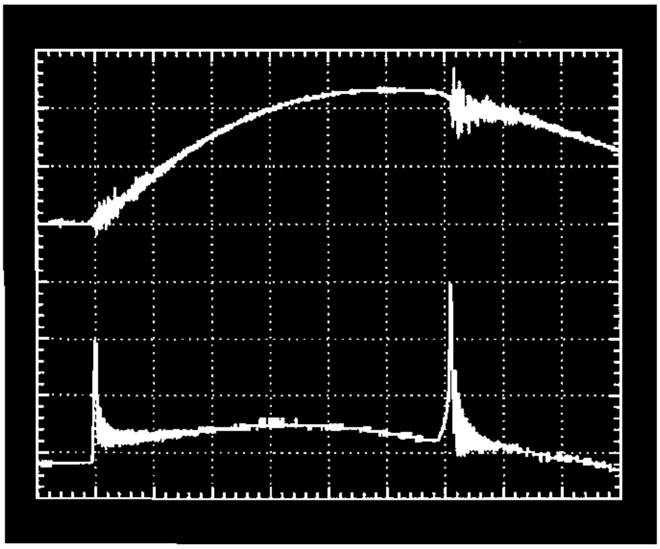

**FIGURE 2.2**
Typical waveforms of the current (upper trace)
and voltage (lower trace)
time scale: 500 ns/div

According to Bostick *et al.* [47], additional to the primary sliding discharge, filamentary radial discharges are often observed.

Mather [29] reported that a singular, azimuthal symmetric prompt initiation of discharge is required for the current sheath to develop. Using a fast image converter camera he confirmed that when the discharge was non-symmetrical, or some radial spokes occurred within the interelectrode region, then the neutron and x-ray yield was lower compared to the normal operation.

Donges *et al.* [41] reported that the discharge occurs at the open end of the accelerator or within the whole interelectrode volume if the initial pressure in the plasma focus vessel is too low, normally below 0.1 mbar. On the other hand, when the pressure value is too high (above 10 mbar for deuterium, 20 mbar for neon) we assist to a radial filamentary discharge between the coaxial electrodes [42] may occur.

Borowiecki *et al.* [44] used various electrode-insulator configurations during the optimization of a 13 kJ plasma focus device. They found that when a knife-edge cathode was used, the breakdown conditions were improved and the system performance turned out to be more reliable and reproducible.

The work done on Poseidon and PF-360 experiments [49] revealed the great importance of the insulator material on neutron yield saturation of the plasma focus, particularly when the input electrical energy exceeds several hundred kilo-joules. In the Poseidon the neutron yield starts to saturate at 300 kJ when Pyrex insulator is used. The situation was considerably improved using a ceramic insulator.

In order to describe the breakdown phase different computational models have been developed. Kolesnikov [50] proposed the first 1-D model. Later, 2-D 2-fluid [51,52] and 2-D 3-fluid [53] MHD models assuming a thin plasma layer or ionized gas as initial conditions were developed for the entire evolution of the plasma focus discharge until the final pinch phase.

### 2.2.2 The Axial Rundown Phase

The next stage of the evolution of plasma focus discharge is known as the axial rundown phase or axial acceleration phase or simply, axial phase. It consists in the propagation of a magnetically driven plasma sheath along the z-axis towards the open end of the electrodes (position 3 in Fig.2.1).

The axial phase is relevant for the subsequent formation of the hot and dense plasma (pinch) in two aspects: (i) the current sheath should arrive to the axis in coincidence with or near the first maximum of the discharge current and (ii) the structure and the $(r, z)$ profile of the plasma sheath should have certain characteristics for a good focusing effect. The first condition is a common requirement to all pinch devices representing the optimization of the energy transfer from the power source (capacitor bank) to the pinch plasma. The duration of the axial phase is usually 1 ~ 4 μs. The second condition includes requirements of axial symmetry, smooth $(r, z)$ profiles and a thin, uniform current sheath structure.

Due to the large values of the discharge current and the low pressures values of the working gas, the sheath pushed by the ***J*x*B*** force moves against a stationary neutral gas, practically, from the very beginning, at supersonic speeds. The mean free paths for both ion-atom charge exchange and elastic collisions are very small in the usual range of filling pressures, hence the moving structure produces a gas-dynamic shock which heats and compresses the neutral gas in its front. Therefore, the sheath will have a complex structure with a compressed and hot neutral layer followed by an ionizing region, a plasma region carrying the current at its trailing edge and a nearly vacuum magnetic field region. The complete structure of the sheath is determined by the pattern of the current that drives it (see the breakdown phase); if this pattern is uniform, the plasma structure will be likewise, while an azimuthal filamented pattern will produce a filamentary structured sheath [48,54,55].

Magnetic probes measurements (detecting only the magnetic piston) optical and spectroscopic diagnostic techniques (Schlieren, shadow and interferometric arrangements, image converter cameras or other light detecting systems) are usually employed for the axial rundown phase. Axial sheath velocities ranging from 1.7 to 15 cm/μs were measured [56,57]. It was found that large fractions (up to 50%) of the current going into the device flow behind the current sheath especially in large DPF machines [58,59]. The thickness of the plasma sheath structure is about 2 ~ 3 cm [60]. Due to the $1/r$ dependence of the magnetic field within the interelectrode region, the current sheath profiles are curved $(r,z)$

functions. The current sheath, maintaining its axisymmetric character, acquires a parabolic shape [61] being thinner in the region near the central electrode [62].

Theoretical descriptions of the dynamics of the axial rundown phase frequently use the so called "snowplow model" (either 1-D or 2-D [63,64]) which have proven to predict reasonably well the current sheath velocity and duration of the phase [65-68] and in its 2-D version also, the profile [69]. The fitting of experimental data to the model requires the introduction of a so called "sweeping efficiency" or mass loss factor interpreted as an incomplete sweeping of the filling gas and a current factor to take into account the current shedding effect. Several other computational models like 2-D 2 fluid time dependent [51], 1-D 3 fluid time dependent [53] and 2-D 3 fluid time dependent [70] MHD codes have been also developed.

At the end of the axial rundown phase, the inner end of the current sheath sweeps around the end of the anode. The outer end of the current sheath continues up the tube sweeping along with it the greater portion of the accumulated plasma in the axial direction. Only a small fraction of the plasma at the end of the axial phase will contribute to the final focus.

### 2.2.3 The Radial Phase

At the end of the axial rundown phase, the current sheath sweeps around the end of the inner electrode (anode) and finally collapses due to the radially inward $\boldsymbol{J}\times\boldsymbol{B}$ force (see position 3 to position 4 in Fig.2.1) in approx. 50 ~ 200 ns, depending on the DPF machine characteristics. This process is similar to Z-pinch phenomenon, but the pinching effect occurs much more rapidly, with enhanced compression and plasma heating.

The radial phase leading to the pinch as the final stage of plasma compression plays the most important role in the plasma focus evolution due to its extremely high energy density, its transient character and for being a rich source of phenomena like emission of intense radiation, high energy particles as well as copious nuclear fusion products.

Using the available experimental data reported, the following paragraphs will describe the radial phase divided into four sub-phases: (i) compression phase, (ii) quiescent phase, (iii) unstable phase and (iv) decay phase [71].

### 2.2.3.1 The Compression Phase

This phase begins with the sweeping of the current sheath around the end of the central electrode, collapses radially with azimuthal symmetry, with a non-cylindrical, funnel-shaped profile and ends when the plasma column reaches the minimum radius when plasma density is at its maximum ($n_e \sim 10^{19}$ cm$^{-3}$).

The main heating mechanism inside the plasma before the front of the current sheath meets along the z-axis is shock heating. Therefore, the electrons with temperature of about 100 eV are cold compared to the ions whose temperature is around 300 eV depending on the speed of gas [72]. After the transformation of plasma structure to plasma column, Joule heating becomes the main heating mechanism [48]. This plasma column will be compressed adiabatically [72] further to form the final focus. Peacock *et al.* [73] observed the onset of the Rayleigh-Taylor instability about 30 ns before the end of this phase. This type of instability is damped out when the radial velocity is diminishing [74].

Towards the end of this phase the magnetic field starts diffusing into the plasma column. Very quickly it will be completely diffused leading to an anomalous high plasma resistance. Also, the inductance of the system is increased [75]. The sharp voltage spike and the current dip (see Fig.2.2) are features typical of a focusing discharge where the large increase of the plasma column impedance has occurred. The high frequency oscillations at the beginning of the signal and also during the focus phase are due to the transmission line connecting the capacitor bank to the electrodes [76]. Final electron temperature will be around 1 - 2 keV. Maximum values of electron density and electron (ion) temperature have been determined by spectroscopy [77], interferometry [71], laser scattering [48] and other methods.

It is often assumed that a Bennett equilibrium exists in the pinch phase, according to which the final temperature should depend only on the current $I$ and the line density $N$ : $T \sim I^2/N$; the lower the line density, the higher the temperature.

Simple computational physical models have been constructed for the radial phase based on the snowplow equation. As is well known this model when applied to a radial compression gives a zero-radius column. Attempts have been made to overcome this by devising a retarding kinetic pressure term. Other attempts use criteria for the minimum radius such as the Larmor radius. However, Lee [78] had shown that these methods are not energy-consistent and therefore should be replaced by an energy balance model which provides the correct end-point for the implosion trajectory, thus giving the correct quasi-equilibrium radius. Combining the conventional snowplow model with an energy-balance criterion enables a complete energy-consistent trajectory to be obtained [79]. Also, the computed pinch length and minimum radius are in agreement with the experimental values.

### 2.2.3.2 The Quiescent Phase

This phase marks the beginning of the expansion of the pinch plasma column.

During this phase of expansion which occurs in radial as well as axial direction, the rate of radial expansion is hindered by the confining magnetic pressure. But due to the "fountain" like geometry of the current sheath, the rate of the axial expansion is unhindered resulting in the formation of an axial shock front.

The sharp change in plasma inductance (started during the compression phase) induces electric field in the plasma column. This electric field will accelerate the ions and the electrons in opposite direction. The relative drift velocity between the electrons and ions will increase and approach the increasing electron thermal velocity. This is the condition for the onset of the microinstabilities such as the electron cyclotron and various forms of beam-plasma instability.

At the end of the quiescent phase the $m$=0 instability develops rapidly due to increasing electron temperature. The plasma column will be compressed again, this time locally due, to the $m$=0 instabilities.

Based on these observations, one can define the pinch lifetime $t_p$ as the time between the first compression and the instant when the $m$=0 instability occurs [33]. The pinch lifetime $t_p$ is correlated with the total neutron yield $Y_n$ as follows: the shorter $t_p$, the higher $Y_n$ for fixed discharge parameters. In comparison to radial Alfvèn transit time of the pinch column, $t_p$ is many times larger, the reason being attributed to strong axial flow, two-dimensional curvature of the current flow, $\boldsymbol{B}\times\nabla\boldsymbol{B}$ drift or the influence of self generated axial magnetic fields.

The length of the pinch column as well as the minimum radius scale to the radius of the central electrode [80-82].

#### 2.2.3.3 The Unstable Phase

The unstable phase is the richest stage of the plasma focus evolution in associated phenomena like soft and hard x-ray emission, fast deuterons and electrons and D-D reaction products (neutrons, protons) if operated in deuterium.

An induced electric field is enhanced locally due to growing $m$=0 instabilities. Therefore, electrons are accelerated towards the inner electrode and ions in opposite direction. Plasma density increases again up to $10^{19}$ cm$^{-3}$.

A fairly large amount of impurities is injected into the plasma column due to the bombardment of accelerated runaway electrons on the anode. The explosion proceeds sequentially along the plasma column. This breaking up corresponds to the second density gradient in the interferometric holograms [48]. This density gradient moves away from the anode slower (20 cm/μs) than the ionization front.

This disruption of the plasma column continues until the whole plasma column has been broken up completely. The plasma density drops. The calculated electron drift velocity from the current density is about $2x10^7$ m/s, which is definitely greater than the electron thermal velocity of $6x10^6$ m/s estimated from the electron temperature. The condition for the onset of microinstabilities is met. This gives also rise to strong plasma heating. As indicated by the large amount of measured Bremsstrahlung radiation the electron temperatures increases up to 4 ~ 5 keV.

#### 2.2.3.4 The Decay Phase

The last phase of the radial collapse and also the last stage of the plasma focus dynamics is the decay phase. The plasma density drops below $2x10^{17}$ $cm^{-3}$.

During the decay phase a large, hot and thin plasma cloud is formed due to the complete breaking up of the plasma column. This plasma cloud emits a large amount of Bremsstrahlung radiation. The soft x-ray emission rises sharply during the pinch decay, it reaches a first peak shortly after the pinch break-up and continues at a high, almost constant level for over 300 ns [83]. The neutron pulse which started from the beginning of the unstable phase reaches its peak during this phase.

## 2.3 X-ray Radiation from Plasma Focus

### 2.3.1 X-ray Emission Processes in Plasmas

#### 2.3.1.1 General

A plasma consists of a collection of electrons and ions and is formed when matter is brought to a highly ionized state. This process of ionization is caused by raising the temperature to a very high level, typically, ~ $5\text{x}10^5$ - $10^7$ K or ~ 50 eV - 1 keV. Such high temperatures exist naturally in stellar atmospheres and can be produced on earth in nuclear explosions or, in a more controlled way by, e.g., pinch devices, tokamaks, sparks and pulsed laser beam focused on to a solid or in a gas.

At a temperature $T_{eV}$ the peak of the blackbody emission spectrum is at a wavelength, in angstrom,

$$\lambda_{peak} = 2500\ T_{eV}^{-1} \tag{2.1}$$

This is known as the Wien displacement law. For the given temperature (above) range, $\lambda_{peak}$ ~ 50 - 2.5 Å, i.e., in the x-ray range. The integrated emitted power $P$(W.m$^{-2}$) is

$$P = 1.03\text{x}10^9\ T_{eV}^4 \tag{2.2}$$

and, typically, useful plasmas have dimensions of ~ 10 - 100 microns (typical size of the localized micropinchs), giving emitted powers of ~ $10^7$ - $10^{10}$ W (the higher temperature plasmas are smaller). Thus plasmas can be very intense x-ray emitters.

The above estimation gives us a conceptual idea of emission from plasmas although generally laboratory plasmas may not be considered as blackbody which is the strongest emitting source compared to any other source (Kochekov Law).

#### 2.3.1.2 Emission Processes

Processes in the plasma which give rise to continuum emission include Bremsstrahlung, from the coulomb interactions between electrons and ions, and recombination radiation, which is emitted by an initially free electron as it loses energy on recombination with an ion. If an already bound electron loses energy by falling to a lower ionic energy state then a line spectrum is obtained. The relative strengths of the continuum and line emissions depend on how the plasma was formed; typically, for a plasma formed from a high-$Z$ material continuum emission dominates, while for a low-$Z$ material line emission can be stronger.

The calculation of the power emitted by processes within the plasma depends on assumptions made about the state of the plasma. Below, the emission processes are qualitatively described.

*Bound-Bound Transitions*

When an electron bound in an ion makes a transition to another bound state of lower energy, a photon with well-defined energy is emitted (Fig.2.3). The spectral line shape depends on the spontaneous lifetime of the upper state (natural broadening), the velocity distribution of the emitting ions (Doppler broadening), perturbations caused by collisions (collisional broadening) and by the influence of electric and magnetic fields (Stark and Zeeman effects). The emitted radiation may also interact with other particles in the plasma (e.g., it may be absorbed) which can distort the line profile. Thus the line profile can give much information about the state of the plasma.

Prior to emission the bound electron has to be excited to a higher energy state, which can take place either by absorption of photons or by collisions with other particles, primarily electrons. At very high temperatures the material will be totally ionized so that bound-bound radiation no longer occurs.

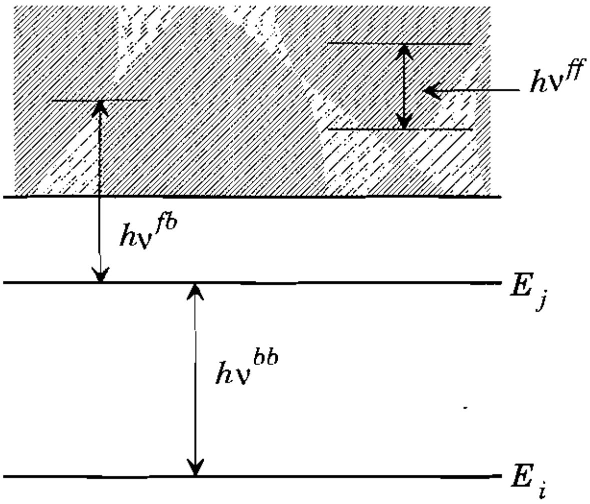


**FIGURE 2.3**
Bound-bound, free-bound and free-free transitions

*Free-Bound Transitions*

A free electron can be captured into a bound state of an ion, thereby reducing the ionic charge by unity. Any excess energy of the electron may be emitted as a photon, giving free-bound or recombination radiation (Fig.2.3). The emission spectrum is a continuum for each bound state with a low-frequency cut-off, the recombination limits, corresponding to the minimum energy needed to remove the electron from the bound state. The shape of the spectrum depends on the free-electron energy distribution and on the energy-dependent capture cross section into the bound state.

A process that competes with this radiative recombination is three-body recombination. This occurs when two free electrons simultaneously collide with ion, one being captured and the other carrying away the excess energy. No radiation is emitted, and so this process, which becomes more probable at higher densities, should in principle be minimized in a plasma to be used as a continuum x-ray source. However, because high electron densities are necessary in x-ray sources, this is not possible in practice. Another process which does not result in radiation is dielectronic recombination.

*Free-Free Transitions*

When a free electron collides with another particle it is decelerated, i.e., it loses energy and makes a transition to a lower energy free state. The excess energy, with a continuum spectrum, is emitted as free-free radiation, i.e., Bremsstrahlung.

In highly ionized high-$Z$ plasma Bremsstrahlung can be a dominant radiation process, with a spectral emission coefficient per unit wavelength peaking at about $6200/T_e$[eV] Å. The emission decreases rapidly with decreasing wavelength.

*Cyclotron Radiation*

In a plasma with a strong magnetic field, such as used to form a pinch plasma, there is another type of emission called cyclotron radiation. The power emitted as cyclotron radiation is ( for a plasma in which the ions are hydrogenic) [84]

$$P_C = 4.4\text{x}10^{-28}\, n_e B^2 T_e \tag{2.3}$$

The ratio of the powers emitted as Bremsstrahlung to that emitted as cyclotron radiation is (for a plasma in which the ions are hydrogenic)

$$\frac{P_B}{P_C} \approx \frac{\omega_P^4}{\omega_C^4}\frac{Z^2 E_H}{T_e} \tag{2.4}$$

where $Z$ is the charge on the ions and $E_H$ = 13.6 eV is the ionization energy of the ground state of hydrogen. For pinch plasmas this shows that, for $P_C$ to be comparable to $P_B$, magnetic flux densities of at least ~ 100 Tesla are required, which is clearly not possible. Thus cyclotron radiation is negligible and will not be considered for the rest of this thesis.

*Other radiation Processes*

There are many other processes which could give rise to radiation from plasmas, but they can safely be ignored except under very special circumstances. They will not be reviewed in detail here and will not, like cyclotron radiation, be considered hereafter.

#### 2.3.1.3 Plasma Sources for X-rays

Common plasma sources, nowadays, are laser-generated plasmas (LGPs) and various types of pinch plasma. In LGPs a pulsed laser beam is focused to a small spot on a solid target, which is heated to a sufficiently high temperature to form the required plasma [85].

The most common type of pinch-plasma sources are the gas-puff z-pinch [86] and plasma focus. An advantage of the z-pinch, over the LGP, is the higher overall conversion efficiency of input electrical power to x-ray emission. Disadvantages of the z-pinch include the smaller range of materials available to form the plasma - the material must be gaseous - and the poor spatial repeatability.

The plasma focus is a special z-pinch which was described in detail in the above sections. Its x-ray emission characteristics are described in more detail in the following section.

### 2.3.2 DPF as an X-ray Emitter

For a long period after its discovery, the plasma focus (PF) has been developed as a fusion device, most of the studies being done in hydrogen or its isotopes, with minor attention paid to the x-ray emission. For the last decade, considerable application potential as an intense (soft) x-ray source [11,87] led to more intensive studies.

The focused plasma, with electron temperature of a few hundred eV to a few keV and electron density of the order of $10^{19}$ $cm^{-3}$ ($10^{25}$ $m^{-3}$), is a copious source of x-rays. It emits x-rays by three processes, namely: Bremsstrahlung (free-free transition); recombination (free-bound transition); and de-excitation (bound-bound transition). The first two processes give rise to the continuum of the x-ray spectrum while the third process produces the characteristic line radiation of the plasma. For a plasma at temperature of $T_e$[eV], the peak of its continuum occurs at the wavelength of

$$\lambda_o = \frac{6200}{T_e} \text{ Å} \tag{2.5}$$

Hence for a plasma at $T_e$ = 1 keV, its x-ray continuum is expected to peak at $\lambda_o$ = 6.2 Å, which is in the soft x-ray region. On the other hand, for a high-$Z$ focus plasma, the characteristic line emission also falls in the soft x-ray region. For example, for a fully ionized argon and neon plasma at sufficiently high temperature, the $K_\alpha$ line radiation have wavelengths of 4.2 Å and 12.132 Å respectively.

Besides making the plasma focus an intense x-ray source which is useful in many applications such as microlithography and x-ray microscopy, the x-ray emitted also provides a convenient means for studying the plasma properties.

The radiation spectrum of the plasma focus in the x-ray region covers a wide range from below 1 keV up to over 500 keV in a time span ranging from few nanoseconds to few hundred nanoseconds. The integrated energy represents a significant fraction of the electromagnetic energy stored in the DPF driver. It can reach up to 20% in a Filippov-type geometry.

The electromagnetic radiative processes of the plasma focus are: quasi-equilibrium thermal radiation from macroscopic plasma structures and radiation due to electron beams interacting with non-plasma targets (i.e. electrodes) and/or with periodic electron density structures [87]. The following electron-ion interaction processes are considered to be responsible for the thermal x-ray component: Bremsstrahlung (free-free transitions), recombination emission (free-bound transitions) and line emission (bound-bound transitions). The cause of dominant hard x-ray emission is attributed to the non-thermal high energy electron beams striking the anode surface. Time-resolved measurements [88] showed that the power law spectrum ($dN_{HX}/dE \sim E^{-a}$, with $a = 2 \sim 4$, $E$ in keV and $N_{HX}$ the hard x-ray flux in photons per cm$^2$) found for the plasma focus in the range 100 ~ 500 keV is the result of the time integration over spectra produced by quasi-monochromatic electron beams with average energies changing over a ten nanoseconds time scale.

Hard x-ray emission was correlated with the neutron production when deuterium was used as the working gas: the total neutron yield is large when the hard x-ray emission is large [89].

The emission of soft x-rays from the plasma focus have long been studied and various diagnostic techniques have been employed over the years. These diagnostics include: (i) pinhole cameras (with one or multiple pinholes and appropriate filters) to record the time-integrated spatial/spectral distribution of the x-ray emitting region, (ii) microchannel plates used in conjunction with pinhole cameras for time- resolved spatial distribution of soft x-rays, (iii) semiconductor detectors with appropriate filters for space-integrated temporal/spatial distribution of the soft x-ray emission, (iv) crystal x-ray spectrographs for space-resolved line spectrum analysis, (v) x-ray streak photography for temporal distribution of the x-rays in one space dimension (radial or axial), and (vi) x-ray films, x-ray resists and x-ray pulse calorimeters for absolute soft x-ray yield measurements.

The soft x-ray (i.e. with energy below 10 keV) emitting source is situated on the electrode axis at the open end of the electrode system in the vicinity of the inner electrode face. The time-integrated images showed that it has a roughly cylindrical shape. Its dimensions are from below 1 mm to over 10 mm in diameter (approximately ~ anode radius), with an axial length from few millimeters to few centimeters. Spectral filtering of the x-ray image revealed a fine structure presenting intensely radiating small macroscopic entities (called by various authors "hot spots" [90], "plasma beads" [91], "bright spots" or "micropinches" [92]) as well as filaments inside and along the axis of the pinch [93].

Choi *et al.* [94,95] reported x-ray "hot spots" with typical dimension of about 100 μm which occur within 5 ns of the first compression (the focus formation) during the period of the stable phase of the pinch. They concluded that the "hot spots" are not the manifestation of the m=0 instabilities which disrupt the pinch column.

A detailed grey level analyses of x-ray images [96] indicated the presence of helical structures of high emissivity at the centre of these images which helps in explaining the production of axial magnetic field and the relaxation of the pinch in the plasma focus.

For a low energy deuterium filled plasma focus device the soft X-ray emission extends over a time interval of about 60 - 70 ns and features three peaks: the first is emitted by the dense pinched plasma column at the end of the compression phase, the second by the unstable plasma column and the third (corresponding to the disruption phase) is due to emission from the face of the inner electrode [97].

Favre *et al.* [98] investigated the temporal and spatial characteristics of the x-ray emission in a 3 kJ DPF operated in hydrogen with an argon admixture. They reported two main periods in the soft X- ray emission corresponding to two successive compressions in the focus.

Zoita *et al.* [99] studied the influence of the radiation processes on the plasma evolution during the pinch and post-pinch phases in experiments with neon-seeded deuterium discharges carried out on a 28 kJ / 60 kV device. They reported dramatic changes in the radiation characteristics of the discharge as well as in the pinch configuration. High aspect ratio (length/diameter » 10) pinches (HARP) emitting large amounts of soft x-rays accompanied by efficient emission of neutrons (and hard x-rays) in the absence of macroscopic instabilities were produced. This confirmed the physical picture obtained from experiments performed with a lower energy plasma focus device [100]. They also concluded that the line radiation as well as the main continuum radiation in the spectral range of 3 - 4 keV are emitted mainly from the intense bright spots having dimensions of about 50 µm. Similar ideas were reported by Presura *et al.* [101] from their investigation of the spectral characteristics of the soft x-ray emission of a plasma focus device operating in deuterium with various additions of argon and argon- krypton.

The x-ray emission characteristics depend strongly on the plasma focus device operating régimes and parameters (e.g. gas filling composition and pressure, stored energy, discharge current, driver impedance, electrode material, shape, profile and configuration, polarity of the inner electrode, etc.). Amongst them, the composition of the gas and the filling pressure have the strongest influence. When deuterium is used, the working pressure for the highest x-ray yield does not coincide with the neutron optimized output pressure [102,103].

For an x-ray optimized plasma focus device, the scaling law of the x-ray output $Y_X$ as a function of the peak discharge current $I_{max}$ and the pinch radius, r, can be written empirically [104] as:

$$Y_X = \frac{I_{\max}^4}{r^2} \tag{2.6}$$

This dependence similar to the scaling law found for z-pinches indicates a better operation at higher voltages for a given stored energy.

However, the exact mechanisms by which high intensity x-ray are emitted in plasma focus are still controversial and more experimental work is required in order to optimize the x-ray production for practical applications.

# Chapter 3

# Radiative Plasma Focus Model

## 3.1 Introduction

Galileo showed that experiment should not be separated from modelling and simulation. An experiment that does not lead to the verification of a physical model or does not suggest the need for a new point of view is essentially useless - its conclusions are non transferable and its results cannot be generalized to other cases. However, simulation is based on physical models and theories with many assumptions. Its validity must be verified by experiments.

In our project work, experiments were conducted and in the meantime the physical model was constructed. The model was based on the common knowledge of the plasma focus and some assumptions. Some of the experimental results carried out in parallel were used as input parameters of the code. The results from the numerical simulation, in turn, can be used to help improve the experiments or to design new experiments. It is very important to be able to generalize the results for other cases of a similar kind.

In this chapter the physical model is introduced in detail. In section 3.2 a simple review of this field is given. Section 3.3 describes the detailed model developed during this project work based on Lee's model [26,105-108] by including the radiation part. Section 3.4 is about numerical computation of the model. Section 3.5 will present some preliminary results. More results will be presented in Chapter 5 where experimental results will be given to compare with the results obtained by numerical computation.

## 3.2 Modelling of Plasma Focus

The key technical and experimental features of plasma focus device are well documented. The situation concerning the theoretical treatment of the device is however quite different. Several theoretical descriptions of the dynamics of the plasma focus have been developed in the past three decades [51,53,63-67,69,70,109,110].

The simple snow-plow model has proven to predict reasonably well the current sheath velocity, duration of the phase and the plasma profile (2-D version) for the axial run-down phase. For the radial phase, however, the simple model based on the snow-plow equation cannot be used. The snow-plow model is essentially a structureless model. The use of it would by itself produce a non-physical final radius of zero. Potter [110] has suggested a slug model which he has applied to the specific case of a constant current, constant length pinch to obtain a collapsing layer with structure. Lee [105-107,111] has extended this slug model to the radial compression phase of the plasma focus, allowing the length of the pinching column and the plasma current to vary self-consistently. The model relates the radial shock speed to the magnetic pressure, the focus axial shock speed to the radial shock speed and the radial piston to the radial shock speed by the careful application of the adiabatic law. The current is computed self-consistently through a plasma-linked circuit equation. This model is capable of yielding trajectory and structure of the plasma. An updated version of this physical model was proposed in Ref. [26]. In this model, the dynamics of the plasma focus is divided into three phases, i.e. the axial acceleration phase, the radial phase and the expanded column phase. Mass factor and current factor were included for the axial phase of the three phases considered. By doing this it was found the model can agree more accurately with the experimental trajectory results when applied to both the standard Mather-type electrode configuration and the double stage electrode geometry in NIE-SSC-PFF focus [112].

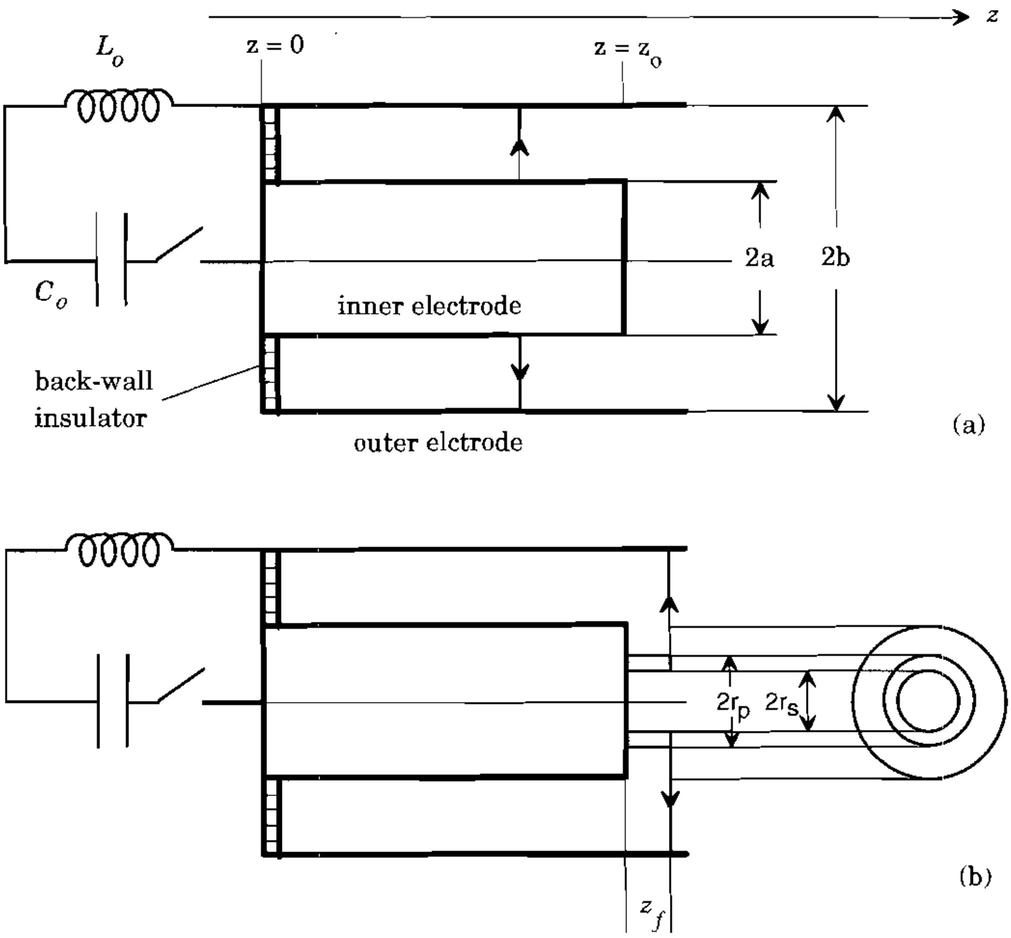


**Figure 3.1**
(a) Axial acceleration phase
(b) Radial compression phase

Fig.3.1 illustrates the two phases of the focus dynamics. In this model when the capacitor at voltage $V_o$ is switched onto the focus tube breakdown first occurs across the back-wall insulator. A current sheath is formed axisymetrically. It lifts off from the backwall and is then propelled by its own $J_r x B_\theta$ force down the annular channel in the $z$-direction. When the current sheath comes to the position $z = z_o$ the radial phase starts. The radial pinch proceeds as shown in Fig.3.1(b).

For the axial phase, a snow-plow model is used in which when the current sheath is at position $z$, all its accumulated mass is also at position $z$. This is an approximation which does not give rise to any fundamental problem in the axial phase.

In the radial phase, however, if this "thin" snow-plow model is used it will give rise to a compression to zero radius unless the compression is correctly terminated by an energy balance principle [78]. However, if a slug-model (with structure) is used, a shock front will separate out from the current sheath (magnetic piston) and a finite thickness plasma layer will result. This layer will be propelled radially inwards by the $J_z x B_\theta$ force. As the plasma layer collapses inwards the whole column elongates (since the compression is open-ended at one end). In the slug-model when the shock hits the axis, the piston stops and a quasi-equilibrium is formed. However, a check with energy balance indicates that the piston will continue to move a little so that the final quasi-equilibrium radius should be determined by energy balance.

The integration of the model starts with the axial acceleration phase, continues into the radial pinch phase and ends when the radial shock front reaches the axis.

## 3.3 Radiative Plasma Focus Model

Based on earlier work, Lee has suggested a radiative plasma focus model by including the radiation part in the previous model [113]. The radiative (slow compression) phase will be added in the model described in Ref. [26]. Also a reflected shock phase is introduced to give a more reasonable start of the quasi-equilibrium (more consistent minimum radius). In the inward shock phase a finite signal communication time between the shock front and the magnetic piston as discussed in Ref. [26] is now employed to solve the problems of (a) unrealistic high sheath speed and (b) the "sudden" stopping of piston when shock front hits the axis. It is found that with this mechanism included in we can obtain more reasonable plasma speed and a more realistic picture of pinching.

We shall begin with the introduction of the general topics related with x-ray radiation from pinch plasmas.

### 3.3.1 General Consideration of X-ray Emission from Plasmas

The emission processes were qualitatively reviewed in Sec.2.3. As is well known, for given electron density and temperature, plasma equilibrium models can be used to calculate the detailed spectra with the knowledge of the rates of transition and related parameters. For our simple model we are concerned only with the total radiation.

In the plasma focus both $T_e$ and $n_e$ in the radiation phase depend strongly on various conditions such as electrode configuration, working gas (here only neon is used) and its pressure, various instabilities and so on. The duration and the size of the focus strongly affect the total radiation. Various types of instabilities are responsible for the focus duration. For comparison with the experimental results the duration time will be chosen according to the mean value from experimentally measured duration.

In this section we shall first discuss how to calculate the temperature, then with this temperature the equilibrium properties of plasmas, then the various types of emission can be described more quantitatively. Most of the formulae will be given directly without the details of derivation, which can be referred to references [114-118].

### 3.3.1.1 Radiation Power Density

Referring to Sec.2.3, for plasma focus the main emissions are Bremsstrahlung, radiative recombination and de-exitation (line radiation), denoted by $P_b$, $P_r$ and $P_l$ respectively. Before giving the formulae we define some notations which are commonly used for the radiation-related quantities in the following sections.

| | |
|---|---|
| $N_e$ | electron number density of plasma ($m^{-3}$) |
| $N_i$ | ion (or atomic) number density of plasma ($m^{-3}$) |
| $N$ | total number density ($m^{-3}$) |
| $z$ | charge number of ions ($z$=0 refers to neutral state) |
| $Z_{eff}$ | effective charge number |
| $N_z$ | concentration of ions in $z$th ionized state ($m^{-3}$) |
| $N_{z,n}$ | concentration of ions in excited state $n$ of the $z$th ionized state |
| $\chi_z$ | ionization potential of $z$th ion (eV) |
| $\chi_{mn}$ | excitation energy from $m$ to $n$ excited state |
| $E_H$ | ionization energy for hydrogen (=13.6 eV) |
| $Z_n$ | atomic number |
| $T_e$ | electron temperature ( in Kelvin) (assumed equal to ion temperature $T_i$) |
| $T_{eV}$ | electron temperature (in eV) |

All these quantities are in the units specified above, except otherwise specifically noted.

Power density of Bremsstrahlung ($P_{b,\nu}$), recombination ($P_{r,\nu}$) and line radiation ($P_{l,\nu}$) as function of photon energy ($h\nu$) or frequency ($\nu$) are listed below ($P_{b,\nu}$ and $P_{r,\nu}$ in unit of $W.m^{-3}.Hz^{-1}$):

$$P_{b,\nu} = 8\pi^2 \frac{16\,(\alpha a_o)^3}{3^{3/2}\pi^{1/2}} g_{ff}\, N_e N_z\, z^2 E_H \left(\frac{E_H}{kT_e}\right)^{1/2} \exp\left(-\frac{h\nu}{kT_e}\right)$$
$$= 6.37\times 10^{-53}\, N_e N_z\, \frac{z^2}{T_{eV}^{1/2}} \exp\left(-\frac{h\nu}{T_{eV}}\right) \tag{3.1}$$

$$P_{r,\nu} = 8\pi^2 \frac{32\,(\alpha a_o)^3}{3^{3/2}\pi^{1/2} n^3} g_{fb}\, N_e N_z\, z^4 E_H \left(\frac{E_H}{kT_e}\right)^{3/2} \exp\left(-\frac{h\nu}{kT_e}\right)$$
$$= 1.73\times 10^{-51} N_e N_z\, \frac{z^4}{n^3\, T_{eV}^{3/2}} \exp\left(-\frac{h\nu-\chi_z}{T_{eV}}\right) \tag{3.2}$$

$$P_{l,\nu} = h\nu\, N_{z,n}\, A_{nm} \quad (\text{W.m}^{-3}) \tag{3.3}$$

where

$$A_{nm} = \frac{2\pi e^2 \chi^2_{mn}[J]}{\varepsilon_o m_e h^2 c^3}\cdot \frac{g_m}{g_n} f_{mn}$$
$$= 6.67\times 10^{-5} \frac{g_m}{g_n} f_{mn} \frac{1}{\lambda^2} \qquad (\text{s}^{-1}) \tag{3.4}$$

and $g_{m,n}$ is the statistical weight at quantum state $m$ and $n$, $f_{mn}$ the oscillator strength.

The corresponding power densities of the three kinds of emission are listed below (all in unit of W·m$^{-3}$),

$$P_b = \int P_{b,\nu}\, d\nu$$
$$= 1.69\times 10^{-38}\, N_e\, T_{eV}^{\frac{1}{2}} \sum_z (N_z z^2) \tag{3.5}$$

$$P_r = \int P_{b,\nu}\, d\nu$$
$$= 5.5\times 10^{-37}\, N_e\, T_{eV}^{-1/2} \sum_z (N_z z^4) \tag{3.6}$$

$$P_l = \sum_\nu P_{l,\nu}$$
$$= 3.95\times 10^{-35} \frac{Z_n^4}{T_{eV}} N_e N_i \tag{3.7}$$

total radiation density $P_{rad}$ is the sum of these three terms,

$$P_{rad} = (P_b + P_r + P_l) \tag{3.8}$$

The radiation yield is,

$$Y = \int_{(t_p)} \left( \int_{(V_p)} dV \cdot P_{rad} \right) dt \tag{3.9}$$

Where $V_p$ is the plasma volume and $t_p$ the lifetime of the pinch plasma (assumed to be homogeneous)

It must be mentioned here $Y$ is the total radiation including the whole spectrum band. For neon, when $T_e$ is over 100 eV, soft x-rays will be the main contributor to this yield.

In the above expression for a particular plasma for which $Z_n$, $\chi_z$ are known it can be seen that $P_{rad}$ is a function of $T_e$, $N_e$, $Z_{eff}$, $z$, $N_z$, $N_{z,n}$, $N_i$ . But $Z_{eff}$, $N_e$, $z$, $N_z$ and $N_{z,n}$ can be worked out for each given $T_e$ and $N_i$ using a plasma equilibrium model (e.g. LTE model, corona model or radiative collisional model). So $P_{rad}$ is a function of $T_e$ and $N_i$. Thus $Y$ is determined by $T_e$, $N_i$, $V_p$ and $t_p$.

The lifetime $t_p$ is strongly affected by various factors. e.g. kinds of instabilities and thus not easy to calculate. In our simple model we took the value from experimental results, which gives typical averaged radiation time of 10 ~ 20 ns (for optimum operation). As for $T_e$, $N_i$ and $V_p$ ($= \pi r_p^2 z_f$, $r_p$ and $z_f$ are the radius and length of the pinch column), they generally depend on several factors such as stored bank energy, electrode configuration, filling gas, external circuit, etc., which require numerical computation starting from the axial run-down phase through the radial compression phase. In this procedure, energy transferred among the magnetic energy, kinetic energy, internal energy and heat energy are considered. The specific heat ratio $\gamma$ , a function of temperature, is an important parameter in connection with this energy conversion.

Several quantities described above are not independent but are related to one another. Sometimes we may need to solve the equations of several quantities for any given point of time. For example, the calculation of $Z_{eff}$ is a function of $(T_e,N_e)$, but the calculation of $T_e$ itself needs $Z_{eff}$ to be its variable. In this case we need to solve the two governing equations to obtain $T_e$ and $Z_{eff}$.

#### 3.3.1.2 Calculation of $N_z$, $N_{z,n}$, $Z_{eff}$

*Simplified Plasma Equilibrium Model*

The emission spectrum of a plasma is determined by the combined effects of the processes discussed above (and also in Sec.2.3.1). If the rates of all these processes were known, in principle the spectrum could be predicted. This, however, requires detailed knowledge of the state of the plasma and is generally not possible. Approximate calculations, using simplified models of the plasma, may be carried out.

The most tractable plasma models are those in which the electron density is either very high or very low. The former can be described by local thermodynamic equilibrium (LTE) and the latter by coronal equilibrium. In plasmas suitable for x-ray sources neither condition is generally satisfied, but in some cases reasonably accurate results may be obtained by assuming that one of these types of equilibrium is valid. In general, however, an intermediate model, e.g., collisional-radiative equilibrium, must be used.

For the plasma focus used in this project (parameters are listed in Tab.4.1 and 4.2 in the next chapter), the applicability of these models can be tested using some approximate limitations obtained.

(A) Local Thermodynamic Equilibrium

An approximate lower limit on $N_e$ [m$^{-3}$] for LTE to apply is [116]

$$N_e > K\, T_{eV}^{1/2}\, \chi_{\max}^{3} \tag{3.10}$$

where $K \sim 10^{19}$ - $10^{20}$ and $\chi_{\max}$ is the highest ionization potential of any of the ions present. Thus, for $T_{eV} \sim 250$ eV and $\chi_{\max} \sim 1360$ eV (of neon), the lower limit on $N_e$ is ~ 2x10$^{29}$. For our machine, with $N_e$ of about 10$^{25}$ m$^{-3}$, this model is obviously not applicable.

(B) Coronal Equilibrium

A similar argument may be used to estimate the electron density $N_e^{max}$ above which the coronal model is not applicable; for hydrogenic ions of charge $z$ one analysis gives, for levels with principal quantum number $n \leq 6$ [119],

$$N_e^{max} \approx 6.5 \times 10^{16}(z+1)^6 T_{eV}^{1/2} \exp\left(0.1(z+1)^2/T_{eV}\right) \tag{3.11}$$

For our machine the typical value is $N_e^{max}$ ~ 2x10$^{24}$. Our electron density is just above this limit. So the coronal model is at least a better model to use than the LTE model.

(C) Collisional-Radiative Equilibrium

The collisional-radiative (CR) model [120] was developed to fill the gap of several orders of magnitude in electron density where neither the LTE model nor the coronal equilibrium are valid. This is a modification of the coronal model which takes into account collisional transitions as well as radiative decay from higher bound levels, and three body as well as radiative recombination. The main difficulty with this model is its complication, need of computer time, etc.

*Coronal Model*

For *simplicity* the corona model was applied as an approximation for neon plasma in this work. In a low density plasma (corona plasma) most of the ions will be in their ground states, and so it is assumed that collisional excitation from ground state is balanced by radiative decay from the upper level to all lower levels, this giving,

$$\frac{N_{z,n}}{N_z} \approx \frac{N_{z,n}}{N_{z,1}} = \frac{N_e C_{1n}}{\sum_{m<n} A_{nm}} \tag{3.12}$$

where

$$C_{mn} = 1.6\times10^{-11}\frac{<g>f_{mn}}{\chi_{mn}T_{eV}^{1/2}}\exp\left(-\frac{\chi_{mn}}{T_{eV}}\right) \quad (\mathrm{m^3.s^{-1}}) \tag{3.13}$$

is the collisional excitation coefficient from ground state to $n$th state, $<g>$ is the Gaunt factor:

$$<g> = 1 \text{ (for atoms), } 0.2 \text{ (for ions)} \tag{3.14}$$

Using Eqn.(3.3) and (3.12), we can express $P_{l,v}$ as,

$$P_{l,v} = hv\frac{A_{nm}}{\sum\limits_{m<n} A_{nm}}N_e N_z C_{1n} \tag{3.15}$$

Similarly, ionization is via collisions which, in equilibrium, is balanced by radiative recombination. The rates of both these processes are proportional to electron density. The state populations of ions of charge $z$+1 and $z$ are related by,

$$\frac{N_{z+1}}{N_z} = 1.27\times10^8\times\frac{\zeta T_{eV}^{3/4}}{\chi_z^{11/4}}\exp\left(-\chi_z/T_{eV}\right) \tag{3.16}$$

with $\zeta$ is the number of electrons of outer shell. Using this equation, the fraction of ionization of states at different temperature may be calculated by using the following procedure.

*Ionization State*

Generally, from one of the three simplified equilibrium models mentioned above, a recursive equation of steady ratio between consecutive ions can be written as:

$$\frac{N_{z+1}}{N_z} = f_z(T_e, N_e) \tag{3.17}$$

where $N_z$, $N_{z+1}$ are the number densities of ions of charge $z$ and $z$+1 ($z$=0 corresponds to the neutral density). Note that $N_o$ denotes the ambient number density of the working gas for the rest of the thesis. For each ionization state the above equation can be rewritten as:

$$\begin{cases} N_1 = N_0 f_0 \\ N_2 = N_1 f_1 = N_0 f_0 f_1 \\ \cdots\cdots\cdots\cdots \\ N_{Z_n} = N_{Z_n - 1} f_{Z_n - 1} = \cdots\cdots = N_0 f_0 f_1 \cdots f_{Z_n - 1} \end{cases} \tag{3.18}$$

Using this equation the total ionic and atomic number density is

$$\begin{aligned} N_i &= \sum_{z=0}^{Z_n} N_z \\ &= N_0 (1 + f_0 + f_0 f_1 + \cdots + f_0 f_1 f_2 \cdots f_{Z_n - 1}) \\ &\equiv N_0 S_f \end{aligned} \tag{3.19}$$

so we have obtained the fraction of neutral density,

$$\frac{N_0}{N_i} = \frac{1}{S_f} \tag{3.20}$$

Substituting this into Eqn.(3.18) we finally obtain $N_z/N_i$ for all the ionization states and the effective ionic charge by

$$Z_{eff} = \frac{N_e}{N_i} = \sum_{z=0}^{Z_n} (z \cdot N_z) \Big/ \sum_{z=0}^{Z_n} N_z \tag{3.21}$$

Using corona model, the result is plotted in Fig.3.2. and $Z_{eff}$ versus $T_e$ curve can thus be calculated using Eqn.3.21 and given in Fig.3.2(b). In this figure we have defined

$$a_z \equiv \frac{N_z}{N_i} \tag{3.22}$$

as the fraction of the plasma which is ionized to the $z$th ionized state.

For our case in the focus pinch radiation phase $T_e$ is measured (see Chapter 5) to be 250 eV ~ 350 eV. We may choose $Z_{eff}$ ~ 8 - 9 for the inward shock phase and 9 for the radiation phase (experimental results showed that the $T_e$ ~ 300 eV, which corresponds to $Z_{eff}$ = 9.2, see Fig.3.2(b)). But the power density is a strong function of $Z_{eff}$, so at each step $Z_{eff}$ will be calculated by solving the equations of $T_e$ and $Z_{eff}$ simultaneously.

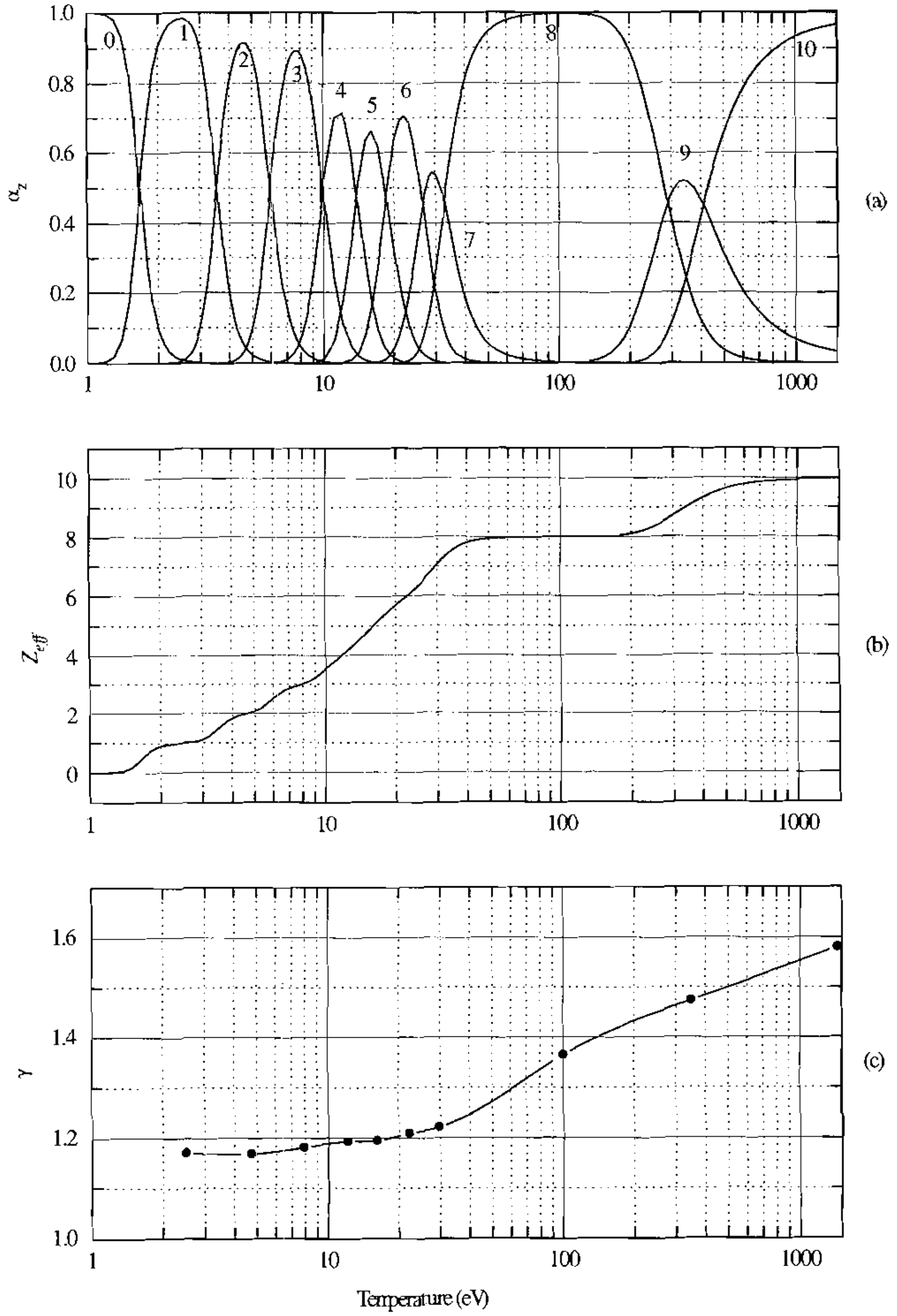


**Figure 3.2**
(a) Fractional density of neon ions as a function of temperature in the corona equilibrium ($\alpha_Z = N_Z/N_i$).
(b) Effective ion charge number as a function of temperature
(c) Specific heat ratio as a function of temperature

### 3.3.1.3 Specific Heat Ratio (γ) of Hot Plasma

The effective specific heat ratio is a very important parameter. Lee has proposed a simplified method to compute the values of the specific heat ratio as function of temperature [121,122]. According to a theory based on energy balance [78,121,122], the radius ratio $r_p/r_o$ of constant-current plasma pinch depends on the value of the effective specific ratio γ of the pinched plasma.

The value of γ may be defined in terms of the enthalpy per unit mass $h$ as

$$h = \frac{\gamma}{\gamma - 1}\frac{k_B T D}{m_i} \tag{3.23}$$

where the departure coefficient is

$$D = 1 + Z_{eff} = 1 + \sum_{z=1}^{Z_n}(z \cdot a_z) \tag{3.24}$$

Here $k_B$ is the Boltzman constant, $m_i$ the mass of atom or ion, $T$ the temperature and $\alpha_z$ the fraction of the plasma which is ionized to the $z$th ionized state. The enthalpy of a plasma such as neon may also be written in terms of its ionization and excitation energies as

$$h = \frac{5}{2}(R_o/M)TD + m_i^{-1}\sum_{z=1}^{Z_n}(a_z \cdot I_z) + m_i^{-1}\sum_{z=1}^{Z_n}(a_z \cdot E_z) \tag{3.25}$$

Here $I_z$ is the total energy required to raise one ion from its unionized state to its $z$th ionized state and $E_z$ is the average excitation energy per $z$th ionized ion. The ionization potentials are known quantities whilst the excitation energies are temperature dependent and can be computed from the tabulated values of atomic and ionic energy levels and the statistical weights of these levels [123], once a suitably converging summation scheme is adopted.

From Eqns.(3.23) and (3.25) we may compute the value of γ by writing

$$\frac{\gamma}{\gamma-1}=\frac{5}{2}+\left(\sum_{z=1}^{Z_n}(\alpha_z\cdot I_z)+\sum_{z=1}^{Z_n}(\alpha_z\cdot E_z)\right)\frac{1}{k_BT_eD} \tag{3.26}$$

where the $\alpha_z$ may be computed for any given temperature by the use of a plasma equilibrium model.

A simple procedure for estimating the values of $\gamma$ from the available curves of the $z$ is suggested by Lee [122]. Noting that as the curve for a particular ionization fraction, $\alpha_z$ say, rises to its maximum value $\alpha_z \leq 1$, at that point the second term of Eqn.(3.26) is dominated by the ionization energy. At this point, if we assume that $\alpha_z \sim 1$, then

$$\sum_{z=1}^{Z_n}(\alpha_z\cdot I_z)+\sum_{z=1}^{Z_n}(\alpha_z\cdot E_z)\approx I_s \quad (s=1,\ldots,Z_n\text{-}1) \tag{3.27}$$

Hence, estimates of the values of $\gamma$ may be readily made at 9 points of temperature, each point at successively higher temperatures corresponding to the maximum values of $z_1$ to $z_9$, by use of the approximate formula

$$\frac{\gamma}{\gamma-1}\approx\frac{5}{2}+\frac{I_s}{k_BT_e(1+s\alpha_s)} \tag{3.28}$$

As $T$ is raised further and $z_{10}$ approaches 1, the approximation (3.28) becomes exact and remains exact for all higher temperatures of $T$. Thus for all values of $T$ higher than that temperature at which $\alpha_{10}=1$ we have

$$\frac{\gamma}{\gamma-1}\approx\frac{5}{2}+\frac{I_{10}}{11\cdot k_BT_e} \tag{3.29}$$

By using the results of the preceding section and the data for neon as tabulated in Tab.3.1. the above simplified procedure can be done. The result is shown in Fig.3.2(c). For our focused plasma the temperature is between 30 eV to 600 eV, where a simple (linear) approximation may be used to calculate $\gamma$, i.e.,

$$\gamma = 1.28 + 4.44\text{x}10^{-4}T_{eV} \tag{3.30}$$

for our model for the whole radial and pinch phase. In our dynamics computation $\gamma$ is calculated for each time step using the equation set of $\gamma$, $T_e$ and $Z_{eff}$.

***Table 3.1*** Data for computation of $\gamma$ for neon

| $s$ | $T$(eV) | $D$~1+$s\alpha_s$ | $I_s$(eV) | $s$ | $T$(eV) | $D$~1+$s\alpha_s$ | $I_s$(eV) |
|---|---|---|---|---|---|---|---|
| 1 | 2.5 | 2 | 21.57 | 6 | 22.1 | 7 | 507.22 |
| 2 | 4.7 | 3 | 62.53 | 7 | 29.6 | 8 | 714.5 |
| 3 | 7.9 | 4 | 125.99 | 8 | 102.1 | 9 | 953.6 |
| 4 | 12.1 | 5 | 223.07 | 9 | 349.1 | 10 | 2,149.43 |
| 5 | 16.1 | 6 | 349.29 | 10 | 1,442.5 | 11 | 3,511.64 |

### 3.3.1.4 Calculation of Temperature $T_e$

*Method I*

For a plasma with inductance $L_p$ and resistance $R_p$, and with the rate of radiation loss of $dQ_{rad}/dt$, the total input power is the product of the voltage across it and the current flowing through it, that is,

$$
\begin{aligned}
P_T &= I_p \cdot V = I_p \cdot \left(\frac{d}{dt}(L_p I_p) + I_p R_p\right) \\
&= I_p^2 \dot{L}_p + I_p L_p \dot{I}_p + I_p^2 R_p
\end{aligned}
\tag{3.31}
$$

here $R_p$ is the plasma resistance with resistivity of Spitzer form

$$
\begin{aligned}
&\eta = 1.033 \times 10^{-4} \times \ln\Lambda \cdot Z_{eff} T_{eV}^{-3/2} \\
&\text{with } \ln\Lambda = 29.27 + \frac{3}{2}\ln T_{eV} - \frac{1}{2}\ln N
\end{aligned}
\tag{3.32}
$$

The rate of change of energy stored in the inductance is,

$$
\begin{aligned}
P_{L_p} &= \frac{d}{dt}\left(\frac{1}{2} L_p I_p^2\right) \\
&= \frac{1}{2} I_p^2 \dot{L}_p + L_p I_p \dot{I}_p
\end{aligned}
\tag{3.33}
$$

Using these two equations the rate of energy being converted to the plasma energy, if accounting for radiation loss, is obtained as,

$$\begin{aligned} P_P &= P_T - P_{L_p} - \frac{dQ_{rad}}{dt} \\ &= \frac{1}{2} I_p^2 \dot{L_p} + I_p^2 R_p - \frac{dQ_{rad}}{dt} \\ &= \frac{1}{2} I_p^2 \dot{L_p} + \frac{dQ_{joul}}{dt} - \frac{dQ_{rad}}{dt} \\ &= \frac{1}{2} I_p^2 \dot{L_p} + \frac{dQ}{dt} \end{aligned} \tag{3.34}$$

where $Q = Q_{joul} - Q_{rad}$ is the total heat energy absorbed by the plasma (here $Q_{joul}$ is the joule heating caused by the plasma resistance of Spitzer form). Plasma energy $E_p$ is thus,

$$E_p = \int P_P \, dt = \int \frac{1}{2} I_p^2 \dot{L_p} \, dt + Q \tag{3.35}$$

From this expression it becomes clear that the term $\int \frac{1}{2} I_p^2 \dot{L_p} \, dt$ in the RHS of the above expression corresponds to the work done on the plasma by the system,

$$W = \int \frac{1}{2} I_p^2 \dot{L_p} \, dt \tag{3.36}$$

The plasma energy is the sum of its kinetic energy $E_k$ and internal energy $U$, i.e.,

$$E_p = \int P_P \, dt = E_K + U \tag{3.37}$$

From above Eqns.(3.35 - 37) we have,

$$U = W + Q - E_K \tag{3.38}$$

After computing the internal energy we can get the temperature $T_e$ for the plasma:

$$T_e = \frac{(\gamma - 1) \cdot U}{N_{ion} \, k \, (1 + Z_{eff})} \tag{3.39}$$

where $N_{ion} = N_i \times V_p$ is the total particle number in the plasma being studied.

*Method II*

In an axial discharge, the self induced azimuthal magnetic field interacts with the current and the ***J*x*B*** force compresses the plasma towards the axis. This is known as the pinch effect. The necessary conditions for the plasma to pinch is that ***J*x*B*** force should exceed the force due to the plasma pressure $P$. The plasma is in an quasi-equilibrium when the magnetic pressure equals the plasma pressure.

Bennet [124] solved this pressure balance to give,

$$8\pi\,(N_e^{\prime}kT_e + N_i^{\prime}kT_i) = \mu I^2 \tag{3.40}$$

where $I$ is the current through the plasma column, $T_{i,e}$ is the ion, electron temperature averaged over the cross section of the pinch, $N^{\prime}_{i,e}$ is the ion, electron line density defined as $\int N_{i,e} 2\pi r dr$ . In our model at the pinch time homogeneous plasma column is assumed and $T_e = T_i$, so we have

$$\left(\frac{\mu I_p}{2\pi r_p}\right)^2 \Big/ 2\mu = (N_i + N_e)\,k\,T_e = N_i(1 + Z_{eff})kT_e \tag{3.41}$$

giving,

$$\begin{aligned} T_e &= \frac{\mu}{k_B \cdot 8\pi^2} \frac{I_p^2}{(1+Z_{eff})N_i r_p^2} \\ &= \frac{b I_p^2}{(1+Z_{eff})\,N_i\, r_p^2} \end{aligned} \tag{3.42}$$

with $r_p$ being the radius of the pinch.

In this method we have implicitly assumed that radiation loss is small compared with the plasma energy and can thus be negligible. This formula can be used for the final quasi-equilibrium phase. As for the rest of the radial phase we can still write a similar expression, by using $P_B = NkT_e$,

$$T_e = \frac{b I_p^2}{(1+Z_{eff})\,N_i(r_p^2 - r_s^2)} \tag{3.43}$$

### 3.3.2 Axial Phase

#### 3.3.2.1 Snowplow Equation of Motion

In the axial phase, the mass entrained by the sheath at a position $z$ (see Fig.3.1a) is: $\rho_o \pi (b^2 - a^2)\, z$. Considering the mass loss effect by means of a mass factor $f_m$<1, the mass carried by the sheath at position z becomes:

$$\rho_o \, \pi \, (b^2 - a^2) f_m \, z \tag{3.44}$$

During the discharge, part of the circuit current $I$ is assumed to remain at the glass insulator (a leakage path which may be characterized by a leak resistance $r_L$). The rest of the current flows in the current sheath that drives the plasma sheath down the focus tube. At any given time $t$, we define the plasma current $I_p$ flowing in the sheath as:

$$I_p = f_i \, I \tag{3.45}$$

with $f_i$<1 the drive current efficiency (current shedding effect) or simply, the current factor.

The force exerted by the self-magnetic field ($B_\theta = \mu I_p / 2\pi r$) of the current sheath integrated over the whole current sheath between $r = a$ to $r = b$ is:

$$\int_a^b \frac{B_\theta^2}{2\mu} 2\pi r \, dr = \frac{\mu f_i^2 I^2}{4\pi} \ln c \tag{3.46}$$

where $c = b/a$, and $\mu = 4\pi \times 10^{-7}$ H/m is the permeability of space.

The equation of motion can be obtained by considering the rate of change of momentum:

$$\frac{d}{dt}\left( \pi \, f_m \, \rho_o (b^2 - a^2) \, z \, \frac{dz}{dt} \right) = \frac{\mu}{4\pi} (f_i \, I)^2 \ln c \tag{3.47}$$

then we have,

$$\frac{d^2z}{dt^2} = \frac{\frac{\mu}{4\pi}(f_i I)^2 \ln c - \pi f_m \rho_o (b^2 - a^2)\left(\frac{dz}{dt}\right)^2}{\pi f_m \rho_o (b^2 - a^2)\, z} \tag{3.48}$$

In this equation $z$ and $I$ are functions of time. To determine the current $I$, the circuit equation is needed.

### 3.3.2.2 Circuit Equation

*General Circuit Equation*

The equivalent circuit of the focus tube is presented schematically in Fig.3.3, where $C_o$, $L_o$, and $R_o$ are the fixed capacitance, inductance, and resistance of the external elements, respectively, $R_p$ and $L_p$ are the plasma resistance (Spitzer form) and inductance respectively, and $h_L$ the leakage resistance. According to Kirchhoff's second law we can write the circuit equation,

$$\frac{1}{C_o}\int I\,dt - V_o + R_o I + \frac{d}{dt}(L_o I) + R_p I_p + \frac{d}{dt}(L_p I_p) = 0 \tag{3.49}$$

Using the relationship $I_p = f_i x I$, we obtain the general circuit equation as following,

$$\frac{dI}{dt} = \frac{V_o - \frac{1}{C_o}\int I\,dt - (R_o + f_i R_p) I - \frac{d}{dt}(L_o + f_i L_p)\cdot I}{L_o + f_i L_p} \tag{3.50}$$

*General tube voltage expression*

From Eqn.(3.49) we have the general expression of the voltage across the focus tube:

$$V = \frac{d}{dt}(L_p I_p) + R_p I_p \tag{3.51}$$

or alternatively,

$$V = V_o - \frac{1}{C_o}\int I\,dt - R_o I - L_o \frac{dI}{dt} \tag{3.52}$$

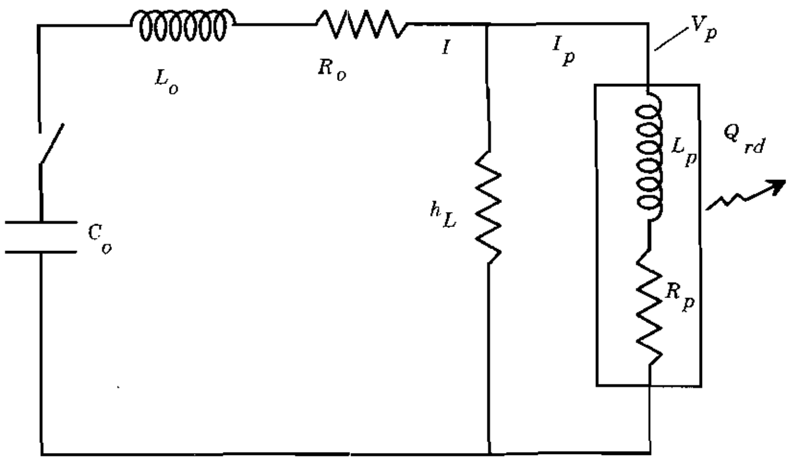


**FGURE 3.3**
Equivalent circuit of the radiative plasma focus

*Circuit Equation of Axial Phase*

In the axial phase the plasma inductance may be written as a function of $z$:

$$L_p = \frac{\mu}{2\pi} z \ln c \tag{3.53}$$

In this phase both the radiation and plasma resistance are neglected. Substituting above equation into Eqn.(3.50) yields the circuit equation for axial phase as,

$$\frac{dI}{dt} = \frac{V_o - \frac{1}{C_o}\int I\,dt - R_o I - \frac{d}{dt}\left(L_o + f_i \frac{\mu}{2\pi} z \ln c\right)\cdot I}{L_o + f_i \frac{\mu}{2\pi} z \ln c}$$

$$= \frac{V_o - \frac{1}{C_o}\int I\,dt - R_o I - \frac{\mu}{2\pi}\ln c\, f_i I \frac{dz}{dt}}{L_o + \frac{\mu}{2\pi} f_i\, z \ln c}$$

(3.54)

Equations (3.48) and (3.54) are the two coupled equations determining the behaviour of $z$ and $I$ for the axial phase.

### 3.3.2.3 Related Physical Quantities

*Tube Voltage*

For axial phase, $R_p$ and radiation are neglected and so

$$V = \frac{\mu}{2\pi} f_i \ln c \left( z \frac{dI}{dt} + I \frac{dz}{dt} \right) \tag{3.55}$$

*Work done*

The work done can be derived by using the Lorentz force $\vec{f}$ exerted by the self-magnetic field,

$$\begin{aligned} W &= \iiint_{(plasma)} dV \cdot \left( \int_0^z \vec{f} \cdot \hat{z}\, dz \right) \\ &= \int_0^z \left( \frac{\mu}{4\pi} I_p^2 \ln c \right) dz \\ &= \int_0^t \frac{dz}{dt} \left( \frac{\mu}{4\pi} f_i^2 I^2 \ln c \right) dt \end{aligned} \tag{3.56}$$

or we can directly use Eqn.(3.36) which gives the same formula as Eqn.(3.56).

*Kinetic energy*

In this model the plasma sheath from anode to cathode is assumed to run down at the same speed, so kinetic energy can be written as,

$$E_k = \frac{1}{2} f_m\, \rho_o\, \pi (b^2 - a^2) z \cdot (\frac{dz}{dt})^2 \tag{3.57}$$

### 3.3.3 Radial Inward Shock Phase

A simplified geometry is assumed for the plasma focus pinch as depicted in Fig.3.1b. When the plasma sheath diffracts around the end of the anode, the radial (compression) phase begins. The current $I_p$ flows through a thin conducting shell at $r_p$. The magnetic pressure $B_\theta^2/2\mu$ due to this current acts as a piston driving a shock front at $r_s$. Between $r_p$ and $r_s$, there is a 'slug' containing the mass swept into it by the shock front.

### 3.3.3.1 Radial Shock Motion

In this section and the next section we will introduce the previously used model in which infinite small distance communication between the shock front and the magnetic piston is assumed.

In the radial phase, the magnetic piston is known to be highly supersonic. Therefore, the speed of sound in the slug is large compared to the speed of the particles. Under these conditions, we may take the assumption that the one quantity that may be taken as uniform across the slug is the pressure $P$. Thus, this pressure may be related by the shock-jump equations to the shock speed $v_s = \frac{dr_s}{dt}$ as:

$$P_s = \frac{2}{\gamma+1}\rho_o v_s^2 \tag{3.58}$$

where $\gamma$ is the specific heat ratio of the gas in the slug.

Further, at the magnetic piston we may equate the pressure $P_s$ to the magnetic pressure $P_B$ so that:

$$P_s = P_B \tag{3.59}$$

where

$$P_B = \left(\frac{I_p}{2\pi r_p}\right)^2 \frac{1}{2\mu} = \frac{\mu (f_i I)^2}{8\pi^2 r_p^2} \tag{3.60}$$

Considering the current shedding effect with the help of a current factor $f_i$, from Eqns.(3.58) to (3.60) we get:

$$\frac{dr_s}{dt} = v_s = -\left[\frac{\mu(\gamma+1)}{\rho_o}\right]^{1/2} \times \frac{f_i I}{4\pi r_p} \tag{3.61}$$

where the negative sign indicates radial inward motion.

### 3.3.3.2 Radial Piston Motion

The slug of plasma is treated as a thermal system. The First Law of Thermodynamics is used for this system:

$$dh = dQ + VdP \qquad \text{where } h = \frac{\gamma}{\gamma - 1}PV \tag{3.62}$$

then we have

$$\gamma P\,dV + VdP = dQ \cdot (\gamma - 1) \tag{3.63}$$

where

$$V = \pi(r_p^2 - r_s^2)z_f \tag{3.64}$$

To eliminate $V$ from Eqn.(3.63) we need to differentiate Eqn.(3.64) to obtain $dV$ as a function of $dr_p$, $dr_s$ and $dz_f$. To do this we need to consider very carefully so that the differential quantities $dr_p$, $dr_s$ and $dz_f$ are applied to a fixed mass of gas. For example when the piston moves by $dr_p$ no new mass of gas introduced into the corresponding new volume $V+dV$. However when the shock front moves from $r_s$ to $r_s+dr_s$ it admits into the new volume $V+dV$ a new mass of gas. This new mass of gas is compressed by a ratio $(\gamma+1)/(\gamma-1)$ and will occupy part of the increase in volume, so that the actual increase in volume available to the original mass of gas in volume $V$ does not correspond to the increment $dr_s$ but to an effective (reduced) increment $dr_s[2/(\gamma+1)]$. This also applies to the increment $dz_f$.

Thus we need to write the differential of Eqn.(3.64) in the following form:

$$dV = 2\pi(r_p dr_p - \frac{2}{\gamma+1} r_s dr_s)z_f + (r_p^2 - r_s^2)\frac{2\pi}{\gamma+1}dz_f \tag{3.65}$$

$$\frac{dV}{V} = \frac{2(r_p dr_p - \frac{2}{\gamma+1} r_s dr_s)z_f + (r_p^2 - r_s^2)\frac{2}{\gamma+1}dz_f}{(r_p^2 - r_s^2)z_f} \tag{3.66}$$

We may also eliminate $dP/P$ from Eqn.(3.63) by writing from Eqn.(3.58) and Eqn.(3.61):

$$\frac{dP}{P} = \frac{2dv_s}{v_s} = 2\left(\frac{dI}{I} - \frac{dr_p}{r_p}\right) \tag{3.67}$$

finally we can obtain,

$$\frac{dr_p}{dt} = \left[\frac{2}{\gamma+1}\frac{r_s}{r_p}\frac{dr_s}{dt} - \frac{r_p}{\gamma I}(1-\frac{r_s^2}{r_p^2})\frac{dI}{dt} - \frac{1}{\gamma+1}\frac{r_p}{z_f}(1-\frac{r_s^2}{r_p^2})\frac{dz_f}{dt} + \frac{4\pi(\gamma-1)}{\mu\gamma(f_i I)^2}\frac{r_p}{z_f}(1-\frac{r_s^2}{r_p^2})\frac{dQ}{dt}\right] \Bigg/ \left[\frac{\gamma-1}{\gamma} + \frac{1}{\gamma}\frac{r_s^2}{r_p^2}\right] \tag{3.68}$$

### 3.3.3.3 Slug Model Considering Finite Time Signal Communication between SF and MP

The model described in the above two subsections faces two problems. Firstly it gives a much faster speed of plasma sheath than experimentally measured values. Secondly, when the shock front hits the axis it gives a picture which is inconsistent with experimental observations (e.g. by streak camera photography [125,126]). From Eqn.(3.68) we see that when $r_s = 0$, the speed of piston ($dr_p/dt$) comes to zero. This is not realistic and results from the assumption of uniform pressure within the slug which requires an infinite small-disturbance speed [26]. It is helpful to look into the physical picture in more detail.

*Physical Picture*

In terms of abundant experimental results available so far, using concepts of shock front (SF) and magnetic piston (MP), the physical picture of the dynamics in radial phase can be depicted. The radial phase starts from the rim of anode at $r = a$ with a zero (or very small) thickness and axial length. The shock front is imploded radially inwards driven by the magnetic piston behind. The shock front collects the gas encountered.

When the shock front hits the axis what happens to the plasma slug is noteworthy. The plasma slug may be thought of as comprising thin cylindrical layers (the layer is thin enough to be treated as homogeneous but thick enough to have sufficient particles inside it for the statistical dynamics to validate), the innermost layer being the shock front and the outermost layer the magnetic piston. When the shock front meets the axis and stops, the layers near the piston will not stop until the increased pressure on-axis is communicated to the layers near the piston. This information is carried out by pressure waves which travel outwards towards the magnetic piston at the local small disturbance speed. These outward pressure waves coalesce to form the reflected shock. Until the reflected shock hits the piston, the increased stagnation pressure in the on-axis region is not felt by the piston. So the piston will continue to move inwards. The piston stops or reverses motion only when this reflected shock front meets it. The position where the reflected shock meets the piston corresponds to the minimum radius of the pinch.

*Improved Slug Model*

To simplify the simulation, the dynamics of the plasma slug is determined by the two boundary layers: the inner most layer (SP) and the outer most layer (MP). Now we consider the communication delay due to the finite small disturbance speed between the piston and shock front. In our model the magnetic piston pressure drives the shock front and the motion of the shock front creates volume for the piston to move into. Hence a communication delay means that the shock front would at any instant "feel" the pressure of the piston at an earlier time, and likewise the piston would "feel" the effect of the shock front at an earlier position [26].

With this assumption of signal communication delay, the picture predicted by the slug model is made clear. The speed of this signal may be taken as the sound speed in the slug. The delay time is determined by this speed and the distance between SF and MP. As the shock front (magnetic piston) will feel the effect of magnetic piston (shock front) at an earlier time during which the magnetic pressure is smaller, the delay effect would slow down both the shock front and piston as they near the axis, as will be shown in Sec.3.5. The effect is also significant after the shock front hits the axis. With the assumption of finite signal communication in mind we may expect the picture as following: the piston continues to move inwards a little after the SF hits the axis because it takes time for the reflected shock to move out to the piston. From the moment the SF hits the axis to the moment the reflected shock front hits the piston we have the "reflected shock phase".

*Equations for Inward Shock Phase*

The equations of shock motion and piston motion Eqn.(3.58) and Eqn.(3.61) in the radial inward shock phase may thus be replaced by the following equations,

$$\frac{dr_s}{dt} = v_s = -\left[\frac{\mu(\gamma+1)}{\rho_o}\right]^{1/2} \times \frac{f_i I\,|_{t_{-1}}}{4\pi r_p\,|_{t_{-1}}} \tag{3.69}$$

$$\frac{dr_p}{dt} = \left\{\frac{2}{\gamma+1}\frac{1}{r_p}\left[\left(r_s\frac{dr_s}{dt}\right)_{t_{-1}}\frac{P_B\,|_{t_{-1}}}{P_B}\right] - \frac{r_p}{\gamma I}\left(1-\frac{r_s^2}{r_p^2}\right)\frac{dI}{dt} - \frac{1}{\gamma+1}\frac{r_p}{z_f}\left(1-\frac{r_s^2}{r_p^2}\right)\frac{dz_f}{dt} + \frac{4\pi(\gamma-1)}{\mu\gamma(f_i I)^2}\frac{r_p}{z_f}\left(1-\frac{r_s^2}{r_p^2}\right)\frac{dQ}{dt}\right\} \Bigg/ \left[\frac{\gamma-1}{\gamma}+\frac{1}{\gamma}\frac{r_s^2}{r_p^2}\right] \tag{3.70}$$

In these two equations the quantities with $|_{t-1}$ refer to their values at the earlier time $t_{-1}$ which is,

$$t_{-1} = d_{SF\text{-}MP}/C_s$$

where $d_{SF\text{-}MP}$ is the distance between SF and MP, $C_s$ is the speed of sound in the slug in the coordinate system moving with the slug and takes the following form,

$$C_s = \sqrt{\frac{\partial P}{\partial \rho}} = \sqrt{\frac{\gamma P}{\rho}} = \sqrt{\frac{\gamma N k T}{N_i m_i}} = \sqrt{\gamma(1+Z_{eff})kT/m_i} \tag{3.71}$$

here $m_i$ is the mass of ion (atom).

### 3.3.3.4 Axial Elongation of the Focus Pinch

Since the compression is open at one end, we expect an axial shock to be propagated in the $z$-direction. Further, we may assume that the pressure driving the radial shock is the same as that driving the axial shock. Thus, the length of the radial compression $z_f$ increases during the compression and this is one of the major factors responsible for the high compression in the plasma focus. We may write:

$$\frac{dz_f}{dt} = -\left(\frac{2}{\gamma+1}\right)\frac{dr_s}{dt} \tag{6.72}$$

### 3.3.3.5 Circuit Equation

In radial phase, the plasma inductance will be expressed as follows,

$$L_p = \frac{\mu}{2\pi} z_o \ln c + \frac{\mu}{2\pi} z_f \ln(b/r_p) \tag{6.73}$$

where both $z_f$ and $r_p$ vary, thus the circuit equation is (using Eqn.(3.50)),

$$\frac{dI}{dt} = \frac{V_o - \frac{1}{C_o}\int I\,dt - (R_o + f_i R_p)I + f_i I \frac{\mu}{2\pi}\left[\frac{z_f}{r_p}\frac{dr_p}{dt} - \ln(b/r_p)\frac{dz_f}{dt}\right]}{L_o + \frac{\mu}{2\pi} f_i\left[\,z_o \ln c + z_f \ln(b/r_p)\right]} \tag{3.74}$$

This circuit equation will be used for the whole radial phase (including shock inward phase, shock reflected phase and slow compression phase) since the expression for $L_p$ is identical for the rest phases.

### 3.3.3.6 Related Physical Quantities

<u>*Tube voltage*</u>

Applying Eqn.(3.51), using $L_p$ from Eqn.(3.73), we have

$$\begin{aligned} V = {} & \frac{\mu}{2\pi} f_i\left[\,z_o \ln c + z_f \ln(b/r_p)\right]\frac{dI}{dt} \\ & + f_i I \frac{\mu}{2\pi}\left[\ln(b/r_p)\frac{dz_f}{dt} - \frac{z_f}{r_p}\frac{dr_p}{dt}\right] + f_i R_p I \end{aligned} \tag{3.75}$$

<u>*Work done*</u>

The magnetic force ($F$) and work done ($W$) are as follows,

$$F = P_B \cdot S = P_B \cdot 2\pi r_p \cdot z_f = \frac{\mu_o f_i^2 I^2}{4\pi r_p} \cdot z_f$$
$$W = \int F \cdot \frac{dr_p}{dt} \cdot dt = \int \frac{\mu_o f_i^2 I^2}{4\pi r_p} \cdot z_f \cdot \frac{dr_p}{dt} \cdot dt \qquad (6.76 - 77)$$

The formulae for the tube voltage and work done will be used for the whole radial phase.

*Kinetic energy*

The kinetic energy is

$$E_k = \frac{1}{2} f_{mr} \frac{N_i}{N_o} \rho_o \cdot V_p \cdot \left[\frac{dr_p}{dt}\right]^2$$
$$= \frac{1}{2} f_{mr} \frac{N_i}{N_o} \rho_o \cdot \pi (r_p^2 - r_s^2) z_f \cdot \left[\frac{dr_p}{dt}\right]^2 \qquad (6.78)$$

Here we take the velocity of MP as the velocity for the whole plasma layer. This is a reasonable approximation since the region at the piston is more significant than the region at shock front from the energy point of view.

### 3.3.4 Reflected Shock Phase

#### 3.3.4.1 Equations of Motion

*Reflected shock front and magnetic piston*

In this phase, the piston is allowed to move towards the axis by assuming a "virtual" forward shock front moving with the on-axis speed of the incident shock. The reflected shock travels outwards with a fraction of the on-axis incident shock speed [127]. For example we may take this fraction as $F_{RF} \sim 0.3$ and the reflected shock speed is then,

$$\frac{dr_r}{dt} = F_{RF} \times \left(\frac{dr_s}{dt}\right)_{on-axis} \qquad (3.79)$$

The piston speed takes a similar form to Eqn.(3.70) as,

$$\frac{dr_p}{dt} = \frac{(\frac{2}{\gamma+1})\frac{r_r}{r_p}\left(\frac{dr_s}{dt}\right)_{on-axis} - \frac{r_p}{\gamma I}\left(1-(\frac{r_r}{r_p})^2\right)\frac{dI}{dt} - \frac{1}{\gamma+1}\frac{r_p}{z_f}\left(1-(\frac{r_r}{r_p})^2\right)\frac{dz_f}{dt}}{(\frac{\gamma-1}{\gamma})+\frac{1}{\gamma}(\frac{r_r}{r_p})^2} \quad (3.80)$$

*Elongation Equation*

$$\frac{dz_f}{dt} = -\frac{2}{\gamma+1}\left(\frac{dr_s}{dt}\right)_{on-axis} \quad (3.81)$$

The circuit equation is the same as Eqn.(3.72). This phase ends when the reflected shock meets the Magnetic piston, i.e. $r_r = r_p$.

### 3.3.4.2 Related Physical Quantities

Tube voltage and work done are the same as those in Sec.3.3.3.

*Kinetic energy*

The plasma enveloped by the reflected shock front is taken as stationary (radially) during this phase, so the kinetic energy is only related with the moving portion between the reflected shock front and magnetic piston. The velocity of the MP is approximated as the velocity of the whole layer. We have

$$E_k = \frac{1}{2}f_{mr}\frac{N_i}{N_o}\rho_o \cdot \pi(r_p^2 - r_r^2)z_f \cdot \left[\frac{dr_p}{dt}\right]^2 \quad (3.82)$$

## 3.3.5 Slow Compression Phase

### 3.3.5.1 Equation of Motion

Assuming that the diffusion of magnetic field into the plasma is not significant in this radiative phase (~ 20 ns), so the plasma is still assumed to be confined by a thin magnetic piston.

*"Piston" Equation*

We can use Eqn.(3.70) as the piston motion for this phase by setting $r_s = 0$, $dr_s/dt = 0$,

$$\frac{dr_p}{dt} = \frac{-\frac{r_p}{\gamma I}\frac{dI}{dt} - \frac{1}{\gamma+1}\frac{r_p}{z_f}\frac{dz_f}{dt} + \frac{4\pi(\gamma-1)}{\mu\,\gamma(f_i I)^2}\frac{r_p}{z_f}\frac{dQ}{dt}}{(\frac{\gamma-1}{\gamma})} \tag{3.83}$$

*Elongation Equation*

$$\frac{dz_f}{dt} = -\frac{2}{\gamma+1}\left(\frac{dr_s}{dt}\right)_{on-axis} \tag{3.84}$$

The circuit equation (Eqn.(3.74)) is coupled with these equations of motion for computation.

### 3.3.5.2 Related Physical Quantities

Tube voltage and work done take the same forms as those in Sec.3.3.3.

During this slow compression phase the kinetic energy is small compared with the plasma energy and thus may be neglected.

## 3.4 Numerical Computation

### 3.4.1 Normalization for Axial and Radial Shock Inward Phase

The governing equations i.e. Eqns.(3.48) and (3.50) for the axial phase, Eqns.(3.69), (3.70), (3.72) and (3.74) for the radial shock inward phase may be written in normalized form for the following purposes: (i) to simplify the system of equations so that its basic functional dependence may be seen more clearly, and (ii) to introduce scaling parameters which enable all ranges of operation of the plasma focus device to be covered simply by a variation of these scaling parameters. The later phases are not normalized except those energy related terms i.e. work done, energy-in and kinetic energy, which are all normalized to the initial stored energy in the capacitor bank.

The identification of the correct scaling parameters is equivalent to identifying the ratios which govern the régimes of operation of the device.

The first step in normalization is to choose the correct reference quantities to normalize the variables. Here we take:

$$\begin{cases} \tau = \dfrac{t}{t_o}; \quad \zeta = \dfrac{z}{z_o}; \quad \iota = \dfrac{I}{I_o} \\ \rho = \dfrac{R_o}{\sqrt{L_o/C_o}}; \\ \zeta_f = \dfrac{z_f}{a}; \quad k_p = \dfrac{r_p}{a}; \quad k_s = \dfrac{r_s}{a} \end{cases} \tag{3.85}$$

where $z_o$ is the length of the axial phase,

$t_o = \sqrt{L_o \cdot C_o}$ ; the angular frequency of the $L_o$-$C_o$ circuit (the short-circuited capacitor bank),

and $I_o = V_o/\sqrt{L_o/C_o}$ the peak current of the $L_o$-$C_o$ circuit.

With this normalization, we will obtain the normalized equations for axial phase and radial inward shock phase.

### 3.4.1.1 Axial Phase

The equation of motion (3.48) becomes:

$$\frac{d^2\zeta}{d\tau^2} = \frac{f_i^2 a^2 \iota^2 - (\frac{d\zeta}{d\tau})^2}{\zeta} \tag{3.86}$$

and the circuit Eqn.(3.50) becomes

$$\frac{d\iota}{d\tau} = \frac{1 - \int \iota\, dt - \beta \iota f_i \frac{d\zeta}{d\tau} - \rho \iota}{1 + \beta f_i \zeta} \tag{3.87}$$

The first scaling parameter α is introduced as a ratio of two characteristic times $t_o$ and $t_a$:

$$a = \frac{t_o}{t_a} \tag{3.88}$$

Thus, $t_a$ appears naturally as a characteristic axial transit time:

$$t_a = \left( \frac{4\pi^2 (c^2 - 1)}{\mu \ln(c)} \right)^{1/2} \cdot \frac{z_o (f_m \rho_o)^{1/2}}{(I_o/a)} \tag{3.89}$$

The second scaling parameter is seen to be a ratio of two inductances:

$$\beta = \frac{L_{z_o}}{L_o} = \frac{\frac{\mu}{2\pi} z_o \ln c}{L_o} \tag{3.90}$$

### 3.4.1.2 Radial Inward Shock Phase

The radial shock motion, the axial elongation of the pinch, the radial piston motion and the circuit equation become:

$$\begin{cases} \dfrac{dk_s}{d\tau} = -\dfrac{a a_1 f_i \iota}{k_p} \dfrac{1}{\sqrt{f_m}} \\[2ex] \dfrac{d\zeta_f}{d\tau} = -\left(\dfrac{2}{\gamma+1}\right) \dfrac{dk_s}{d\tau} \\[2ex] \dfrac{dk_p}{d\tau} = \dfrac{\left(\dfrac{2}{\gamma+1}\right)\dfrac{k_s}{k_p}\dfrac{dk_s}{d\tau} - \dfrac{k_p}{\gamma \iota}\left(1-\left(\dfrac{k_s}{k_p}\right)^2\right)\dfrac{d\iota}{d\tau} - \dfrac{1}{\gamma+1}\dfrac{k_p}{\zeta_f}\left(1-\left(\dfrac{k_s}{k_p}\right)^2\right)\dfrac{d\zeta_f}{d\tau}}{\left(\dfrac{\gamma-1}{\gamma}\right) + \dfrac{1}{\gamma}\left(\dfrac{k_s}{k_p}\right)^2} \\[2ex] \dfrac{d\iota}{d\tau} = \dfrac{1 - \int \iota \, d\tau + \beta_F f_i \iota \dfrac{\zeta_f}{k_p}\dfrac{dk_p}{d\tau} + f_i \beta_F \ln\left(\dfrac{k_p}{c}\right) \iota \dfrac{d\zeta_f}{d\tau} - \rho \iota}{1 + f_i \beta - f_i \beta_F \ln\left(\dfrac{k_p}{c}\right)\zeta_f} \end{cases}$$

(3.91 - 94)

where $\rho = R_o / \sqrt{L_o / C_o}$ .

These four equations form a closed set of equations which may be integrated for $k_s$, $k_p$, $k_f$ and $\iota$..

### 3.4.1.3 Normalization of Tube Voltage

*Axial phase*

$$v = f_i \beta \left(z \frac{d\iota}{d\tau} + \iota \frac{dz}{d\tau}\right) \tag{3.95}$$

*Radial shock inward phase*

$$v = f_i\left(\beta - \beta_F \ln(\frac{k_p}{c})\, z_f\right)\frac{d\iota}{d\tau} - f_i\,\beta_F\left(\ln(\frac{k_p}{c})\frac{dz_f}{d\tau} + \frac{z_f}{k_p}\frac{dk_p}{d\tau}\right)\cdot \iota \qquad (3.96)$$

where,

$$\begin{cases} a1 = \left(\dfrac{(\gamma+1)(c^2-1)}{\ln c}\right)^{\frac{1}{2}} \dfrac{F}{2} \\ \beta_F = \dfrac{\beta}{F \ln c} \\ F = z_o/a \end{cases} \qquad (3.97)$$

### 3.4.2 Description of Numerical Computation

#### 3.4.2.1 Numerical Method for Integrating

To compute this model, the integration of the equations of this model has been performed using a simple linear approximation method [67,128] i.e. for any variable, its value at time step ($n$) will be related to the value of the previous step ($n$-1) as,

$$A|^{n} = A|^{n-1} + \left.\frac{dA}{dt}\right|^{n-1} \cdot \Delta t \qquad (3.98)$$

with $\Delta t$ the time increment.

This method was checked against a Runge-Kutta method and found to be of sufficient accuracy when time-increment for each phase is chosen as follows (in Tab.3.2):

***Table 3.2.*** Time increments set for each phase

| | |
|---|---|
| axial phase | 1 ns |
| radial inward shock phase | 2 ps |
| radial reflected shock phase | 2 ps |
| slow compression phase | 0.2 ps |

#### 3.4.2.2 Computational Procedure

Initial conditions at $\tau = 0$ for the axial phase [128] is:

$$\begin{cases} \zeta = 0 \, ; \quad \dfrac{d\zeta}{d\tau} = 0 \, ; \quad \dfrac{d^2\zeta}{d\tau^2} = \dfrac{f_i}{\sqrt{f_m}} \sqrt{\dfrac{2}{3}} \, a \, ; \\ \\ \iota = 0 \, ; \quad \dfrac{d\iota}{d\tau} = 1 \, ; \quad \int \iota \, d\tau = 0 \, . \end{cases} \tag{3.99}$$

The axial phase ends when the plasma sheath reaches the end of the anode i.e. $\zeta = 1$ (or $z = z_o$).

The radial phase starts with both the shock front and magnetic piston are at the rim of the anode i.e.

$$k_s = 1, \; k_p = 1.. \; (\text{or } r_s = r_p = a) \tag{3.99}$$

and stops when the shock front hits the axis of anode i.e. $k_s = 0$ (or $r_s = 0$). Then the radial reflected shock phase starts.

The reflected shock phase inherits: $I$, $\int I dt$, $\left(\dfrac{dr_s}{dt}\right)_{on-axis}$, $r_p$ and $z_f$ from the last phase. This phase stops when the reflected shock meets the magnetic piston i.e. $r_s = r_p$.

The slow compression phase inherits $I$, $\int I dt$, $\left(\dfrac{dr_s}{dt}\right)_{on-axis}$, $r_p$ and $z_f$ from last phase and is computed for 10 ns, which is the mean value of experimentally measured focus duration.

The numerical code for this model was written using the programming language Borland C++ Version 4.5.

## 3.5 Computational Results

The radiative plasma focus model described above is applied to our NIE-SSC-PFF compact plasma focus and results in agreement with experimental observations were obtained. In this section a typical set of results will be presented. Some results are shown in Chapter 5 where the experimental results will be compared with the results obtained from this simulation.

### 3.5.1 Typical Results

Computation is done for a typical case of neon plasma focus operating under the optimum condition (determined by experiments) of 13 kV charging voltage, 2.5 mbar pressure. The input parameters and the corresponding scaling parameters are summarised in Tab.3.3. The experimentally measured current factor $f_i \sim 0.8$ is used. By using this current factor and matching the arrival time of plasma sheath to that measured by magnetic probe (see Chapter 5, Sec.5.2.2) the mass factor $f_m \sim 0.046$ for the rundown phase is obtained and used for this computation.

***Table 3.3*** Parameters of a typical discharge for simulation

| fixed parameters | | adjustable parameters | | scaling parameters | |
|---|---|---|---|---|---|
| | 110 ns | $V_o$ | 13 kV | c | 3.37 |
| $C_o$ | 30 μF $L_o$ | $P_o$ | 2.5 mbar | F | 17 |
| $b$ | 3.2 cm | $Z_n$ | 10 | $I_o$ | 215 kA |
| $a$ | 0.95 cm | $W_M$ | 20 | $t_o$ | 1.82 μs |
| $z_o$ | 16.3 cm | $f_i$ | 0.8 | $t_a$ | 1.15 μs |
| $R_o$ | 0.12 ohm | $f_m$ | 0.046 | α | 1.59 |
| | | $f_{mr}$ | 0.4 | β | 0.36 |
| | | $F_{RF}$ | 0.3 | $\beta_F$ | 0.01 |
| | | $t_p$ | 10 ns | ρ | 0.2 |

Fig.3.4 shows the comparison between the recorded signals and computed curves for both current and voltage during the first 4 μs. The current curve fits the experimental signal well. The simulated voltage spike is sharper and has a larger amplitude than the experimental one. This may be explained by the low frequency response of the resistive voltage probe.

The trajectory of the plasma sheath in the radial phase and its velocity are shown in Fig.3.5. The computational model gives the final radial velocity of the imploding plasma sheath values about 30 cm/μs and the length of the pinched column values around 8 mm, in good agreement with the experiment. By introducing a reflected shock phase a minimum compression radius of ~ 0.4 mm is obtained, which agrees with results from shadowgraphy and schlieren photography done on the *same* machine. It takes about 4 ns after the shock front hits the axis for the piston to reach its minimum radial position, which is the starting point of the slow compression phase. The plasma column is found to continue contracting, as shown in Fig.3.5(a), during the whole radiative phase. This is due to the very large radiation rate from neon plasma which exceeds the Joule heating rate. When the radius becomes very small we expect hot spots to be formed as observed experimentally. Therefore the last few ns of compression is not expected to agree with experimental observation, since we have not included hot spots in our modelling.

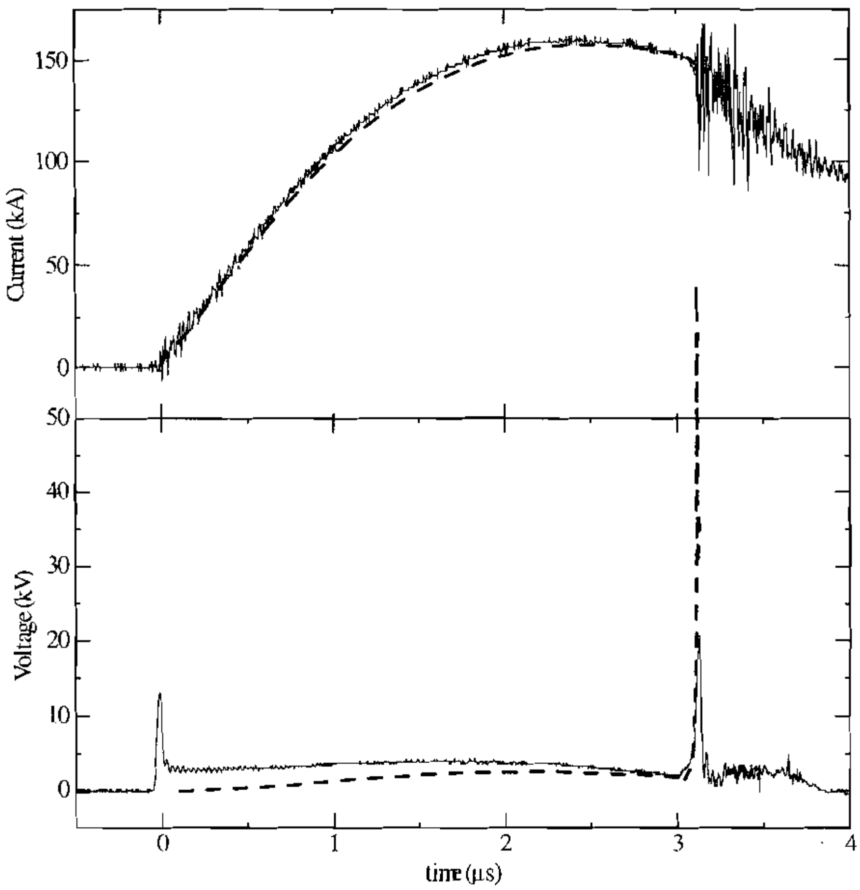


**FIGURE 3.4**
Comparison between the experimental data (full lines) and results from the numerical simulation (dashed lines) for current and voltage signals. conditions: discharge at 13 kV neon at 2.5 mbar.

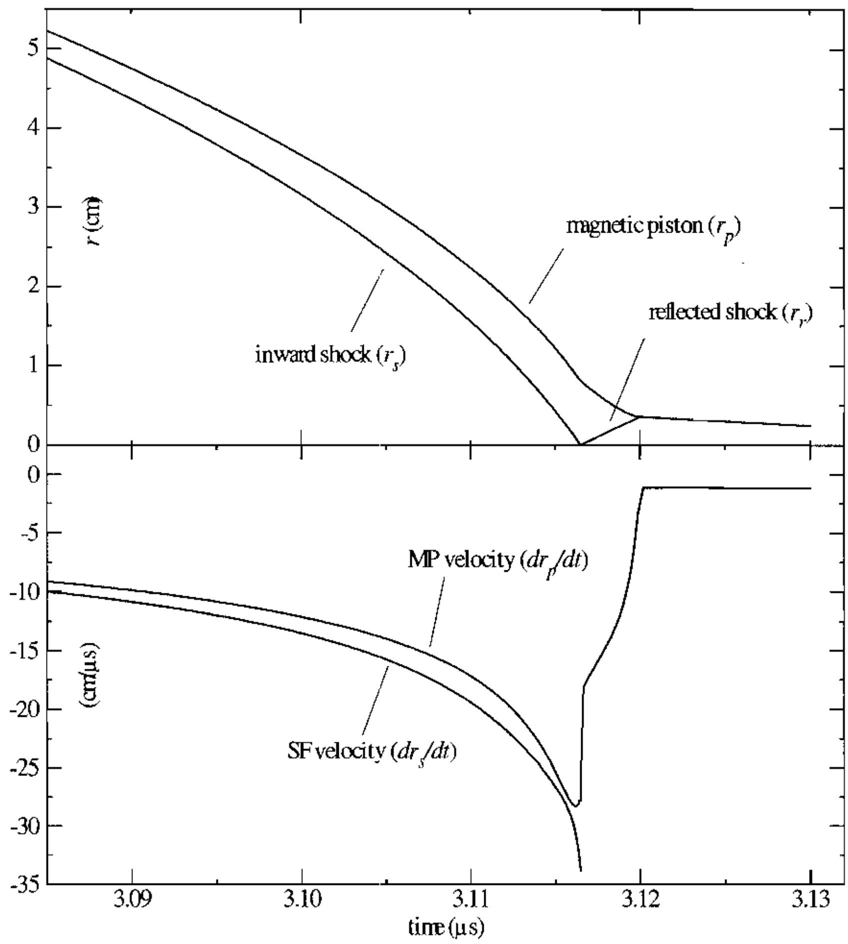


**FIGURE 3.5**
Upper plot: trajectories of radial inward shock ($r_s$), reflected shock ($r_r$) and magnetic piston ($r_p$).
Lower plot: inward shock speed ($dr_s/dt$) and magnetic piston speed ($dr_p/dt$) conditions: discharge at 13 kV neon at 2.5 mbar.

The average electron temperature of 360 eV and electron density of ~ $10^{26}$ $m^{-3}$ are given by the computation for this particular case, as shown in Fig.3.6(a). At this condition the neon plasma is highly ionised, as can be seen in Fig.3.6(b), where $\alpha_8$, $\alpha_9$, $\alpha_{10}$ are the fraction of ions at 8th, 9th, and 10th ionised levels respectively. The curves in Fig.3.6 start from the beginning of the reflected shock phase and the vertical dotted line marks the end of the reflected shock phase and the start of the radiative phase (or the slow compression phase). Fig.3.6(c) shows the comparison among the line emission rate, recombination emission rate and the Bremsstrahlung rate, the joule heating rate is also shown for comparison with the radiation. We see that the line emission dominates the total radiation and the Bremsstrahlung is very small as compared to the other two emission mechanisms. The area under each curve is the x-ray yield contributed by each mechanism:

$E\_line = 8.5$ J (line radiation)

$E\_rec = 3.2$ J (radiative recombination)

$E\_brem = 0.4$ J (Bremsstrahlung)

which show that the line radiation takes 70% of the total yield, the radiative recombination takes 27% and the Bremsstrahlung 3%. It is noted that the radiation computed here includes the whole emission spectrum, mainly in the x-ray region. For the application of SXR lithography which is our main objective, we are more interested in a specific wavelength range below 20 Å. More discussion of that specific wavelength range is given in Chapter 5 Sec. 5.4.2 and 5.4.3.

### 3.5.2 Discussion

The simple radiative plasma focus model gives a clear picture of the dynamics in the radial phase as well as quantitative results of the x-ray emission from neon plasma focus. With the finite speed of small disturbance and reflected shock included into the model we obtained more realistic physical picture of the radial inward compression and minimum compression radius. An electron density of $10^{26}$ $m^{-3}$ and an electron temperature of 360 eV are computed using the model. For neon plasma at this temperature the line radiation is found to be the strongest feature, whereas the Bremsstrahlung is relatively weak. As the joule heating rate is small compared to the radiation loss, radiative collapse is predicted by this model.

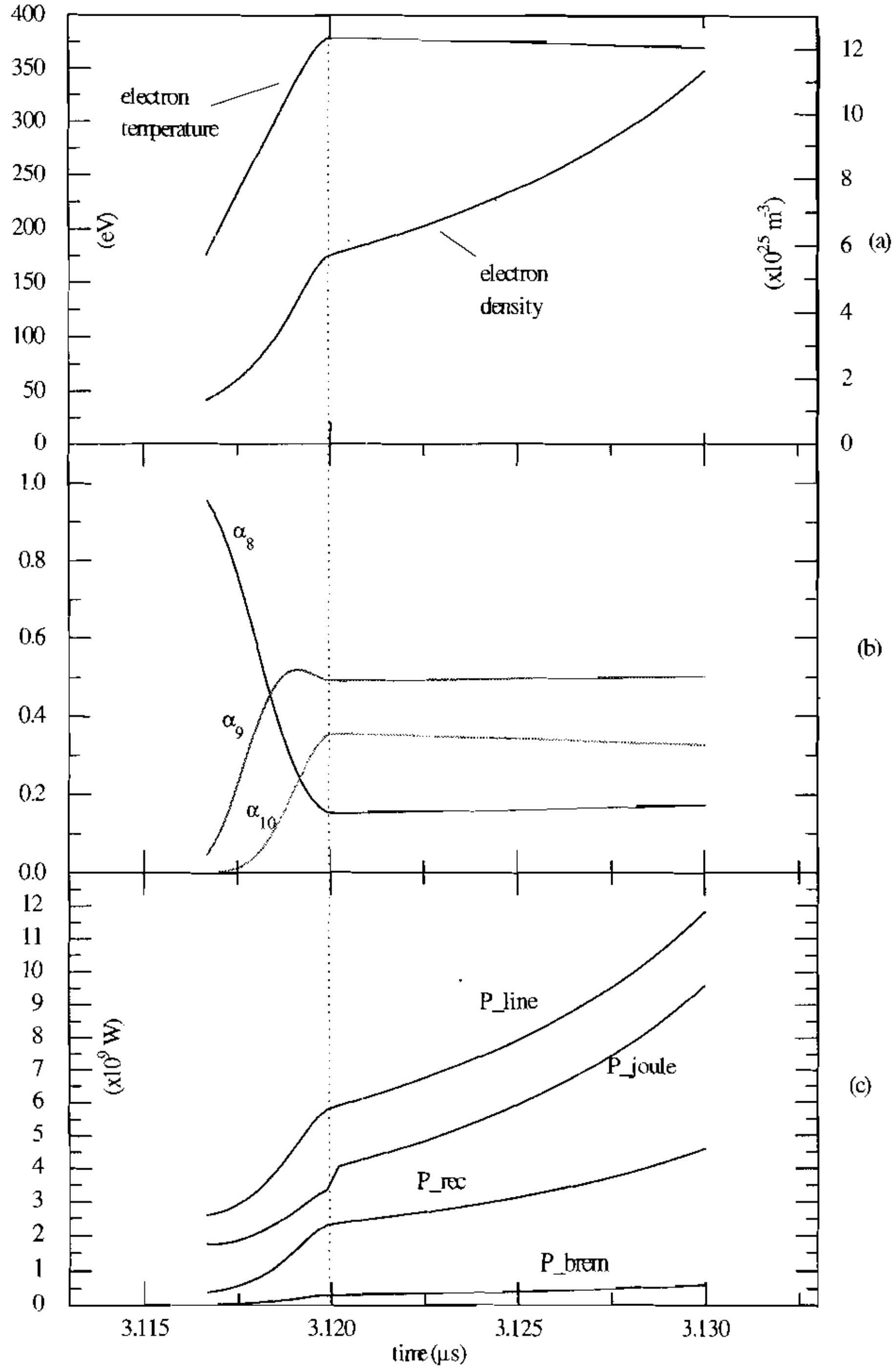


**FIGURE 3.6**
(a) electron temperature and density.
(b) fraction of 8th, 9th, and 10th ionised state for neon ion.
(c) *P_line*, *P_rec* and *P_brem* are emission rates from line radiation, recombination and Bremsstrahlung respectively; *P_joule* is the joule heating rate.
conditions: discharge at 13 kV neon at 2.5 mbar.

The simple model presented in this chapter assumes that the pinched column is uniform in nature. Experimentally we observe hot spots with different aspect ratio (length to radius) which will affect the dynamics and radiation of the final phase of the focus. This could be the major cause of the discrepancy between the simulated values and the measured ones. Another factor of concern in this model is that we have not been able to fix satisfactorily the mass factor for the radial phase. The result is found to be quite sensitive to the value we assign to this quantity. The radiation time which we assumed to be the measured pinch life time, is of course also of primary importance. Experimentally two or three peaks in the x-ray bursts are observed, so the effective radiation time used in the model is probably longer than the actual radiative phase. Despite of all the factors listed above, our relatively simple model still gives quantitative emission rates which are in the same order of magnitude when compared with measured values, thus giving a basic understanding of the plasma focus as a radiation source.

# Chapter 4

# Apparatus and Diagnostic Techniques

## 4.1 The Plasma Focus Device: NIE-SSC-PFF

The National Institute of Education - School of Science - Plasma Focus Facility (NIE-SSC-PFF) is a 3.3kJ/15kV plasma focus device designed from the UNU/ICTP PFF [129]. Basically, the NIE-SSC-PFF consists of the following subsystems (see Fig.4.1):

- driver (high-voltage charger, capacitor and high-voltage cables),
- switch (spark gap),
- focus tube (discharge chamber, input flanges and electrode system),
- vacuum system (vacuum pump, manometer(s), valves, working gas container, etc.),
- triggering electronics (high voltage transformer),
- control & sync. electronics (master pulse trigger generator, high-voltage trigger unit and delay units)

- diagnostics (Rogowski coil(s), high-voltage probe, magnetic probe(s), visible spectroscopic system, axial speed detector, soft x-ray spectrometer(s), and calorimeter),
- DSO (Digital Storage Oscilloscope) and
- computer analysis system (computer and software packages)

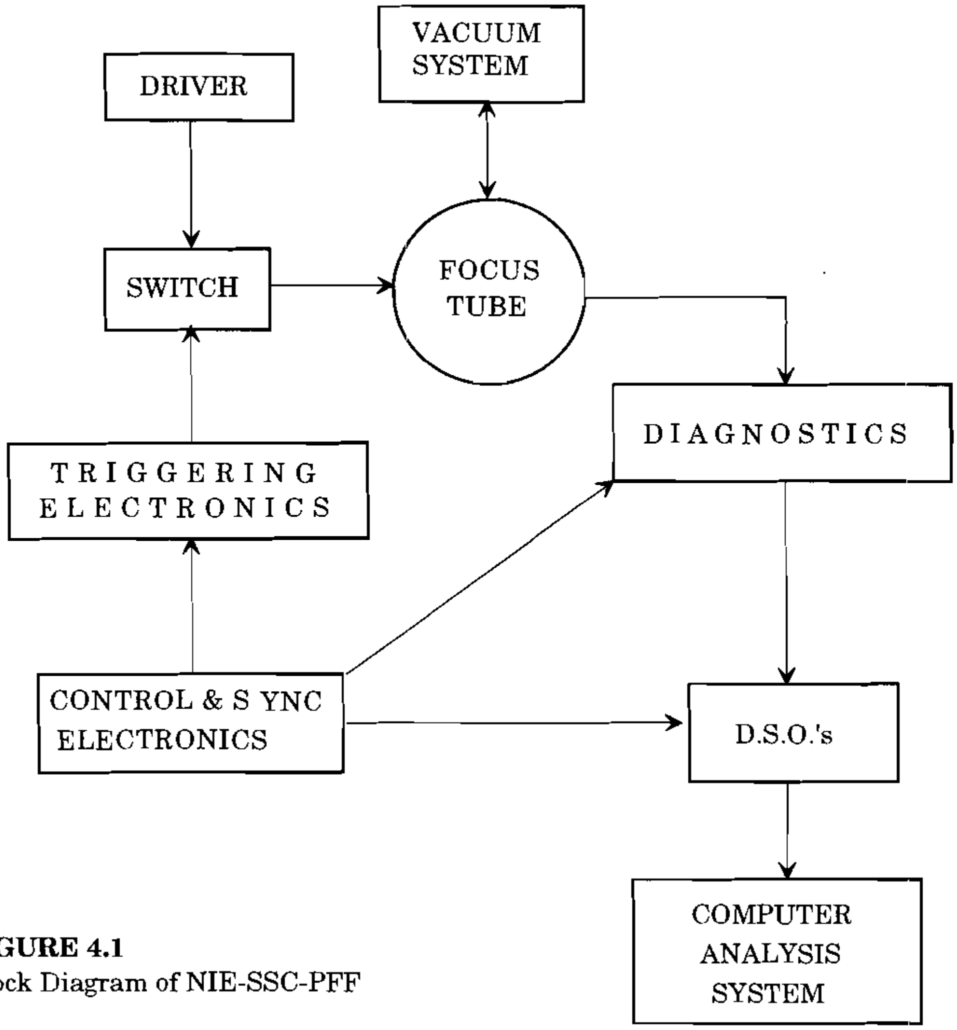


**FIGURE 4.1**
Block Diagram of NIE-SSC-PFF

## 4.2 Description of NIE-SSC-PFF

### 4.2.1 System Arrangement

A simple parallel-plate spark gap with a swinging cascade configuration (see Fig.4.2) was developed giving a low inductance at minimum cost. The ratio of the gap is 3:2 (4.5 - 3 mm). The gap is triggered via an isolating capacitor from an 800-V SCR unit via a TV transformer that was found to have a step-up ratio of 17 times and rise time of 1 μs. The parallel-plate spark gap is made from 0.5-in.-thick copper plates and proved maintenance free for 200 discharges between 13-15 kV before requiring cleaning. The triggering jitter was found to be within ±50 ns.

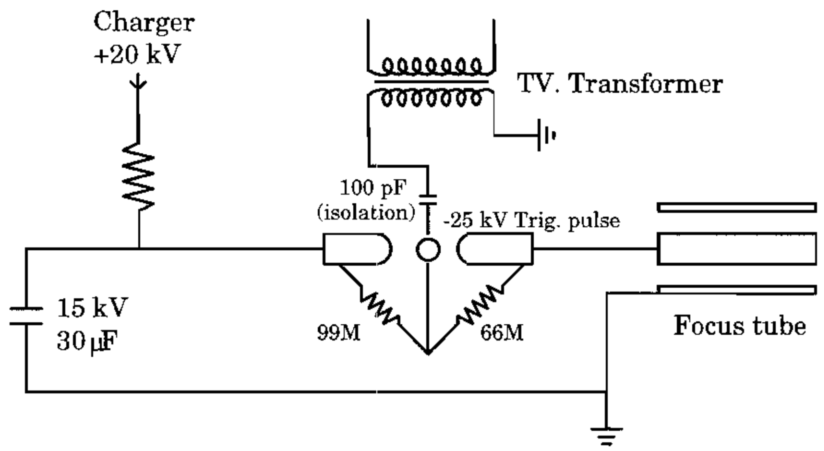


**FIGURE 4.2**
Circuit for the swinging-cascade spark gap and focus tube.

The arrangement for the capacitor, the connecting plates, the spark gap, and the output coaxial cables is shown in Fig.4.3(A). To keep the inductance low, the earth plate of the capacitor (labeled no. 5) is extended nearly up to the anode and insulation is provided by a nylon cap (no. 4) around the anode stud. The cap dips into a pool of oil (no. 7) that is prevented from splashing out by means of an O-ring (no. 8). Mylar sheets (no. 6), 2 in. wider all around than the conducting plates, sandwiched by polyethylene sheets (no. 10) complete the insulation between the HV plate (no. 12) and the Earth plate as shown in Fig.4.3(A). The Earth plate (no. 5) runs unbroken to the output position where the Earths of the coaxial cables connect. On top of the insulating sheets the HV plate is connected to the spark gap. Between the spark gap electrodes and all along it is placed a 0.5-in.-diam copper tubing (no. 15) that acts as the trigger electrode. The output plate of the spark gap is connected to the focus tube by means of 16 coaxial cables (no. 16) used in parallel.

Essential to the structure of the focus tube is the backwall (see Fig.4.3B) insulator. The glass insulator (no. 26) plays an important role in the symmetrical formation of the current sheet and has to be properly mounted to avoid being broken by vibration. In the present design this glass insulator is mounted in a rubber holder which when compressed tightly and symmetrically by the brass flange (no. 25) grips the glass insulator. The rubber holder also acts as a vacuum and high voltage seal. Fig.4.3(B) also shows the anode collector plate (no. 18) and the cathode collector plates (no. 22) onto which the coaxial cables connect.

The plasma chamber (no. 30) consists of a 30-cm length of 6.5-in.-diam mild steel tubing that is chromed. Vacuum is provided by a single stage rotary pump reaching an ultimate base pressure ~ 0.005 torr. The system was adjusted for a leakage rate of less than 2 μ/min and pressure is read with a mechanical diaphragm gauge. This level of vacuum proved to be sufficient for operating with good focus in various gases and good neutron yield when operated in deuterium.

Another view of the NIE-SSC-PFF plasma focus with more details is shown in Fig.4.4, where the available diagnostic windows are also shown. There are three circular windows with two on the side and one on the top. Two rectangle windows are built for optical diagnostics as well as for other measurements. In this work we used it for holding the plane crystal spectrograph and speed detector. The focusing region is about the same height as the two side circular windows. The top window is protected from the strong shock wave by a plate with a small aperture to let through the radiation. This arrangement also reduces the highly energetic particles in the axial direction.

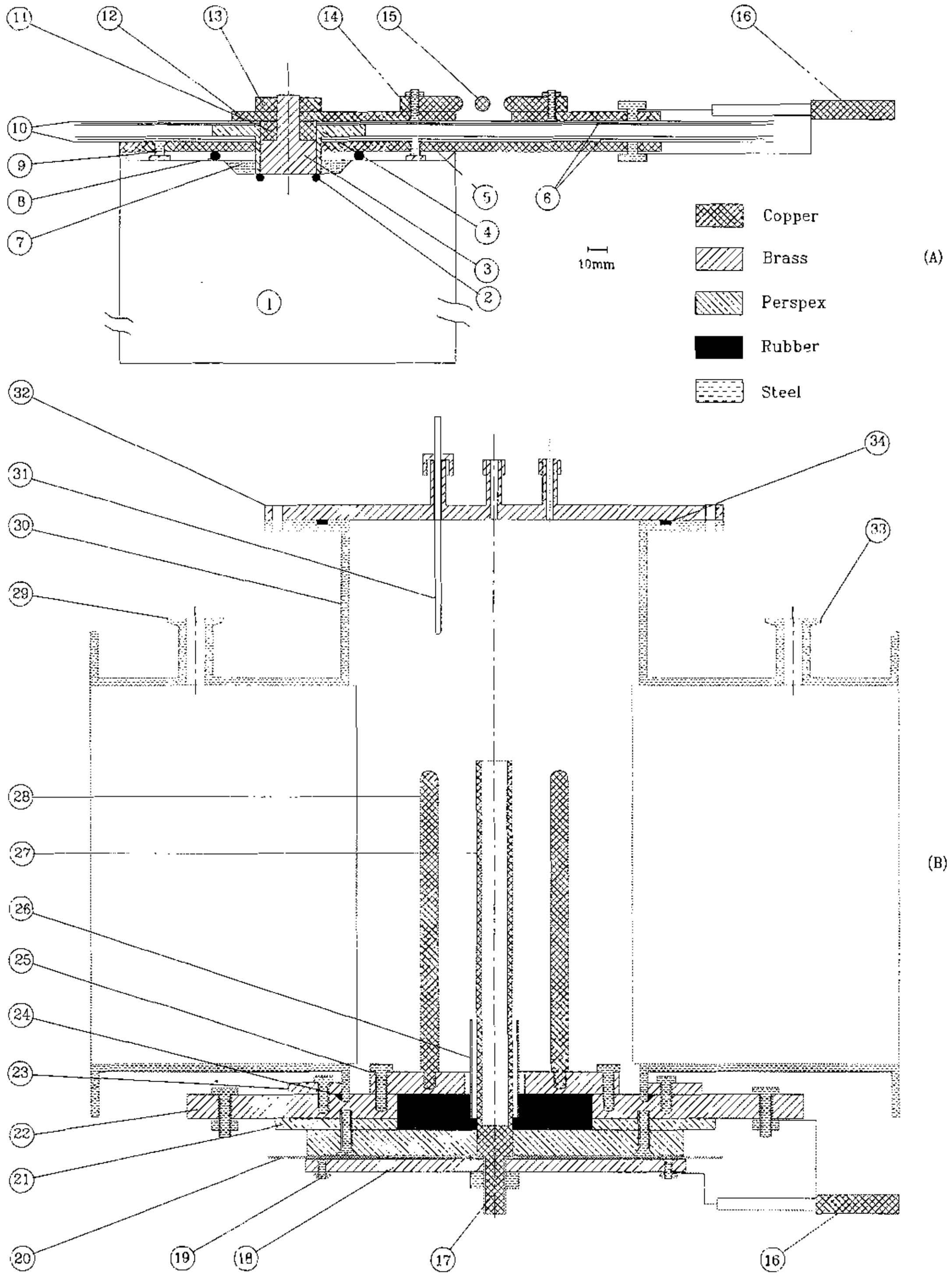


**FIGURE 4.3** Diagram of NIE-SSC-PFF: (A) The capacitor connecting plates, the spark gap, and output coaxial cables. 1=capacitor; 2=capacitor O-ring seal; 3=nut; 4=nylon cap; 5=earth plate; 6=Mylar film; 7=oil; 8=O-ring seal; 9=earth stud; 10=polyethelene film; 11=copper ring; 12=high-voltage output plates; 13=lock nut; 14=HV electrode for swinging cascade spark gap; 15=trigger electrode; 16=output cables; (B) The plasma focus tube. 17=stud of anode; 18=anode collector plate; 19=connecting points for coaxial cables; 20=5-mil Mylar film; 21=perspex spacer; 22=cathode collector plate; 23=flange; 24=O-ring seal; 25=cathode support plates; 26=glass insulator; 27=focus anode; 28=focus cathode(6 rods); 29=outlet to diaphragm gauge and vacuum pump; 30=chamber; 31=glass jacket for magnetic probe; 32=top flange; 33=inlet for test gas; 34=O-ring.

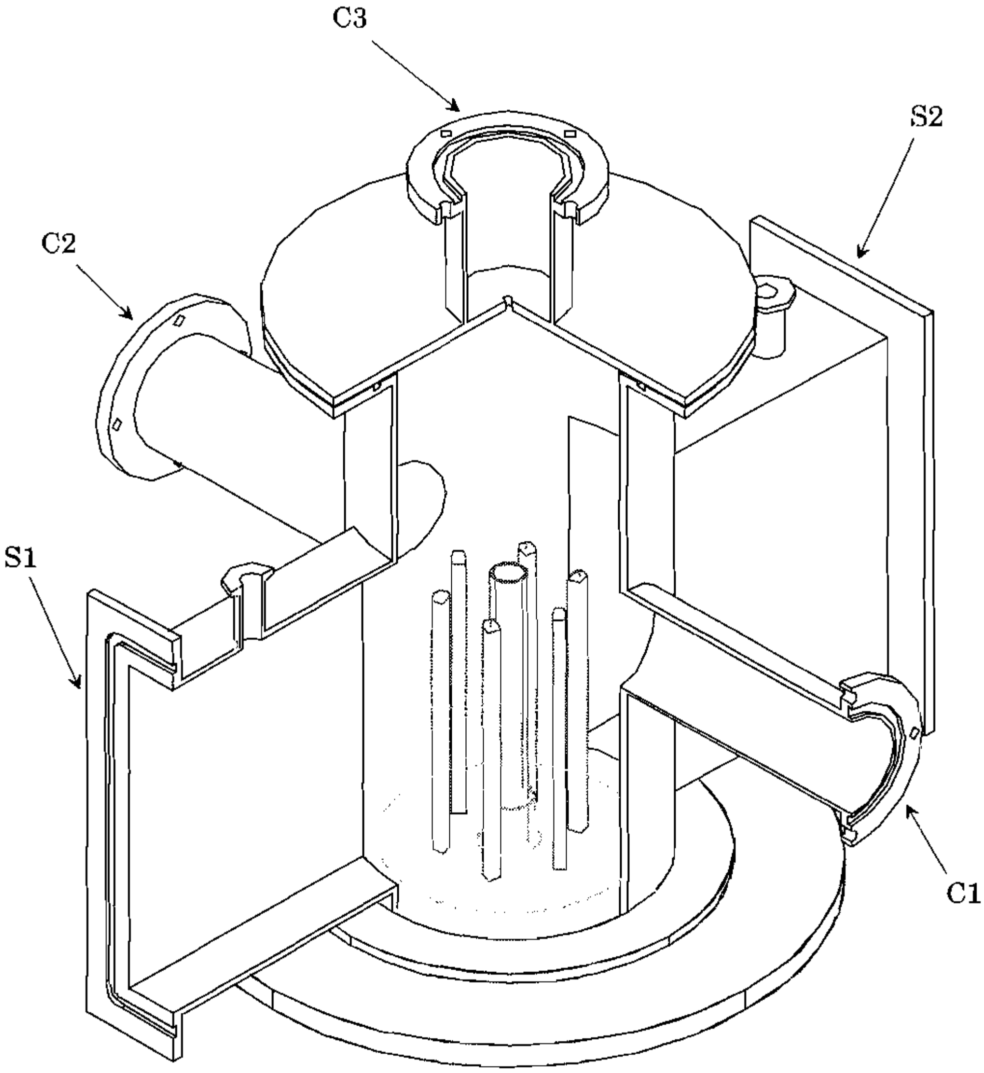


**FIGURE 4.4**
3D view of NIE-SSC-PFF plasma focus
showing the two circular (C1, C2), two square (S1, S2) windows for side-on mesurements and one circular widow (C3) on the top for end-on detection. The focusing region is about the same height as that of the centres of the side circular windows (C1,C2)

### 4.2.2 Equivalent Circuit and Parameters of NIE-SSC-PFF

The NIE-SSC-PFF may be represented by an equivalent circuit as illustrated in Fig.3.3 in Chapter 3. The electrical feeding network (capacitor, switch, cables, and input flanges) consists of the capacitance $C_o$, inductance $L_o$, and resistance $R_o$. For the focus tube, the electrical representation consists of the plasma inductance and resistance, $L_p$ and $R_p$, respectively, and leakage impedance $h_L$. In our calculation (see Sec.3.3.1), $R_p$ was considered negligible for the axial phase and in a Spitzer form during the radiative phase.

The design parameters of NIE-SSC-PFF are summarized in Tab.4.1. The values of the electrical parameters of the NIE-SSC-PFF obtained using the Rogowski coil calibration procedure are listed in Tab.4.2.

***Table 4.1*** Design parameters of NIE-SSC-PFF

| | |
|---|---|
| capacitance | $C_o$ = 30 μF |
| inductance | $L_o$ = 110 nH |
| impedance | $Z_o = \sqrt{L_o/C_o}$ = 60.5 mΩ |
| charging voltage | $V_o$ = 14 kV |
| anode radius | $a$ = 0.95 cm |
| cathode radius | $b$ = 3.2 cm |
| length of electrode | $z_o$ = 16 cm |

***Table 4.2*** Experimentally measured parameters of NIE-SSC-PFF

| | |
|---|---|
| resistance | $R_o$ = 11.9 mΩ |
| peak discharge current in short-circuit | $I_{max}$ = 200 kA |
| typical rise time | $t_{a,exp}$ = 2.9 μs |
| typical axial velocity | $v_{ax}$ ~ 6-10 cm/μs |
| typical radial velocity | $v_{radial}$ ~ 25 cm/μs |

## 4.3 Basic Electrical Diagnostic Methods

### 4.3.1 Rogowski Coil

#### 4.3.1.1 Introduction

The Rogowski coil [21] is a multi-turn solenoid bent into the shape of a torus and is used to measure the high current due to the capacitor bank discharge. The design of Rogowski coil is given in Fig.4.5. The coil is terminated with a low-inductance resistor, $r$. The equivalent circuit is given in Fig.4.5b, where $L_c$ and $r_c$ are respectively the inductance and resistance of the coil, $I$ is the discharge current , and $\iota$ is the circuit current of coil. The circuit equation can be rewritten as:

$$L_c \frac{d\iota}{dt} + (r + r_c)\iota = k\frac{dI}{dt} \qquad (4.1)$$

a) If $L_c \frac{d\iota}{dt} >> (r + r_c)\iota$ , then from (4.1) we can obtain: $\iota = \frac{k}{L_c} I$ , so the output voltage will be:

$$V_o = r\iota = r\frac{k}{L_c} \times I = k_1 I \qquad (4.2)$$

In this case the Rogowski coil acts as a current transformer.

b) If $(r + r_c)\iota >> L_c \frac{d\iota}{dt}$ then from (4.1) the output will be:

$$V_o = r\iota = (\frac{rk}{r_c + r})\frac{dI}{dt} \qquad (4.3)$$

Under this condition the coil can be used to measure the derivative of current ($dI/dt$).

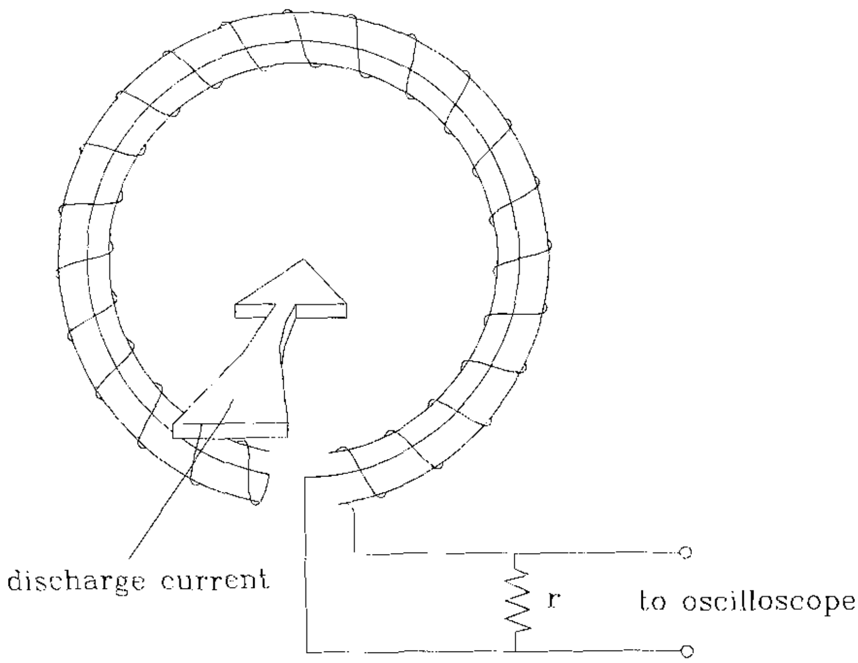


**FIGURE 4.5a**
Rogowski coil used as a current transformer when a small integration resistor of negligible inductance is employed

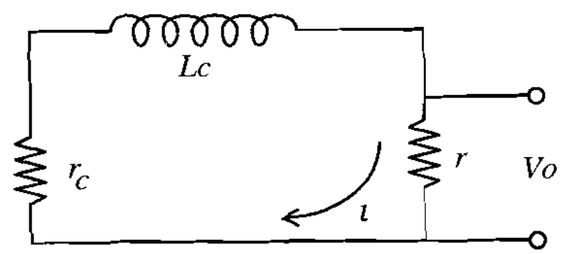


**FIGURE 4.5b**
Equivalent Circuit of Rogowski Coil

### 4.3.1.2 Calibration

The Rogowski coil, when used as a current transformer, need to be calibrated. For a L-R-C discharge system with the known charging voltage and capacitance, the following two methods can be used for determining the absolute current flowing through the Rogowski coil. The coil is thus calibrated against this absolute current. The plasma focus system, with the electrodes shorted from the end, was employed as such a simple L-R-C circuit to do the calibration.

Method I

For a simple L-R-C circuit, when the capacitor charged to voltage $V_o$ is discharged to a L-R load, the equation which governs the current flowing through the circuit can be written as,

$$L\frac{dI}{dt} + I \cdot R = V_o - \frac{1}{C}\int I dt \qquad (4.4)$$

For $\frac{R^2}{4L^2} < \frac{1}{LC}$ , which is the case for our machine, the solution of above equation takes the form of damped sinusoid,

$$I = \frac{V_o}{L\omega}\exp\left(-\frac{R}{2L}t\right)\sin(\omega t) \qquad (4.5)$$

where

$$\omega = \frac{2\pi}{T} = \sqrt{\frac{1}{LC} - \frac{R^2}{4L^2}} \qquad (4.6)$$

The first two peak currents and the reversal ratio are:

$$\begin{cases} I_1 = \frac{V_o}{L\omega}\exp\left(-\frac{R}{2L}\cdot\frac{1}{4}T\right) & (a) \\ I_2 = \frac{V_o}{L\omega}\exp\left(-\frac{R}{2L}\cdot\frac{3}{4}T\right) & (b) \\ f \equiv \frac{I_2}{I_1} = \exp\left(-\frac{R}{2L}\cdot\frac{1}{2}T\right) & (c) \end{cases} \qquad (4.7)$$

From Eqn.(4.7c) we have,

$$\frac{R}{2L} = -\frac{2}{T}\ln f \qquad (4.8)$$

Substituting it into Eqn.(4.6) and eliminating $R$, we can obtain,

$$L = \frac{T^2}{4\pi^2}\frac{1}{1 + \frac{1}{\pi^2}\ln^2 f} \qquad (4.9)$$

Substituting Eqn.(4.8) and Eqn.(4.9) into Eqn.(4.7a) we finally get,

$$I_1 = \frac{V_o}{L\omega}\exp\left(-\frac{1}{2}\ln f\right) = \frac{\pi C_o V_o}{T} 2\left(1+\frac{1}{\pi^2}\ln^2 f\right)\sqrt{f} \qquad (4.10)$$

Method II

Lee has used a simpler formula [130] for the determination of discharge current. For the actual peak current flowing, assumed to be a slightly damped sinusoid:

$$I_1 = \frac{\pi C_o V_o (1+f)}{T} \qquad (4.11)$$

In practice, to get more accurate values we measured several consecutive peak values and take the average,

$$f = \frac{1}{4}\left(\frac{V_5}{V_4}+\frac{V_4}{V_3}+\frac{V_3}{V_2}+\frac{V_2}{V_1}\right) \qquad (4.12)$$

The same procedure applies to the determination of $T$, the periodic time. Several cycles are taken to get the average of $T$.

Thus by measuring $f$ and $T$ from the oscillogram $I_1$ may be computed in kA and compared to the oscilloscope value of $V_1$ in volts. Then the calibration factor for the coil may be written as

$$k_1 = \frac{I_1}{V_1} \text{ A/volt} \qquad (4.13)$$

The calibration factor for the coil used in our experiments was determined to be: $k_1 = 1.425 \times 10^3$ A/volt using the methods described above.

### 4.3.2 Voltage Probe

High-voltage resistive divider are commonly used because of their easy design and fabrication. A wide band voltage probe for work below 100 kV was reported by Keller [131].

In our application, the transient voltage across the plasma was measured using a resistive voltage probe. This probe was connected at the lower end of the focus tube across the anode and cathode (input) flanges.

The high-voltage probe is a resistive divider as shown in Fig.4.6 consisting of a series of ten 510 ohm/1W resistors shunted by a 51 ohm resistor at one end of the chain. The probe is enclosed in a copper tube of 20 mm diameter. The electrical insulation between the high voltage point and the copper casing at ground potential is provide by flexible PVC pipe. The output signal is attenuated 100 times. The frequency response of this high-voltage probe limits its response time to about 20 ns. The divider is then connected to the oscilloscope through a attenuation terminal. The final attenuation was determined to be 2305.

Further discussions and interpretation of the voltage signals recorded in our experiments will be given in Chapter 5 of this thesis.

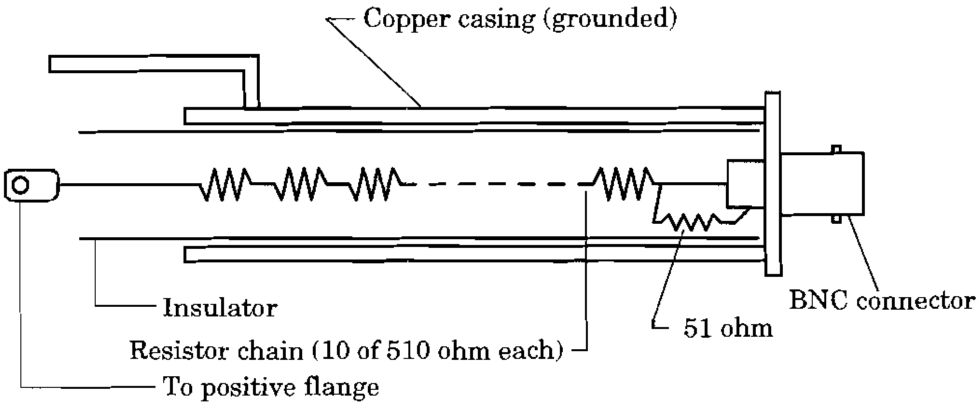


**FIGURE 4.6**
Schematics of Voltage Probe

## 4.4 Optical Measurement of Plasma Sheath Velocity

### 4.4.1 Design of Light-pipe Detector

The luminous information from the current sheath provides one way of measuring the velocity or even the thickness of the moving current sheet [132]. By measuring the difference of arrival times of current sheet at two points of known distance apart we are able to obtain the average speed over that distance. Optical photodiodes of fast rise time combined with two light pipes put in parallel can be used for such purpose. We applied detectors using several specially designed light-pipes to monitor the speeds of the current sheath at several points along the run-down direction and thus study the evolution characteristics in axial rundown phase. The light-pipes (one of them is shown in Fig.4.7) used for these measurements are oriented such that they are perpendicular to the axis of the plasma focus and the open end of the light-pipe "views" a small segment of the anode. So arranged, the detectors yield information on the speed and luminosity of the plasma sheath during the axial rundown phase of the discharge.

The photodiodes used for this detector are of type BPX65 PIN-Si diodes, with a response time of less than 0.5 ns. The parameters of the speed detector have to be carefully chosen to fulfill the requirements. The distance between the two pipes must be small enough so that the speed measured by these two points can be taken as the instantaneous velocity. As for our case the distance of $s$ = 1.5 cm was chosen. Near the end of the rundown phase (from three quarters of the whole length of electrode) we can use as large as 2.5 cm because the current sheath is running at a relatively constant speed during that period of time.

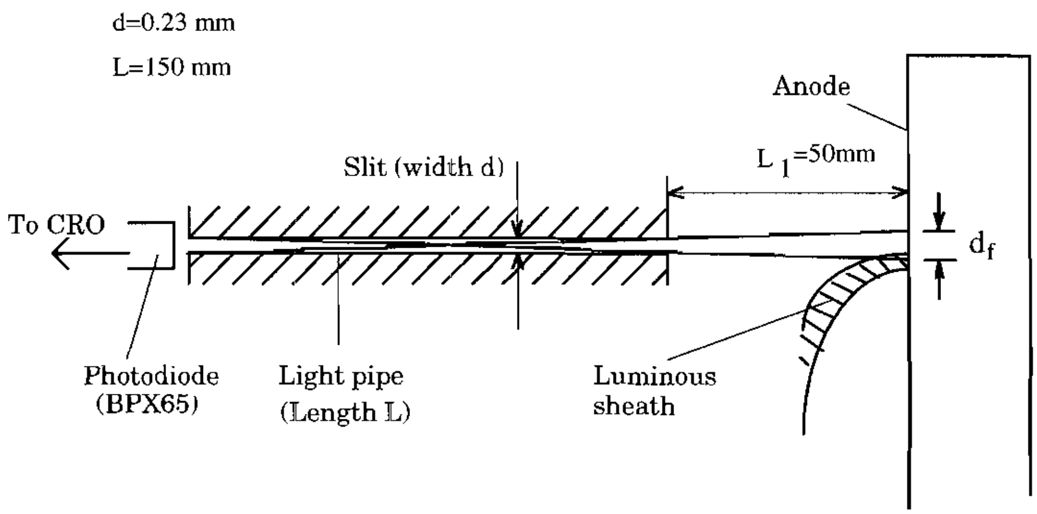


**FIGURE 4.7**
Diagram of the light-pipe

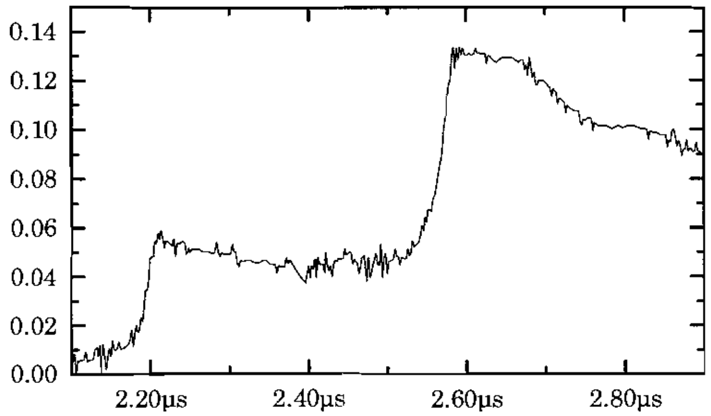


**FIGURE 4.8**
Typical trace from two light-pipes that are fanned together as centre electrode of PF is operated positive, showing rise time of less than 30 ns

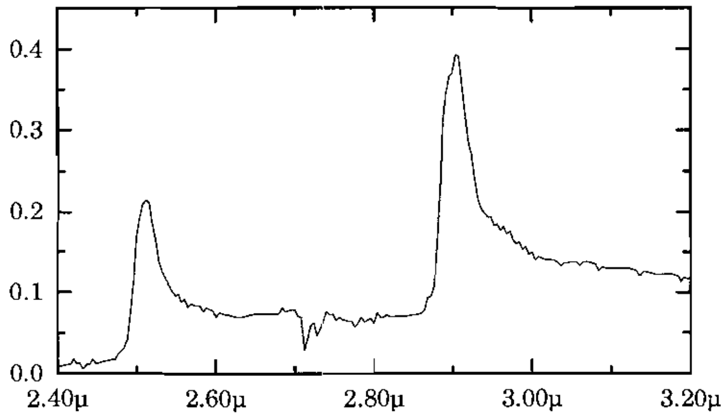


**FIGURE 4.9**
Typical trace from two light-pipes that are fanned together as centre electrode of PF is operated negative, showing rise time of less than 20 ns

Assuming $s$ = 1.5 cm is used, for typical axial velocities of 5 ~ 10 cm/μs, the time taken for the plasma sheet to move between the fields of view of adjacent pipes is 150 ~ 300 ns. The response time of the photodiode is significantly less than 1% of this time interval, and consequently the uncertainty in the velocity measurement is determined by geometrical factors which are the topic of the following discussion.

From Fig.4.7 we can deduce the width of window through which each photodiode can "view" the luminous plasma:

$$d_f = \frac{L_1 + L}{L} \cdot d \tag{4.14}$$

Assuming the rise time (i.e. the time measured from the moment corresponding to 10% of the total height of signal to that corresponding to 90% of the total height of signal) of output signal is $t_r$ and we use the arrival time of the peak of the output signal to indicate the position of plasma luminous sheet, then the measurement accuracy can be considered to be $\Delta t \sim \frac{1}{5} t_r$ . Aiming for an uncertainty of less than 5% in the measured velocity, i.e.

$$\frac{\Delta t}{\Delta T} < 5\% \tag{4.15}$$

we obtain

$$t_r < 5\% \times 5 \times \Delta T = 5\% \times 5 \times 150(ns) = 37.5(ns) \tag{4.16}$$

So the dimensions of $L$, $L_1$, $d$ (i.e. $d_f$) have to be properly selected to meet the condition: $t_r$ < 37.5 ns and at the same time $d_f$ should be big enough so that the output signal is comparatively large with respect to noise. In practice these dimensions were determined by trial and error. The finalised design schematic is illustrated in Fig.4.7 where dimensions were chosen to be: $L$ = 150 mm, $L_1$ = 50 mm, $d$ = 0.23 mm, which give $d_f$ ~ 0.3 mm. When the plasma sheet became steady the rise time was observed to be $t_r$ ~ 35 ns as shown in Fig.4.8 for positive polarity and $t_r$ ~ 15 ns for negative polarity (Fig.4.9).

### 4.4.2 Optical Probe Array for Study of Axial Dynamics

To do a simple evolution study in rundown phase, a detector comprising eight parallel equidistant light-pipes with a photodiode at one end of each was adopted. The distance between adjacent light-pipes is $s$ = 1.5 cm and the eight pipes are best placed such that they view the last 12 cm of the (16 cm long) anode. This gives us a good picture of evolution of plasma sheath in the axial phase.

To optimise use of the oscilloscope channels, the outputs of the eight photodiodes are fanned together in pairs to give four output signals from the whole detector. The most logical and convenient choice of pairs is such that there are three intervening diodes between the members of each pair (i.e. 1 with 5; and 2 with 6, etc.). Although two photodiode signals are now superimposed on the same oscilloscope channel this is not a serious disadvantage as the step-like output from each photodiode permits an easy separation of the two signals (see Fig.4.8 and 4.9). The leading edge of the "step" corresponds to the arrival of the front of the plasma sheath in the field of view.

### 4.4.3 Axial Speed Detector

To obtain the current shedding factors and information of current profile in the rundown phase, three magnetic probes were employed to measure the magnetic fields at $z$ = 12 cm. At the same time two light-pipes separated by 2 cm were used to monitor the average speed of current sheath. The set-up of this speed detector together with the magnetic probe array will be presented in Sec.4.5.2.

## 4.5 Magnetic Probe Measurements

### 4.5.1 Basic Design

The magnetic probes are principally used to measure the magnetic field and the amount of the current (and current distribution) actually flowing in the plasma. They are also used to determine the velocity of the current sheath in the axial phase of plasma focus.

A sketch of the construction of the probe is shown in Fig.4.10a. The magnetic probe is a 7-turn coil made by winding SWG32 enameled copper wire onto a small plastic sleeve of about 1 mm diameter. The coil and the connecting wire are enclosed in a glass tube of 4 mm outer diameter to provide the electric insulation and protection against the plasma. The twisted pair of connecting wires are electro-magnetically shielded by a aluminum foil coating. The leading wires of the magnetic probe are glued firmly at the end of the glass tube so that any rotations of the glass tubing does not produce conical movements of the probe coil.

Fig.4.10b gives the equivalent circuit, where $L_c$ and $r_c$ are the inductance and resistance of the coil, respectively and $R_{50}$ equals to the matching impedance of the cable which is 50Ω. According to the Faraday's law we can write the circuit equation:

$$L_c \frac{di}{dt} + (R_{50} + r_c)\, i = \frac{d\Phi}{dt} = ns\frac{dB}{dt} \qquad (4.17)$$

where

$\Phi$ : magnetic flux

$B$: magnetic field

$i$: inducted current in the coil

$n$: turns of the coil

$s$: area of the coil

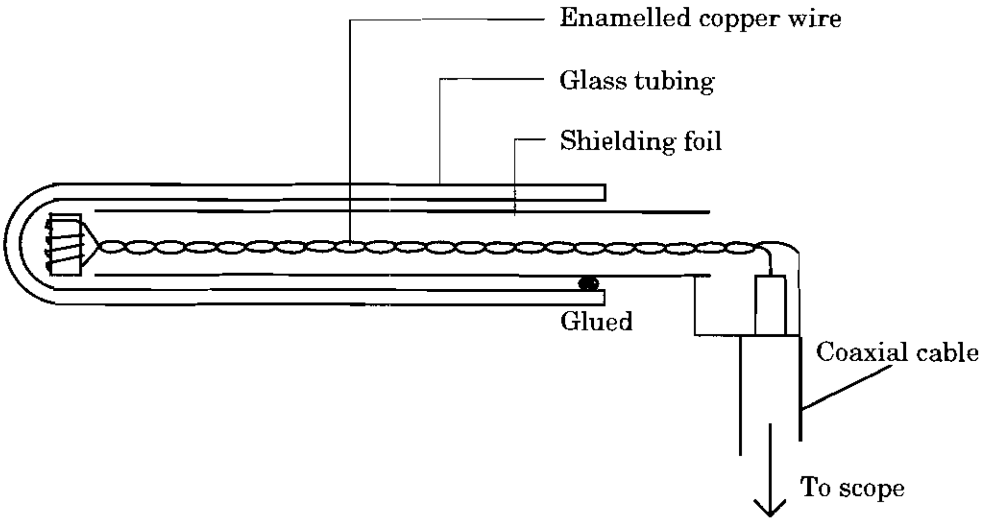


**FIGURE 4.10(a)**
Sketch of magnetic probe

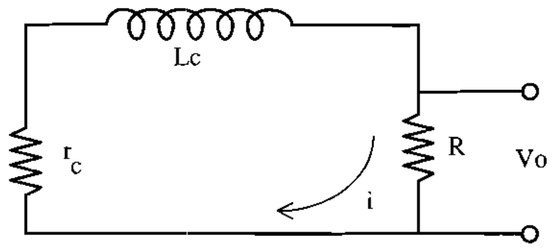


**FIGURE 4.10(b)**
Equivalent circuit of magnetic probe

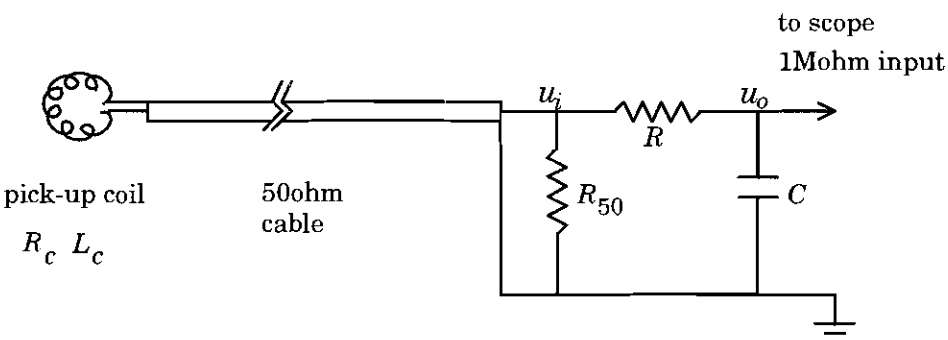


**FIGURE 4.11(c)**
R-C circuit used to integrate the signal picked up by the coil

The left side of Eqn.(4.17) can be written as $\sim(\omega L_c + r_c + R_{50})i$, with $w$ being the angular frequency of magnetic field which in our case is less than 100M s$^{-1}$. For the coil with 7 turns ($n$) of SWG32 wire, 1 mm diameter (corresponding area $s$) and 1 mm length ($l$), the parameters are estimated and tested to be:

$$L_c \sim \mu \cdot n \times \frac{s}{l} \sim 7nH \tag{4.18}$$

and

$$r_c < 0.1\Omega \tag{4.19}$$

For the signal of magnetic field slower than 100M s$^{-1}$, we have $\omega L_c + r_c <$ 0.8<<$R_{50}$=50 ohm and thus the output voltage is:

$$V_o = R_{50} \cdot i \approx ns \cdot \frac{dB}{dt} \tag{4.20}$$

We can obtain the magnetic field by either adding a R-C integral circuit at the terminal or integrating the derivative signal ($dB/dt$) using computational software.

If R-C integration circuit is used (shown in Fig.4.10c), assuming characteristic angular frequency of signal is $\omega$, four conditions can be deduced for the whole detector, i.e.:

$$\begin{cases} |r_c + j\omega l_c| << R_{50} \\ R_{50} << |R + 1/(j\omega C)| \\ |1/(j\omega C)| << R \\ |1/(j\omega C)| << 1\,\text{M}\Omega \end{cases} \tag{4.21}$$

In our case $R$ = 10 k$\Omega$, $C$ = 9400 pF are chosen to meet the above requirements.

### 4.5.2 Magnetic Array for Determination of Current Shedding Factor

*Set-up*

To experimentally determine the current shedding factor needed for the computational model (see Chapter 3), we set up an experiment shown schematically in Fig.4.11. Three probes are placed in between the electrodes, at radial distances of 12, 16, 24 cm respectively from the axis of anode and 12 cm high from the bottom. The coils of the probes are located with the axes azimuthally such that maximum amplitude can be obtained for each coil.

*Calibration*

Calibration was conducted by shorting the electrodes at the end and measuring the voltage and current signal. After calibration we took out the shorting connectors without changing the positions of probes.

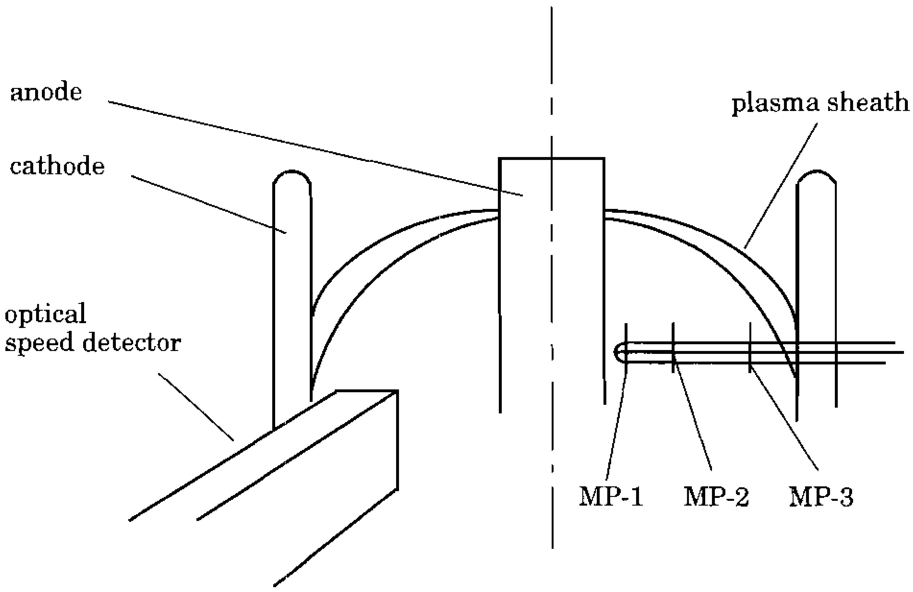


**FIGURE 4.11**
Experimental set-up of 3-MP array for measuring current shedding factors and current profile
locations of probes: $r_1$ = 12 cm; $r_2$ = 16 cm; $r_3$ = 24 cm from axis and $z$ = 12 cm high from bottom

## 4.6 X-ray Diagnostics

### 4.6.1 X-ray Pinhole Camera

The time-integrated spatial information of the soft x-ray emissions is provided by pinhole images. Fig.4.12 shows the cross-section of the construction of the pinhole camera and its position relative to the plasma pinch column. The camera consists of the pinhole mount, the channel and the film holder. The camera views the plasma column from a radial position. The film holder holds a circular piece of film. The plasma is imaged in an off-axis position to one side. After each recording of the plasma discharge, a new exposure area is brought into position by rotating the film holder by 90° to record the next discharge. Thus four consecutive shots are recorded on each film. The camera is vented through a light baffle (1 mm in diameter) to enable filling with the working gas at the working pressure.

In all experiments, a 50 μm pinhole were used, covered with a 7 μm thick aluminum foil which acts as a filter for visible light.

The pinhole camera can be mounted on the side or top circular windows to obtain both the side-on and end-on pinhole images. An aperture is put in front of the pinhole, about 4 cm away from it, to attenuate the strong shock wave and debris in order to protect the pinhole and the filter from damage.

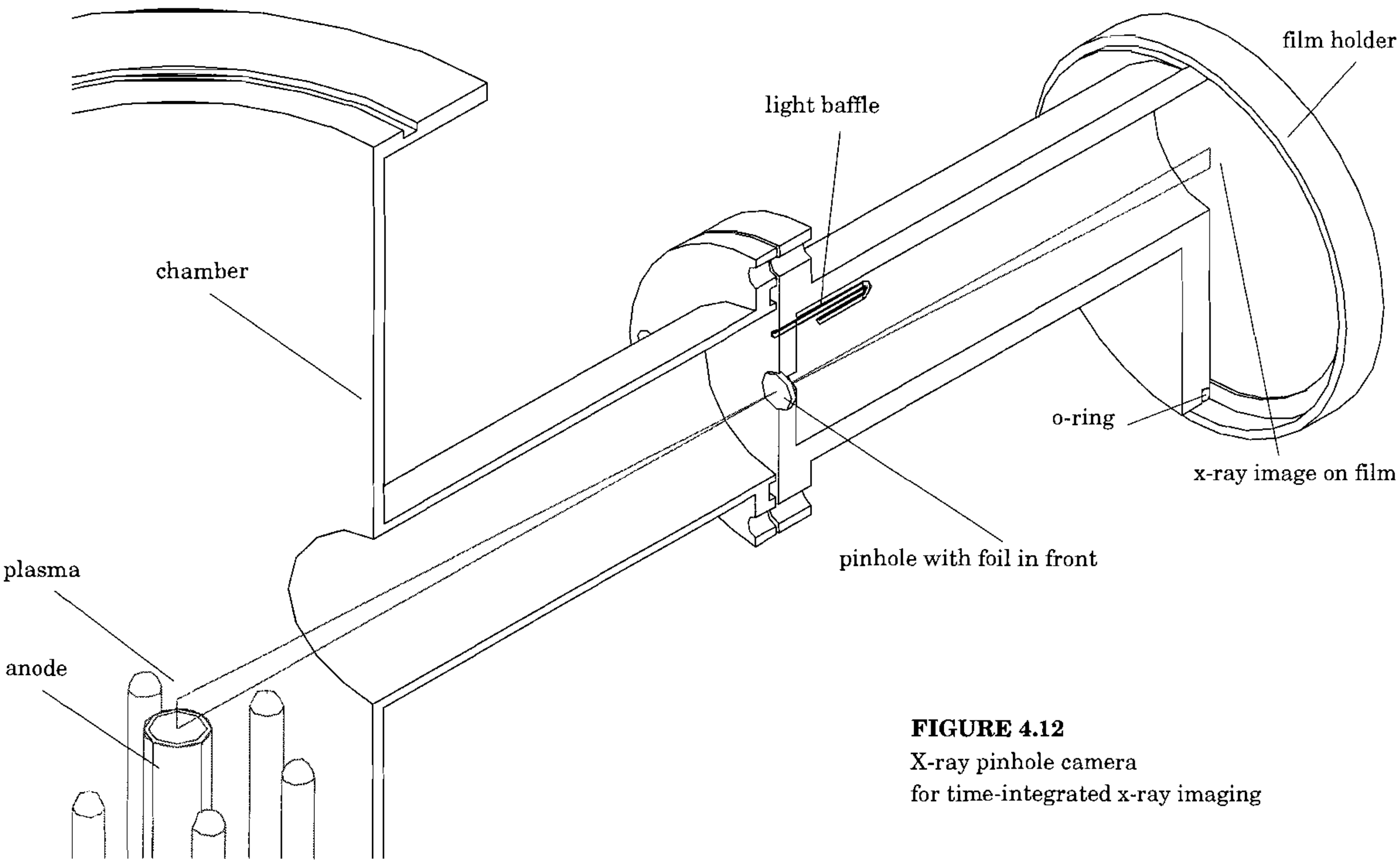


**FIGURE 4.12**
X-ray pinhole camera
for time-integrated x-ray imaging

### 4.6.2 Pinhole Transmission Grating Spectrograph

#### 4.6.2.1 Basic Structure and Parameters

A pinhole transmission grating is used to give information simultaneously about the spatial and spectral characteristics of SXR source from the plasma focus [133]. The grating consists of a metal film with a large number of evenly spaced parallel lines or grooves. In this project, we use a diffraction grating consisting of a flat gold film in which 1000 lines per mm had been ruled through. The grating is incorporated into two pinholes with diameters of 50 micron and 25 micron, which are mounted on one frame to form two pinhole transmission gratings. (see the magnified picture in Fig.4.13). The grating leads to wavelength selection, while the pinhole gives spatial information on the individual wavelength separately.

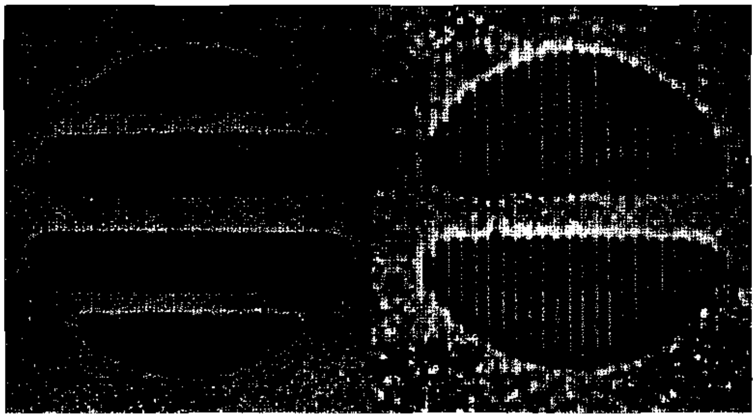

**FIGURE 4. 13**
Two pinhole transmission gratings
left: 50 micron dia. (magnified 800x)
right: 25 micron dia. (magnified 1600x)
In the grating they are 3 mm apart. Their images have been put side-by-side here.

The pinhole-grating spectrograph is suitable to be used to survey the soft x-ray emission from spectral range of 5 Å to 200 Å. It could be used for absolute measurements of x-ray emission if no foil is put in front of the grating. However, typically a foil is necessary to block interfering visible or UV light [134-137]. Also to attenuate the strong shock wave resulting from the disassembly of the focus compression we used a filter to protect the grating. As a result the absolute measurement of total energy could not be made.

According to diffraction principle, the distribution of diffraction light on the focal plane is [138]

$$y = C'a\frac{\sin u}{u}\frac{\sin Nv}{v}\sin 2\pi\left(\frac{t}{T}-\frac{r_o}{\lambda}-\frac{(N-1)(a+b)\sin\theta}{2\lambda}\right) \qquad (4.22)$$

here $u = (\pi a\sin\theta)/\lambda$, $v = [\pi(a+b)\sin\theta]/\lambda$, $N$ is the number of grooves. The amplitude and intensity may be expressed as

$$A = C'a\frac{\sin u}{u}\frac{\sin Nv}{\sin v} \qquad (4.23)$$

$$I = C'^2a^2\frac{\sin^2 u}{u^2}\frac{\sin^2 Nv}{\sin^2 v} \qquad (4.24)$$

where $C'$ is a constant, $a$ is the width between two metal grooves, $N$ is the total number of lines or grooves for a grating. When $U,V >> W >> (a+b)$ above equations can be used approximately for the pinhole transmission grating configuration, here $(a+b)$ being the grating constant which is the distance between adjacent grating lines and $W$ the width of the pinhole.

Complete constructive interference of the waves occurs when the path difference is satisfied with

$$(a+b)\sin\theta_k = \pm k\,\lambda \qquad k = 0, 1, 2\ldots \qquad (4.25)$$

$\theta$ is the angle the rays are diffracted from the incident direction, and $d\sin\theta$ the path difference between adjacent rays. The grating constant is given by

$$d = a + b \qquad (4.26)$$

The relationship between x-ray wavelength $\lambda_y$ and one-dimension spatial position $y$ on the film was obtained by following the spectrograph's geometry shown in Fig.4.14. Considering $\theta_a = \arctan\frac{y_a}{L}$ from the geometry and $\lambda_a = \frac{d}{k}\sin\theta_a$ from grating equation (4.25), a simple analytical expression for the relationship between wavelength $\lambda_a$ and position $y_a$ can be obtained as following,

$$\lambda_a = \frac{d}{k}\sin\left[\arctan\left(\frac{y_a}{L}\right)\right] \tag{4.27}$$

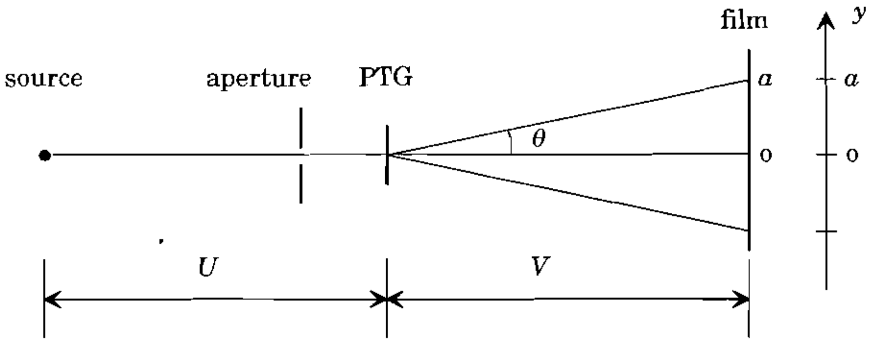


**Figure 4.14**
Pinhole transmission grating (PTG) spectrograph geometry and soft x-ray diffraction trace

In this work after the SXR wavelength are determined, the lines are identified by comparison of the measured wavelength with other observations (e.g. by crystal spectrograph). Furthermore we also use empirical isoelectronic extrapolation [139].

### 4.6.2.2 Resolution and Dispersion

The light intensity in the focal plane vanishes when $v = k'\pi/N$ (see RHS of Eqn.(4.24)), and $k' \neq N, 2N, 3N, \ldots\ldots$, that is,

$$(a+b)\sin\theta_{I=0} = \pm k'\frac{\lambda}{N}, \quad k' = 1,2,3,\ldots,N-1,N+1,\ldots,2N-1,2N+1,. \tag{4.28}$$

We may rewrite above equation as

$$d\sin\theta_{k,I=0} = (kN+1)\frac{\lambda}{N}, \qquad k = 1,2,3,.. \tag{4.29}$$

Since $\theta_{k,I=0} = \theta_k + \Delta\theta$ , substituting (4.25) into (4.29) gives

$$\Delta\theta = \frac{\lambda}{N(a+b)\cos\theta_k} \tag{4.30}$$

here we approximate $\cos(\Delta\theta) \approx 1$ , and $\sin(\Delta\theta) \approx \Delta\theta$ for soft x-ray diffraction. As can be seen from Eqn.(4.30), the width of spectral line will be very narrow with increasing number of $N$.

According to grating equation (4.25), we have angle dispersion equation

$$\frac{d\lambda}{d\theta} = \frac{(a+b)\cos\theta}{k} \tag{4.31}$$

Corresponding to spectral line minimum angle width $\Delta\theta$, the minimum wavelength difference $\Delta\lambda$ can be obtained to be

$$\delta\lambda = \Delta\lambda = \left(\frac{d\lambda}{d\theta}\right)\Delta\theta \tag{4.32}$$

Substituting Eqn.(4.30), (4.31) into (4.32) yields

$$\delta\lambda = \frac{\lambda}{kN} \tag{4.33}$$

and we obtain the resolution for grating spectrograph (GS)

$$R = \frac{\lambda}{\Delta\lambda} = kN \tag{4.34}$$

This is only a theoretical result. Practically various factors will affect the value $R$ and reduce the resolution below the theoretical value. High resolution spectra may be obtained with increasing $k$ and $N$ number. However, there are some technological problems in building a grating with large $N$ and increasing $k$ value will result in spectral line overlap. For example, when

$$k_1\lambda_1 = k_2\lambda_2 \tag{4.35}$$

where the lines $\lambda_1$ and $\lambda_2$ will be superimposed on the same place. In practice, only the first few orders are easily observed.

According to [140-142], we built a PTGS as shown in Fig.4.14. The basic parameters are listed in Tab.4.3. If the diameter of the soft x-ray source is $S$ = 200 μm and the distance from source to PTGS is $U$ = 200 mm as seen in Fig.4.14, the angle dispersion caused by x-ray source is

$$\Delta\theta_s = \arctan(S/U) = 0.05^o \tag{4.36}$$

and for a wavelength of 13 Å, the source broadening is obtained to be

$$\Delta\lambda_s = \sqrt{d^2 - \lambda^2}\,\Delta\theta_s = 2.7\,\text{Å} \tag{4.37}$$

***Table 4.3*** The basic parameters of PTGS using the 50 μm grating

| | | |
|---|---|---|
| Grating constant | $d = 1/N_o$ | 1x10$^{-3}$ mm |
| Range of wavelength | $\lambda_{min}$ to $\lambda_{max}$ | 3 to 300 Å |
| Incident angle | $\beta_{in}$ | ~ 0° |
| Dispersion (for 1.3 nm) | $\theta = \arcsin(\lambda/d)$ | 0.07° |
| Diameter of grating | $W$ | 50 μm |
| Total number of grooves | $N_{tot} = W x N_o$ | 50 |
| Resolution ($k$ = 1) | $R_t = k\, N_{tot}$ | 50 |
| Width of spectral line | $\Delta\lambda_t = 1/R_t$ | 0.243 Å |
| Source to PTGS | $U$ | 200 mm |
| Film to PTGS | $V$ | 400 mm |
| Magnification of image | $\alpha = V/U$ | 2 |

Assuming the profiles of the lines of electron transition and source broadening are Gauss-form distributions, the total width of the spectral line is obtained to be

$$\Delta\lambda = \sqrt{\Delta\lambda_s^2 + \Delta\lambda_g^2} \approx 2.7\ \text{Å} \tag{4.38}$$

It is clearly seen that $\Delta\lambda_s >> \Delta\lambda_t$ and the PTGS' resolution is mainly determined by the source broadening. Relatively, the diameter of an x-ray source produced by laser is quite small (50 ~ 100 μm) and its source broadening is $\Delta\lambda_s$ = 0.5 ~ 2 Å. For PF, the size of the plasma is about 200 ~ 400 μm, and its source broadening is $\Delta\lambda_s$ = 2.5 ~ 4 Å. It is better to increase distance $U$ to minimize FWHM $\Delta\lambda_s$ of spectral line. The parameter $U$ is mainly limited by magnification of the image $\alpha = V/U$ and intensity on film $I \sim 1/(U+V)^2$.

The spatial resolution of the spectrum only depends on the diameter of the PTG itself. Its principle is similar to a pinhole camera. In our two PTGs, their diameters are 50 and 25 μm respectively. The distance from the soft x-ray source to the PTGS is 200 mm, and the distance from the PTGS to the recording film is 400 mm, so that the magnification of the image of the soft x-ray source is 2 times and the spatial resolutions are about 60 and 30 μm respectively. A better spatial resolution of the spectra can be achieved if we decrease the diameter of the pinhole.

#### 4.6.2.3 Set-up

Fig.4.15 shows the installation of the PTG with $U$ = 200 mm, $V$ = 400 mm. It must be noted that an aperture has to be added in front of the grating to prevent the strong shock wave from damaging it. The size of the aperture is 4 mm in diameter.

It is important for the PTG detection system to be properly aligned. The grating has to be polarized in parallel to pinch column (vertical direction in our case) to get the spatial resolution along the column direction. In practice, a He-Ne laser was employed as a "virtual" source to align the system.

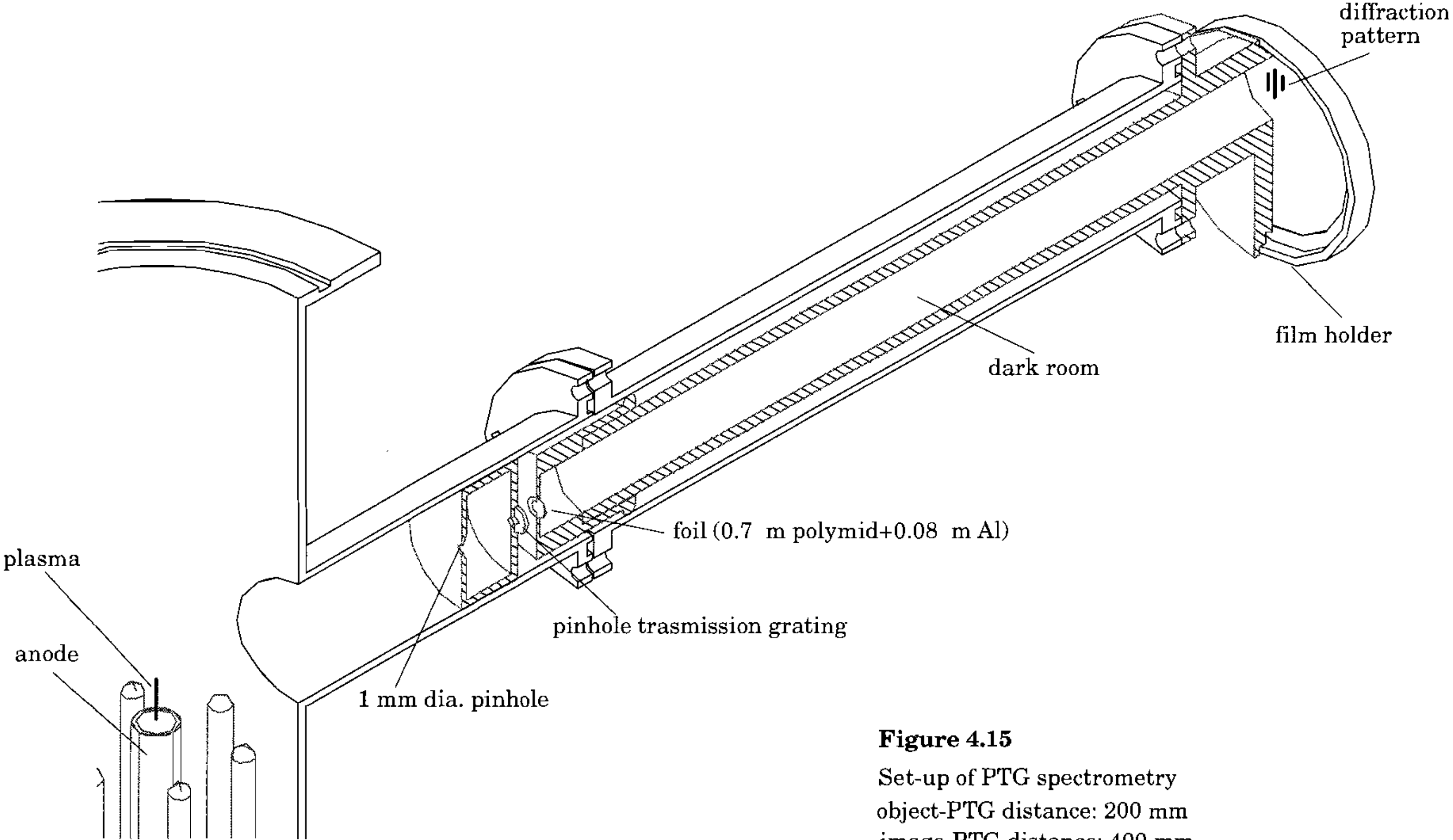


**Figure 4.15**

Set-up of PTG spectrometry
object-PTG distance: 200 mm
image-PTG distance: 400 mm

#### 4.6.2.4 Recording Films

(A) *General*

No-screen x-ray films and double layers films are widely used in spectroscopic and photometric investigations of hot plasmas in the range of x-ray photon energies from 10 eV up to 50 - 100 keV. These films are also used in pinhole cameras for the recording of x-rays plasma images. High space resolution (around 1 micron), spectral and absolute sensitivity (less than 0.1 photons per sq. micron for some wavelength) and ease of development allow these films to be used for many experiments in plasma physics.

Several types of films have been examined for use as soft x-ray detectors. The no-screen films (Kodak No-screen film, S-5F No-screen film) are very sensitive, and suitable to be used in various grazing grating spectrographs for soft x-ray (50 ~ 300 Å) recording [143]. The no-screen films are usually soft and very easily damaged. In our experiments with a PTGs and a crystal spectrograph (described in next section) for SXR (3 ~ 300 Å) measurements, several soft x-ray films such as Kodak direct exposure film, S-5F film can be used. We employed two Kodak films, TMG/RA-1 and TMS/RA-1, in these experiments. The sensitivities of these two types of film were compared, showing that the Kodak TMG/RA-1 is slightly more sensitive in the x-ray range of our interest than Kodak TMS/RA-1. Therefore we mostly used Kodak TMG/RA-1 as the recording film.

(B) *Calibration*

In general, high resolution films of low sensitivity developed for photographic applications have not been calibrated in the x-ray range. Calibrations data for commercially available x-ray films are generally limited to energies of 100 keV and greater, which is not of primary interest for plasma applications. For soft x-ray range some calibrations have been done [144-147]. It is reported [144] that the absolute sensitivity of some films is quite dependent on the ambient condition (e.g. pressure) under which calibration is conducted.

A relative calibration for the film used in this project work (TMG/RA-1) is carried out using the flat crystal spectrograph developed for measuring the emission spectrum from the plasma focus source (see Sec.4.6.3.6). The films after processing are scanned by microdensitometer which is calibrated as well.

(C) *Processing*

Exposed films are processed following this procedure: At first the films are developed in Kodak T-MAT developer for 4 minutes and after that rinsed for 30 seconds in fresh, running water with continuous agitation. They are then put in Kodak GBX Fixer and Replenisher for 3 minutes with 5 seconds agitation in every 30 seconds. Finally we wash the fixed films in clean, running water (about 25°C) for at least 10 minutes. The films are then dried at room temperature. The temperature of developer and fixer is controlled at 26±0.5°C.

### 4.6.3 Crystal Spectrograph

#### 4.6.3.1 Flat Crystal Spectrograph

The x-ray crystal spectrograph with spatial resolution is one of the most powerful diagnostic tools for dense plasma focus experiments [148]. A variety of available crystals with forms such as flat or curved, and with suitable lattice constant, diffraction coefficients and mechanical properties offer the possibility to make an optimum choice of the dispersive element and spectroscopic scheme in accordance with the aims of the diagnostics. Among the parameters relevant for optimization, spectral range, luminosity, dispersion, spatial and spectral resolutions are very important. There are various schemes for measuring the soft x-ray using diffraction from a flat single or double crystal, a curved crystal, or a layered synthetic microstructure [148-150].

In this work we developed a crystal spectrograph which has an adjustment system of five degrees of freedom. It has not only the advantage of easy adjustment, high efficiency and high spectral resolution, but also the capability of providing spatially resolved spectrum in one dimension over 1 ~ 50 Å wavelength range. A TlAP crystal was used, and the spatially resolved spectra of Ne, Ar ions from our plasma focus are obtained.

### 4.6.3.2 General Considerations and Precautions

The x-ray crystal spectrograph follow the general theory of Bragg x-ray diffraction equation

$$m\lambda = 2d\sin\theta \quad (4.39)$$

here $m$ is the order of diffraction, $2d$ is the crystal lattice constant, $l$ is the x-ray wavelength, and $\theta$ is the x-ray diffraction angle. It is very easy to install different forms of the crystals (flat and curve) in our spectrograph for various purposes. Using a curved crystal enables us to measure wider range of x-ray spectrum. However it is very difficult to obtain an analytical solution for the relation between the position and the x-ray wavelength. Generally a flat crystal is used to measure x-ray spectral line and make x-ray diagnostics.

*Adding a slit to give spatial resolution in the axial direction*

A slit perpendicular to the source column, which is vertical in our experiment, is added in between the source and crystal giving spatial resolution along the direction of the source column. Fig.4.16 illustrates the schematic diagram of the set-up. When the 4-cm crystal is used a pinhole is employed also to obtain the zero-order spectrum, i.e. the pinhole image of the source. The pinhole image can be at the long wavelength side of the spectra or at the short wavelength side, depending on the pinhole position due to the limited room of the square window on which the crystal spectrograph is mounted. Usually the pinhole image is formed at the long wavelength side (right of the spectrum in Fig.4.16) when the spectrum for shorter wavelength regime is taken, whereas for measuring the long wavelength part of the spectrum it is at the short wavelength side.

The slit, centre lines of the crystal (longitudinal direction), the film and the centre of the “stray-light-stop”-slit must be in the same plane which is perpendicular to the asymmetrical axis of the focus and about 5 mm above the top surface of the anode. To make sure these requirements are met, a simulation light source is used to do the alignment.

From Fig.4.16 one may notice that the image slit must be parallel with the film, namely, the angle between the slit and crystal must be equal to $\alpha$, which is the angle between the film and crystal, in order to get the same image-to-object ratio along the whole film. This ratio can be worked out from the detailed parameters of the positions for the slit, film, crystal and focusing region.

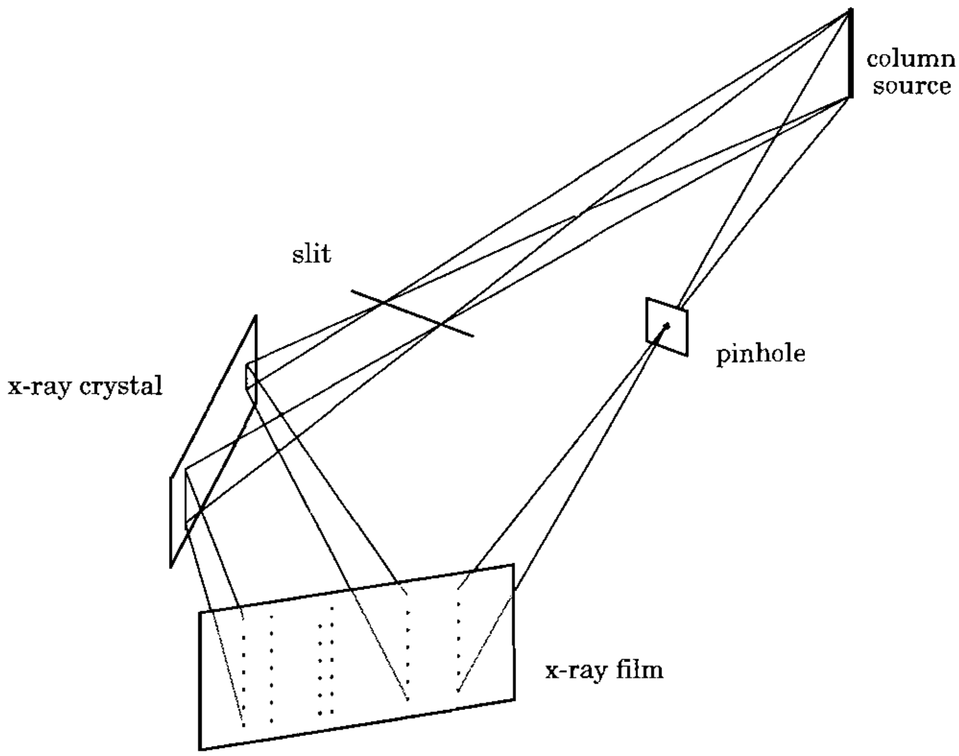


**Figure 4.16**
Schematic diagram of the spectrograph with a soft x-ray source. For the 4-cm crystal a pinhole is also employed to obtain the 0-order spectrum i.e. the integral image of the source. The position of the pinhole image can be at the long wavelength side or the short wavelength side.

*Relevant Parameters*

Fig.4.17 shows a top view of the spectrograph. The positions of the square window and x-ray source are also illustrated. The coordinate system is shown in the figure, with the origin at the focus and x-axis pointing radially outwards and coinciding with the centre line of the square window. Using the following symbols,

$L_R$ length of the flat crystal

$\theta_1,\theta_2$ incident angles at two ends of the crystal

$\alpha$ angle between the crystal and film

$\beta$ angle between crystal and the side wall of square window

$(l_1,h_1),(l_2,h_2)$ coordinates of the two ends of crystal some expressions governing this spectrograph can thus be deduced and listed as follows,

$$\begin{cases} \theta_1 = \beta + \tan^{-1}\dfrac{h_1}{l_1} \\ \theta_2 = \beta + \tan^{-1}\dfrac{h_2}{l_2} \end{cases} \tag{4.40a,b}$$

with

$$\begin{cases} h_2 = h_1 + L_R \sin\beta \\ l_2 = h_2 + L_R \cos\beta \end{cases} \tag{4.41a,b}$$

According to Bragg diffraction law (Eqn.(4.39)) the wavelength range that can be measured by this spectrograph is determined by the corresponding minimum and maximum incident angles $\theta_1$ and $\theta_2$ , which are adjustable through changing $h_1$, $l_1$ and $\beta$. It can be shown that for a wider wavelength range one end of the crystal should be located as near as possible to the source to be measured. Among the parameters, $h_1$ and $l_1$ are limited by the width of the square window and the nearest distance from the focus, respectively. So $h_1 \leq 30$ mm (the width of the square window is 60 mm) and, due to the outer electrode and the strong shock wave, $l_1 \leq 80$ mm. Using Eqn.(4.39), with the consideration of restrictions mentioned above, we have designed a few set of parameters suitable for measuring spectra of different wavelength ranges, listed in Tab.4.4. For simplicity, hereafter these configurations will be represented by FCS-A, FCS-B, FCS-C, FCS-D and FCS-E corresponding to the five configurations listed in Tab.4.4.

***Table 4.4*** Five configurations of the flat crystal spectrograph (FCS)

| FCS configurations | A | B | C | D | E |
|---|---|---|---|---|---|
| *LR* (mm) | 40 | 40 | 40 | 40 | 80 |
| $l_1$ (mm) | 93.5 | 94.5 | 88.5 | 88 | 79.5 |
| $h_1$ (mm) | 27 | 27 | 25 | 22 | 26.5 |
| β | 18° | 18° | 10° | - 4° | 14° |
| α | 51.7° | 52° | 57° | 71° | 36° |
| pinhole | SW+ | SW+ | LW++ | LW++ | No |
| $\theta_1$ | 34.39° | 33.95° | 25.77° | 10.04° | 32.44° |
| $\theta_2$ | 24.57° | 24.31° | 18.04° | 6.97° | 16.6° |
| $U^{+++}$: (mm) object distance | 84.2 | 83.4 | 83.1 | 83.5 | 80.9 |
| $V^{+++}$: (mm) image distance | 76.1 | 77.3 | 77.5 | 86.3 | 74.7 |
| image-to-object ratio | 0.90 | 0.93 | 0.93 | 1.03 | 0.92 |
| *d*: (μm) slit width | 50 | 50 | 50 | 50 | 50 |
| $\lambda_1$ (Å) | 14.56 | 14.4 | 11.21 | 4.49 | 13.83 |
| $\lambda_2$ (Å) | 10.72 | 10.63 | 7.98 | 3.13 | 7.38 |

Notes

+ SW: pinhole image is formed at short wavelength side

++ LW: pinhole image is formed at long wavelength side

+++ $U = \underline{A_1S'}$ (see Fig.4.16)

$V = \underline{A_1A_2}$ (see Fig.4.16)

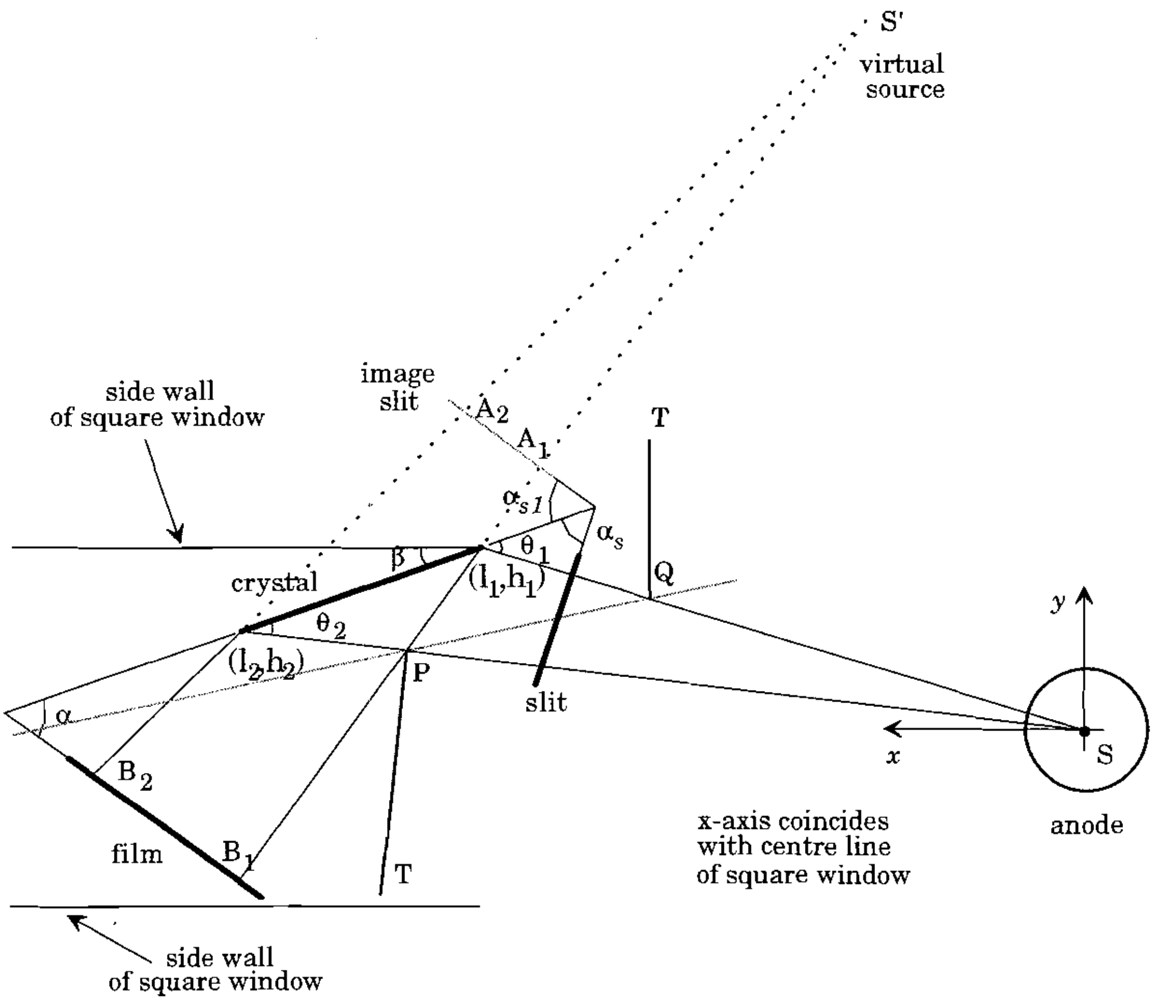


**FIGURE 4.17**
Top view of the flat crystal spectrograph showing that:
(a) the angle between film and crystal must be equal to the angle between slit and crystal;
(b) two stops are employed and the extension line of PQ drawn from the edges of these stops must not cross the film region.

*Stops for blocking out the "stray radiations"*

Radiations which are not from the plasma focus column and not in the soft x-ray region are *called* "stray radiations" in this work. They are (1) the visible and UV light in the low photon energy side and (2) hard x-rays at the high photon energy side of the soft x-ray regime. In principle, for the spectrometer the photons will be selectively, according to their wavelengths, diffracted and recorded down on the film. It seems that only a cover of thin foil on the film is needed to prevent exposure by visible light. But we found that this is not sufficient. At first a stop is put in between the focus column region and the x-ray film to avoid direct exposure by the stray radiation of the source. But it is found that a strong background is still on the film. Fig.4.18 shows an example of this case. It is not possible to identify clearly the spectrum with the uneven strong background.

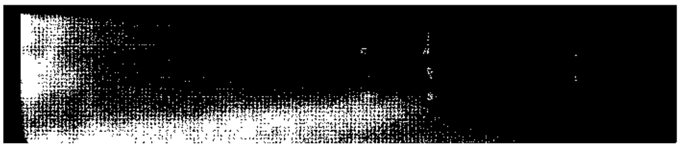

**FIGURE 4.18**
Strong background caused by x-ray radiation in a big plasma region makes it difficult to identify the spectrum of interest

The stray visible light is blocked out by the foil in front of the x-ray film, so the background must be caused by stray x-rays that came from a bigger x-ray source that emits from a large volume in front of the anode. It is known that x-rays are emitted from the very big volume of copper jet [151]. An experiment is carried out to study this "big source" by putting two detectors using windowless BPX-65 photodiodes on opposite circular windows. A small stop is put in between the focusing column and a BPX65 diode to block the radiations from the small focusing region. The other one directly measures the x-ray. It is found that the stray x-ray is weak when neon gas is filled. But it is comparable with the x-rays from focusing column when deuterium or argon were used. The rays coming from the big source (other than the source from focusing column), in spite of its weakness, when directly exposed onto the film, is comparable with the spectrum intensities of interest which are very weak due to the diffraction of the crystal.

Two stops $\underline{PT}$ and $\underline{QT}$ are used in the horizontal direction to avoid these stray rays, shown in Fig.4.17. It can be seen that the extension line formed by the two edges denoted by “P” and “Q” must not go through the x-ray film in order to reduce stray rays from directly exposing onto the film. Practically a simulation alignment is done first to position the “P” and “Q” points and thus the two stops (by using a simulation light source), before its mounting in the chamber.

In the vertical direction the stray rays are sufficiently reduced if the stops PT, QT and the rim of the slit are wide enough. It is found that 2 cm is enough for our configurations listed in Tab.4.4.

An example of improved spectrum is shown in Fig.4.19 for comparison with Fig.4.18 where stops are not used.

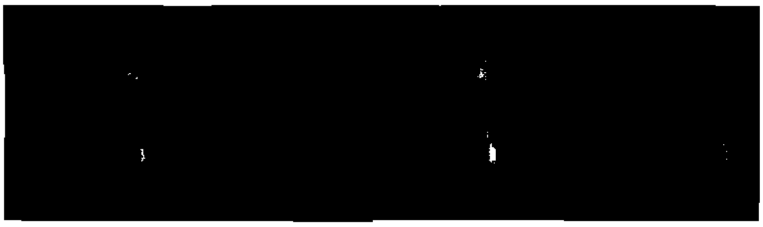

**FIGURE 4.19**
An example of improved spectrum, with stops to reduce stray x-rays

### 4.6.3.3 Data Analyzing --- Identification of the Spectrum

Formulae for x-ray crystal spectrograph have been established by Kopper at Livermore laboratory and by Hirano in Gunma University. For example for the spectrograph geometry shown in the Fig.4.20, one derives a simple analytical expression for the relationship as follow

$$MA = F\cot(\alpha + \arcsin\frac{\lambda}{2d}) \qquad (4.42)$$

where $MA$ is the distance between the line position $A$ and projection $M$ on the film, $F$ is the distance between image $S'$ and film $M$, and $\alpha$ is the angle of crystal plane with respect to the film.

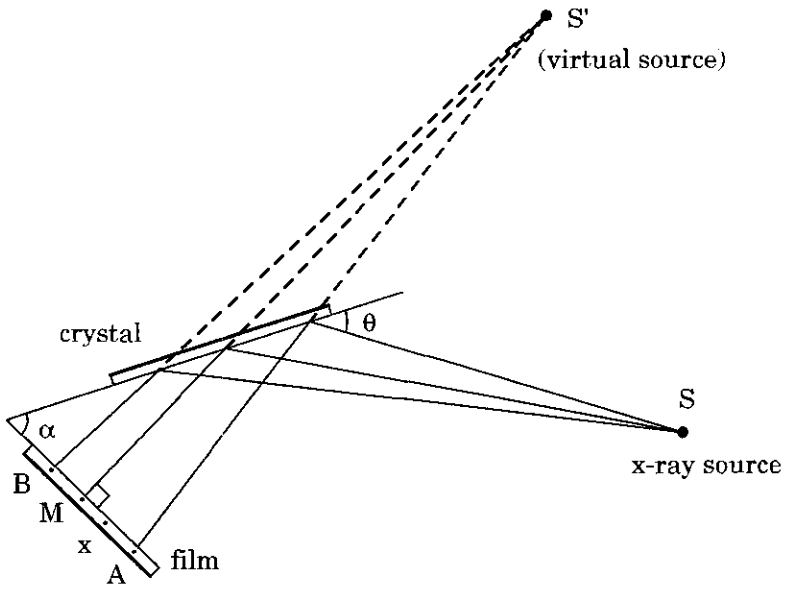


**FIGURE 4.20**
Crystal spectrograph's geometry and x-ray diffraction trace.

In practice, it is difficult to measure the geometry of the spectrograph accurately. Therefore the observed wavelengths are determined with reference to two reference lines for which the wavelengths are known. Assuming that the known wavelength $\lambda_A$ and $\lambda_B$ at the $A$ and $B$ positions (Fig.4.20), the unknown wavelength $\lambda_x$ of the spectral line on the film then is given by

$$\lambda_x = 2d\sin\left[\operatorname{arccot}\left(\cot(a+\arcsin\frac{\lambda_A}{2d}) - \frac{L_{Ax}}{F}\right) - a\right] \tag{4.43}$$

with

$$\begin{aligned} F &= L_{AB}\left[\cot(a+\arcsin\frac{\lambda_A}{2d}) - \cot(a+\arcsin\frac{\lambda_B}{2d})\right]^{-1} \\ &\equiv L_{AB}\cdot H^{-1} \end{aligned} \tag{4.44}$$

where $L_{AB}$ is the separation between line $\lambda_A$ and line $\lambda_B$ on the film plate, $L_{Ax}$ is the distance from line $\lambda_A$ to the line $\lambda_x$ studied. From the above equations, one may see that the errors in the determination of wavelength arise mainly from the errors of the reference lines' wavelengths, the separations and $\alpha$. In the present work, spectral lines are measured two or more times and then the results are averaged. The wavelengths are calculated using several known lines on the film. $F$ and $\alpha$ are taken as non-variable parameters, and the iteration is performed by least square fit. Finally the corresponding wavelengths at arbitrary positions are evaluated. Compared with the polynomial fitting of the dispersion curve, this method has the advantage of more convenience, wider wavelength coverage and higher accuracy.

A line may be identified after wavelength determination by comparison of the measured wavelength with previous observation of various ions' spectra. On the other hand, the identification of the lines in the present work is mainly made on the basis of empirical isoelectronic extrapolation or interpolation.

#### 4.6.3.4 Resolution and Dispersion

In Eqn.(4.43), the accuracy of $\lambda$ is dominated by the uncertainties of $L$, $\alpha$, $\beta$ and $\delta$. Therefore, the incremental change in the wavelength is described as

$$\Delta\lambda = \left(\frac{\partial\lambda}{\partial L}\right)_{a,\beta,\delta}\Delta L + \left(\frac{\partial\lambda}{\partial a}\right)_{L,\beta,\delta}\Delta a + \left(\frac{\partial\lambda}{\partial \beta}\right)_{L,a,\delta}\Delta\beta + \left(\frac{\partial\lambda}{\partial \delta}\right)_{L,a,\beta}\Delta\delta \qquad (4.45)$$

where $\Delta L$, $\Delta\alpha$, $\Delta\beta$ and $\Delta\delta$ are uncertainties in the measurement of the location of the distance between reference wavelength and wavelength studied, in setting the angle of the crystal, in fluctuation of the soft x-ray source and in quality of the crystal, respectively. In general, we scan the film with large amplification and this method is used to greatly decrease the relative error of measurement on the parameter $\Delta L / L$. The dispersions $\partial\lambda/\partial L$ and $\partial\lambda/\partial a$ are obtained from Eqn.(4.43) , and the results of the parameters of $(\partial\lambda/\partial L)(\Delta\delta/\lambda)$ and $(\partial\lambda/\partial a)(\Delta a/\lambda)$ are estimated to be 0.03%. The parameter $(\partial\lambda/\partial L)(\Delta\delta/\lambda)$ only depends on the quality of the crystal, and it is about 0.02% for TlAP crystal ($2d$ = 25.78 Å). In our DPF system the x-ray source is fairly large, producing a large value for the parameter $(\partial\lambda/\partial L)\Delta\beta$

and results in serious source broadening on spectral lines. A pinhole was used to decrease the source broadening.

The spatial resolution only depends on the width of the slit in front of the spectrograph. In our spectrograph, the distance from the x-ray source to the slit is 80 - 85 mm, and the distance from the slit to the recording film is 75 - 85 mm. This configuration indicates that the amplification of the image of the x-ray source is ~ 0.94 times and the spatial resolution is 50 μm. A better spatial resolution of the spectra can be obtained if we narrow the width of the slit. However a narrow slit will result in loss of intensity.

#### 4.6.3.5 Set-up

The set-up is shown in Fig.4.21. An electrical shutter (not shown) is employed in front of one of the stops (the other one is not shown) and opened only when the plasma is focusing properly (as judged from the 5-channel detector), since normally a few shots of conditioning are needed after opening the chamber, mounting the film and refilling the working gas. Detectors simultaneously used are current, current derivative, tube voltage and the 5-channel SXR PIN detector. The pinhole transmission grating is used for some discharges during this series to compare the results with this spectrometer.

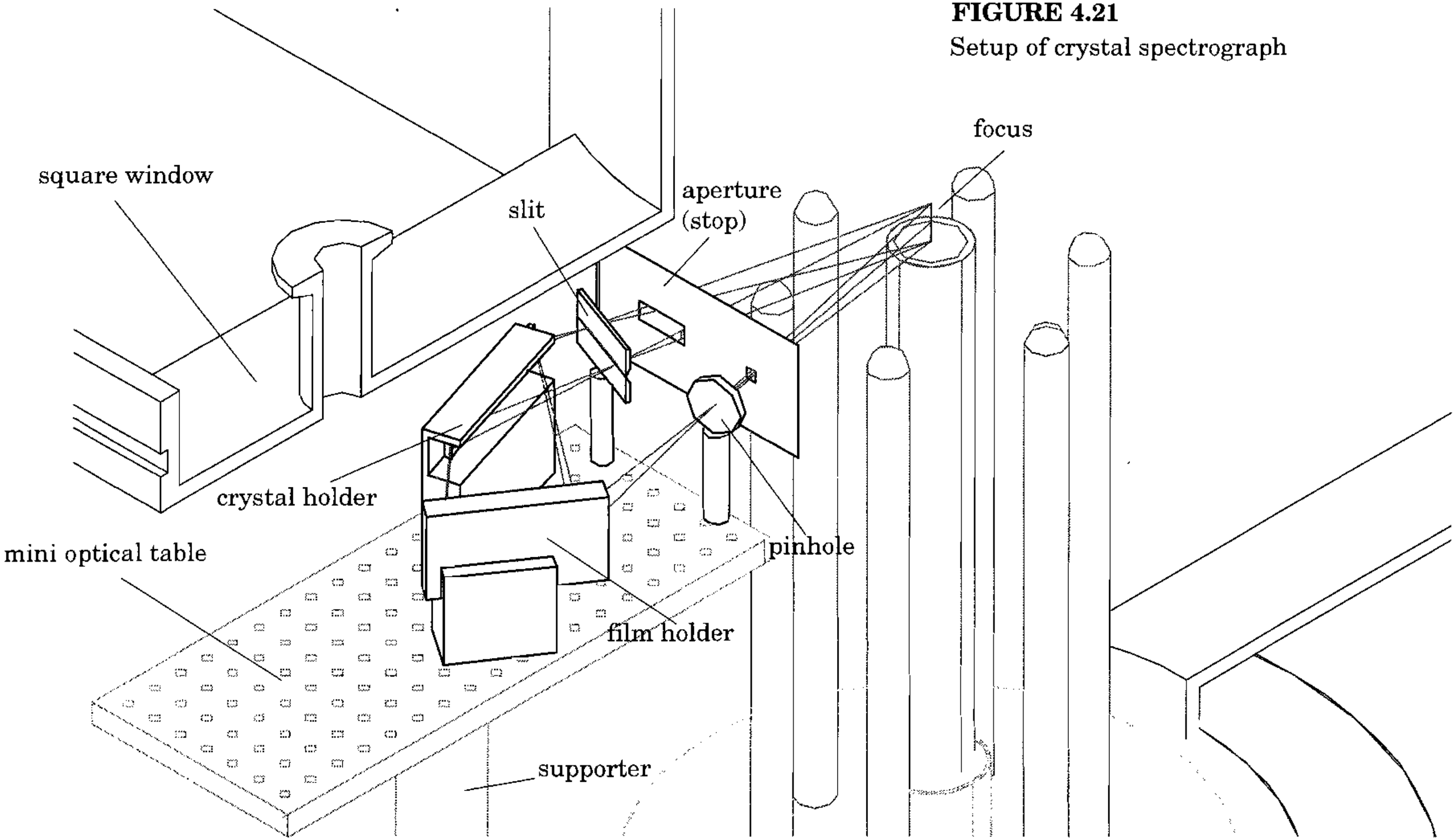


**FIGURE 4.21**
Setup of crystal spectrograph

#### 4.6.3.6 Calibration

Assuming that $X(\lambda)$ is the time integrated spectrum (absolute) emitted from the focus and

$D(\lambda,I)$ sensitivity of the recording film (density versus impinged intensity $I$ at wavelength $\lambda$)

$f(\lambda)$ transmission coefficient of the working gas along the light path and the foil mounted in front of the film

$G(\lambda)$ geometry factor after accounting for all the geometrical parameters (using $2d\sin\theta = m\lambda$ again)

then we obtain the relationship between the absolute source spectrum and intensity $P(\lambda)$ as follows:

$$\begin{aligned} P(\lambda) &= X(\lambda) \cdot f(\lambda) \cdot D(\lambda,I) \cdot G(\lambda) \\ &= X(\lambda) \cdot C(\lambda,I) \end{aligned} \tag{4.46}$$

Amongst these factors $f(\lambda)$ and $G(\lambda)$ are calculated after carefully considering the geometry of the spectrograph. What remains is to obtain the film sensitivity $D(\lambda,I)$.

For low energy photon $D(\lambda,I)$ is expected to be strongly dependent on the wavelength of the incident photon, especially near the characteristic absorption edge energies given in the Tab.4.5 for the silver-bromide and for the carbon, nitrogen, and oxygen constituents of the gelatin in the photographic emulsion of the film [146,147,152,153]. As a fortunate coincidence the range of our measurement 8 - 14 Å, does not encompass any absorption edges. In this work we are able to assume that the film response to photon energy is uniform over the range of interest 8 Å to 14 Å which is in very small spectral regime. So it is sufficient to obtain $D(\lambda,I) \sim I$ at one wavelength.

**Table 4.5** Absorption edges

| Edge | E(eV) | λ(Å) |
|---|---|---|
| Br-$M_4$ | 71 | 174.6 |
| C-K | 284 | 43.7 |
| N-K, Ag-$M_{4,5}$ | 398 - 402 | 30.9 - 31.2 |
| O-K | 532 | 23.4 |
| Br-$L_{3,2}$ | 1553 - 1599 | 7.8 - 8.0 |
| Ag-$L_{3,2}$ | 3351 - 3526 | 3.5 - 3.7 |

We have conducted a simple relative calibration for the film used (Kodak TMG/RA-1) by using the flat crystal spectrograph developed in the work. The procedure is: (a) enlarge the slit to 5 mm so that axial resolution is lost and instead a uniform exposure along the axial direction (i.e. vertical direction on the film) is expected, whereas in the horizontal direction of the film we still get the spectrum of the source. Five strips of foil with increasing thicknesses ( 7 μm Al + $n$ x 1.9 μm Mylar, $n$ = 0,1,2,3,4 ) are placed in front of the film across different vertical positions to get information with different incident intensities in the vertical direction. By doing so, the so-called relative "master-curve" of the film is obtained. An example of the film is illustrated in Fig. 4.22. The film is densitometered along the vertical direction at the wavelength 10 Å. The relative master-curve at the wavelength 10 Å is shown in Fig. 4.23, where the optical density is the total density of the film minus the fog density.

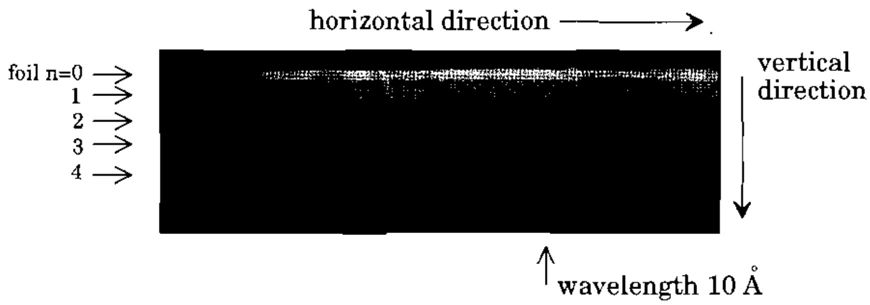


**FIGURE 4.22**
Example of film for relative calibration with five different filters in parallel

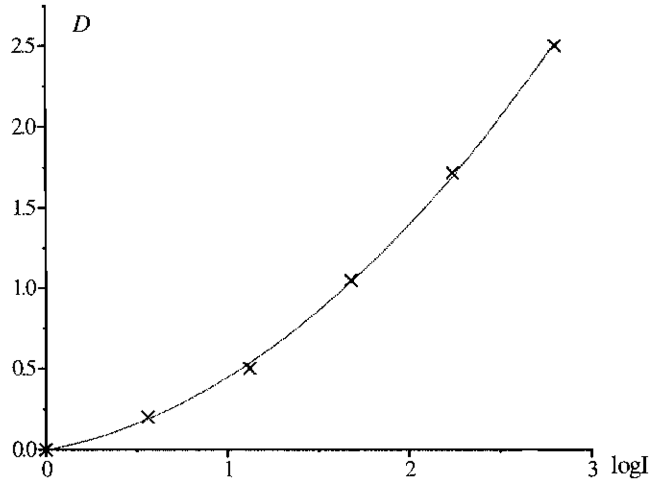


**FIGURE 4.23**
multi layer exposure method to obtain the relative "master-curve" at wavelength 10 Å

### 4.6.4 The 5-Channel PIN Detector

#### 4.6.4.1 BPX65 as Soft X-ray Detector

There is an increasing number of semiconductor detectors which can be used for the detection of x-rays, e.g., surface barrier, ion-implanted and avalanche junction diodes and charge coupled devices to name but a few.

When a semiconductor detector absorbs an x-ray photon of energy $h\nu$, $h\nu / w$ electron-hole pairs are produced where $w$ is the average energy needed to create an electron-hole pair. The collected charge is proportional to $h\nu$. For silicon at room temperature $w$ = 3.62 eV (see [154]). The quantum detection efficiency is given by [154]

$$Q = \frac{h\nu}{w}\exp(-\mu_d t_d)\cdot\left[1-\exp(-\mu_s t_s)\right] \qquad (4.47)$$

where the first exponential term describes absorption in the dead layer (on the front surface of the detection area) of thickness $t_d$ and the second gives the efficiency for stopping x-rays in the depletion (sensitive) region of thickness $t_s$. It can be seen that there exists an energy range over which semiconductor detectors can be used. The lower limit is determined by absorption in the dead layer and the upper limit by incomplete absorption. Lower energy x-rays may be detected if the dead layer can be thinned.

Since both the electrons and holes have large mobilities, and since the collection distances are short, it is possible to achieve relatively short collection times. This is an important advantage for measurements of pulsed x-ray sources.

According to Ref. [155], the pair creation energy $W$ is, in general, a function of the photon energy. It is usually assumed that W is a constant for photon energies well above the band gap of Si ($\sim 10 \text{x} E_g$ [156]). Recently however, Monte Carlo simulations of the pair creation energy [157] show a significant photon energy dependence up to a few hundred eV. We have assumed here a photon energy-independent value of 3.70±0.07 eV as measured recently by Krumrey and Tegeler [158].

BPX65 PIN (a detector normally used in the optical range) was chosen for our system. The glass window is removed for application to x-ray detection. The typical parameters of this diode are listed below [159]:

| | |
|---|---|
| radiant sensitive area | 1 mm$^2$ |
| intrinsic Si wafer thickness | 10 micron |
| dead layer thickness | 0.5 micron |
| risetime (typical) (900 nm) | 0.5 ns |
| dark current | <5 nA (nom 1 nA) |

### 4.6.4.2 Set-up of the 5-Channel Detector

An array of five windowless BPX65 photodiodes is used in this project, both to obtain spectral information (in combination with filters) and for time-resolved x-ray measurements. It is based on the detector introduced in Ref. [160]. Filters suitable for the wavelength range 1 to 20 Å are selected for our purpose. Each diode is reverse-biased at 50V with the circuit illustrated in Fig.4.24(b)

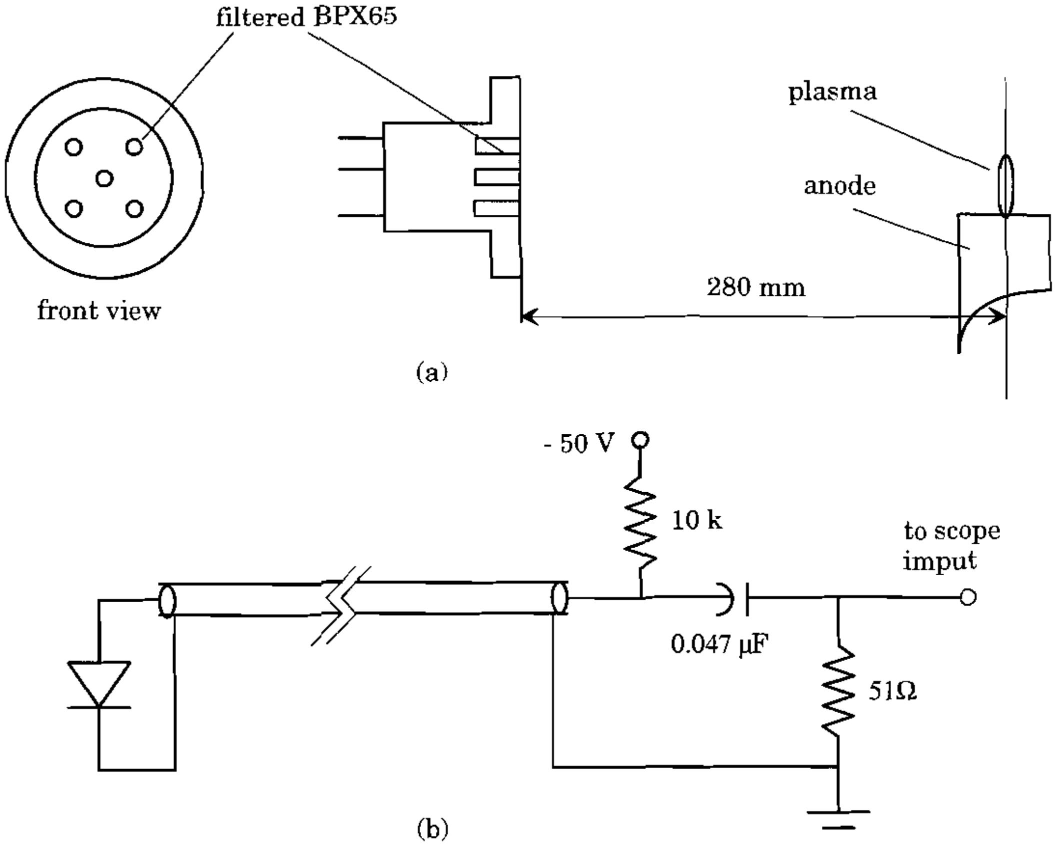


**FIGURE 4.24**
Five channel PIN x-ray detector
(a) experimental arrangement; (b) electrical circuit

The absorption combinations of the five channels are:

| | |
|---|---|
| X1 (channel 1): | 149 μm aluminized mylar |
| X2 (channel 2): | 12 μm aluminized mylar |
| X3 (channel 3): | 24 μm aluminized mylar |
| X4 (channel 4): | 24 μm aluminized mylar+10 μm Cu |
| X5 (channel 5): | 20 μm Be |

According to Eqn.(4.47) we are able to work out its conversion efficiency. Fig.4.25 shows the sensitivity curve in wavelength range from

1 to 20 Å. The overall sensitivity of the filter photodiode combination as a function of wavelength is then obtained by $f(\lambda) = Q(\lambda)\ \exp[-\mu(\lambda) \cdot d]$ and shown in Fig.4.26.

With the absolute transmission curve, the soft x-ray signals may be (i) correlated with the discharge current, current derivative, voltage and other time-resolved signals for a better understanding of the plasma focus processes, (ii) applied to get the spectral information for the calorimeter (introduced later) to evaluate the absolute SXR yield, (iii) used to estimate total SXR yield and (iv) used as a base for any other measurements such as pinhole transmission grating and crystal spectrography.

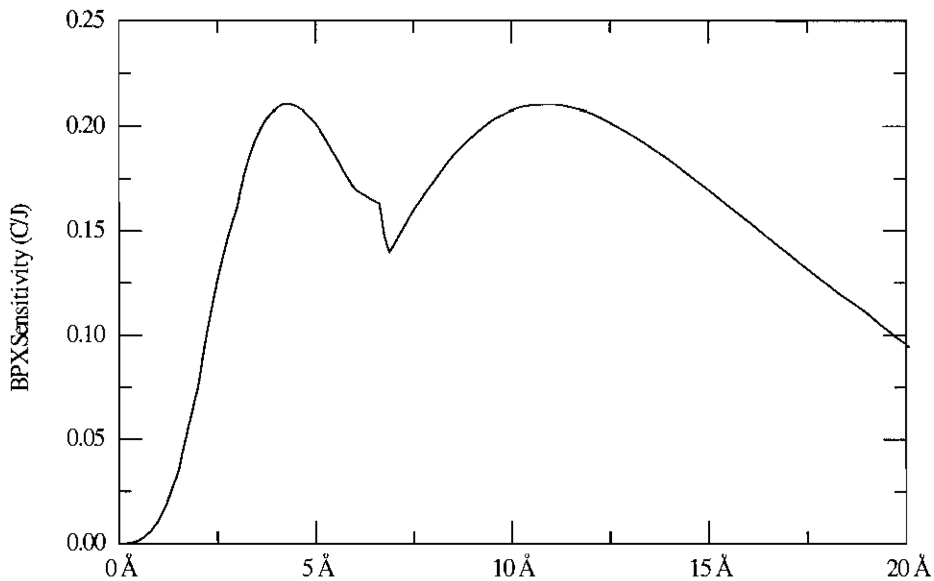


**FIGURE 4.25**
BPX65 sensitivity in wavelength range <20 Å

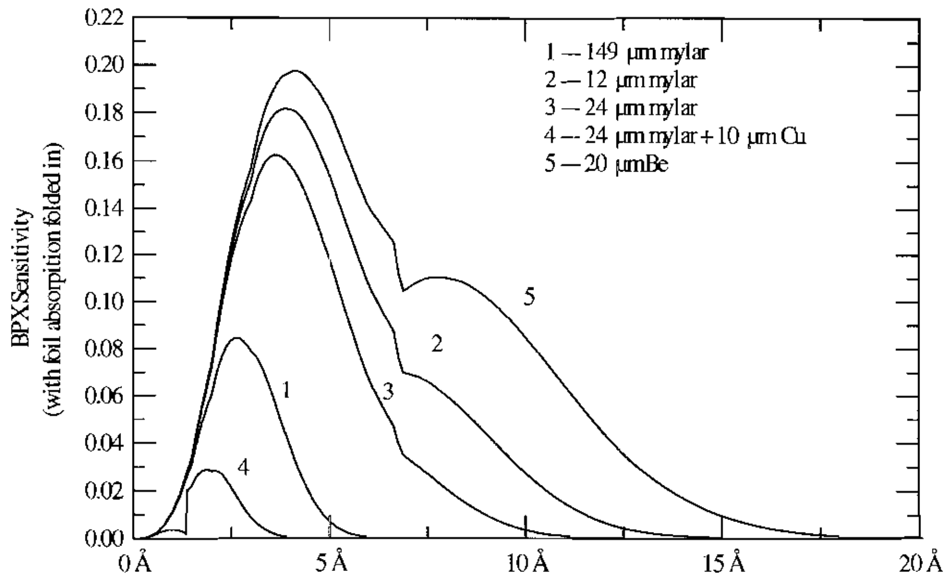


**FIGURE 4.26**
Sensitivity curve of BPX65 with the foil absorption folded in

## 4.6.5 X-ray Detector Based on Photoelectric Effect

### 4.6.5.1 Operating Principle of the Detector

It is well known that for photon energies below 100 keV the dominant interaction with matter is the photoelectric effect. The absorption of one photon of energy $h\nu$ by an atom will result in the ejection of an electron (a photoelectron) of kinetic energy:

$$\varepsilon = h\nu - B_\alpha \tag{4.48}$$

where, $B_\alpha$ is the binding energy of the atomic shell from which the electron is ejected ($\alpha = K, L, ...$). Photoelectrons are preferentially emitted from the most tightly bound shell which is energetically possible (i.e. $B_\alpha < h\nu$). The photoelectric cross-section is a strong function of the incident photon energy and the atomic number $Z$ of the absorber material.

For a beam of x-rays ($h\nu$ < 100 keV) impinging on a metal surface many of the ejected photoelectrons will be stopped within the bulk of the material, and others will lose a significant fraction of their kinetic energy before leaving the metal surface. Hence the kinetic energy $\varepsilon = h\nu - B_\alpha$ represents a maximum energy limit for the photoelectrons leaving the metal surface. It should also be noted that the probability of a photoelectron escaping the metal surface is dependent upon i) the depth below the metal surface at which it is emitted and ii) the "range" and therefore kinetic energy of the ejected photoelectron; both of which are in turn dependent upon the energy of the incident photon.

A parameter of considerable importance for the operation of this detector is the efficiency of photoelectron emission ($f_b$) from the metal surface (i.e. on average the number of electrons emitted per incident photon). This is dependent upon the photoelectric cross-section and the probability of escape of the photoelectron from the metal surface and is hence clearly a complicated function of the photon energy. Indeed the parameter $f_b$ is best taken from experiment. In this work data from T.A Dellin [23] are used.

A time-resolved soft x-ray detector has been developed (see Fig.4.27) for which the principle of operation is based on the photoelectric as discussed above. The x-ray impinge on a metal plate (see Fig.4.27) which is maintained at a fixed negative potential by an R-C biasing circuit. Most of the resulting photoelectrons will be collected by a wire grid placed in front of the metal plate (and maintained at ground potential), giving rise to a current pulse through the detector. The resulting voltage signal developed across the 51Ω impedance matching resistor is recorded on one DSO channel. Although the wire grid will prevent some of the incident x-rays from reaching the metal plate, the x-ray flux from the plasma focus is sufficiently intense that this not a problem. Indeed it is necessary to further reduce the x-ray flux on the detector by placing a circular metal aperture in front of the wire grid

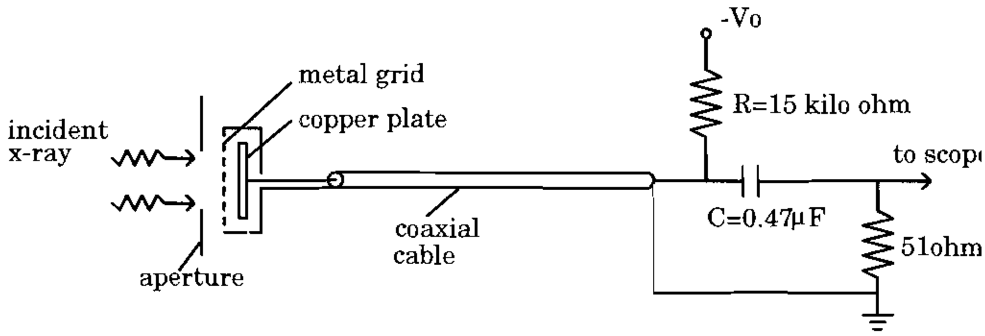


**FIGURE 4.27**
Diagram of x-ray detector

### 4.6.5.2 Design

a) Material of the plate and size of the aperture

Proper material of plate and aperture size are selected so that the output signal is in the range of tens of volts, which corresponds to a collection current of the order of 1 A. This is sufficient to give a good signal-to-noise ratio, but not so high as to result in breakdown between the grid and the plate. From reference [23] we know the efficiency of photoelectric effect depends on material of the target and the absolute energy spectrum of the x-ray source. We determined the most suitable material of the plate and aperture size by experiments. Plates of aluminum, copper and lead have been tried with several sizes of aperture. We finally chose copper as the target material for the detector plate and an aperture diameter 5 mm.

b) Biasing voltage and distance between the grid and the plate

Each photoelectron ejected from the surface will be collected by the grid which is positive relative to the negatively biased plate. The time for electron to move from the surface of plate to the grid should be very short, as this determines the rise-time and therefore timing resolution of the detector.

Assuming:

$V_o$: voltage on the capacitor

$V_s$: signal voltage on output resister R

$q_o$: initial velocity of photon-electron on the surface of plate

$q_1$: final velocity of the electron

$a$: acceleration of the electron

$l$: distance between grid and plate

In terms of the law of conservative of energy and law of kinetics, we have

$$\frac{1}{2}mq_1^2 - \frac{1}{2}mq_o^2 = e(V_o - V_s) \tag{4.49}$$

$$q_1^2 - q_o^2 = 2al \tag{4.50}$$

where $m$ and $e$ are respectively the mass and charge of the electron. From Eqns.(4.49) and (4.50) we obtain

$$a = \frac{e(V_o - V_s)}{ml} \tag{4.51}$$

$$q_1 = \sqrt{[e(V_o - V_s) + \frac{1}{2}mq_o^2)\frac{2}{m}} \tag{4.52}$$

So we obtain the transit time of electron

$$t = \frac{q_1 - q_o}{a} = \frac{\sqrt{[e(V_o - V_s) + \frac{1}{2}mq_o^2]\frac{2}{m}} - q_o}{\frac{1}{ml}e(V_o - V_s)} \tag{4.53}$$

We only consider the case when $q_o$ = 0, with corresponding time $t_o$, since electrons with $q_o$>0 will move faster and thus take less time to reach the grid than $t_o$. We must have

$$t_o = l \times \sqrt{\frac{2m}{e(V_o - V_s)}} \tag{4.54}$$

$V_s$<100 V, so choosing $V_o$ = 300 V and $l$ = 2 mm we obtain $t_o$<0.5 ns which is fast enough since the width of x-ray pulse in our case is of the order of 10 ~ 150 ns and the rise time is about 3 ns.

### 4.6.6 Calorimeter

#### 4.6.6.1 Principle of the Calorimeter

A calorimeter has been used to measure the absolute soft x-ray yield from NIE-SSC-PFF plasma focus.

Fig.4.28 shows schematically the diagram of the calorimeter used for measuring the total x-ray yield. One of the principal advantages of using a calorimetric detector is its flat response to radiations of different wavelengths provided of course that the radiation is fully absorbed by the exposed surface of the detector. The surface of the detector used for these measurements is tantalum with suitable absorption properties for soft x-rays. This detector comprises a thermocouple chain in which each alternate metal junction of dissimilar metals is in thermal contact with the absorbing material on which the soft x-rays impinge. The other junctions are held at near constant temperature by being placed in contact with a heat reservoir. The rise in temperature (a fraction of a degree in our case) of the absorber material gives rise to a thermoelectric potential which is amplified before input to a peak holding circuit and display. This detection system is suitable for measurements on pulsed sources (of duration less than 400 ms) of any radiation wavelength greater than 0.05 Å. As the aim of this experiment is to measure soft x-ray flux, a 20 micron beryllium foil was placed in front of the calorimeter to shield it from visible and infrared radiation.

#### 4.6.6.2 Calibration

A suitable means of calibrating this detection system is by depositing a pulse of energy, of known magnitude, in the absorber material through a built-in resistor (2), as shown in Fig.4.29. A square pulse of 100 μs duration and of varying magnitude was applied to the calibration resistor ($R$ = 17.3 ohm), and the meter reading (in arbitrary units) as a function of the deposited energy was obtained, as shown in Fig.4.30.

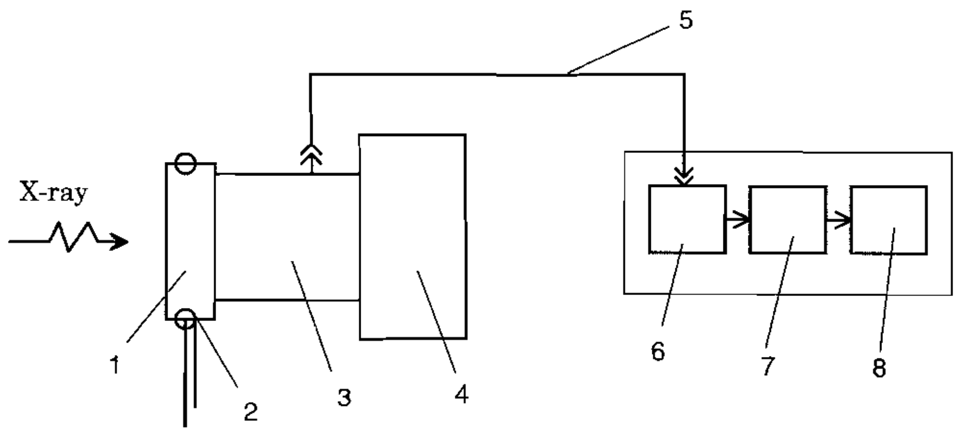


1. Absorber 2. Calibration resistor 3. Thermal couples
4. Base plate with constant temperature
5. Shielded signal cable 6. Amplifier
7. Peak signal holder 8. Digital meter

**FIGURE 4.28**
Schematic diagram of calorimeter for SXR yield measurement

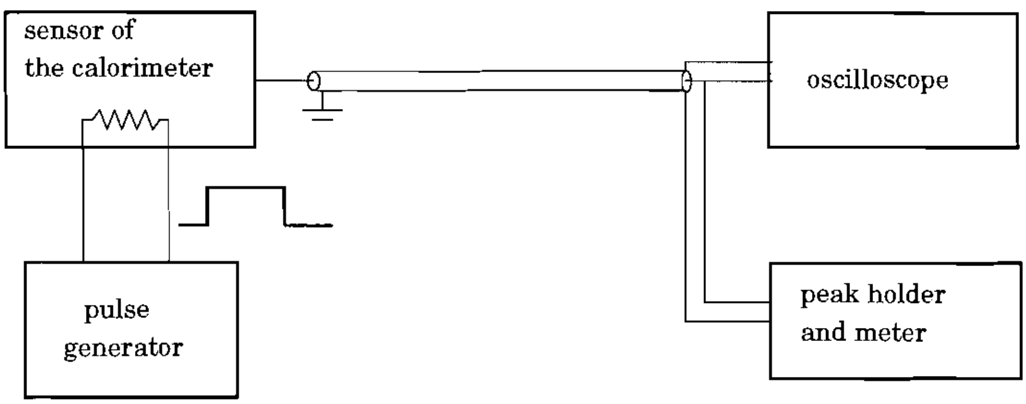


**FIGURE 4.29**
The set-up for calibrating system

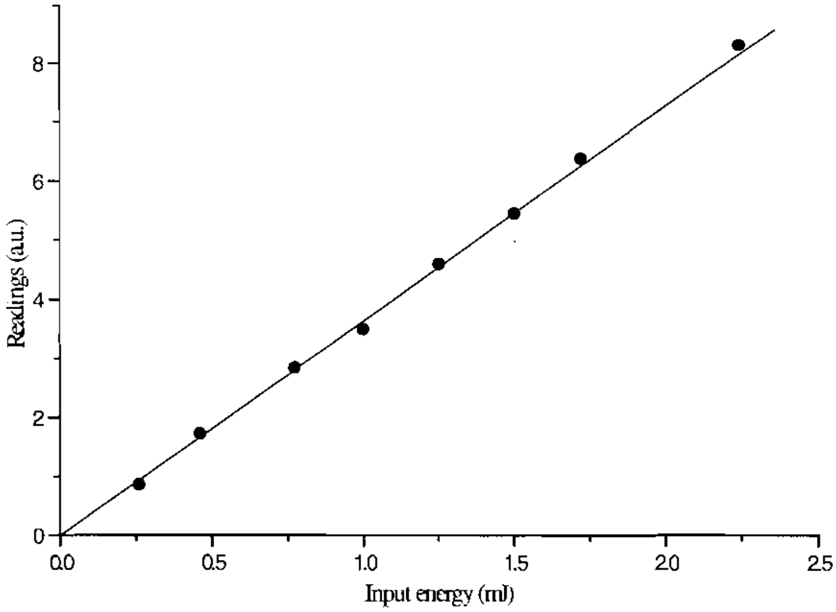


**FIGURE 4.30**
Calibration of the calorimeter.

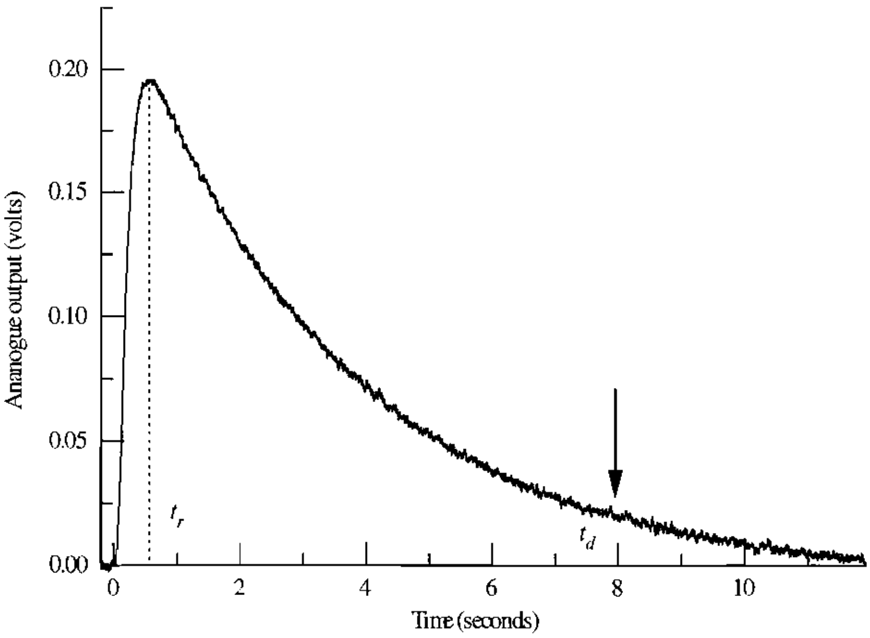


**FIGURE 4.31**
Analog signal from the calorimeter without "peak-holder"

The reading displayed on the meter is the peak value obtained by the peak holder circuit (7). Fig.4.31 shows a typical voltage signal from the thermocouple chain when the peak holding circuit is eliminated, for an input electrical energy of 1.5 mJ. It can be seen that it takes $t_r$ ~ 0.5 s for the signal to peak and $t_d$ ~ 8 s to drop to 10% of its peak value. Measurements revealed that both $t_r$ and $t_d$ change only slightly when the input energy varied from 0.02 mJ to 2.5 mJ. In our case, the pulsed energy incident on the detector is of the order of 0.2 mJ and the repetition rate is ~2 shot/minute, clearly within the operational limits of this detector.

The calibration was repeated with a pulse of 190 ns. It was confirmed that the calorimeter gave the same calibration constant for both pulses.

## 4.7 Data Acquisition and Analysis System

1 GSa/s, 250 MHz Hewlett Packard (HP™) digital logic analysers (DSO) of model 16500A was used to collect up to 10 channels of data for one discharge. The time-resolution achieved with our system is better than 2 ns.

The data taken by the DSO were then transferred to a PC via GPIB by using a program which was developed in C language. 8000 data points for each channel can be transferred under DOS environment using this particular program. The data stored in disk(s) (hard disk or diskettes) can be easily manipulated by computers enabling us to apply powerful tools (such as scientific graphics, etc.) as well as allowing us to write our own software to analyze the data, which is the case described in the following chapters. Origin™ 3.5 for Windows™ was used for basic data analysis.

# Chapter 5

# Experimental Results

## 5.1 Introduction

In this chapter, the experimental observations on the small plasma focus and data analysis are presented. Experiments were carried out under various operating conditions with (a) three different working gases, neon or argon or deuterium, and (b) positive and negative polarities. Here positive (negative) polarity means the central electrode is operated at initial positive (negative) voltage. The discharges were carried out at 14 kV or 13 kV charging voltages for both polarities. The filling pressures for the three working gases were varied between 0.5 ~ 10 mbar for neon, 0.4 ~ 2 mbar for argon and 0.5 ~ 10 mbar for deuterium. Detectors (current transformer, current derivative, resistive voltage divider, optical speed detector, magnetic probes, x-ray pinhole camera, 5-channel PIN soft x-ray (SXR) spectrometer, pinhole transmission grating spectrograph, crystal spectrograph and SXR calorimeter) were employed to study the basic and x-ray emission characteristics as well as some related topics in NIE-SSC-PFF plasma focus device. More emphasis is given to the neon plasma focus concerning its SXR radiations.

The first part (section 5.2) presents the results obtained during preliminary experiments to understand the evolution and dynamics of plasma. These include basic electrical diagnostics, optical probing and magnetic field probing.

The second part (section 5.3) is devoted to the experimental work of x-ray observations. The diagnostics employed include x-ray pinhole imaging, space resolved pinhole transmission grating spectrography, crystal spectrography, time-resolved 5-channel PIN SXR detector, and calorimetric detector. Detailed description, interpretation of the results and discussions will be presented.

The experimental results will be compared with the numerical simulation based on theoretical model described in Chapter 3. Discussion and summary will be given in the final section.

We present mainly the results of the focus in neon. Argon and deuterium plasmas are not discussed in detail as they have been discussed in earlier research on *this* or similar machine [33,98,126].

## 5.2 Basic Measurements

### 5.2.1 Current and Voltage Waveforms

The current of the main circuit, the derivative of current and the voltage across the focus tube were monitored for every discharge. From these signals or by applying some simple calculations based on them, a great deal of information can be extracted from them such as the transit time of each phase, focusing quality, input energy and gross dynamics of the plasma focus. Furthermore, they are used to correlate with other time-resolved signals to yield more information.

The following are summarized results extracted from these signals. Some of them will be presented in Sec.5.3.4 where correlations with the time-resolved 5-channel SXR results are made so as to get a better understanding of the gross dynamics concerning SXR emissions.

#### 5.2.1.1 Gross Dynamics of Plasma Focus

Voltage probe signal corroborated with discharge current evolution and soft x-ray emission profiles were investigated and reported on this *same* focus device operated in argon in Ref. [33]. Two distinct evolution patterns or regimes, i.e. one with single voltage spike and the other with multiple voltage spikes, were identified. It was thought that multiple voltage spikes correspond to a sequence of compressions. The focus usually occurs with multiple voltage spikes in the argon plasma.

For neon plasma focus similar regimes (single and multiple spikes) were observed in this work. However in neon the focus usually occurs with a single spike. Fig.5.1 and 5.2 show typical waveforms with multi-spike pattern for both neon and argon plasmas. Fig.5.3 shows typical trace with single spike pattern for neon plasma. We found that for neon focus the probability of single spike discharge is much larger than that for argon focus, giving about ~ 65% (34 out of 51 discharges in one of the experimental series) compared with argon for which only ~ 20% of the focusing occurs with a single feature. At optimum pressure in neon only single spike focus are observed. Multiple spikes are observed when working pressure is relatively low, i.e., below 1.2 mbar (for 13 - 14 kV charging voltage).

For the multi-spike case we found that the first spike with risetime of 3 ns and duration of 10 ~ 20 ns corresponds to a first compression, the second spike comes after 200 ~ 300 ns with duration of 10 ~ 50 ns corresponding to a second compression. For the single spike case the pulse is basically similar to the first pulse of the multi-spike signal.

In the case of negative polarity, different features were observed compared to that of positive polarity. The pattern or feature with single voltage spike becomes predominant when operated in negative polarity regardless of focusing quality. In fact, more than 95% of the discharges exhibit single spike focus. Fig.5.4 shows a typical trace. More details will be described in Sec.5.3.4 where correlation with SXR detector is made.

Comparing Fig.5.4 with Fig.5.3 we see that it takes longer for the plasma focus operated at negative polarity to breakdown than its positive counterpart. The data analysis shows that for neon focus higher pressure corresponds to faster breakdown. For pressure below 1 mbar the time of breakdown phase is varied from 50 to 300 ns for 13 kV charging voltage. From the voltage signals we found that the time delay for the breakdown is different for different experimental condition (gas, gas pressure, charging voltage, polarity, etc.). There is evidence that the focusing quality is affected by this time delay.

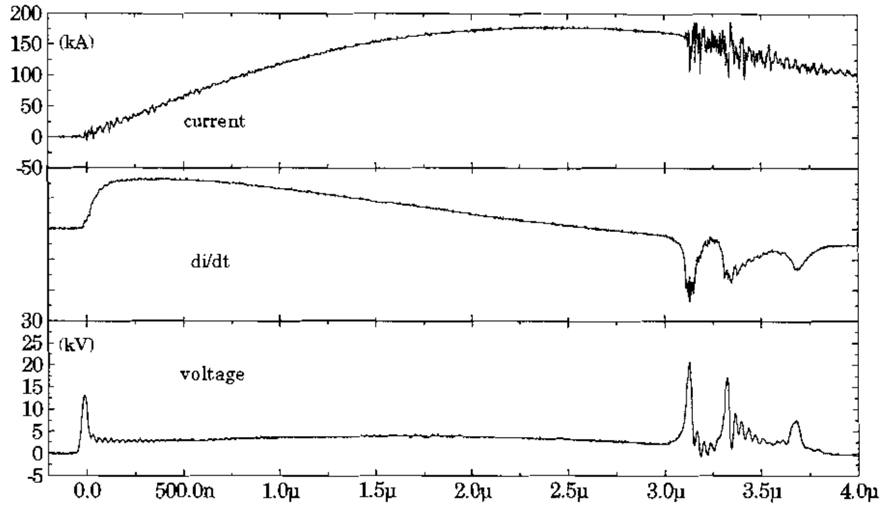


**FIGURE 5.1**
Current, $di/dt$ and voltage signals showing multi-spikes for neon plasma focus

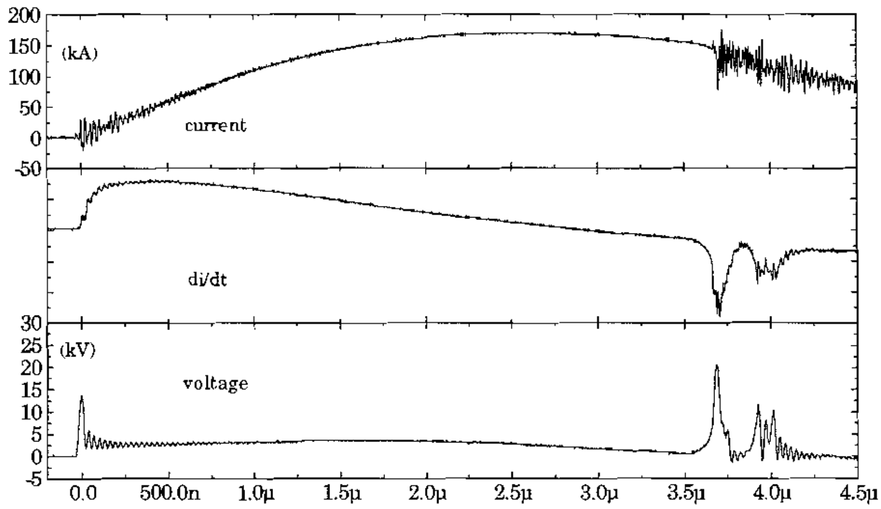


**FIGURE 5.2**
Current, $di/dt$ and voltage signals showing multi spikes for argon plasma focus

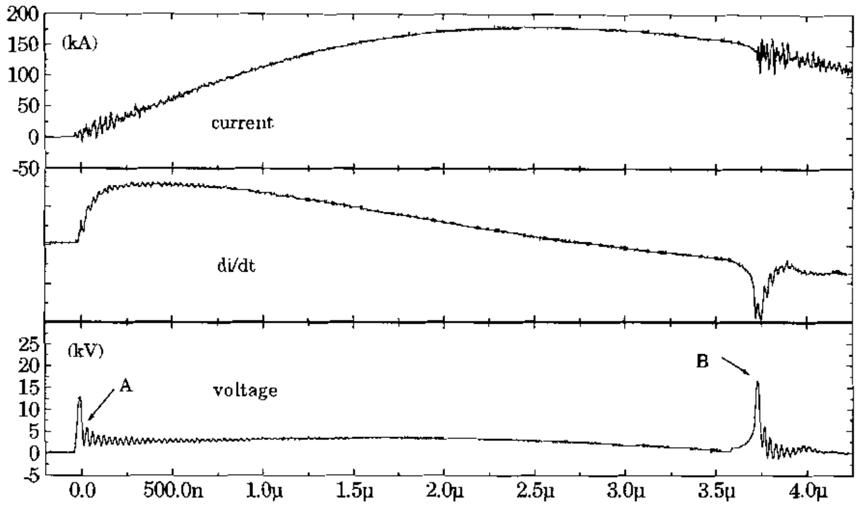


**FIGURE 5.3**
Current, $di/dt$ and voltage signals showing single spike for neon plasma focus operated at positive polarity

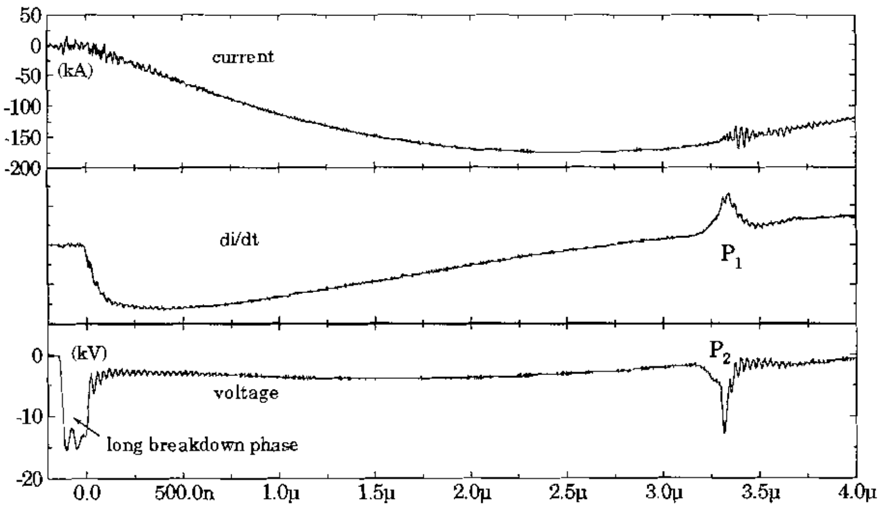


**FIGURE 5.4**
Current, $di/dt$ and voltage signals showing single spike for neon plasma focus operated at negative polarity

### 5.2.1.2 Focusing Quality

*Electrical input energy and focusing quality*

The dip in current signal and the spikes in voltage and $dI/dt$ signals are indicative of focusing quality. It is found that big current dips and voltage spikes are always accompanied by large radiation bursts.

Another meaningful quantitative information can be extracted out of the voltage and current waveforms. Fig.5.5 shows a typical $V(t)I(t) \sim t$ curve. The product $V(t)I(t)$ is actually the total power input to the discharge tube. The unshaded area under the curve represents the energy pumped into the discharge tube if there was no focus action of the current sheath. The shaded area represents the additional energy pumped into the tube during the formation of the dense plasma focus. Results based on this way of calculation will be presented in the following sections where other power densities are to be compared with this input power.

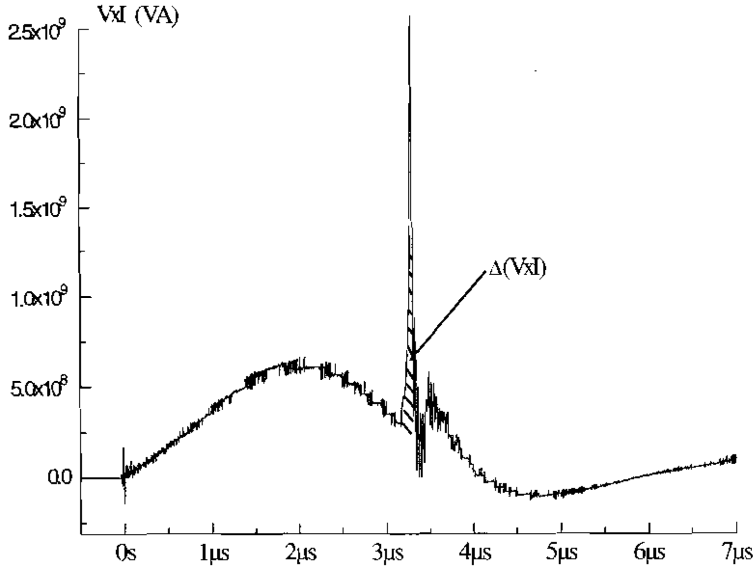


**FIGURE 5.5**
Graph of input power [$V(t)I(t)$] versus time

#### 5.2.1.3 Focusing Time

*Focusing time vs. various experimental conditions*

"Focusing time" is taken as the time from breakdown ('A' in Fig.5.3) to the end of compression when the plasma is compressed to its minimum radius as indicated by the voltage spike ('B' in Fig.5.3). In this way, $t_{axial}$ excludes the duration of the breakdown phase of about 100 ns (as big as 300 ns for the negative case). Fig.5.6 shows a summary for different experimental conditions.

*Summary*

In Fig.5.6, the focusing time, average velocity of the plasma sheath (averaged in the run-down phase) and the input energy (see proceeding section) are shown for three different experimental conditions. The results are summarized in Tab.5.1. It is seen from these results that to obtain a better focusing the pressure must be chosen such that the focusing time is about 3.5 μs for neon plasma focus for both positive and negative polarities for this focus device.

***Table 5.1*** Comparison of focusing time, speed of plasma sheath and quality under different conditions (neon focus)

| charging voltage and polarity | optimum pressure (mbar) | focusing time (us) (optimum$^{+}$) | average speed cm/us (optimum) | input energy (J) (optimum) |
|---|---|---|---|---|
| 14 kV, positive | 3 to 5.5 | ~ 3.5 | ~ 4.5 | ~ 65 |
| 13 kV, positive | 2 to 4 | ~ 3.5 | ~ 4.5 | ~ 60 |
| 13 kV, negative | 1.3 to 2.5 | ~ 3.5 | ~ 4.5 | ~ 40 |

$^{+}$ "optimum" in this table means operation corresponding to maximum input energy measured by area of *VxI* spike. This optimum condition also produces maximum x-ray yield (see Sec.5.3.5).

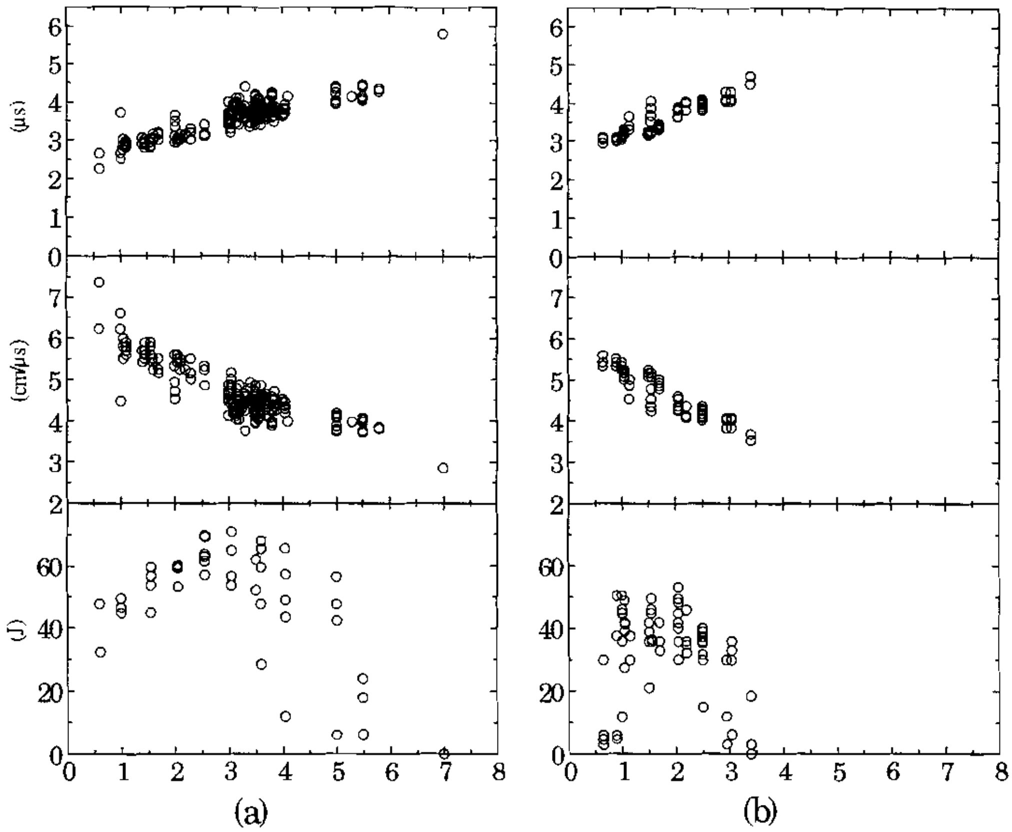


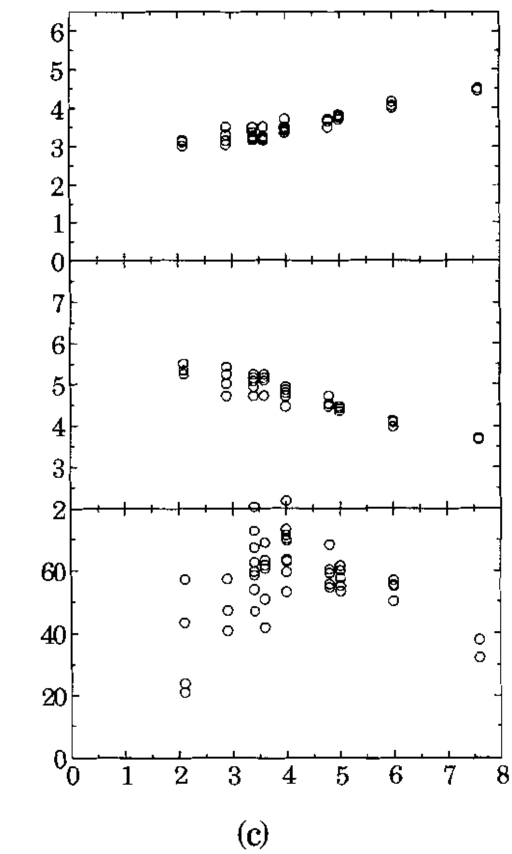


**FIGURE 5.6**
Comparison of focusing quality under different conditions

Descriptions for (a), (b) and (c)
upper graphs: focusing time (μs)
middle graphs: average speed of plasma sheath (cm/μs)
lower graphs: input energy (J)
horizontal axis: pressure (mbar)

Conditions
(a) charged voltage 13 kV, positive polarity
(b) charged voltage 13 kV, negative polarity
(c) charged voltage 14 kV, positive polarity
working gas: neon

#### 5.2.1.4 Correlation with other time-resolved diagnostics

The first sharp peak of the $dI/dt$ signal or the voltage signal (see $P_1$ and $P_2$ in Fig.5.4 is normally taken as a reference time (zero time) for studies in the pinching phase, such as shadowgraphy, etc. Any one of these signals can be set as a time reference, with which other time-resolved signals can be correlated. More details will be presented in the section 5.3.4, where the time-resolved SXR detection is described and the signals from this 5-channel PIN detector will be analyzed, with the comparison to the electrical signals.

### 5.2.2 Magnetic Field Probing

#### 5.2.2.1 Radially Located 3-MP Array

It is a well known fact that in almost all plasma focus devices, a fraction of the total current does not flow through the pinch region but links the anode and cathode elsewhere, particularly in the vicinity of the insulator [58,68,161].

To determine the fraction of the total current which constitutes the pinch current in the NIE-SSC-PFF facility, a three-magnetic-probe array (3-MP) as described in the previous chapter (Sec.4.5.2), combined with a speed detector, was used to measure the pinch current. A sketch of the geometry of the electrodes and position is given in Fig.4.11. The total current was measured by the current probe which had been calibrated. These three probes were calibrated too, as described in Chapter 4 Sec.4.5.2. Fig.5.7 shows some typical traces obtained using the probe array. The derivatives of magnetic field were also measured together with the magnetic field.

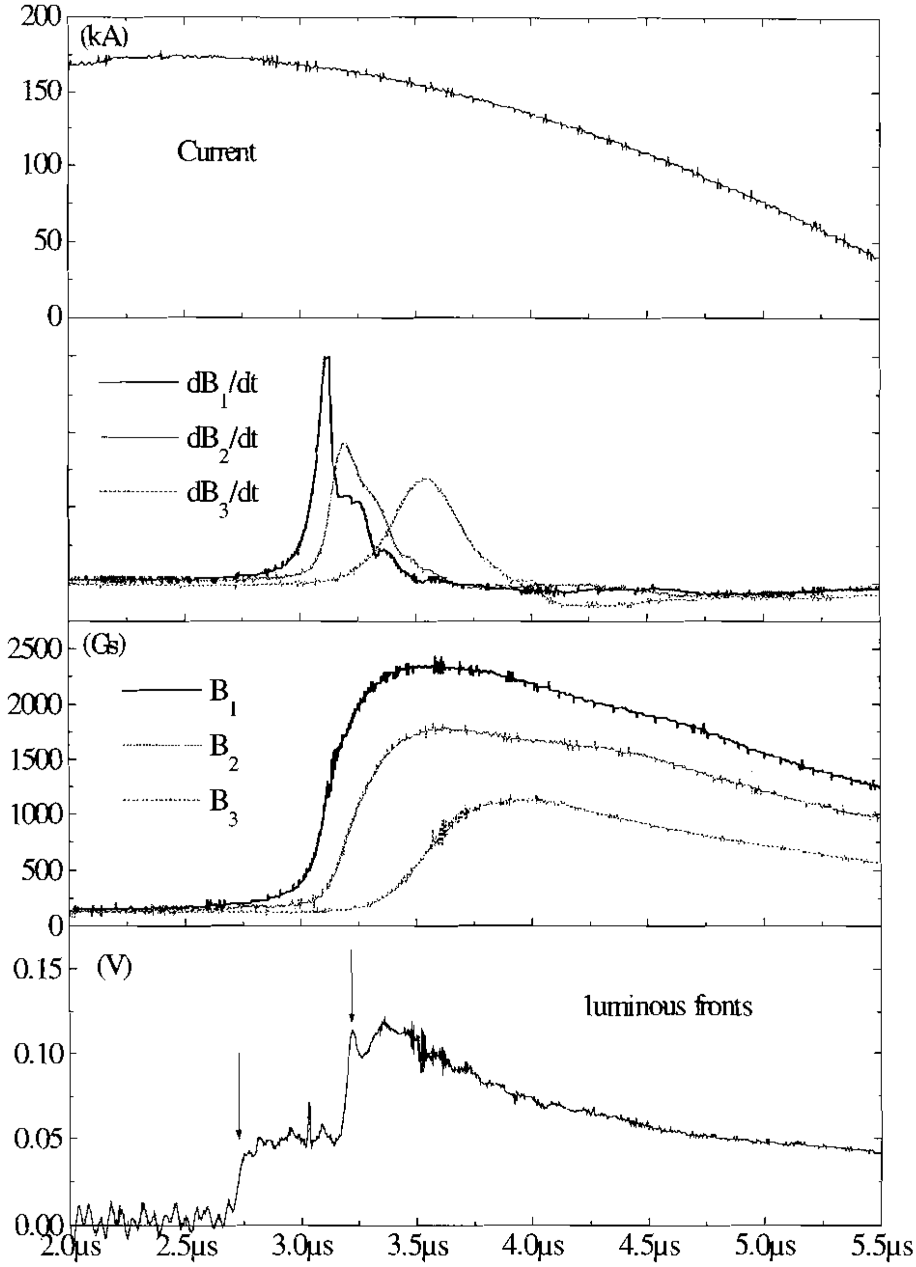


**FIGURE 5.7**
Typical traces of 3-MP probes and optical speed detector
Conditions: 13 kV charging voltage, 2 mbar neon pressure

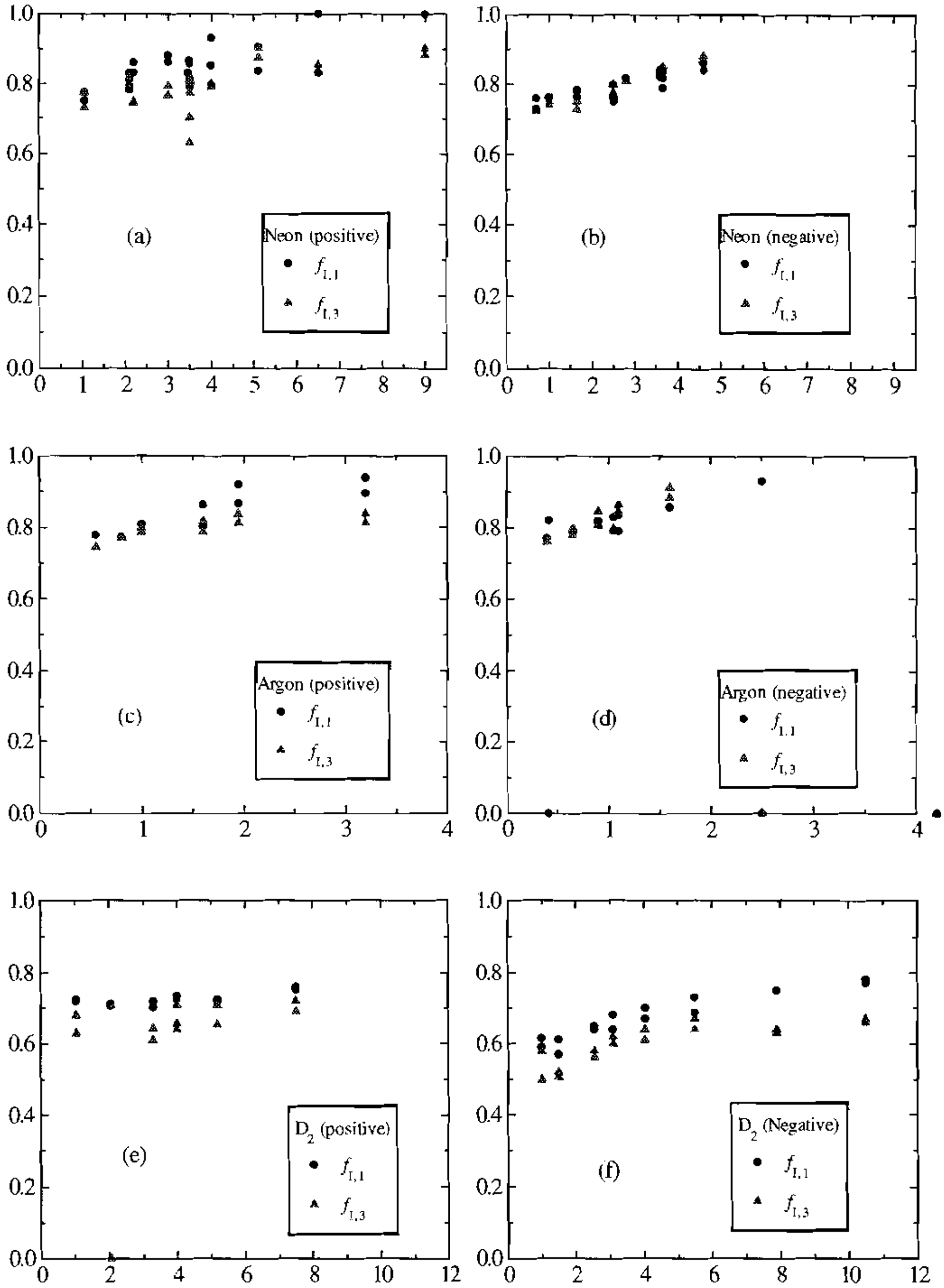


**FIGURE 5.8**
3-MP array used to measure current factors for neon, argon and deuterium operated at positive and negative polarities.
horizontal axis: pressure (mbar)
vertical axis: current factor
$f_{I,1}$ stands for factors measured by MP-1 (the nearest to the anode), $f_{I,3}$ stands for factors measured by MP-3 (the furthest from the anode). Charging voltage: 13 kV.

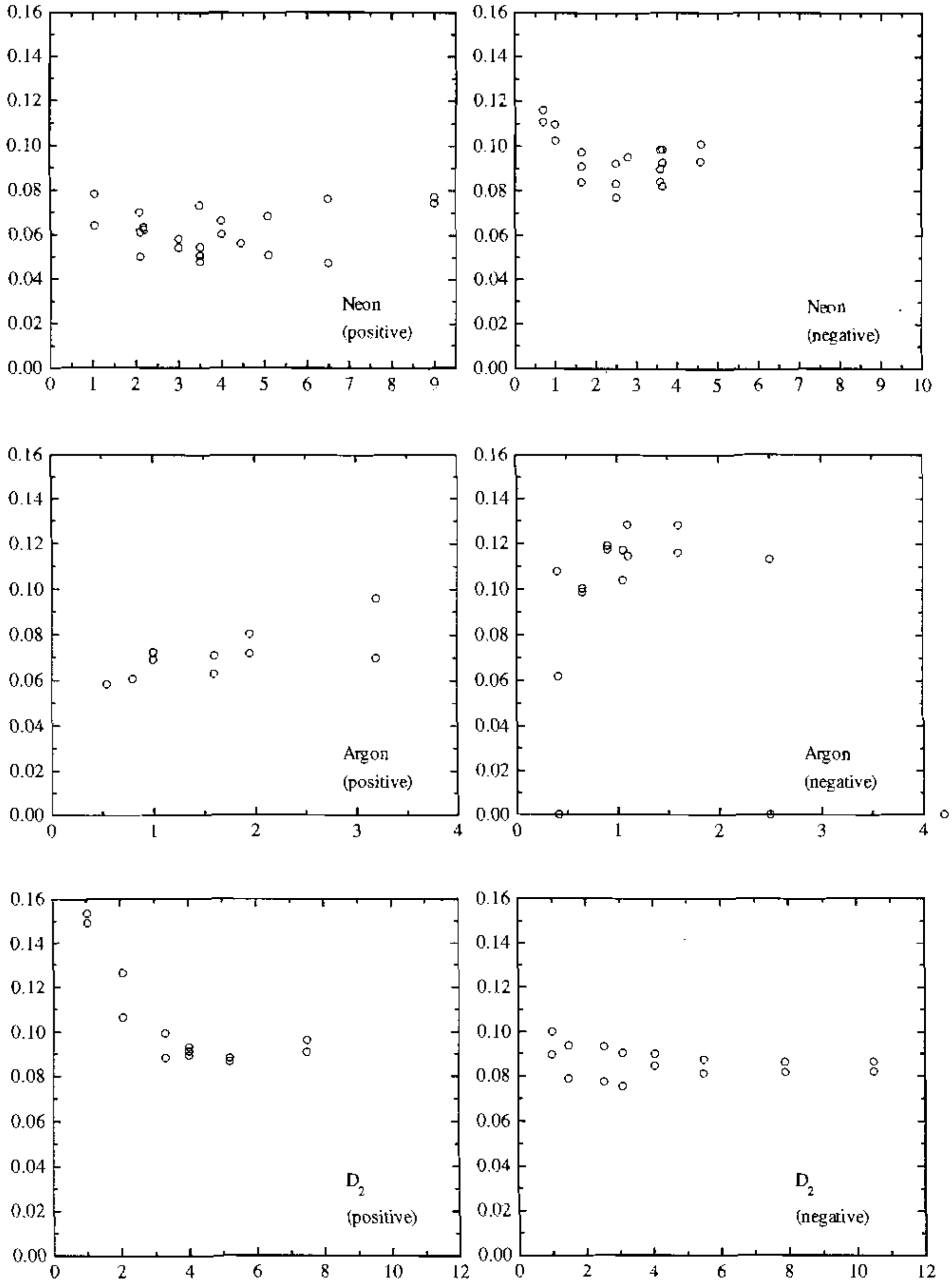


**FIGURE 5.9**
Comparison of mass factors for the axial run-down phase under different conditions.
Listed are neon, argon and deuterium plasma foci operated at positive and negative (specified in brackets) polarities.

horizontal axes: pressure in mbar
vertical axes: mass factor

#### 5.2.2.2 Current Factors

Fig.5.8 shows the final results for three types of working gas, i.e. deuterium, argon and neon operated at positive and negative polarities.

These results (current factors) were used as input parameters for the model (see Chapter 3 Sec.3.5).

In a cylindrical geometry the magnetic field is related to the current in a simple (linear) manner, for the 3-MP probe that is,

$$B_i = k_i I_i \qquad i = 1, 2, 3 \tag{5.1}$$

here $k_1$ = 7.4x10$^{-3}$, $k_2$ = 6.1x10$^{-3}$, $k_3$ = 7.5x10$^{-3}$ (unit: Tesla/volt) are the calibration factors for the three probes and $I_{1,2,3}$ is the current flowing past each probe. The current factor can thus be calculated by

$$f_{I,i} = I_i / I_T \qquad i = 1, 2, 3 \tag{5.2}$$

where $I_T$ is the total current measured by the current probe. The bigger the current factor the bigger the fraction of the total current contributing to the plasma pinch with less current left behind.

Fig.5.8(a)-(f) list the results for three kinds of working gas under positive and negative polarity operations. The following are some conclusions:

(a) For the same gas and same pressure the current factor of the positive polarity operation is higher than that of negative operation. This means the plasma focus operated at positive polarity has a higher efficiency compared to negative polarity from the point of view of energy input to pinch region.

(b) Current factor obtained by the probe which is nearer to the anode has bigger value (especially for deuterium plasma). This could indicate that the plasma sheath is dense near the centre electrode and is much more diffusive near the outer electrode.

(c) At the same radial position, neon and argon plasma have bigger current factor.

#### 5.2.2.3 Mass Loading Factor

In the axial phase the effective mass loading on the current sheath is known [162] to be considerably below that expected from the operational density. This reduced mass loading or mass-shedding effect is due primarily to the severe canting of the current sheath in the axial phase. This mass shedding factor is difficult to be measured experimentally. In this work we choose the value of mass factor combined with the experimentally measured current factor for each pressure using the computation model described in Chapter 3, such that the computed value of arrival time of the plasma sheath match the time measured by the magnetic probe signal (the peak of the $dB/dt$ signal).

The computed results are shown in Fig.5.9. We can see that the mass factor is of the order of 0.1. Pressure probing could be used directly to measure the mass factor and is suggested for future work.

#### 5.2.2.4 Profile Characteristics

The axial speed detector, located radially at the same height as the 3-MP array, was employed simultaneously to monitor the speed of the current sheath. With the information of speed and the 3-MP signals, we are able to roughly obtain the current profile at the moment when the plasma sheath sweeps through the MP.

If we assume that the plasma sheath sweeps by the 3-MP probe as a steady profile at a relatively constant velocity in the position where the MP and speed detector are located, then we can make the following analysis.

Fig.5.10 schematically illustrates the current profile and its position with respect to 3-MP probe. We can write,

$$a_1 = \tan^{-1}\frac{r_2 - r_1}{v \cdot (t_2 - t_1)}$$

$$a_2 = \tan^{-1}\frac{r_3 - r_2}{v \cdot (t_3 - t_2)}$$

$t_{1,2,3}$ is the time when the current sheath passes through the MP-1,2,3. The peaks of the $dB/dt$ signal will be taken as the time $t_{1,2,3}$. The maximum of $dB/dt$ corresponds to the maximum current density if we note that for a steady current profile ( $j_r(z')$ ) in the coordinate system staying with the current sheath moving with speed $v$ in a cylindrical system,

$$B(z_o, t) = \frac{\mu}{2\pi r_o} \int j_r(z' - z) \times 2\pi r_o dz$$

and so
$$\frac{dB}{dt} = \mu \cdot j_r(z')$$

$\tan\alpha_{1,2}$ are the averaged slopes of segments S1-S2 and S2-S3 of the current sheath (see Fig.5.10). Smaller $\alpha_{1,2}$ values mean more steeply canted current sheaths. The results are shown in Fig.5.11.

Some conclusion can be yielded from Fig.5.11. At lower working pressure the plasma sheath is more canted. This is in agreement with experimental observations by Schlieren and shadowgraphy [62]. For the same gas and same pressure the plasma sheath is more canted for the positive polarity than for the negative polarity.

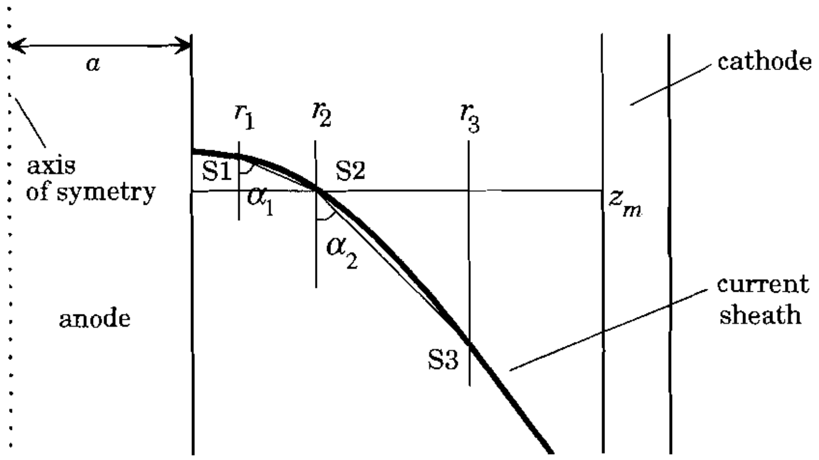


**FIGURE 5.10**
Schematic of current profile characteristics

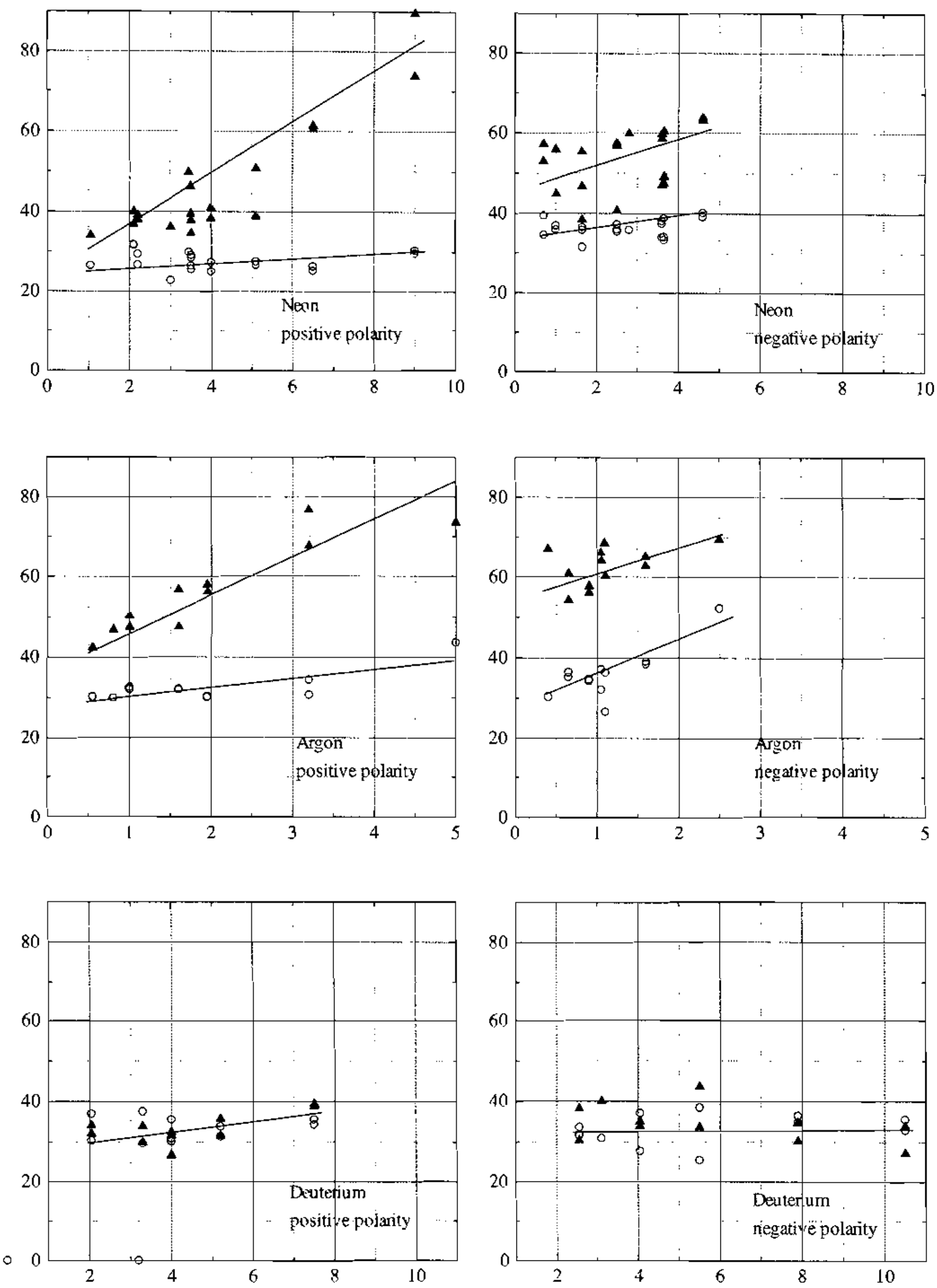


**FIGURE 5.11**
Results calculated from 3-MP probe showing
incline angles of current sheath at segments of S1-S2 and S2-S3. (Fig. 5.10)
upper triangle: angle between S1-S2 and the axis
circle: angle between S2-S3 and the axis
vertical axis: angle (degree)
horizontal axis: pressure (mbar)

### 5.2.3 Optical Probing

#### 5.2.3.1 Axial Speed Detector

The set up for monitoring the axial velocity of the plasma sheath is described in detail in Sec.4.4.3. Two light pipes were employed. This detector was developed to collaborate with the 3-MP array probes (the above section) to study the characteristics of the current profile. The results had already been presented in last section.

Fig.5.12-14 show some typical signals for different experimental conditions. We obtain the velocity for negative polarity more accurately than for positive polarity because the signals for negative polarity appear sharper. It is also found that the higher the pressure, the sharper the pulse.

With positive polarity, the rising edge is used as the arrival time, whereas in the case of negative polarity the peak points of signal may be used as the arrival times giving better accuracy.

It is best for it to be used for neon and argon plasma operated in negative polarity. At low pressure, the detector is no longer applicable because of the weak emission and also the signal is very small with respect to noise. The emission intensity of plasma, as well as the spectrum of the emission, has to be considered when selecting the photodiodes to be used. In this work BPX65 photodiodes were used.

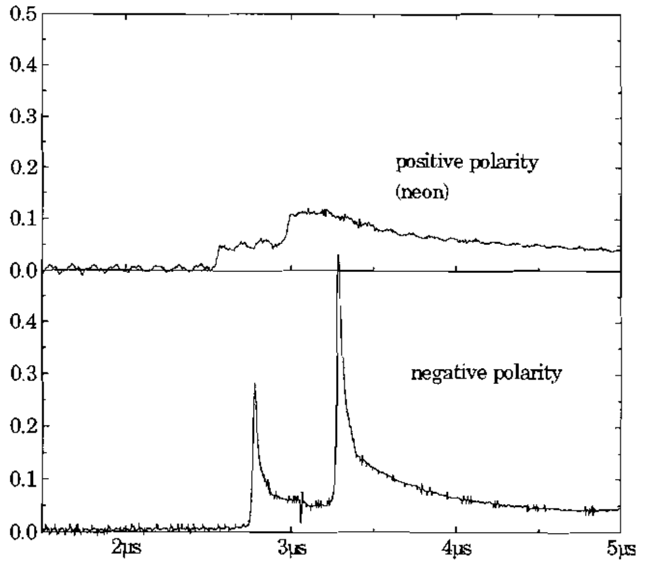


**FIGURE 5.12**
Signals of speed detector for neon plasma with same pressure for different polarities

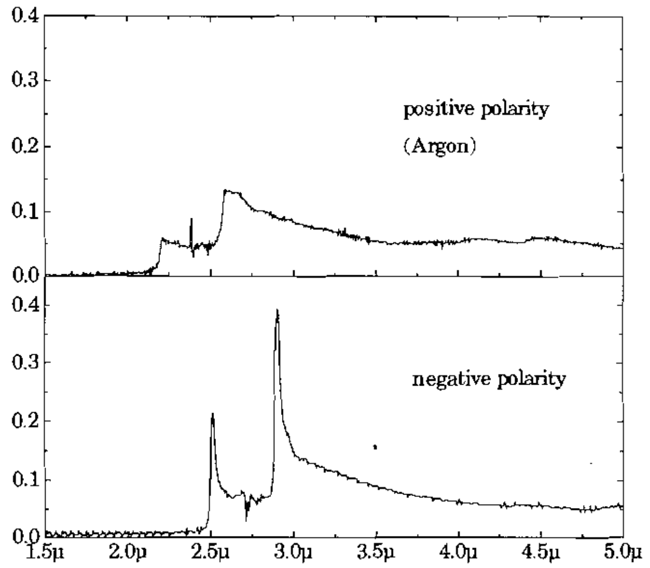


**FIGURE 5.13**
Signals of speed detector for argon plasma with same pressure for different polarities

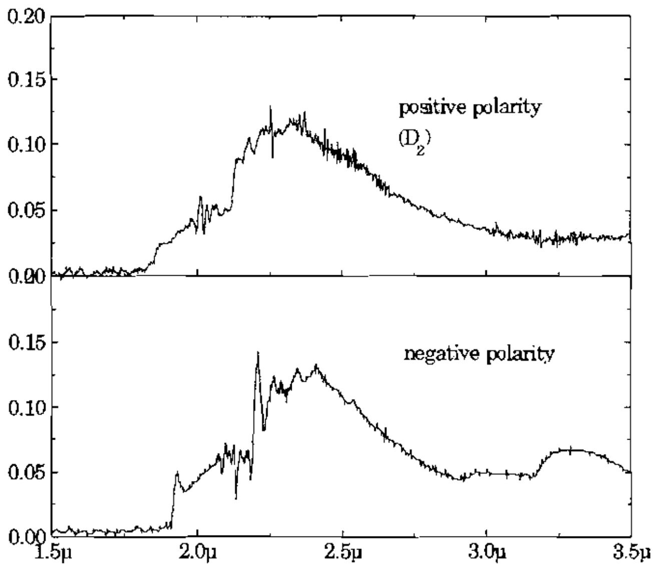


**FIGURE 5.14**
Signals of speed detector for deuterium plasma with same pressure for different polarities

#### 5.2.3.2 Measurements with 8-light pipes

*Comparison of experimental results with numerical simulation*

The set up of the 8-light pipe detector is introduced in detail in Chapter 4, Sec.4.4.2. Fig.5.15 is the light-pipe signal of a typical shot. From Fig.5.15 we can obtain the positions of the plasma sheet and thus the velocities. The results are plotted in Fig.5.16. A computational dynamic model developed by Lee (see Chapter 3) has been applied to calculate the $v$-$t$ trajectory using the same experimental parameters of gas pressure, charging voltage, electrode sizes, etc. The theoretical curve of $v$-$t$ is also shown in Fig.5.16 for comparison. We can see that the experimental results are in good agreement with the computational model.

Another conclusion we can extract from Fig.5.15 is that the signals of pipes which are located at $z$ = 4.5 cm, 6 cm, 7.5 cm are either very weak or "diffusive" relative to those located further away than these 3 pipes from the bottom plate of the electrodes, which indicates that the plasma sheet becomes steady only after it has traversed approximately the first 8 cm of the anode (i.e. about half way along the PF). This phenomenon was observed for a wide pressure range for this plasma focus.

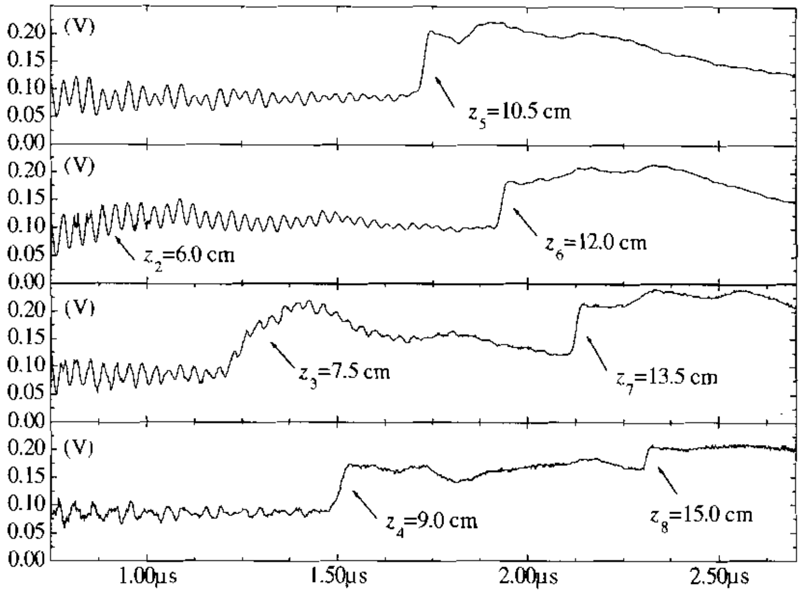


**FIGURE 5.15**
Traces monitored by optical detector made of 8 light-pipes

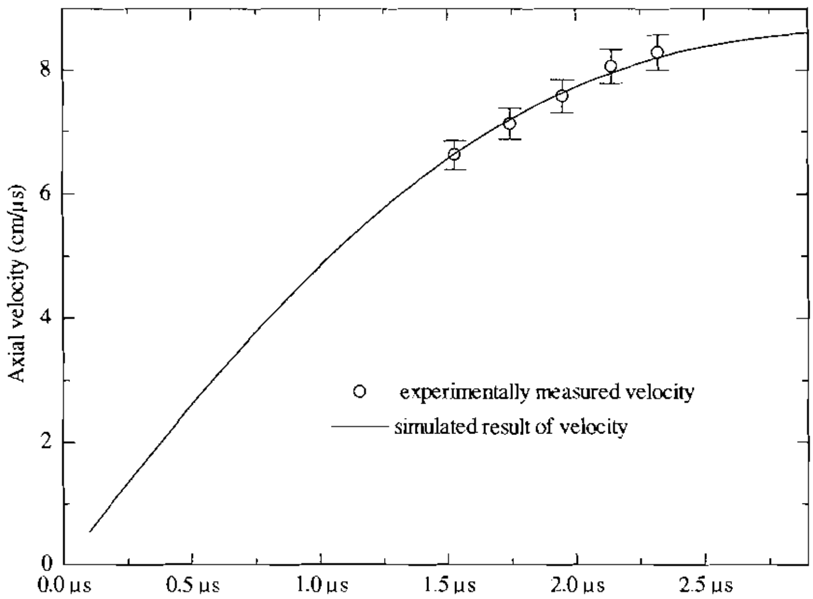


**FIGURE 5.16**
Speed measured by the optical probe (see Fig.5.16) and comparison with numerical simulation (with $f_m$ = 0.1, $f_i$ = 0.68, Pressure: 3.45 mbar and charging voltage: 13.5 kV)

## 5.3 X-ray Observations

Having studied the plasma dynamics, this work proceeds to soft x-ray measurements.

### 5.3.1 X-ray Time Integrated Pinhole Photography

Integral measurements of x-ray emissions were made with a pinhole camera which records the soft X-radiation on Kodak TMG/RA-1 film. Radiations from plasmas with deuterium, argon and neon as working gases were found to be sufficient to expose the film on a single shot basis.

X-ray pinhole images were collected with both end-on and side-on viewing to determine the dimensions of the plasma emission. The images were micro-densitometered and computer analysed to give the detailed contour of the image. For single discharges, the end-on x-ray images were nearly circular with weak lobe structure (see Fig.5.17). The size of the emission was determined from the half-maximum values of orthogonal lineouts of the image intensities. For the image shown, equal half-maximum value of 300 micron were found while other images ranged from 280 to 360 micron in diameter.

Images from multiple shots were also nearly circular with diameters varying to about 750 micron for images of 7 shots (see Fig.5.18). From Fig.5.18 it is seen that the anode rim is visible as a bright circle coaxially surrounding the radiating pinch. This could be due to electron bombardment of the anode.

Both end-on and side-on images were processed for one sequence. The side-on image of plasma emission had the appearance of a thin column with a 6 - 8 mm length (see Fig.5.19-20). The diameter of the column was estimated using transverse lineouts along the emission image. For multi-discharge exposure (Fig.5.21) the diameter was < 700 micron on average. All the images of the DPF discharges indicate that the plasma emission is centred at the axis.

For neon plasma focus we can summarize the results for this machine as following,

1. The size of SXR source viewing axially from the top is about 0.3 mm in diameter for a single discharge;

2. The focusing column is located at the axis of symmetry the electrodes. The length of the column is 6 - 8 mm;

3. The radial position of the focus is not stable, but the radial shift is within 0.2 mm. The diameter of the column exposed for 7 discharges is 0.7 mm.

4. Bright spots were observed. For lower pressure (with the same charging voltage) the spots tend to assume a cylindrical shape (we may also call it a hot-spot which has a large aspect "length-to-radius" ratio). In the case of higher pressure, more point-like spots, i.e. with aspect ratio close to 1, were observed.

A typical pinhole image for argon plasma is also shown in Fig.5.22. Hot spots of dia. of 100 - 300 μm and aspect ratio of 1 to 5 were observed for argon plasma. The resolution is limited by the pinhole size.

The gross dimension of the source measured by the pinhole camera agrees with the radiative plasma focus model, although the hot spots can not be predicted by the simple model.

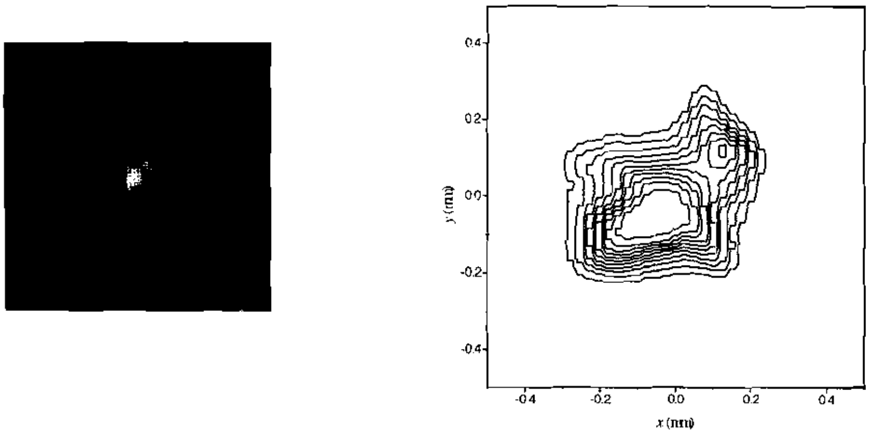


**FIGURE 5.17**
End-on pinhole image for single discharge
and its equi-density contour
conditions: 13 kV, 3 mbar neon

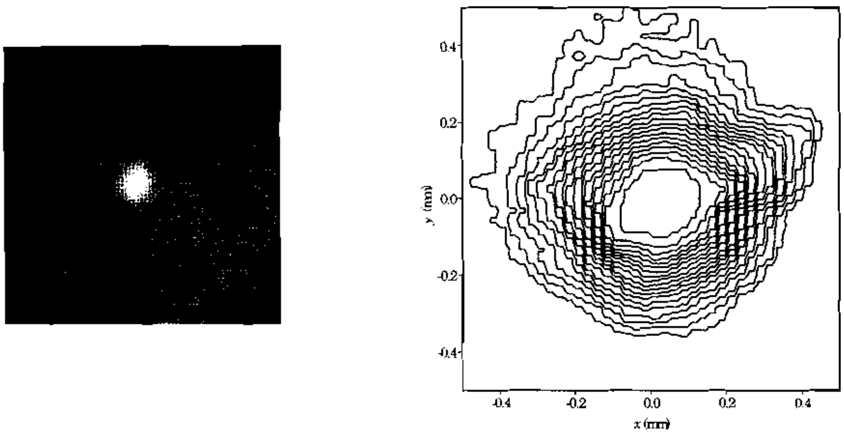


**FIGURE 5.18**
End-on pinhole image
for 7 discharge
and its equi-density contour
conditions: 13 kV, 2.9 mbar neon

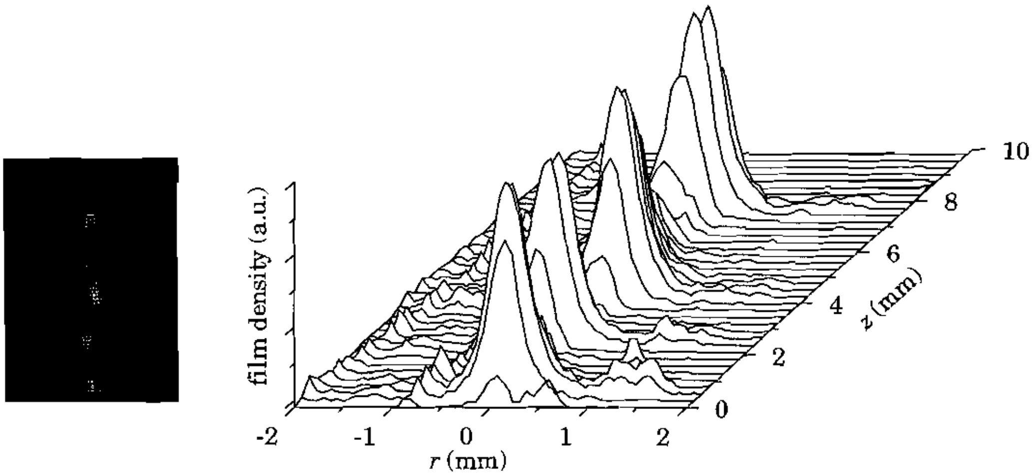


**FIGURE 5.19**
Side-on pinhole image for single discharge and its 3D view showing several hot spots
conditions: 13 kV, 4.1 mbar neon

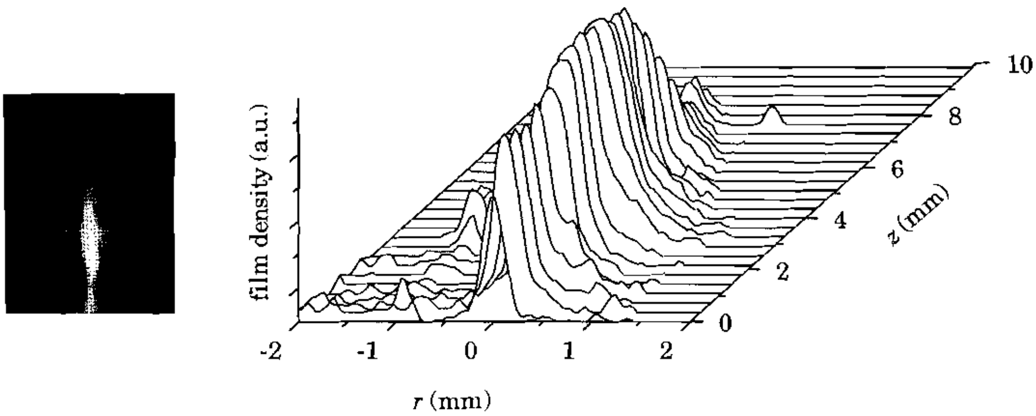


**FIGURE 5.20**
Side-on pinhole image for single discharge and its 3D view showing one uniform column
conditions: 13 kV, 2 mbar neon

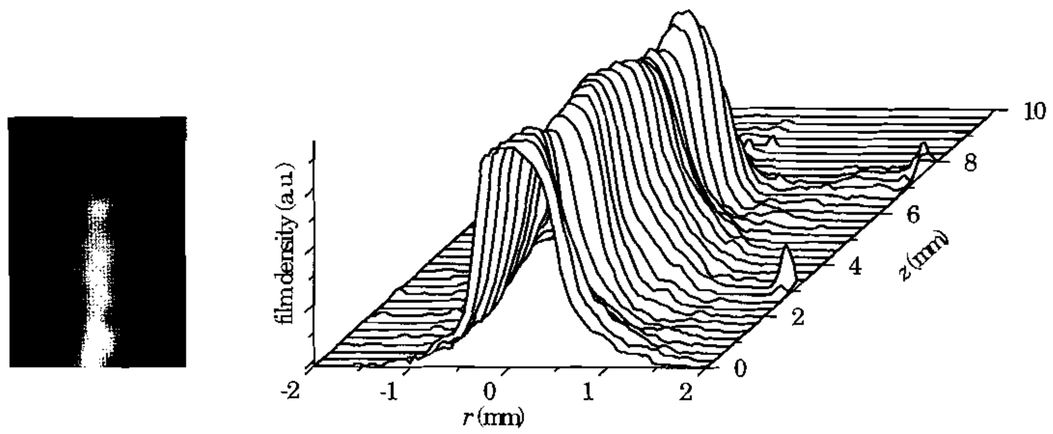


**FIGURE 5.21**
Side-on pinhole image for 7 discharge and its 3D view showing bigger diameter than single exposure conditions: 13 kV, 2.5 mbar neon

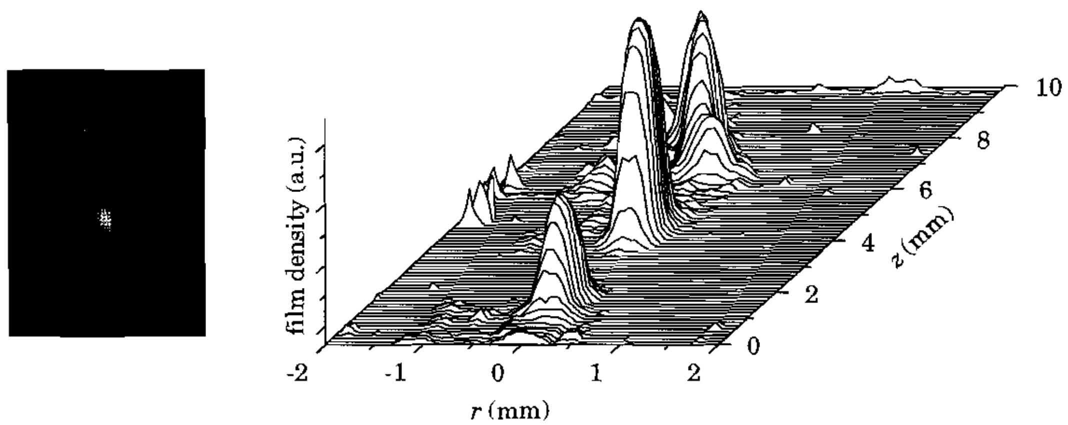


**FIGURE 5.22**
Hot spots observed in argon plasma viewed side-on conditions: 13.5 kV, 0.9 mbar argon.

## 5.3.2 Pinhole Transmission Grating Spectrography

### 5.3.2.1 Experimental Conditions

Two experiments were done in the Laser produced plasma (LPP) and compact plasma focus (CPF) as shown in Fig.5.23. LPP experiment was carried out on the Nd-glass laser facility. The laser beam was focused onto the flat surface of an Au (or Al) target with an aspheric lens. The resulting size of the focal spot had a diameter of 80 μm. The 1.064 μm laser light had a FWHM of 1 ns, with output energy of 5J, and corresponding power density on the target is $4x10^{13}$ W/cm$^2$. The detailed LPP device was described in Ref. [139].

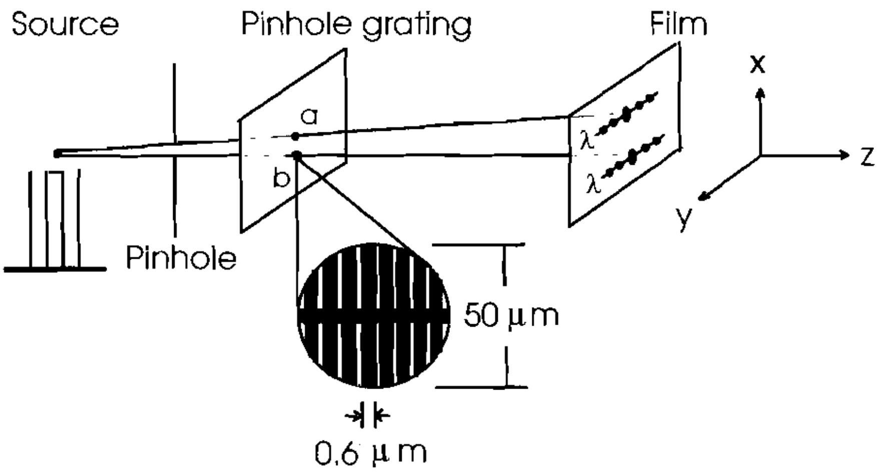


**FIGURE 5.23**
Schematic diagram of x-ray experiment with two pinhole gratings (symbol *a* and *b* ) spectrograph

### 5.3.2.2 Experimental data and results

The pinhole transmission grating spectrograph (PTGS) developed in this work has been described in Sec.4.6.2. It enables us to study a wide range of soft x-ray emission characteristics both in LPP and CPF systems. Moreover the PTGS has two-dimension spatial resolution and the position of the detector is very flexible. A PTGS can be installed with two pieces of pinhole gratings as seen in Fig.5.23.

The plasma x-ray sources produced by laser or PF are quite different. In general, the emission of soft x-ray from a LPP is very bright and the diameter of the source is very small. PF are characterized by high intensity, column-like source (viewed side-on) and wide spectral emission range. Viewed end-on it approximates a spot source but with a fairly large diameter. Those properties of the plasma source demand that our PTG spectrograph must have a flexible adjustment system. Moreover there is a strong shock wave resulting from the intense plasma compression. The spectrograph was designed to accommodate this strong shock.

A typical x-ray spectrum of the laser plasma x-ray emission obtained by a PTGS with a diameter of 50 μm is shown in Fig.5.24(a). The photo or spectrogram from the same LPP source using a 25 μm PTGS taken at the same time is shown in Fig.5.24(b).

Generally the x-ray energy transmitted by a PTGS with diameter of 50 μm is larger than that transmitted through a small diameter PTGS. The intensity of N-band spectrum in Fig.5.24(a) is more than two times stronger than that in Fig.5.24(b), and it is impossible to record P-band spectral emission from LPP in Fig.5.24(b). The full width half maximum (FWHM) $\Delta\lambda$ of O-band and N-band spectra in Fig.(a) is also larger than that in Fig.(b). The interesting observation is that the 0th-order diffraction obtained by the two different PTG spectrographs have almost the same intensity. Following Chaker's and Shnopper's methods on spectral data process [140,163,164], we obtain the real distributions of x-ray spectral lines emitted from the LPP.

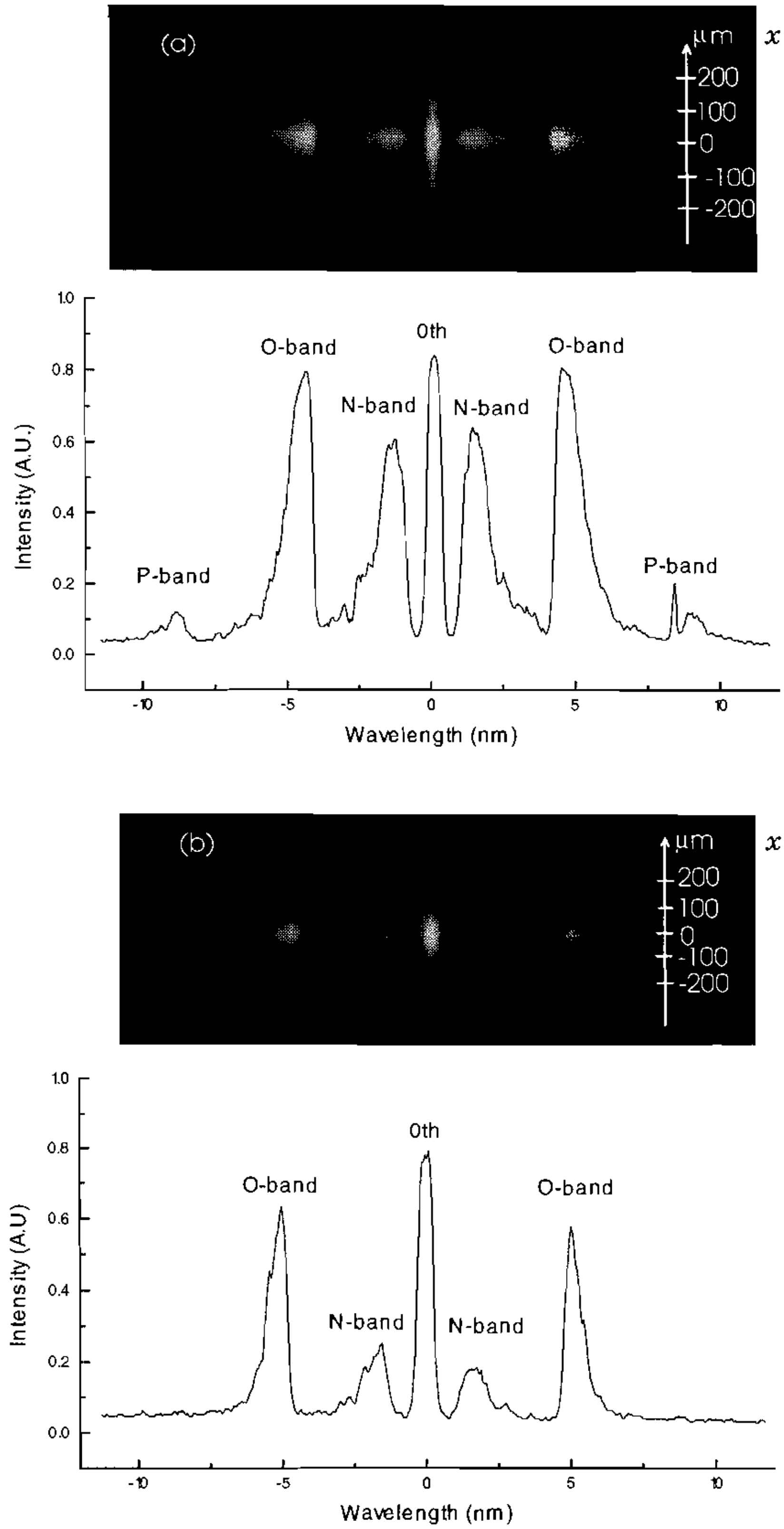


**FIGURE 5.24**
x-ray spectra from LPP emission and their microdensitometer tracings of the spectrograms at $x$=0. (a) the diameter of PTG: $D_1$=50$\mu m$; (b) $D_2$=25$\mu m$.

Using the PTGS the spatial structures of the plasma and the spectral lines with different intensity distributions were obtained. Fig.5.25(a) and (b) present microdensitometer tracings of the spatial distributions of the 0th-order and other spectral bands.

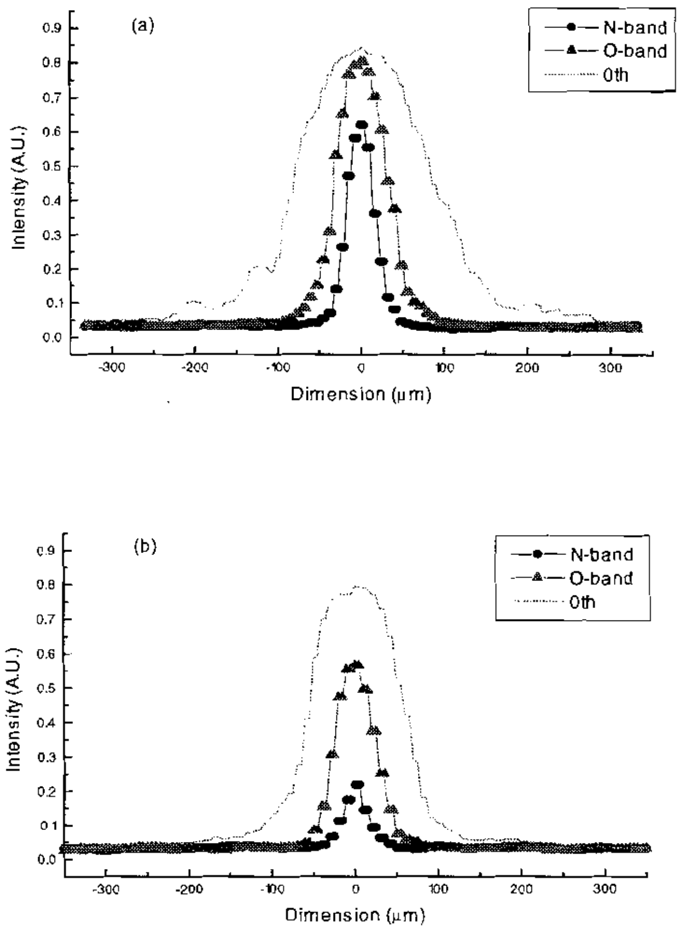


**FIGURE 5.25**
(a) and (b), The spatial distributions of the x-ray intensities for LPP, obtained from the curves in Fig.5.24(a) and (b).

It is very easy to align and take various images of sources and x-ray spectra from LPP with PTGS. However, there are quite different characteristics in the PF experiment with PTGS. The first factor is the very strong shock wave and the second is a big size of x-ray source [165], we installed a shock protection pinhole in front of the PTGS to minimize the shock wave effect. The experimental results show that the shock wave in PF will break our PTG if we choose a shock protection pinhole with a diameter of 4 mm or bigger. We cannot select a pinhole with too small a diameter because it will limit the region of measurement and make the system more difficult to be aligned. Furthermore, a small pinhole will also reduce the x-ray intensities to too low a level. We used a diameter of 2 mm. The third factor is that there is strong visible light in addition to the x-ray, and we have to use an Al foil to block out the visible light. The Al foil also absorb part of soft x-ray energy, particularly the extreme UV ray (wavelength 50 - 500 Å). Theoretical estimation indicates that the absorption coefficient for 30 A soft x-ray is almost 20 times more than that for 8 A x-rays if the attenuating coating is made of a 100 nm thick Formvar film plus a 400 nm thick aluminum film [139]. With this film in place we two or three pulses of x-ray radiation from PF for recording suitable image on film.

Following a method described in Chapter 4, Sec.4.6.2, we have identified and classified those spectral lines which belongs to the electron transitions of N-, O- and P-band neon ions over wavelength ranging from 11 to 100 Å. The intensity of the O-band spectrum is the strongest and the region of that ion's expansion is the largest.

A typical example of the spectrum obtained side-on from Ne filled PF is shown in Fig.5.26. X-ray radiation mainly comes from electron transitions of K- and L-band in neon ions. It is very difficult to identify a single spectral line in Fig.5.26. Comparing with our soft x-ray results obtained by a crystal spectrograph (to be introduced in the next section), it can be deduced that K-band mainly consists of electron transitions of $1s$-$np$ lines from H-like ion and $1s^2$-$1s2p$ lines from He-like ion, L-band mainly consists of the lines of the electron transition from Li-like neon ion. In Fig.5.29, we find two lines which we mark by symbols "*a*" and "*b*". The line $\lambda_a$ may be the 2nd-order diffraction of K-band because $\lambda_a = 2\lambda_{K\text{-band}}$. For $\lambda_b$ mainly comes from emission from impurity ions.

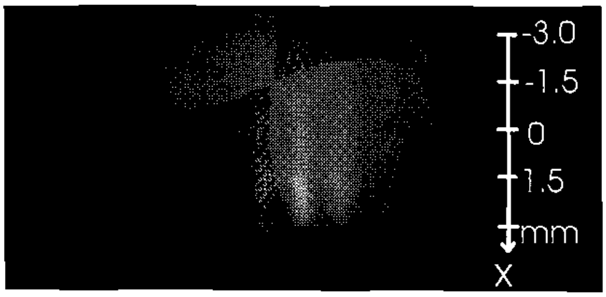


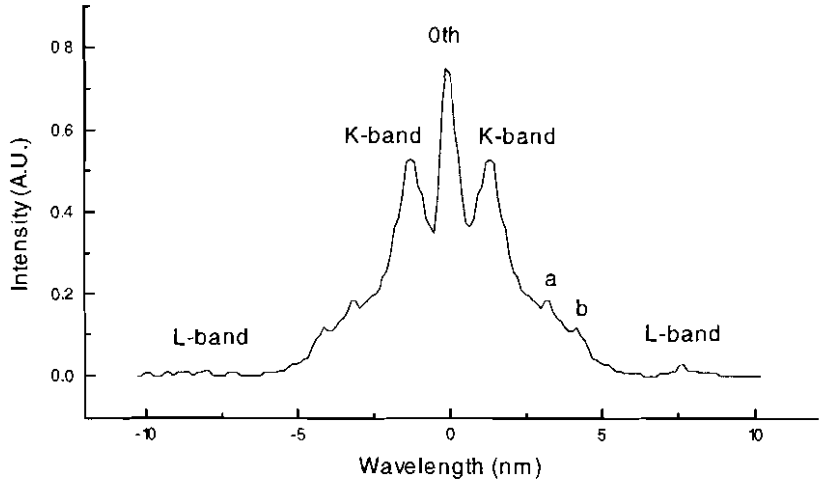


**FIGURE 5.26**
Side-on x-ray spectrum emitted from PF and its microdensitometer tracing at $x$ = 1.5 mm. The diameter of the PTG is $D$ = 50 $\mu m$.

Comparing the results for the LPP (Fig.5.24) and the PF (Fig.5.26) it is seen that the resolution and spectral overlap for the PTGS image of the PF are inferior. This is because of the big plasma source in PF. The diameter of the plasma x-ray source is estimated to be 300 μm for single discharge.

Fig.5.27 shows the spatial distributions of 0th-order diffraction spectrum and K-band intensities scanned along the $x$-axis. The image of plasma emission is a thin column of 7 mm length. The spatial distribution of intensity shows a non-uniform structure. This structure, in fact, is mainly due to a cloud of the plasma situated within the space in between the electrodes with several localized bright spots.

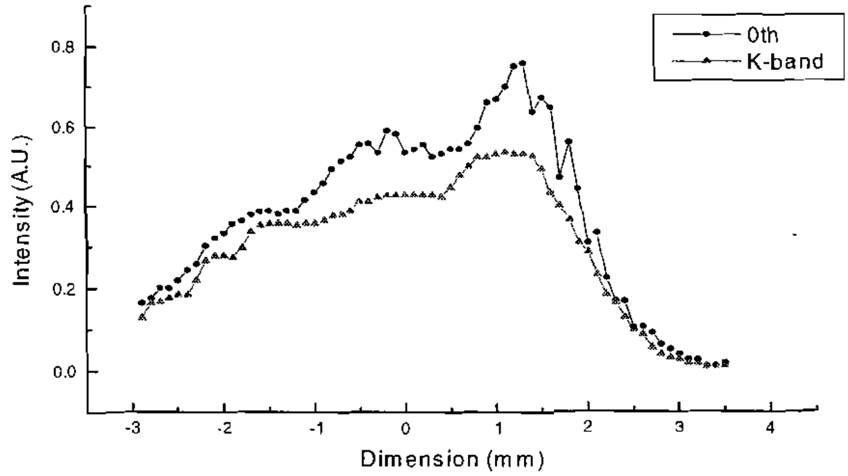


**FIGURE 5.27**
Spatial distributions of PF x-ray intensities, scanned from Fig.5.26.

A similar study of the plasma soft x-ray emission features from Ar filled PF was also made. We also observed a few clear spectral lines. The strongest band of soft x-ray emission is localized at the wavelength of 27 Å region. Based on the empirical isoelectronic extrapolation or interpolation, we identify those lines to be L-band emission from Ar ions.

### 5.3.2.3 Summary

A pinhole transmission grating spectrograph for soft x-ray measurements was designed for use in the LPP and the PF. This spectrograph provides two-dimension spatial resolution simultaneously with spectrum over 3 - 300 Å wavelength range.

The PTGS is used to measure spectra emitted from LPP. However owing to strong shock wave and big size source in the PF experiment, an additional pinhole has to be introduced. Two or three pulses of x-ray radiation from PF are needed for an exposure.

### 5.3.3 Flat Crystal Spectrography

#### 5.3.3.1 General

A transmission grating spectrograph is used to obtain spectra of wide wavelength range but with rather limited resolution (a few Å), mainly to check the overall spectrum of the emission as a preliminary step. In fact, the spectral region of interest is within 5 Å to 15 Å if neon gas is used for the purpose of x-ray lithography. A flat crystal spectrograph (described in Sec.4.6.3) is then used to achieve better resolution. Five configurations are tested to give satisfactory results.

For these five configurations (FCS-A ~ E, listed in Tab.4.4), FCS-A was mainly for preliminary test of the spectrograph and FCS-D was devoted to argon plasma. We found that argon plasma focus is a very weak emitter of soft x-ray and thus difficult to be recorded, unless a slit of bigger gap is used unfortunately with reduced spatial resolution. With neon this problem of intensity does not exist. Neon focus has sufficient intensity.

Before further descriptions of the results we list in Tab.5.2 - 4 the spectral lines, recombination continua range and satellite lines of the highly ionized neon plasma in the soft x-ray region taken from Ref. [166].

***Table 5.2*** Classification of x-ray emission spectral lines of a highly ionized neon plasma.

| no | ions | transition | terms | wavelength (A) |
|---|---|---|---|---|
| 1 | Ne IX | $1s^2$ - 1s2p | $g^1S$ - $^1P^0$ | 13.447 |
| 2 | Ne X | 1s - 2p | $g^2S$ - $^2P^0$ | 12.132 |
| 3 | Ne IX | $1s^2$ - 1s3p | $g^1S$ - $^3P^0$<br>$g^1S$ - $^1P^0$ | 11.568<br>11.544 |
| 4 | Ne IX | $1s^2$ - 1s4p | $g^1S$ - $^3P^0$<br>$g^1S$ - $^1P^0$ | 11.008<br>11.001 |
| 5 | Ne IX | $1s^2$ - 1s5p | $g^1S$ - $^1P^0$ | 10.765 |

| | | | | |
|---|---|---|---|---|
| 6 | Ne IX | $1s^2$ - 1s6p | $g^1S$ - $^1P^0$ | 10.646 |
| 7 | Ne X | 1s - 3p | $g^2S$ - $^2P^0$<br>$g^2S$ - $^2P^0$ | 10.240<br>10.238 |
| 8 | Ne X | 1s - 4p | $g^2S$ - $^2P^0$ | 9.708 |
| 9 | Ne X | 1s - 5p | $g^2S$ - $^2P^0$ | 9.481 |
| 10 | Ne X | 1s - 6p | $g^2S$ - $^2P^0$ | 9.362 |

***Table 5.3*** Recombination continua of hydrgen-like, helium-like and lithium-like ions for neon

| Ions | Spectral Limit (Å) |
|---|---|
| Ne X | < 9.126 |
| Ne IX | < 10.4 |
| Ne XIII | < 52 |

***Table 5.4*** Satellite lines of neon plasma

| no | ions | transition | terms | wavelength (Å) |
|---|---|---|---|---|
| a | Ne IX | 1s2p - $2p^2$ | $1P^0$ - 1D | 12.355 |
| b | Ne IX | 1s2p - $2p^2$ | $3P^0$ - 3P | 12.323 |
| c | Ne IX | 1s2p - 2s2p | 3S - $3P^0$ | 12.308 |
| d | Ne IX | 1s2p - 2s2p | 1S - $1P^0$ | 12.26 |
| e | Ne IX | 1s2p - $2p^2$ | $1P^0$ - 1S | 12.172 |

### 5.3.3.2 Evaluation of Plasma parameters - General Consideration

*Determination of $T_e$ from intensity ratios in line spectra*

Using coronal equilibrium model (Eqns.(3.12- 13) ) and Eqns.(3.3- 4) we have,

$$P_{l,n} = h\nu_n \frac{A_{n1}}{\sum_{m<n} A_{nm}} N_e N_z C_{1n} \tag{5.5}$$

The ratio of $\frac{A_{n1}}{\sum_{m<n} A_{nm}}$ is equal to unity for the resonance lines. $C_{1n}$ is obtained by Eqn.(3.13). We may write the radiation power for the four lines of our interest as,

$$P_{Ly_\alpha} = h\nu_{Ly_\alpha} \frac{A_{2p-1s}}{A_{2p-1s}} N_e N_9 C_{1s-2p}$$
$$= \frac{e<g>f_{1s-2p}}{T_{eV}^{1/2}} N_e N_9 \exp\left(-\frac{h\nu_{Ly_\alpha}}{T_{eV}}\right)$$
$$= 2.13 \times 10^{-31} T_{eV}^{-1/2} N_e N_9 \exp(-1024.7/T_{eV}) \tag{5.6}$$

Following the same procedure we obtain,

$$P_{Ly_\beta} = 4.05 \times 10^{-32} T_{eV}^{-1/2} N_e N_9 \exp(-1214.1/T_{eV}) \tag{5.7}$$

$$P_{He_\alpha} = 1.31 \times 10^{-31} T_{eV}^{-1/2} N_e N_8 \exp(-924.5/T_{eV}) \tag{5.8}$$

$$P_{He_\beta} = 3.3 \times 10^{-32} T_{eV}^{-1/2} N_e N_8 \exp(-1075.3/T_{eV}) \tag{5.9}$$

From Eqn.(3.16) we have,

$$N_9 = 0.874 \times T_{eV}^{3/4} \exp(-1196/T_{eV}) \cdot N_8 \tag{5.10}$$

From above equations one can see intensity ratio between any two of these four lines may be used to determine the temperature. Usually we adopt the following three ratios for our case,

$$\frac{P_{Ly_\alpha}}{P_{Ly_\beta}} = 5.26 \times \exp\left(\frac{189.4}{T_{eV}}\right) \tag{5.11}$$

$$\frac{P_{He_\alpha}}{P_{He_\beta}} = 3.97 \times \exp\left(\frac{150.8}{T_{eV}}\right) \tag{5.12}$$

$$\frac{P_{Ly_\alpha}}{P_{He_\alpha}} = 1.42 \times T_{eV}^{3/4} \exp\left(-\frac{1296}{T_{eV}}\right) \tag{5.13}$$

These three ratios vs. $T_e$ are plotted in Fig.5.28.

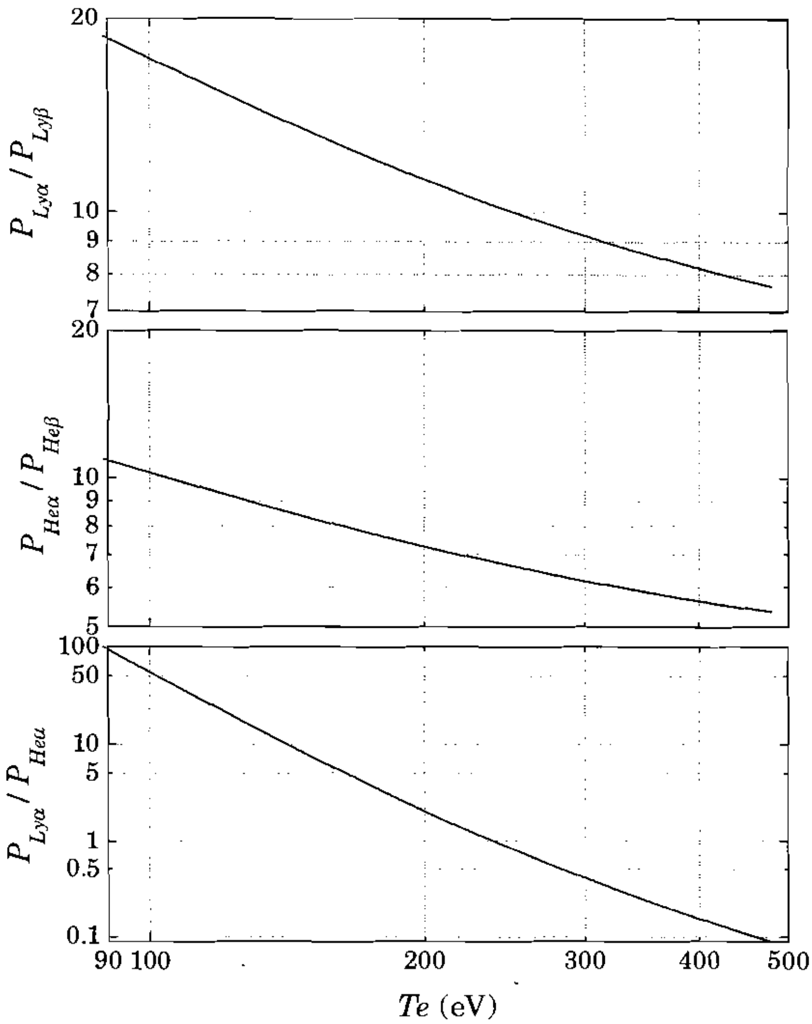


**FIGURE 5.28**
Relative line intensity ratios versus electron temperature
(for coronal plasma)

<u>*Determination of Te by continua*</u>

From Eqn.(3.1 - 2) it is noted that both Bremsstrahlung and recombination emission power are proportional to exp($-h\nu/T_{eV}$). Generally we may write the continuum spectrum part as,

$$P_{con} = G\exp\left(-\frac{h\nu}{T_{eV}}\right) \qquad (5.14)$$

taking logarithm of this expression gives,

$$\log(P_{con}) = \log G - \frac{1}{T_{eV}}h\nu \qquad (5.15)$$

so it can be seen clearly that $1/T_{eV}$ is the slope of $\log(P_{con})$~$h\nu$ curve.

*Estimation of electron density*

Because of limitations resulted from the source broadening, some means of $N_e$ determination can not be used. But for "hot spots", which are small in size (diameter), we may still be able to apply some methods to make an estimation.

For neon the plasma density could be determined from the density-sensitive dielectronic Ne IX $2l2l'$ satellite line to Lyman alpha at 12.323 Å, based on the theoretical predictions by Seely [167]. In this work estimations were done for several cases at which the focusing column was rather small (hot spot areas) so that the resolution was relatively high (note that the resolution of the this spectrograph is mainly limited by the source broadening).

Another method is the use made of the lowering of ionization potential based on the plasma field modelling of Sewart and Pyatt [168]. This method needs very high spectrum resolution since the potential lowering is of the order of 10 eV. It was not used in this work.

### 5.3.3.3 Observations with Spectrograph FCS-B

*Introduction*

FCS-B is devoted to the longer wavelength portion of the spectrum region of our interest. Strong line emission is in this regime. Pinhole imaging is simultaneously employed with the image formed at the short wavelength side to the whole spectrum being measured. $f(\lambda) \cdot G(\lambda) \sim \lambda$ for this configuration is evaluated and plotted in Fig.5.29. The other parameters are referred to Sec.4.6.3.

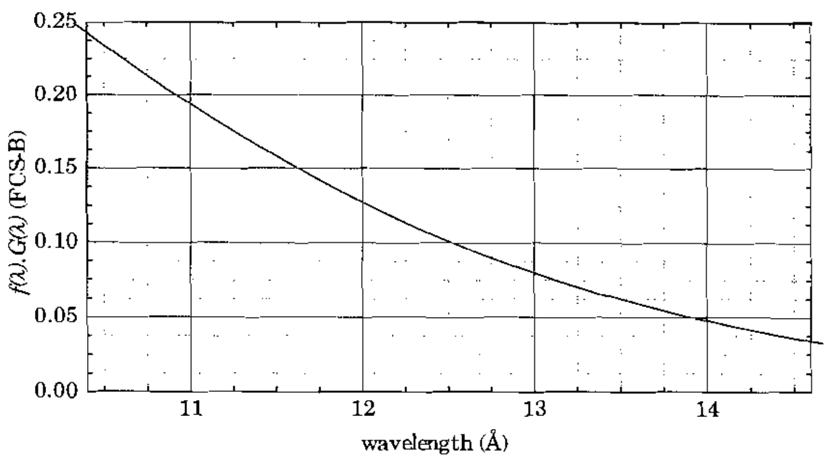


**FIGURE 5.29**
$f(\lambda).G(\lambda) \sim \lambda$ curve for configuration FCS-B

*Example*

An example of the spectra (symbol 1 - 5) and x-ray pinhole image (on left side, symbol 'a') obtained from the Ne gas-filled CPF using this configuration is shown in Fig.5.30. Experimental conditions are: charging voltage 13 kV, neon pressure 3.3 mbar, 5 shots superimposed. Spectral lines no.1 to no.5 can be easily identified, all exhibiting similar structure to the pinhole image (symbol 'a').

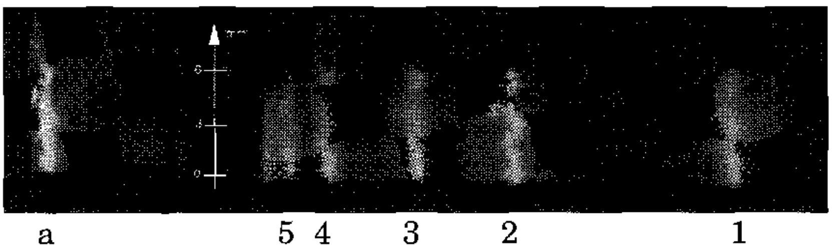


**FIGURE 5.30**
Example of the spectrum obtained from a neon gas-filled CPF using FCS-B configuration (3.3 mbar) (5 discharges)
1 - 5: spectrum lines
a: pinhole image

*Spectrum identification*

Spectral lines no.1 and no.5 (see Tab.5.2) are chosen as the reference lines, i.e. $\lambda_A$ = 13.447 Å and $\lambda_B$ = 10.765 Å for determination of spectrum using Eqn.(4.43) (see Sec.4.6.3). $L_{AB}$ is measured to be 19.69 mm, so $H^{B}_{1,5}$ = -8.214 and $F^{B}$ = - 2.39. The measured value of $F$ agrees very well with the calculated $F$ ( = - 2.41).

Fig.5.31(a) shows the microdensitometer tracing at axial position $z$ = 3 mm above the surface of the anode.

The tracings along each line (no.1 - 5) and the pinhole image are illustrated in Fig.5.32(a) and (b). It is seen more clearly now that the line spectra show similar structure to the pinhole image along axial direction.

In general, the intensity of satellite spectrum is observed to be quite weak and the spectral peak intensities from electron transition 1$s$-$np$ states of H-like ions are a few times stronger than that of He-like ion lines. The other lines are found to be much weaker than these two lines.

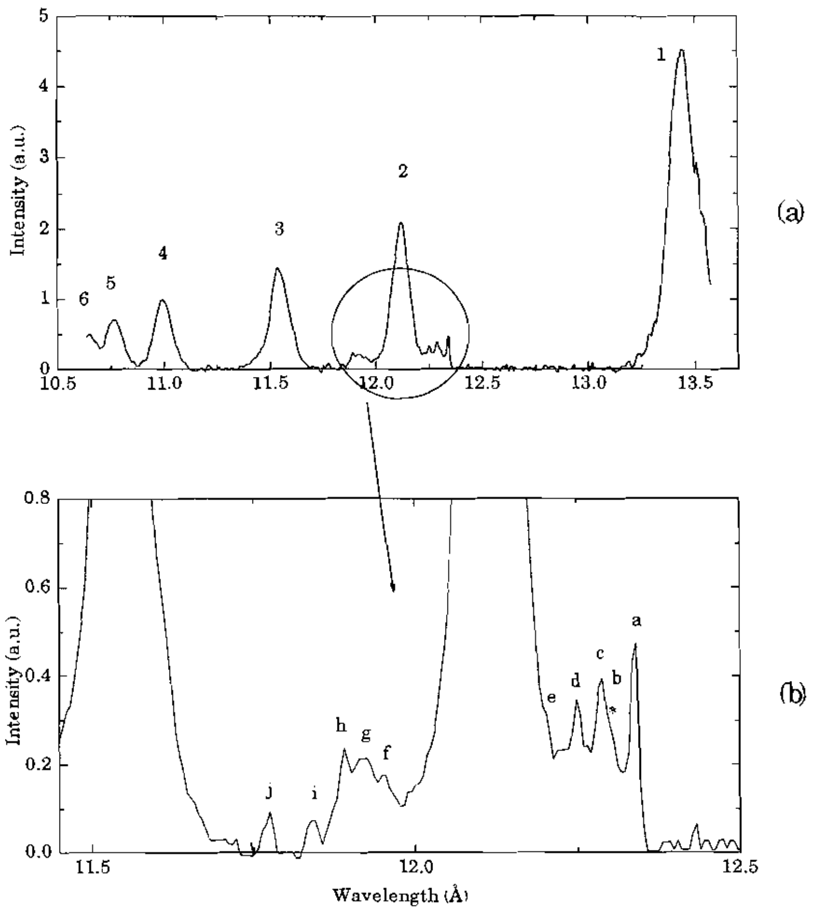


**FIGURE 5.31**
The microdensitometer tracing of x-ray emission spectrum of a highly ionized neon plasma.

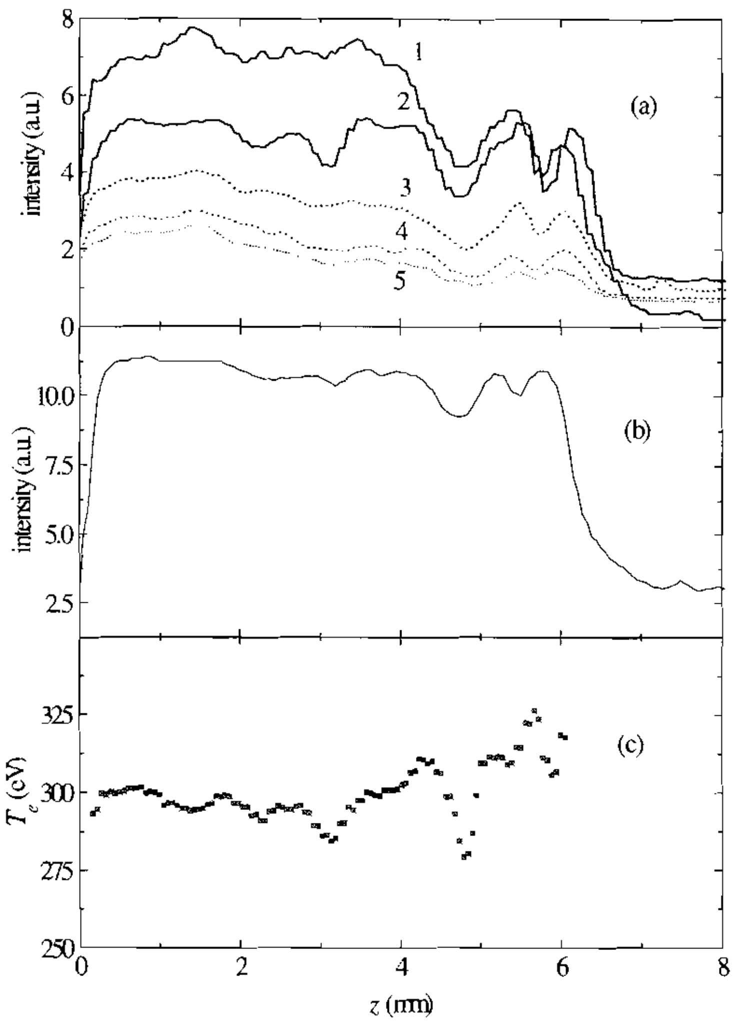


**FIGURE 5.32**
spatial resolved spectra and pinhole imaging (from Fig.5.30)
(a) spatial distribution of SXR spectral intensities
(b) lineout trace of x-ray pinhole image
(c) electron temperature (eV)

*Evaluation of plasma parameters*

The electron temperature is estimated by the relative ratio method. Comparing the experimentally measured ratios with that the theoretical ratios given in Fig.5.28, we obtain the axial space resolved value of electron temperature shown in Fig.5.32(c). We can see from this figure that the temperature in the hot spots is higher than the other place. The averaged electron temperature in the hot spots is estimated to be ~ 300±50 eV.

Using several combination spectral lines and a resonance line of 1s2-1s2p electron transition, the plasma electron density can be estimated [169]. However, the large size of the x-ray source in our CPF has caused source broadening and resulted in overlap of combination lines and resonance of $1s^2$-1s2p. For those hot spots with small size, however, the plasma density could still be determined from the density-sensitive dielectronic Ne IX *2l2l'* satellite line to Lyman alpha at 12.323 Å, based on the theoretical predictions by Seely [167]. Comparing with this model the relative intensity of the $2p^2\ ^3P_2$-$1s2p\ ^3P_2$ transition (as an example, see Fig.5.31b, a magnified portion from Fig.5.30a, indicated by an asterisk) corresponds to an electron density of ~ $10^{21}$ $cm^{-3}$ in the DPF plasma formation. The average density along the whole column may be a bit smaller than this value. This result is in agreement with theoretical modelling in Chapter 3, where $n_e > 10^{20}$ $cm^{-3}$ is estimated.

### 5.3.3.4 Observations with Spectrograph FCS-C

*Introduction*

FCS-C is devoted to the shorter wavelength portion (continuum by radiative recombination, in our case) of the spectrum region. Pinhole imaging is simultaneously employed with the image formed at the long-wavelength side to the whole spectrum being measured. $f(\lambda)\cdot G(\lambda) \sim \lambda$ curve for this configuration is evaluated and plotted in Fig.5.33. The other parameters are referred to Sec.4.6.3.

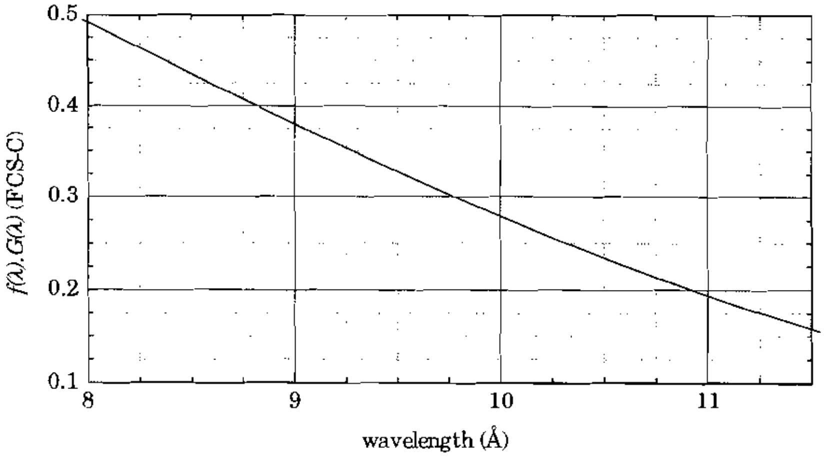


**FIGURE 5.33**
$f(\lambda).G(\lambda) \sim \lambda$ curve for configuration FCS-C

<u>*Spectrum identification*</u>

spectral lines no.4 and no.8 (see Tab.5.2) are chosen as the reference lines, i.e. $\lambda_A$ = 11.004 Å and $\lambda_B$ = 9.708 Å. (see Sec.4.6.3). $L_{AB}$ is measured to be 9.19 mm, so $H^C_{4,8}$ = -17.746 and $F$ = 0.52 mm.

The image of the CPF x-ray source shows a complex structure as seen in Fig.5.34. Spatial distribution of the soft x-ray intensities and the spectrally analyzed image are compared in Fig.5.35

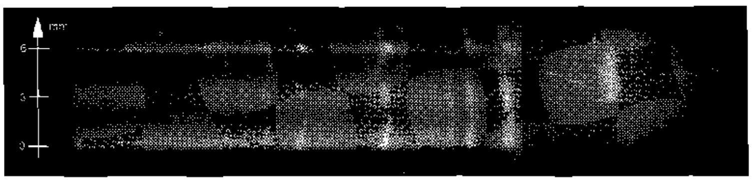


**FIGURE 5.34**
Example of the spectrum obtained from a neon gas-filled CPF using FCS-C configuration (3.2 mbar neon, single shot)
4 - 9: spectrum lines
a: pinhole image

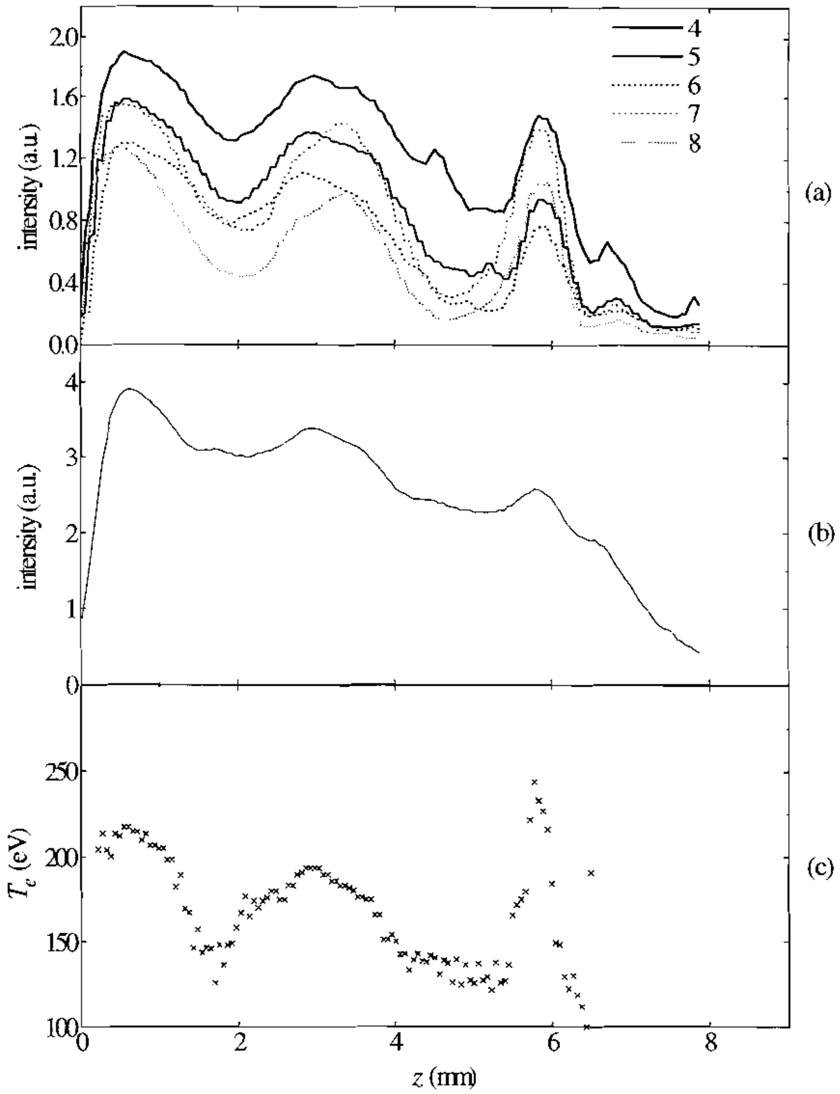


**FIGURE 5.35**
Spatial resolved spectra and pinhole imaging
(a) spatial distribution of SXR spectral intensities
(b) lineout trace of x-ray pinhole image
(c) electron temperature determined by slope of the logarithm of continua

There is a column of the plasma with several localized bright spots. These spots are circular and sharp-edged indicating that they are actually the source of x-rays. The size of each of these spots is estimated to be typically 100 mm in diameter. The side-on image of plasma emission is the appearance of a thin column with a 5.0 ~ 8.0 mm length.

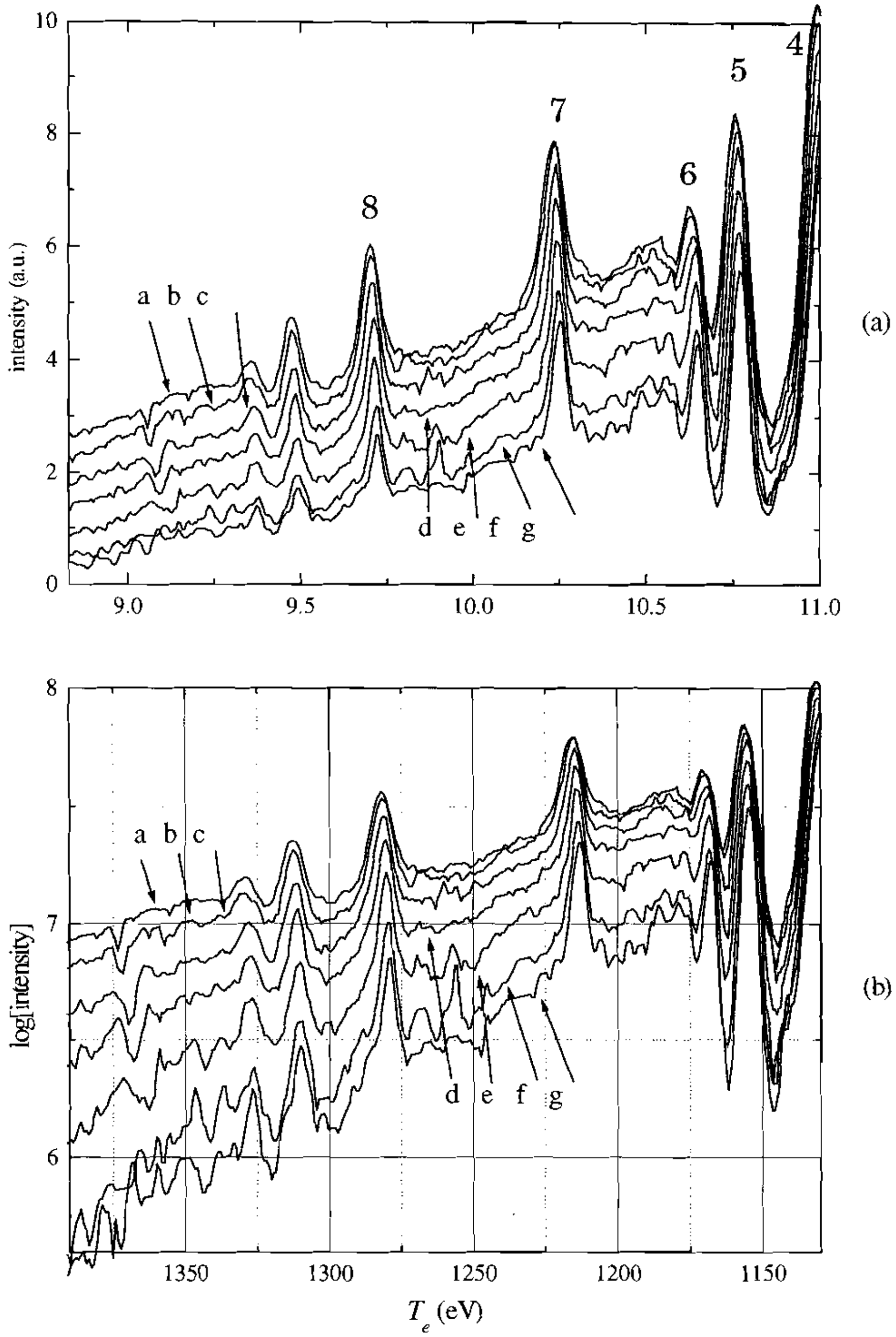


**FIGURE 5.36**
The spatial distribution of the soft x-ray spectral intensities.
(a) near the first hot spot above the anode at $z_a$ =0.45, $z_b$ =0.6 $z_c$ =0.75, $z_d$ =0.9, $z_e$ =10.5, $z_f$ =11, $z_g$ =12.5. (units: mm)
(b) logarithm of the intensities corresponding to curve Fig.(a). (note that a constant is canceled when calculating log($I$).)

*Evaluation of plasma parameters*

Besides the temperature by line intensity ratios presented above, the plasma temperature can also be determined from the logarithm intensity variation (linear slope) of the free-bound continuum (see Sec.5.3.3.2 for detail). Fig.5.36b shows the logarithm intensity versus photon energy for 7 points at the neighborhood of one of the hotspots. It is seen clearly that in the hotspot the temperature is higher than its surrounding area, noting that steeper slope corresponds to lower temperature (see Sec.5.3.3.2). In fact, a simple code was developed for this method of determining $T_e$ along the whole plasma column and the results are shown in Fig.5.35(c), where we see that the electron temperature is ~ 175±50 eV for this particular case.

### 5.3.3.5 Observations with Spectrograph FCS-E

*Introduction*

FCS-E is devoted to the spectrum region between 8 to 14 Å. Pinhole imaging is not employed because of the limitation of the room housing the spectrograph. $f(\lambda)\cdot G(\lambda) \sim \lambda$ for this configuration is evaluated and plotted in Fig.5.37. It is noted that there is a cutoff at $\lambda$ = 7.95 Å due to the absorption edge of aluminum foil. So the spectrum data for wavelength below 7.95 Å is no longer reliable, this setting a cutoff for the spectrograph (unless other foil is adopted instead of aluminum). The other parameters are referred to Sec.4.6.3.

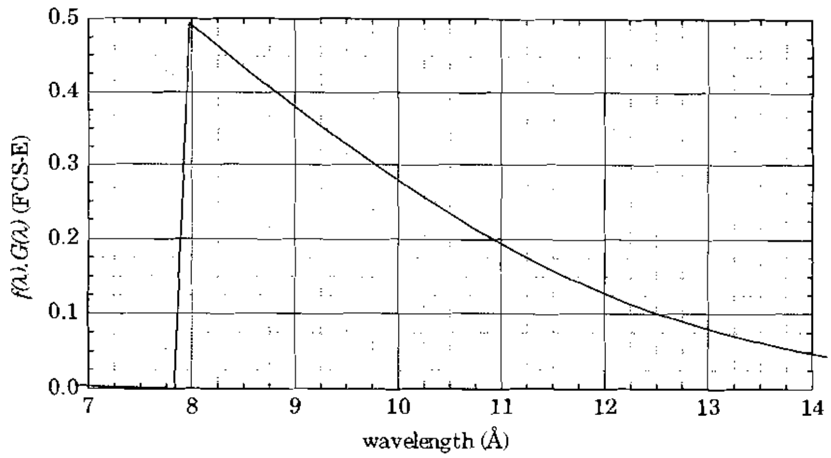


**FIGURE 5.37**
$f(\lambda).G(\lambda) \sim \lambda$ curve for configuration FCS-E

*Spectrum identification*

spectral lines no.1 and no.5 (see Tab.5.2) are chosen as the reference lines, i.e. $\lambda_A$ = 13.447 Å and $\lambda_B$ = 10.765 Å. (see Sec.4.6.3). $L_{AB}$ is measured to be 21.46 mm, so $H^E{}_{1,5}$ = - 6.842 and $F^E$ = - 3.14 mm.

*Examples*

Two typical spectra for neon plasmas are presented in Fig.5.38(a) and Fig.5.39(a). They are taken for two different operational gas pressures, one is low (1.7 mbar) and the other is relatively higher pressure of 3.85 mbar. The corresponding tracings are shown in Fig.5.38(b) and Fig.5.39(b) respectively. The tracings are the spectra of the integrated intensity along the source column (in axial direction). The x-ray emission below 8 Å is found to be very low. The spectrum is composed mainly of line radiations (Ne X and Ne IX) and the continua (Ne X and Ne IX). Using line ratio method and the decline of continuum the average electron temperatures for both cases are estimated and listed in Tab.5.5.

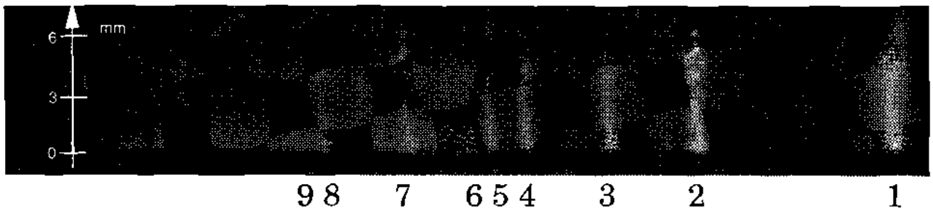


**FIGURE 5.38(a)**
Typical spectrum (1.7 mbar neon, 13 kV, single discharge)
1 - 9: spectrum lines

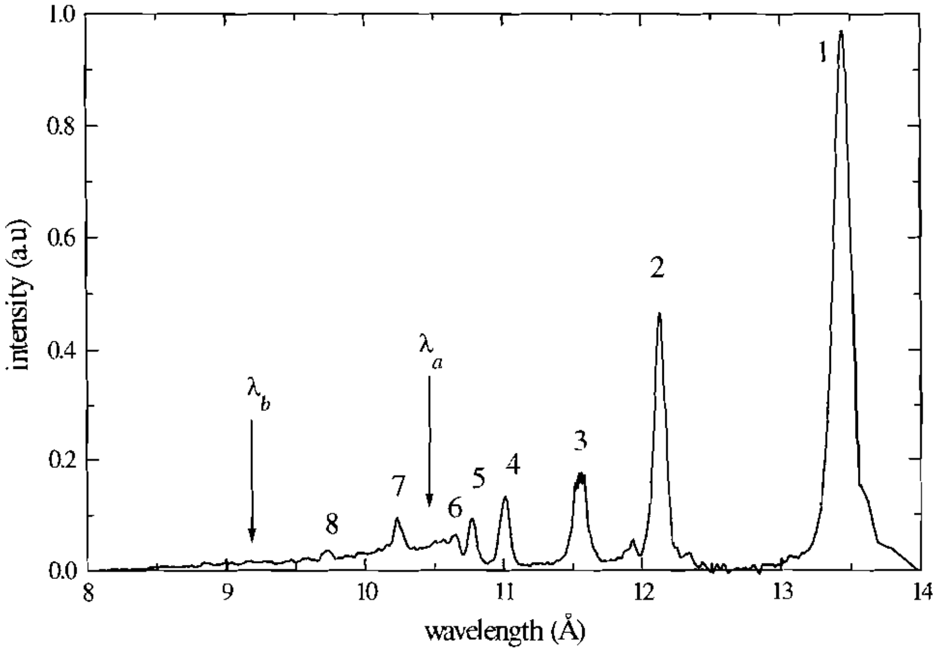


**FIGURE 5.38(b)**
X-ray emission spectrum of neon plasma
(integrated along the whole column)
at charging voltage of 13 kV, pressure of 1.7 mbar)


**FIGURE 5.39(a)**
Typical spectrum (3.85 mbar neon, 13 kV, single discharge)
1 - 9: spectrum lines

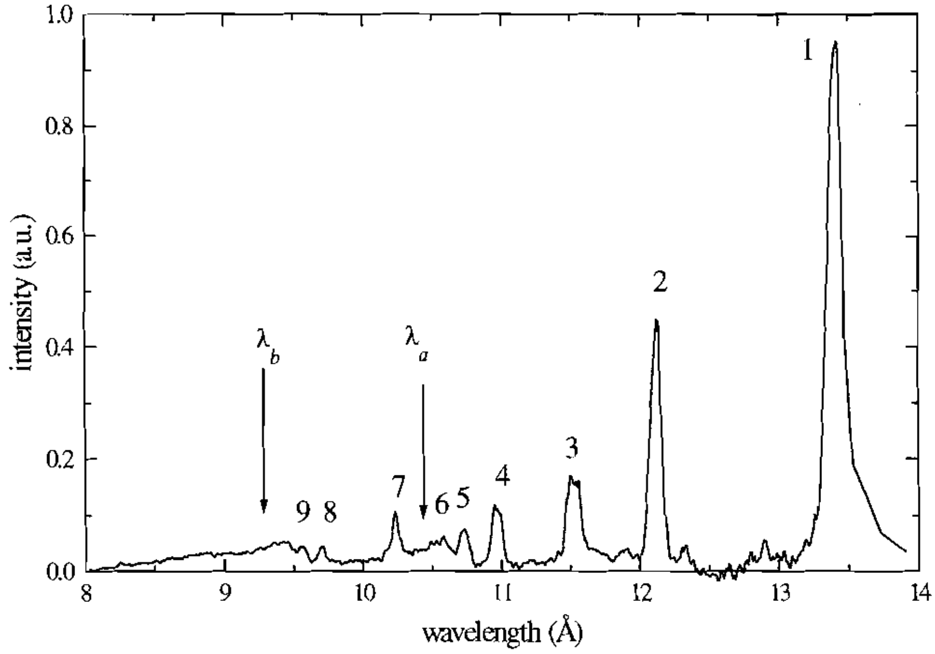


**FIGURE 5.39(b)**
X-ray emission spectrum of neon plasma
(integrated along the whole column)
at charging voltage of 13 kV, pressure of 3.85 mbar)

**Table 5.5** Plasma temperature and line radiation percentage determined from spectra of the neon plasma focus

| experimental conditions | $T_e$ (eV) | $T_e'$ (eV) | percentage of Ly-α line | percentage of He-α line |
|---|---|---|---|---|
| 1.7 mbar | ~ 300 eV | ~ 165 eV | 38% | 15.5% |
| 3.85 mbar | ~ 380 eV | ~ 200 eV | 47% | 13% |

note:

$T_e$: electron temperature by relative amplitudes of Ne IX and Ne X lines
$T_e'$: electron temperature by decline of recombination continuum

Fig.5.38 and 5.39 are only two examples. From a number of spectra (with axial space resolution) obtained at pressures varying from 1.5 mbar to 5 mbar, we can conclude that (a) at pressure higher than ~ 3 mbar (at 13 kV charging voltage) more hot spots with small aspect ratio are observed, whereas at lower pressure uniform source column (or hot spots with large aspect ratio) is more often observed; (b) the temperature is estimated to be higher for the case when very bright hot spots of small aspect ratio are observed; (c) the electron temperature is about 250 ~ 400 eV as estimated by relative line ratio method and about 160 ~ 220 eV as estimated by the decline of the logarithm of continua; and (d) the Ly-α is the most intensive line, taking 38 ~ 48% of the total radiation, the He-α line is about 2 ~ 3.5 times weaker than Ly-α line in our experiments.

#### 5.3.3.6 Summary

A new compact flat crystal spectrograph for the soft x-ray region in our plasma focus facility operated in neon was designed and examined. The design of the spectrograph makes it easy to align and use, with good spatial resolution over one dimension and a spectral range of 3 - 30 Å.

Strong soft x-ray spectral emissions from CPF are observed. High space resolution is achieved in the observation. A detailed study of the CPF parameters and structure were carried out.

At pressure higher than the optimum, the results show a complex x-ray spatial and spectral distribution. The column of plasma has several localized bright spots. The size of each of these spots was estimated to be typically 100 μm in diameter and their temperature was estimated to be ~ 350 eV. At relatively lower pressure we observe uniform plasma column more frequently with electron temperature at a lower value of just under 300 eV.

For comparison a similar study of the plasma x-ray emission from Ar-gas filled CPF was also made. We still observed a few clear spectral lines. However, the area of x-ray emitted from Ar plasma was obviously limited, and the spectral intensity is very weak.

### 5.3.4 Filtered PIN Diodes Detection

The x-ray measurements and analysis presented in the last three subsections (Sec.5.3.1, 5.3.2 and 5.3.3) all use film as recording material. It is more convenient to directly record the electrical signals which can be readily stored in computer for analyzing. In fact, scintillator combined with CCD (or MCP) may be employed instead of using film for faster and easier measurements and analysis of x-ray emission.

In this section results using a semiconductor detector are presented. We use a 5-channel detector which is capable of monitoring time-resolved x-ray emission rate with spectral resolution. We will first concentrate on its application in measuring the time evolution characteristics of x-ray emission from plasma focus. More analysis will be conducted in Sec.5.3.5 where total x-ray yield is obtained from this PIN detector as well.

#### 5.3.4.1 Characteristics of the 5-channel Detector

*Response characteristics of BPX65*

For the PIN diodes used in this detector (BPX65 type) there exists a linear response (photonic current vs. incident light intensity) region.

According to the data provided by manufacturer, the saturation current for BPX65 diode (reversly biased at 50V) is ~ 100 mA, which corresponds to measured voltage of ~5V with 50 ohm termination. A simple experimental set-up is used to determine experimentally the linear region. Two photodiodes (assumed identical) with identical beryllium filter (20 μm) are placed at different radial distances ($S_1$ = 220 mm and $S_2$ = 550 mm) from the plasma focus x-ray source (see Fig.5.40). Thus both photodiodes receive x-rays from the same source but with different intensities. The ratio of the intensities at these two positions is determined by the geometrical factor $S_2^2/S_1^2 = 6$. Fig.5.41a shows the curve of ratio between the two outputs (*PIN*-1 / *PIN*-2) detected versus *PIN*-1. It can be seen from this graph that when the signal is bigger than 4.5 V the response is no longer linear, but that PIN-1 is showing saturation effect. It is noted that the working gas will slightly vary the spectra received by the two photodiodes because of the difference of distances. The result is that the intensity ratio is varied by the gas by a factor of $f$ ~ 0.8 in this particular experiment. So the effective factor is $S_2^2/S_1^2/f = 7$ as shown in the regime of Fig.5.41 where both PIN-1 and PIN-2 are linear.

For calculation of total x-ray yield (described in next section) the integral of the PIN signal, which is proportional to the collected charge created by photons in PIN (see Sec.4.6.4.1), is more important. Fig.5.41b shows another curve of ratio of the integrals of the two signals (*PIN*-1 and *PIN*-2) versus the integral of *PIN*-1. We found that the integral or the charge is always proportional to the input intensity, at least in the intensity range of this series of calibration experiment which actually covers the range of our interest in this whole project work. Thus even when we operate with the PIN diode above its linear limit, the integral of its signal still gives a correct value as though it were not saturated. For yield measurement, depending on the integral of the signal, a saturated signal may still be used.

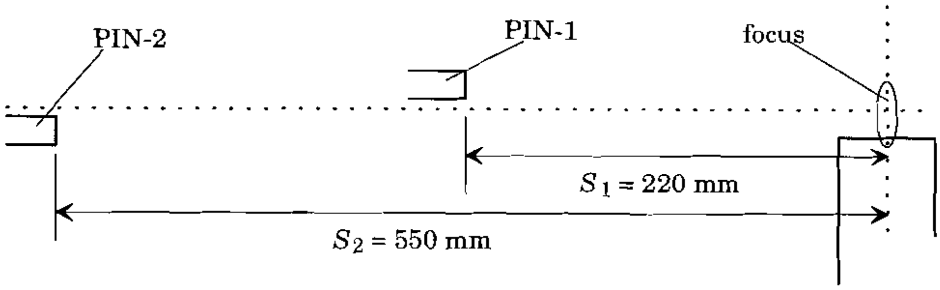


**FIGURE 5.40**
Set-up for determination of linear operating range for BPX65 PIN

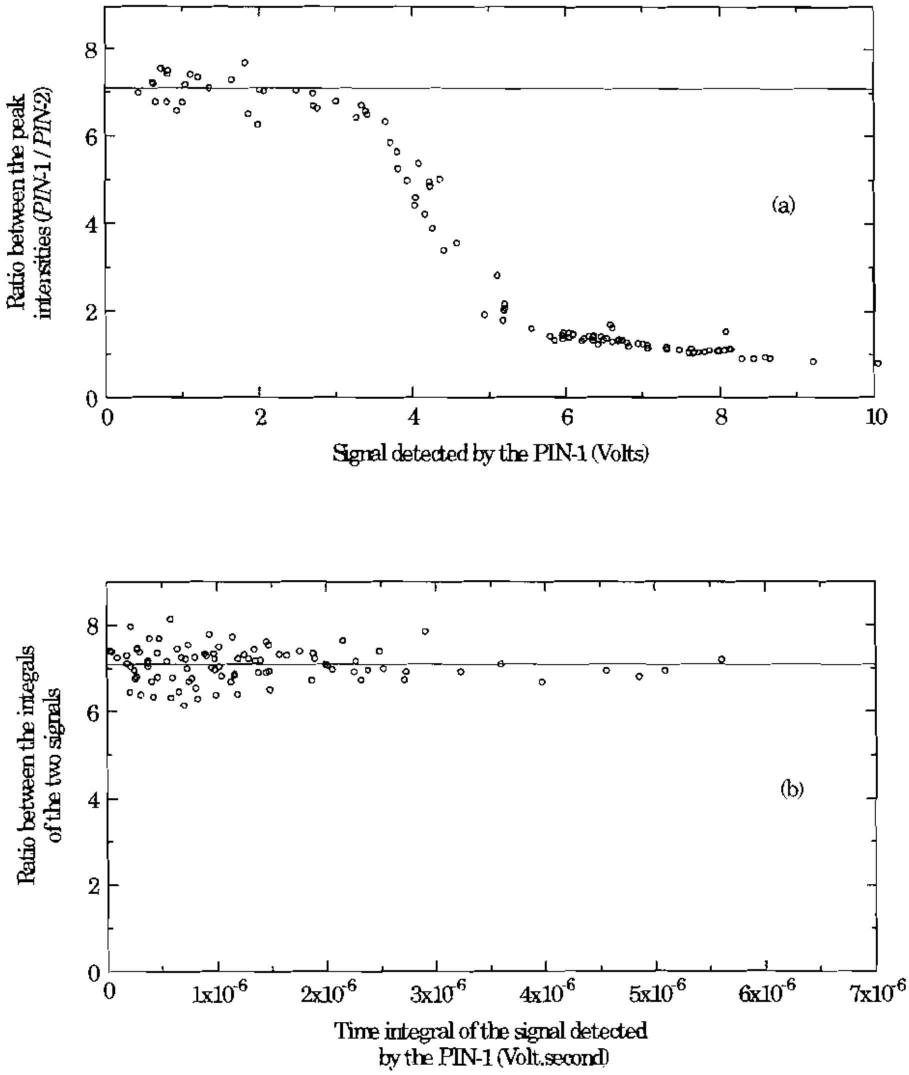


**FIGURE 5.41**
Linear response region determination of BPX65 photodiode
(a) ratio between two signals which is proportional to the photonic current
(b) ratio between integrals of the two signals which is proportional to the collected charge produced by photons

*About the 5-channel detector*

The sensitivity curve of the 5-channel detector is shown in Fig.4.26 in the previous chapter. For our purpose we may extract the spectral information from five signals in terms of different wavelength ranges (see Fig.5.42) separated by $\lambda_A$ = 1.4 Å, $\lambda_B$ = 4 Å , $\lambda_C$ = 6 Å and $\lambda_D$ = 12 Å. Characteristics of signals corresponding to each range are summarized in Tab.5.6. We roughly estimate the spectra of the source by checking the measured signals against this table.

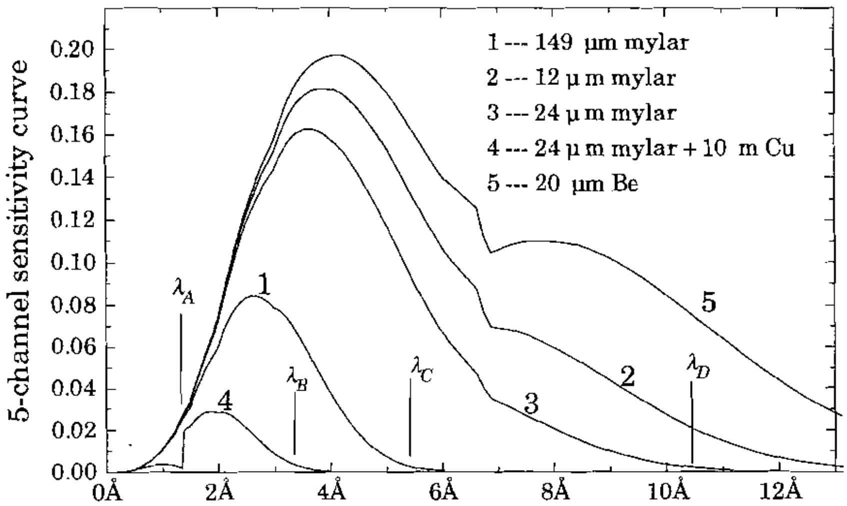


**FIGURE 5.42**
Sensitivity curve of 5-channel detector

***Table 5.6*** The 5-channel detector in terms of wavelength ranges

| wavelength ranges | characteristics | descriptions |
|---|---|---|
| λ <1.4 Å | X4 ~ 0<br>X1,2,3,5 are the same | characteristic lines of copper |
| 1.4 Å < λ <4 Å | 5 signals are significant | argon plasma |
| 4 Å < λ <6 Å | X4 ~ 0 | (argon plasma) |
| 6 Å < λ <12 Å | X4,1 ~ 0 | (neon plasma) |
| λ > 12 Å | X4,1 ~ 0; X3 is small | neon plasma |

#### 5.3.4.2 Time correlation observations

An example of x-ray emission rate from argon is shown here in Fig.5.43 for comparison with previous work on a similar machine [33,98]. As has already been observed in these references typically two separate soft x-ray bursts are observed. The first peak of the first x-ray burst corresponds to the peak of the voltage spike (which corresponds to the time of maximum compression) within an accuracy of ±10 ns, while the second burst appears some 300 ns later (at which time the pinch column has already disrupted). An average FWHM value of about 20 ns may be assigned to each of the x-ray bursts.

In this project work we use neon gas for the first time in this focus device. Fig.5.44 shows a typical discharge in neon gas. Voltage, $dI/dt$, current signals are presented for correlation analysis. All the PIN signals exhibit very sharp rise at the beginning when the focus is compressed to its minimum radius which can be identified by first sharp negative peak in the $dI/dt$ signal or the rise of voltage (slightly delayed due to its slower frequency response as explained in Sec.4.3.2).

In contrast to the argon focus for which ~ 80% of the discharges show a multi-burst feature ("A" and "B" in Fig.5.43), the neon plasma focus, operated at similar conditions as argon, is dominated by one burst. This one pulse is composed mostly of two or three (sometimes even more) peaks, shown in Fig.5.44 and Fig.5.45 respectively. Again an averaged FWHM value of about 20 ns (similar to argon focus) may be assigned to the soft x-ray burst. This experimental value is consequently used for the time duration of the radiative phase in our modelling in Chapter 3 Sec.3.5.

Harder (>2 keV) x-rays were observed in argon for some shots occurring in the late bursts. For neon this feature is almost never observed. This is an advantage as far as application for x-ray lithography is concerned. In the case of negative polarity (in neon), multi-burst feature was not observed at all and hence no hard x-ray was emitted.

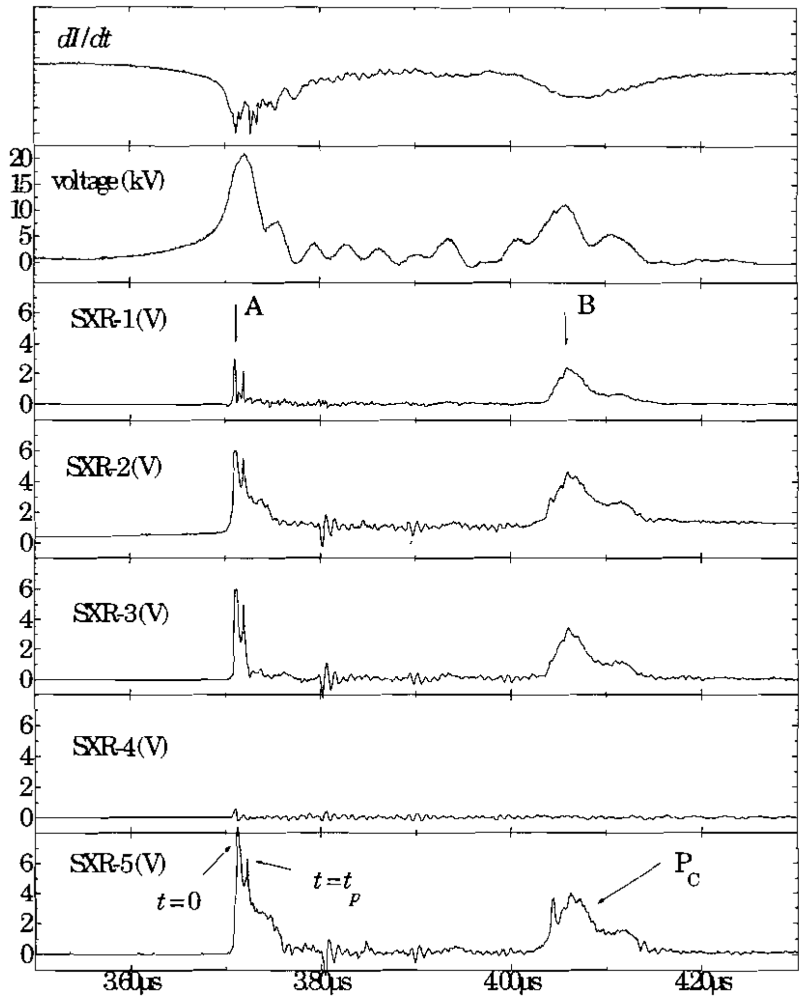


**FIGURE 5.43**
Example of x-ray emission rate ($dY_x/dt$) from the 5-channel PIN detector (plasma focus discharge at 13 kV in argon at 1.0 mbar)

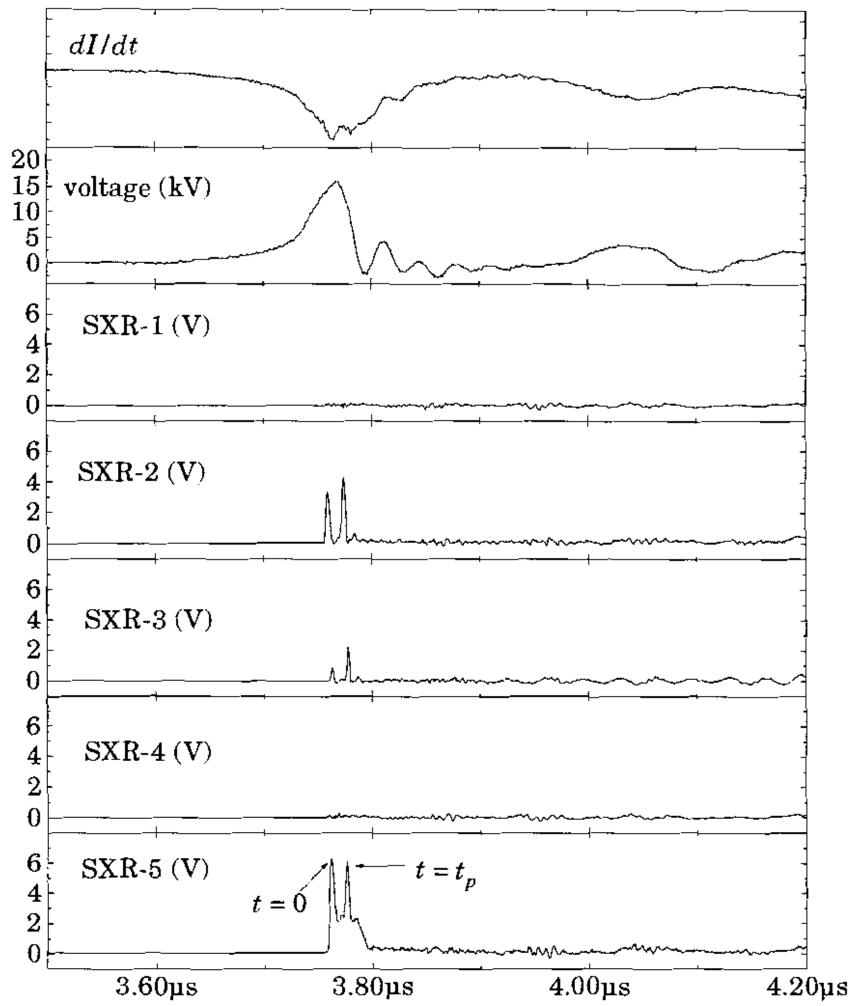


**FIGURE 5.44**
Typical traces of soft x-ray emission rate ($dY_{SX}/dt$) plasma focus discharge at 13 kV in neon at 3 mbar

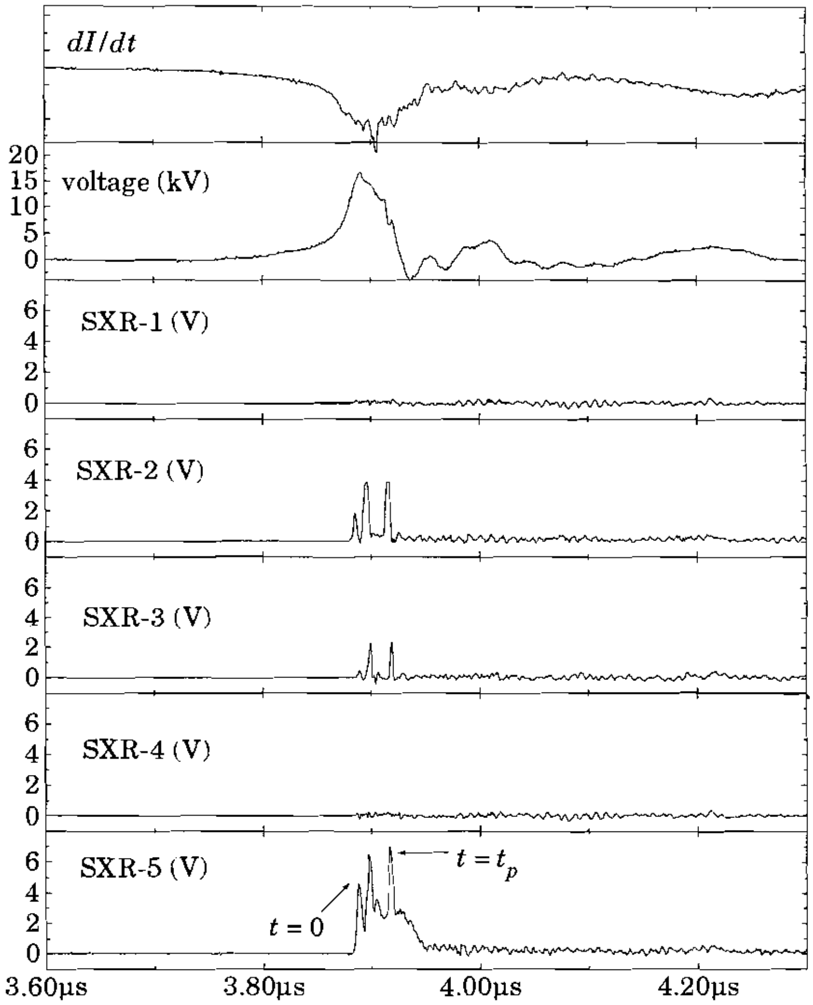


**FIGURE 5.45**
Typical traces of soft x-ray emission rate ($dY_{SX}/dt$) plasma focus discharge at 13 kV in neon at 4.3 mbar

### 5.3.4.3 Comparison with Signals Detected by the Photoelectric Effect X-ray Detector

`Assuming the x-ray spectrum is $E(\lambda,t)$, what the detector based on the photoelectric effect measures is: $P(t) = \int E(\lambda,t) f_b(\lambda)\, d\lambda$ . Hence without further refinement such a measurement tells us little about the absolute energy spectrum $E(\lambda,t)$ of the x-rays. However more complete information is obtained by using this detector in conjunction with various absorber materials placed in front of the entrance aperture. By selectively absorbing different ranges of wavelengths we attempt to unfold the $E(\lambda,t)$ spectrum. If relative intensity of x-rays in the spectrum proves to be reproducible then it should be possible to determine the total emitted x-ray energy from $P(t)$. In Fig.5.46 the typical x-ray signal measured by this detector, the 5-channel PIN, $dI/dt$ signals are also presented for comparison. The x-ray signals measured by both types of detector are very consistent in timing.

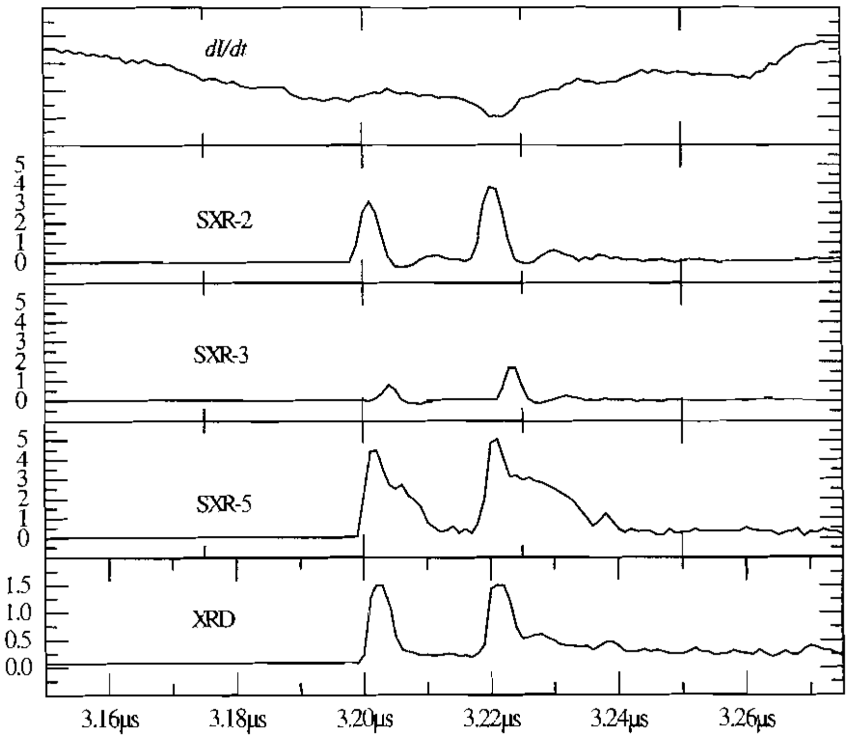


**FIGURE 5.46**
Comparison of x-ray measurements by 5-channel SXR detector and (photoelectric effect) x-ray detector

### 5.3.5 Total X-ray Yield Determinations

#### 5.3.5.1 Methods for Determining X-ray Flux

As was mentioned in Sec.4.6.4, the filtered PIN diodes (with windows removed) are used to diagnose not only the time-resolved information but also the spectrum band information and the total flux. This is one of the methods adopted in this project of estimating the total SXR yield.

The other method employed, which is rather direct in principle, was the calorimetry (described in detail in Sec.4.6.6). The radiation energy impinged onto the sensor of this detector is directly read out from its control panel. For plasma focus, however, the source is actually a complex one with soft x-rays being only a small part of the total radiation. As a consequence a filter has to be used in front of the sensor to block out the radiation (and also energetic particles) which is not of interest. So we need the (relative) spectrum information to work out the total flux.

The relative spectrum is easier to obtain compared to the absolute one. The crystal spectrograph, for instance, could be used for this purpose. In this work, a 5-channel detector is employed. The 5-channel PIN detector is used to estimate x-ray flux on a single shot or repetitive basis. Comparison between two methods for determining x-ray flux is thus available. The spectrum results obtained by the 5-channel detector is also compared with those from the crystal spectrograph presented in the above section for comparison and verification.

#### 5.3.5.2 Experimental Set-up

The calorimeter and the 5-channel PIN detector were mounted inside the vacuum chamber as shown in Fig.5.47, being at distances of 230 mm and 276 mm from the focus respectively. The field of view of each detector is centred in the plane normal to the axis of the PF gun and about 5 mm above the top surface of the anode. Between the focusing region and the detectors two apertures of 6 mm diameter were used to prevent shock waves from damaging the filters.

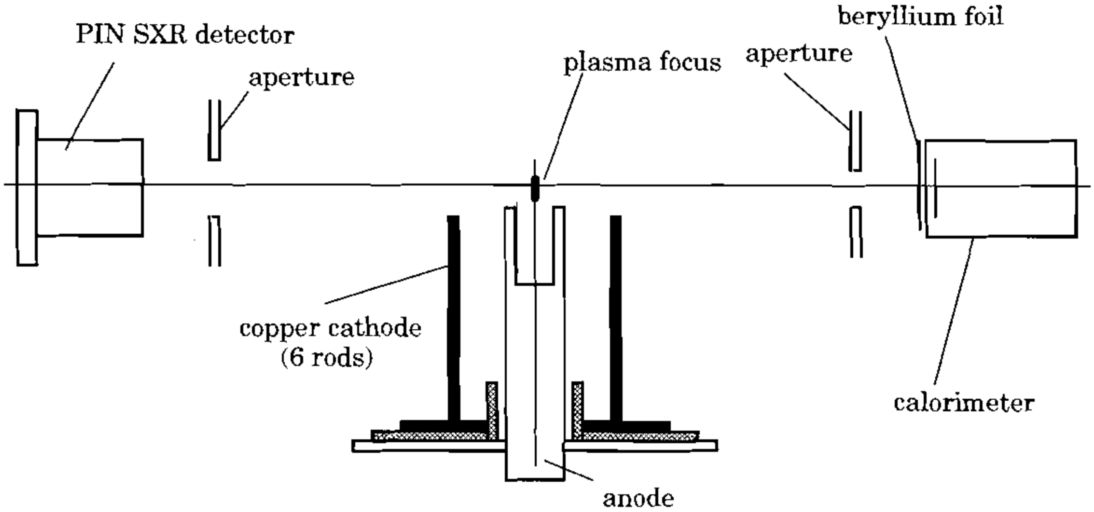


**FIGURE 5.47**
Total x-ray yield measurement set-up using a calorimeter and PIN detector

Other diagnostics employed simultaneously were a voltage probe comprising a resistive divider, and two Rogowskii coils to measure the discharge current and its first derivative.

### 5.3.5.3 Estimation of Total X-ray Yield by PIN detector

*Assumption of simple source spectrum*

Varying the charging voltage (13 kV and 14 kV) and its polarity and the filling pressure from 2 mbar to 7.5 mbar, experiments were carried out to determine the effect on the x-ray yield. Fig.5.44 and Fig.5.45 show typical sets of oscillograms. Channels 2 and 5 show large signals. Channel 3 has a small signal while channel 1 and 4 have no signal. Referring to the sensitivity plot (Fig.5.42) and Tab.5.5, this means that the x-ray spectrum is mainly in the wavelength region longer than 7Å. This result is in agreement with our previous results obtained by crystal spectrograph. It is also consistent with Prasad *et al.* [24,25], where it was reported that 60% of the total x-ray output is due to the He-α and Ly-α lines centred at 12.9 Å and 40% is in the H-like and He-like continuum centred at 9.8Å when operated in neon. In general, It is found [24,25] that for neon plasma focus the hydrogenlike alpha line (Ly-α) at 13.447 Å and the helium alpha line (He-α) at 12.132 Å are the most intense features of the neon spectra, whereas the other line radiations and the free-to-bound continua are rather weaker.

To simplify the estimation of total SXR yield and to compare with data analyzed in similar ways [24], we assume that the x-rays from this neon plasma focus comprise three parts of spectra, i.e., two peaks at $\lambda_1$ = 13.447 Å (Ly-α) and $\lambda_2$ = 12.132 Å (He-α) and a square shape from $\lambda_3$ = 8 Å to $\lambda_4$ = 11.568 Å (He-β) (see spectrum trace in Fig.5.38, 5.39). This assumption can be written as

$$X(\lambda,t)=\begin{cases} X_1(t)\delta(\lambda-\lambda_1) & \lambda=\lambda_1 \\ X_2(t)\delta(\lambda-\lambda_2) & \lambda=\lambda_2 \\ \dfrac{X_3(t)}{\lambda_4-\lambda_3} & \lambda_3<\lambda<\lambda_4 \\ 0 & \lambda\neq(\lambda_1 \text{ to } \lambda_2),\ \lambda_3,\ \lambda_4 \end{cases} \tag{5.16}$$

where $X(\lambda,t)$ is the x-ray output from source at wavelength λ and time $t$ (J/m.s). Let $f_i(\lambda)$ be the sensitivity of the $i$th channel of the detector accounting for the absorption by the filter(s) in front of the photodiodes and neon gas between the detector and source, and $P_i(t)$ the signal measured by the $i$th channel of the detector (volts), Using equation (1) we then have

$$\begin{aligned} P_i(t) &= k_p \int X(\lambda,t)\cdot f_i(\lambda)\,d\lambda \\ &= k_p\cdot\left(f_i(\lambda_1)\cdot X_2(t)+f_i(\lambda_2)\cdot X_2(t)+\int_{\lambda_3}^{\lambda_4} f_i(\lambda)\,d\lambda\cdot X_3(t)\right) \end{aligned} \tag{5.17}$$

where $k_p=\dfrac{s}{4\pi r^2}R$ , with $r$ = 276 mm being the distance between the diode and focus region, $s$ = 1 mm$^2$ the detection area of the sensor and $R$ = 50 ohm the resistance of the terminator. $k_p$ = 5.1x10$^{-5}$ (ohm) is the factor after taking into account all these geometrical and electrical parameters.

Integrating Eqn.(5.17) for $t$ and applying it to channel 2 ($P_2$), channel 3 ($P_3$) and channel 5 ($P_5$) gives:

$$\int P_i(t)\,dt = k_p \cdot \left( f_i(\lambda_1) \cdot \int X_2(t)dt + f_i(\lambda_2) \cdot X_2(t) + \int_{\lambda_3}^{\lambda_4} f_i(\lambda)\,d\lambda \cdot X_3(t) \right) \qquad i = 2,3,5 \tag{5.18}$$

We can solve this set of equation by using the coefficients from Fig.4.26. For 3 mbar neon pressure we can obtain,

$$\begin{cases} \int X_1(t)\,dt = -4.5\times10^7 \int P_2dt + 1.21\times10^8 \int P_3dt + 7.29\times10^6 \int P_5dt \\ \int X_2(t)\,dt = 2.2\times10^7 \int P_2dt - 8.7\times10^7 \int P_3dt - 8.12\times10^5 \int P_5dt \\ \int X_2(t)\,dt = -1.67\times10^5 \int P_2dt + 1.09\times10^7 \int P_3dt + 1.78\times10^3 \int P_5dt \end{cases} \tag{5.19}$$

where $\int P_2(t)\,dt$, $\int P_2(t)\,dt$ and $\int P_5(t)\,dt$ can be easily evaluated from signals acquired by the digital oscilloscope. Because the absorption coefficient is dependent on the neon pressure, in practice a computer program is written for the calculation. Total x-ray yield is,

$$W = \int\int X(\lambda,t)\,d\lambda dt = \int X_1(t)\,dt + \int X_2(t)\,dt + \int X_3(t)\,dt \tag{5.20}$$

The results are shown in Fig.5.48(A). For each filling pressure we fire 10~15 shots and take the average value for the data point. The same procedure is followed in the next two sections. The three terms at the right side of Eqn.(5.20) correspond to energy at two alpha lines (13.447 Å, 12.132 Å) and at the range from 8 Å to 11.568 Å respectively. These three terms are evaluated separately and the data shows that in average 44% of the total energy is at 13.447 Å, 20% at 12.132 Å and 36% in the wavelength range of 8 ~ 11.568 Å.

### 5.3.5.4 Estimation of Absolute X-ray Yield by Calorimeter

To determine the absolute soft x-ray yield from the calorimeter signal it is necessary to correct for the absorption of the 20 μm Be foil placed in front of this detector by making use of the spectral information derived from the 5 channel PIN detector. Using the results from the proceeding section, i.e. 44% of the total yield is at 13.447 Å, 20% at 12.132 Å and 36% in the range between 8 Å and 11.568 Å, the total yield $W$ is related to the reading ($Q$) from the meter by:

$$W \cdot [0.44 \times f_n(\lambda_1) f_b(\lambda_1) + 0.2 \times f_n(\lambda_1) f_b(\lambda_2) + 0.36 \times \int_{\lambda_3}^{\lambda_4} f_n(\lambda) f_b(\lambda)\, d\lambda] \cdot k_c = Q \tag{5.21}$$

where $k_c$ is the factor after taken into account the geometrical parameters, $f_b(\lambda)$ and $f_n(\lambda)$ are the transmission coefficients for the x-ray through 20 micron Be foil and the neutral neon gas respectively. It is noted that $f_n(\lambda)$ is dependent on the pressure of neon gas. A program is written to calculate the total x-ray yield from Eqn.(5.21) and the results are shown in Fig.5.48(B). In this calculation of total yield we have assumed an isotropic source whereas in actual fact the emission is stronger in the axial direction. This means that our estimate, based on a measurement in the radial direction, gives a slight underestimate.

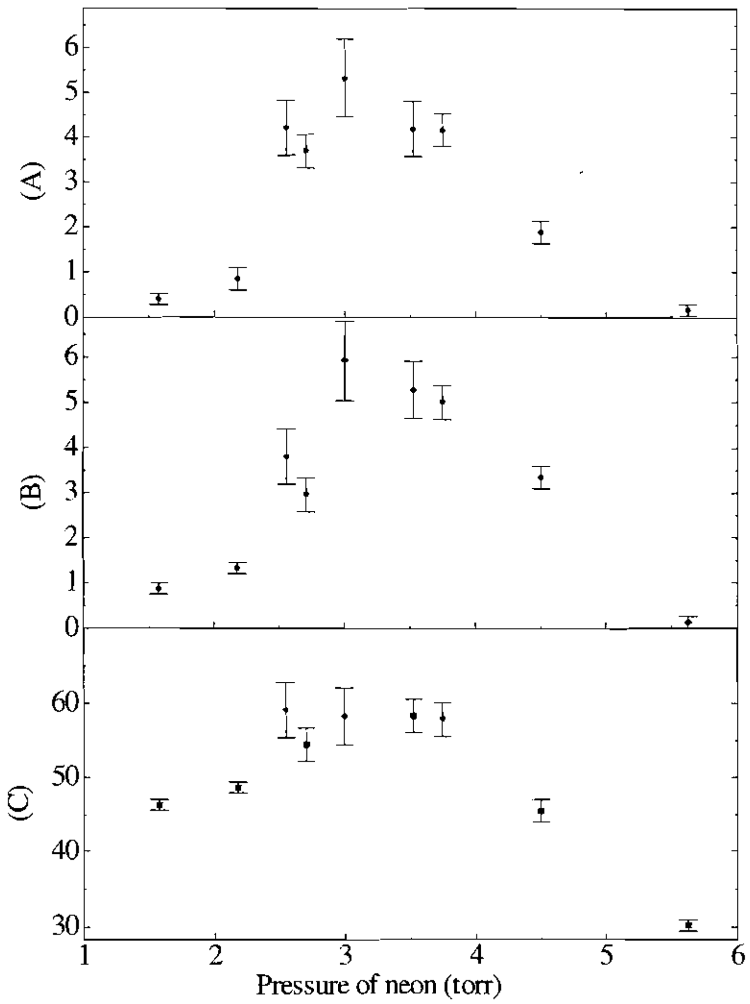


**FIGURE 5.48**
(A) X-ray yield measured by 5-channel detector (joules)
(B) X-ray yield measured by calorimeter (Joules)
(C) Input energy (Joules) into focus computed from the voltage spike and current dip of the focus

### 5.3.5.5 Operating with Different Charging Voltages and Polarities

With the central electrode connected via the switch to the positive terminal of the capacitor, charging voltages of 14 kV and 13 kV are used, with corresponding stored energies of 2.9 kJ and 2.5 kJ respectively. Negative polarity was also studied for comparison with positive polarity. The final results are given in Fig.5.49. Note that Fig.5.49a is the same as that in Fig.5.48(A and B). It is shown here for comparison. The 5-channel detector is used to estimate the x-ray radiation. The input energy calculated from the *VxI* (product of current and voltage) peak (see Sec.5.2.1.2) is also listed for each case. The current used here is the current flowing through the pinch, which is obtained by multiplying the total current by the current shedding factor measured with magnetic probing presented in Fig.5.8.

The effect of different experimental conditions on the SXR yield is summarised in Tab.5.7 below.

***Table 5.7*** Effect of different experimental conditions on the SXR yield.

| charged voltage (kV) | polarity | energy storage (kJ) | optimum pressure (mbar) | input energy (J) | x-ray yield+ by 5-channel (J) | x-ray yield+ by calorimeter (J) |
|---|---|---|---|---|---|---|
| 13 | positive | 2.54 | ~ 2.5 | ~ 55 | 3.5 | - |
| 13 | negative | 2.54 | ~ 1.9 | ~ 40 | 1.5 | - |
| 14 | positive | 2.94 | ~ 4 | ~ 65 | 5.5 | 6 |

+ at source, into $4\pi$

From Fig.5.48, 5.49 and Tab.5.7, some conclusions are as follows:

1. The SXR yield for 14 kV charging voltage is larger than that for 13 kV charging voltage at the optimum pressure. This is understandable because of the difference of stored energies. In fact, the input energy into the focus for 14 kV is significantly greater than that for 13 kV voltage, as illustrated in Fig.5.49(a) and (c).

2. At the same pressure and charging voltage, the x-ray output for

the case of positive polarity is about 2~3 times larger than that of negative polarity.

3. At positive polarity, the plasma focus operated at 14 kV gives good focusing in a wider pressure range than that at 13 kV charging voltage. Comparing the positive polarity with negative polarity it is seen that the operational pressure for good x-ray yield at positive polarity has a much wider range than that at negative polarity. So operating at positive polarity is preferable.

4. There is no linear relationship between the input energy and the x-ray yield. But from Fig.4.49 we still can see that a larger input energy corresponds to a larger x-ray output. So to get more x-rays it is better to have a system which gives more efficient conversion from stored energy into the energy of the pinched plasma.

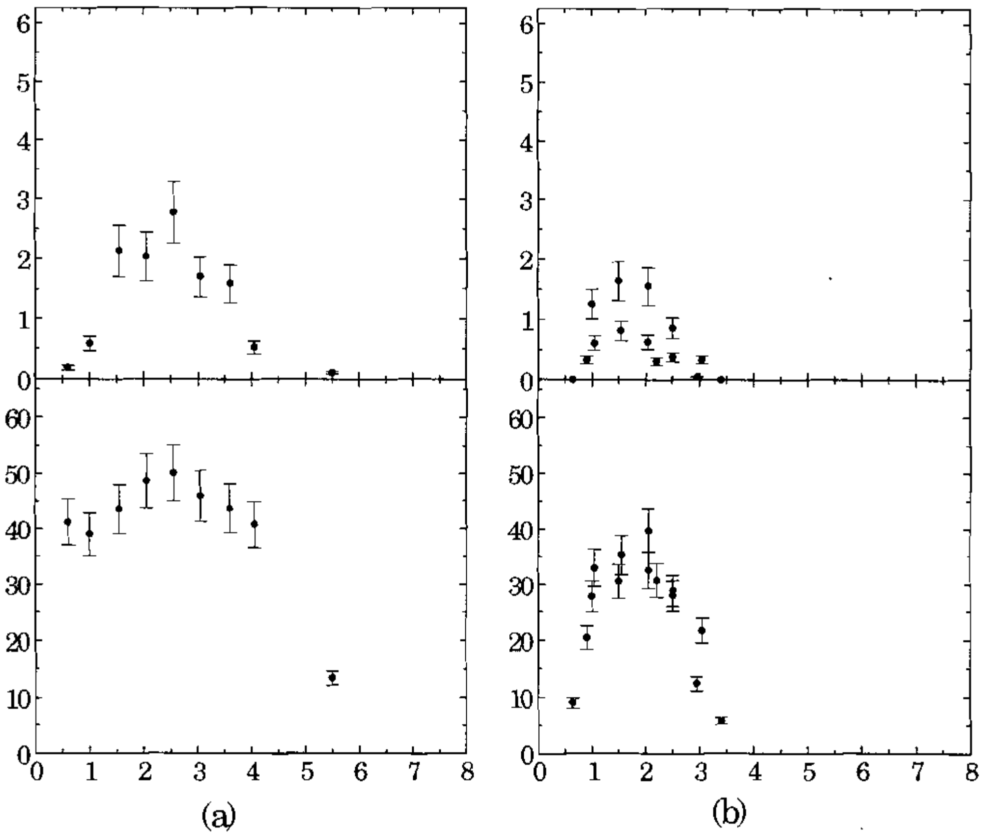


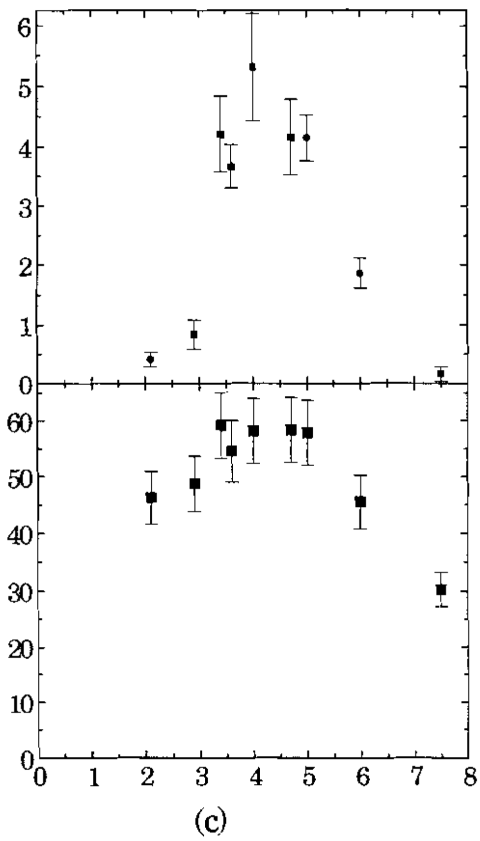


**FIGURE 5.49**
Correlation between x-ray output and the input energy under different conditions

Descriptions for (a), (b) and (c)
upper graph: x-ray yield measured by the 5-channel detector (J)
lower graph: input energy (J)
horizontal axis: pressure (mbar)

Conditions
(a) charged voltage 13 kV, positive polarity
(b) charged voltage 13 kV, negative polarity
(c) charged voltage 14 kV, positive polarity
working gas: neon

### 5.3.5.6 Reproducibility of X-ray Emission

The reproducibility of the x-ray emission of the machine has been tested . The x-ray output was monitored by the 5-channel detector. It is found that it maintains good focusing quality and produces large amounts of x-rays for over 100 shots in about 2 hours without re-pumping and refilling the working gas for this device. The results are shown in Fig.5.50. We found that for this device the first 5 discharges after gas refilling always has better focusing and produces larger x-ray yield (about twice as much as the following shots). In the next 30 shots the output (focusing quality) become steady. The decrease of the output in this device mainly results from the steady increase in pressure due to a combination of outgassing and leakage.

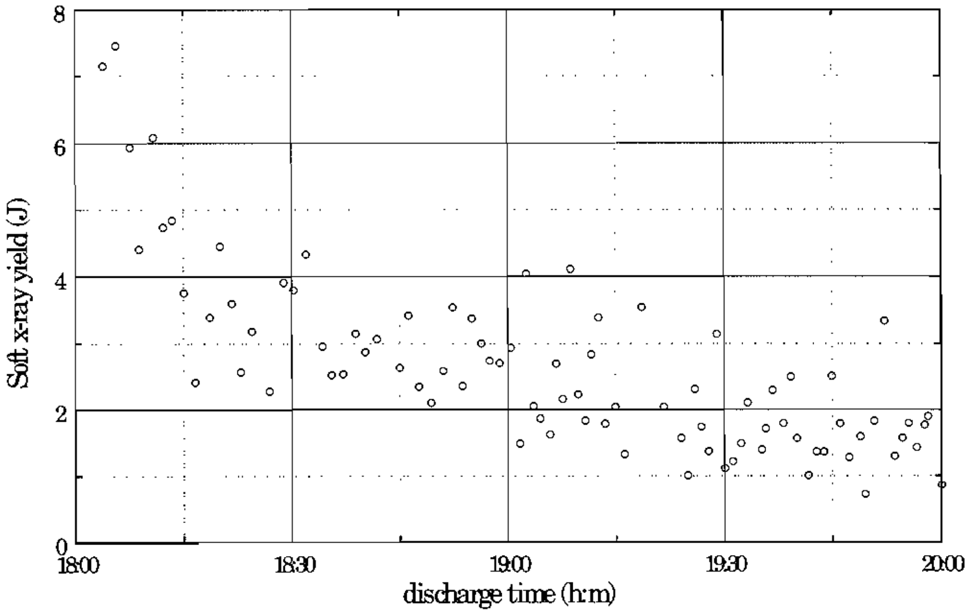


**FIGURE 5.50**
X-ray output as a function of time
conditions: 13 kV, 2.5 mbar neon.
1.2 min interval between discharges

#### 5.3.5.7 Discussion and Summary

A calorimeter correlated with a multichannel PIN detector has been successfully used to measure the total x-ray yield generated from a small plasma focus device. The calorimeter is calibrated absolutely using its built-in calibration resistor. In this work, the final uncertainty in the absolute soft x-ray flux results mainly from the approximation of the derived spectrum and the way we divide the spectral range into two peaks and a flat portion. The calorimeter can also be used for other radiation sources such as z-pinch plasma source, laser-produced plasma source, etc., although it may not be suitable for sources with a repetition rate higher than 1 Hz.

For a charging voltage of 14 kV, with 2.9 kJ stored energy, the optimum operational pressure in neon for this machine is found to be close to 4 mbar. The total SXR yield is averaged at 6 J/shot.

The outputs of the 5-channel PIN detector show that the x-ray emission is within the wavelength range of >8 Å, with 64% of the total yield >12Å, corresponding to the two most intense alpha lines from Ne IX and Ne X and their satellite lines. Results obtained by both detectors were consistent. Current and voltage measurements show that ~ 2% of the stored electrical energy (40 ~ 65 J) is pumped into the focus region, out of which 6 J soft x-ray is emitted when operated at optimum filling pressure.

It seems that the soft x-ray yield has a better correlation with the input energy compared to the neutron and hard x-ray yield.

## 5.4 Discussion

### 5.4.1 Summary on X-ray Measurements

The six methods used to monitor the x-ray emission from our small plasma focus and the main results are listed in Tab.5.8.

***Table 5.8*** X-ray diagnostics used in the project ("x-ray" in the table means soft x-ray)

| Diagnostics | Applications | Main results (neon focus) |
|---|---|---|
| Pinhole camera | time-integrated spatial distribution of plasma x-ray emissivity, i.e. x-ray image of the source (side-on and end-on) | 1. viewing side-on: column-like source with a length of 6 ~ 8 mm<br>2. viewing end-on: circular source, ~ 300 μm in diameter for single discharge and 600 μm in diameter for 7 discharges |
| Pinhole transmission grating spectrograph | space resolved x-ray emission spectrum (survey overall spectrum) | N- and O-band spectrum are identified for Au target LPP device<br>K-band and L-band are identified for PF device |
| Flat Crystal spectrograph | x-ray emission spectrum with high resolution and spatial resolution in axial direction | 1. spectrum is in the wavelength range 8 ~ 14 Å. spectrum lines of interest were identified.<br>2. Ly-α and He-a lines are the most intense features, totaling 55~67% of the total SXR yield. (agree with 5-channel detector)<br>3. electron temperature: 250 ~ 350 eV, by relative intensities of Ne IX and Ne X lines,<br>200 eV, by decline of recombination continuum<br>4. electron density: order of $10^{21}$ $cm^{-3}$<br>5. simple spectrum model of two peaks (at 13.447 Å and 12.132 Å) and a flat portion (from 8 Å to 11.568 Å) is found to be a reasonable approximation. |

Table continued

| | | |
|---|---|---|
| 5-channel PIN detector | 1. time-resolved x-ray signal;<br>2. time-resolved x-ray spectrum band (using 5 channels with different filters);<br>3. estimation of total x-ray yield (with computed absolute sensitivity curve) | 1. x-ray emission starts from the first minimum compression, two or more peaks in x-ray output for each burst;<br>2. pulse width: 10 ~ 20 ns;<br>3. spectral distribution of x-ray energy is 44% at 13.447 Å, 20% at 12.132 Å and 36% in the wavelength range of 8 Å ~ 11.568 Å.<br>4. total yield at source into $4\pi$ estimated to be 5.5 joules at optimum condition (14 kV, 4 mbar) |
| (Photoelectric effect) X-ray detector | time-resolved x-ray information | x-ray signals with fast risetime (<2 ns) is obtained, results are in good agreement with those measured by 5-channel SXR detector |
| X-ray Calorimeter | total x-ray flux<br>(relative spectrum information is needed when using filter in front) | total x-ray yield (at source into $4\pi$) ~ 6 joules is measured for neon plasma operated at optimum condition (14 kV, 4 mbar) (in agreement with results from 5-channel detector) |

### 5.4.2 Comparison with Numerical Computation

In Chapter 3 a radiative model was introduced and some typical results were presented. But the radiation calculated there included the whole spectrum range, although at high temperature the x-ray part is predominant. From Ref. [166] (see Tab.5.3) we know that the recombination part in the wavelength range shorter than 20 Å (which is the spectral regime of our interest) is contributed only by the 10th and 9th ionised ions for neon plasma and from Eqn.(3.6) we can write the formulae of the corresponding power densities as,

$$P_{r,10} = 5.5\times10^{-33}\,T_{eV}^{-1/2}N_eN_{10} \tag{5.22}$$

$$P_{r,9} = 3.61\times10^{-33}\,T_{eV}^{-1/2}N_eN_{9} \tag{5.23}$$

The line radiation in the x-ray region is only contributed by the transitions in ions on 9th and 8th ionised levels. As for Bremsstrahlung the spectrum is dependent on the electron temperature, the wavelength corresponding to the maximum radiation from Bremsstrahlung is given by Eqn.(2.5). At the conditions of our operation we expect that the Bremsstrahlung is negligible compared to the other two emission mechanisms. Fig 5.51 shows the results for the two alpha lines ($P_{Ly\alpha}$ and $P_{He\alpha}$), recombination emission ($P_{rec\text{-}10}$ and $P_{rec\text{-}9}$) and Bremsstrahlung from the model which uses the same input data as that presented in Chapter 3 Sec.3.5. The x-ray yields contributed by them are listed below,

$E_{Ly\alpha} = 5.53$ J

$E_{He\alpha} = 2.18$ J

$E_{rec10} = 1.55$ J

$E_{rec9} = 1.48$ J

$E_{brem} = 0.4$ J

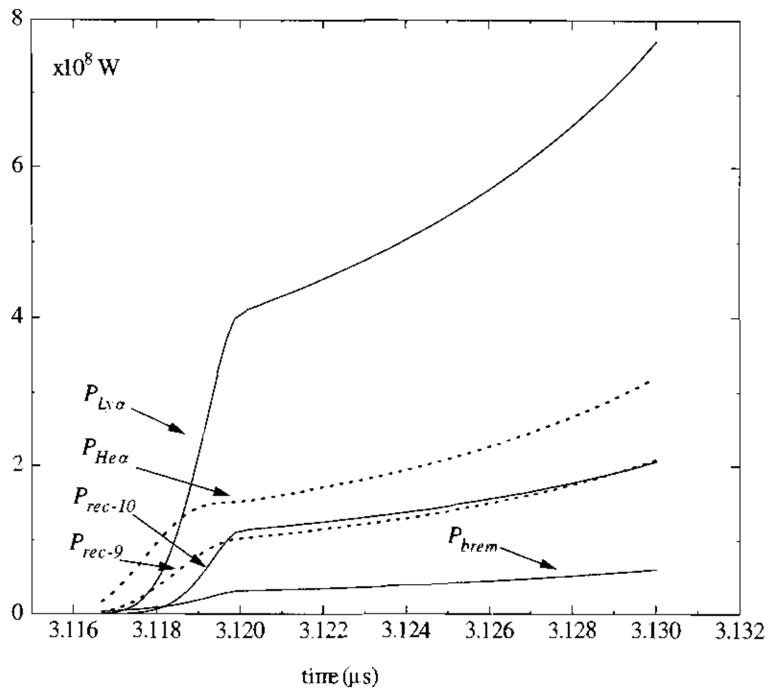


**FIGURE 5.51**
Computational results of two lines and recombination radiation from 10th and 9th ionised neon ions.

As is known, the two alpha lines have the strongest intensities in the total line radiation (see Eqn.(5.6) to (5.9)). To simplify the discussion we may assume that the line emission from the lines other than the two alpha lines comprises 20% of the total line radiation. So the total radiation from this model is 12.6 J in which the Ly-α line takes 43.5%, He-α 17%, the rest lines 12%, 10th recombination 12.5%, 9th recombination 12% and Bremsstrahlung 3%. These properties agree quite well with the experimentally measured spectrum, although the total x-ray yield from the model is higher than the experimental result. The discrepancy could be due to the assumptions used both in the model and in the analysis of experimental data. In the theoretical aspect these assumptions are the coronal model, a uniform plasma column, duration of radiation and some input parameters. In the experimental aspect these assumptions are the spectral response of the film, the way of dividing the spectrum into two-peaks and one flat portion, and the calibration or estimation of the sensitivity of the detectors.

### 5.4.3 Neon Plasma Focus for SXR Source

As discussed in Chapter 3 and the preceding subsection for neon plasma we may use the following radiation model: two lines (Ly-α, He-α) and the recombination ($P_{rec\text{-}10}$ and $P_{rec\text{-}9}$), Bremsstrahlung taken as negligible and radiation from lines other than the two K-alpha lines comprises 20% of the total line radiation. Then the total x-ray power may be written as,

$$P = 1.2 \times (P_{Ly\alpha} + P_{He\alpha}) + P_{rec-10} + P_{rec-9} \tag{5.24}$$

where $P_{Ly\alpha}$, $P_{He\alpha}$, $P_{rec\text{-}10}$ and $P_{rec\text{-}9}$ are from Eqn.(5.6), (5.8), (5.16) and (5.17) respectively. $N_{10}$, $N_9$ and $N_8$ are obtained from Eqn.(3.16).

Using Eqn.(5.18) the x-ray yield is then,

$$\begin{aligned} Y_X &= P \cdot V_p \cdot t_p \\ &= k \cdot f(T_{eV}) \cdot N_e^2 V_p t_p \end{aligned} \tag{5.25}$$

where $N_e$, $V_p$ and $t_p$ are the electron density, plasma source volume and pinch duration respectively. $k$ is a constant.

$f(T_{eV}) \sim T_{eV}$ is plotted out in Fig.5.52. From this graph we see that for a plasma with fixed values of $N_e$, $V_p$ and $t_p$ the maximum output takes place at temperature ~ 400 eV. When the temperature is higher than 300 eV the Lyman-α line dominate the spectrum. Generally, for plasma focus the electron temperature has a strong relationship with the density and plasma volume. The pinch duration is also affected by many factors like various instabilities. But we still can make a conclusion that the electron temperature between 300 ~ 500 eV is suitable for a neon plasma focus to be SXR source in our preferred wavelength range. Too high a temperature is not suitable for strong x-ray radiation as the decrease in line radiation is faster than the increase in Bremsstrahlung. The role of Bremsstrahlung may also be considered. Inclusion of Bremsstrahlung will not significantly affect the maximum total emission in the SXR yield or the electron temperature at which the maximum yield occurs. At high temperature above 1 keV, contribution from Bremsstrahlung will become more significant. Bremsstrahlung will dominate the emission above 5 keV and at 40 keV it will emit the same amount of radiation as the neon plasma at 400 eV. However the spectral range at that high temperature are not in the spectral range of interest to SXR lithography. So our conclusion regarding the optimum temperature for SXR yield in a neon plasma remains unchanged. The optimum range is 300 - 500 eV.

It is noted here that the above discussion is based on a coronal plasma model.

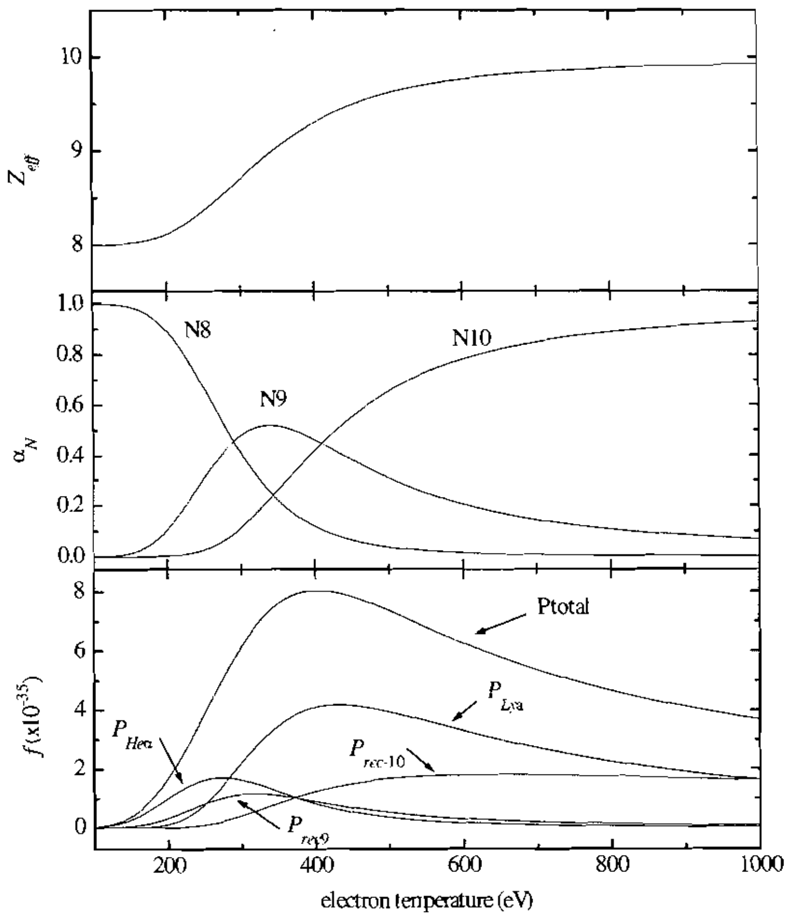


**FIGURE 5.52**
X-ray emission vs. electron temperature
(a) $Z_{eff}$
(b) fractions of 8th, 9th and 10th ionised ions
(c) $f(T_{eV})$

# Chapter 6

# Conclusions and Suggested Future Work

## 6.1 Conclusions

This thesis reports investigations on a 3 kJ compact plasma focus. Both experiments and computational simulation were carried out under various operational conditions with (a) three different working gases, neon, argon or deuterium, and (b) the central electrode operating at initial positive and negative charging voltages (i.e., positive and negative polarities).

The discharges were carried out at 14 kV or 13 kV charging voltage for both positive and negative polarities. The filling pressures for the three working gases were varied between 0.5 ~ 10 mbar for neon, 0.4 ~ 2 mbar for argon and 0.5 ~ 10 mbar for deuterium. A current transformer, a current derivative Rogowski coil, a resistive voltage divider, a PIN optical speed detector and magnetic probe arrays were used to study the evolution, gross dynamics, and discharge characteristics of this plasma focus device.

Current shedding factor is measured by three radially located magnetic probes (3-MP). For the same gas and same pressure the current factor of the positive polarity operation is higher than that of negative operation. Neon and argon plasma have bigger current factor than deuterium plasma under the same condition, suggesting that a bigger fraction of the total current drives the neon and argon plasmas relative to deuterium plasma. The mass loading factor in the axial rundown phase is obtained by using the experimentally measured current factor and by matching the arrival time of plasma sheath in the computational model with that determined by the magnetic probe. The mass factor is found to be 0.04 ~ 0.08 for neon and argon focus. Deuterium focus has a higher mass loading factor (0.08 ~ 0.16).

The profile of the plasma sheath in the axial rundown phase is studied using the 3-MP probe. At lower pressure the plasma sheath is more canted. For the same gas and same pressure the plasma sheath is more canted for the positive polarity than for the negative polarity.

A simple optical speed detector made of two light pipes with PIN photodiodes as sensors was developed and used to monitor the axial velocity of the plasma sheath. This detector was used in collaboration with the 3-MP array probe to study the characteristics of the current profile. Another detector with 8 light pipes was used to obtain speeds at several positions along the axial direction. It is found using this detector that the plasma sheet becomes steady only after it has traversed 8 cm from the backwall.

The main goal of this project work is to study the x-ray emissions from plasma focus. we have carried out detailed experiments only in neon because it is known from preliminary experiments that the neon plasma focus emits SXR in the wavelength range suitable for SXR lithography. We studied the neon focus both experimentally by various x-ray diagnostics and theoretically by a radiative plasma focus model. A variety of diagnostics was developed and used to monitor the radiation from the neon plasma focus in the soft x-ray regime (5 to 20 Å) under conditions of 14 kV and 13 kV charging voltages at both polarities. For comparison, measurements of emission from argon plasma was also conducted.

Using an x-ray pinhole camera, images were recorded with both end-on and side-on viewing to determine the dimensions and spatial extent of the neon plasma emission. For single discharges, the end-on x-ray images were nearly circular. The size of the emission was determined to be 280 to 360 microns in diameter. Images from multiple shots were also nearly circular with diameter varying to about 700 microns for images of 7 shots. The side-on image of plasma emission had the appearance of a thin column with 6 - 8 mm length. For multi-discharge exposure the diameter was less than 650 microns on average. All the images of the PF discharges indicate that the plasma emission is centred at the axis.

A pinhole transmission spectrograph was developed allowing one to study a wide range of soft x-ray emission characteristics. It provides two-dimensional spatial resolution simultaneously with spectrum over 3 - 300 Å wavelength range. K-band and L-band spectra for neon plasma focus were identified. For Au target Laser plasma N- and O-band spectra were clearly identified. This spectrograph is found to be a good detector to survey the specified spectrum.

For the wavelength range of our interest (from 5 to 20 Å), a flat crystal spectrograph was then developed and used to obtain the spectrum with higher resolution. Three configurations were designed for different purposes, i.e., focusing on the line radiation part, continuum part, or a wider spectrum range. For neon plasma focus the emission is found to be mainly in the wavelength range from 8 to 14 Å. The hydrogen-like alpha line (Ly-$\alpha$) at 13.447 Å and the helium alpha line (He-$\alpha$) at 12.132 Å are the most intense features of the neon spectra, contributing 53 ~ 67% of the total spectrum emission. From the spectroscopic information the electron temperature is estimated to be 300 ~ 380 eV using the method of ratio of line intensities and 160 ~ 250 eV by the slope of the logarithm of the continua. The electron density is estimated to be $10^{21}$ cm$^{-3}$.

Bright spots within the plasma column were observed both from pinhole imaging and the spatially resolved flat crystal spectrograph. For lower pressure these 'hot spots' assumed a longish shape. In the case of higher pressure, point-like spots were observed. The temperature in the hot spots is higher than the rest of the plasma column.

A 5-channel PIN SXR detector was designed for detection of radiation in the soft x-ray region. The absolute sensitivity of the photodiode used (BPX65) was computed. It was used to obtain the time-resolved x-ray signals, to estimate the x-ray spectrum and to evaluate the total SXR yield. The neon focus is found to be a better soft x-ray emitter (>5 Å) than argon and deuterium. Hard x-rays are more rarely observed compared to argon and deuterium foci. Usually one x-ray burst with two or three peaks are observed. The x-ray pulse has a duration of 10 ~ 20 ns on average. With the help of five different filters each covering one PIN diode, the approximate spectrum information was unfolded. Using an assumption of dividing the spectrum into two-peaks and one-flat-portion we estimated the following: ~ 44% of the total x-ray energy is at 13.447 Å (He-$\alpha$), 20% at 12.132 Å (Ly-$\alpha$) and 36% in the wavelength range of 8 ~11.568 Å. This is consistent with the results from crystal spectrography.

Another time-resolved SXR detector based on the photoelectric effect was made and tested. The rise time of this detector was less than 0.5 ns and was suitable for the x-ray measurement for our purpose in this work. The results are in good agreement with those from PIN detector. This detector is easily fabricated.

Total SXR yield was successfully measured by calorimeter correlated with the 5-channel detector. The calorimeter has a flat response to radiations of different wavelength. The detector was calibrated using an absolute method. At the charging voltage of 14 kV and the corresponding optimum pressure of 4 mbar, total SXR yield of 6 J/shot into $4\pi$ steradians was observed from this plasma focus.

The total x-ray yield estimated by the 5-channel PIN detector is consistent with that from the calorimeter. The SXR yield for 13 kV charging voltage at positive and negative polarities was also measured by the 5-channel detector. Comparing the three conditions (14 kV, positive; 13 kV, positive and 13 kV, negative) we found (a) the SXR yield for 14 kV charging voltage is 5.5 J (by 5-channel detector), larger than the other two which are 3.5 J and 1.5 J respectively; (b) at the same pressure and charging voltage, the x-ray output for the case of positive polarity is about 2 ~ 3 times larger than that for negative polarity; (c) The focus operated at 14 kV and positive polarity has the widest optimum operational pressure range, whereas the focus at 13 kV and at negative polarity has a very narrow range of pressure giving good focusing. The input energy into the plasma taken by integrating the peak of the product of the current and voltage signals was also calculated for comparison. It is found that higher input energy into the focus corresponds to higher x-ray output. It is surmised that this is because the soft x-ray emission is related to the plasma thermal energy which is related to the energy input into the focus.

The optimum pressures for charging voltages of 14 kV at positive polarity, 13 kV at positive polarity and 13 kV at negative polarity are close to 4 mbar, 2.5 mbar and 1.9 mbar respectively. The energy input into the pinched plasma of 40 ~ 65 J is measured from the area of $V\times I$ spike at optimum conditions, corresponding to ~ 2% of the bank stored energy. This is low for a plasma focus and is due to the large (110 nH) stray inductance of the discharge system.

The reproducibility of this plasma focus as an x-ray source has been tested. It is found that it maintains good focusing quality and produces large amount of x-rays over 100 shots in 2 hours without re-pumping and refilling the working gas. The decrease of the outputs at the last shots results from leakage and outgassing.

In parallel with the experiments, a radiative plasma focus model was developed. Based on earlier work, in this thesis the radiative part was added in to simulate the radiation from the pinched plasma. To calculate the radiation power densities and the ionisation levels a corona model was used. In the axial phase both current shedding factor and mass factor are fixed with reference to experimental data. In the radial inward shock phase the finite signal communication delay was considered and a reflected shock phase was included, which gives a more realistic picture of plasma sheath motion and minimum compression radius.

Computation is done for a typical case of neon plasma focus operating at 13 kV and 2.5 mbar pressure. The minimum radius of 0.2 ~ 0.3 mm is obtained and the speed of imploding plasma sheath is 30 cm/μs, which are in agreement with the work done on similar machines. The gross dimensions of the pinched plasma from simulation agrees with that obtained by side-on x-ray pinhole imaging. The average electron temperature of 360 eV and electron density of ~ $10^{26}$ $m^{-3}$ are computed. The line emission is predominant in the total emission and Bremsstrahlung is small compared to line and recombination radiations. Computing for 10 ns in the radiative phase we obtain total yield of ~ 11 J, in which the line radiation takes 70%, the radiative recombination takes 27% and Bremsstrahlung only 3%.

The model is also useful to obtain the optimum electron temperature for soft x-ray (<20 Å) yield. For a neon (coronal) plasma a temperature from 300 eV to 500 eV is found to be suitable to give strong x-ray emission in soft x-ray regime.

## 6.2 Some Suggestions for Future Studies

The diagnostics employed in this work, the plasma focus model and even the plasma focus system itself can definitely be improved. We shall list a few suggestions in this final part of the thesis for further studies in this area in future.

To get a faster recording of the spectral information on a shot-to-shot basis an intensified CCD combined with x-ray scintillator may be used instead of using x-ray film which needs tedious processing. A curved crystal can be used to obtain a wider spectral range with high resolution. The time-resolved spectral information is most difficult to obtain, but also of most importance and may be carried out in future to study in more detail some x-ray related topics such as the formation of hot spots.

In the aspect of modelling, the collisional-radiative plasma equilibrium model instead of the coronal model in the radial phase may be used to obtain more accurate results. Of course, a magnetohydrodynamic (MHD) model for plasma focus including radiative terms may be a good choice for simulating the plasma focus.

As for the focus device, we have already found both by experiments and by the dynamic model [26] that the present focus machine has a low efficiency of energy conversion when used as a SXR source. This is expected because of the high external (stray) inductance of 110 nH of this device. This stray inductance is very large compared to the focus tube inductance which rises from a low value to some 20 nH at the end of the axial phase and then to some 40 nH during the radial phase. The computation shows that only 3% of stored energy goes into the energy of the focussed plasma. This low proportion of energy transferred to the focussed plasma is consistent with the voltage-current measurements which indicates also a low proportion (of the order of 2%) of stored energy converted into electromagnetic energy transferred to the focus pinch region.

To gain further insight computations were also carried out with the same system but with $L_o$ reduced to 10 nH. As expected there is a dramatic change to the distribution of energies in various parts of the system, with more than 10% of stored energy going into the plasma. Moreover reducing $L_o$ from 110 nH to 10 nH almost doubles the current into the focus tube whilst also almost halving the current rise time. This allows, indeed requires [82] a corresponding increase in anode radius '$a$' and a decrease in anode length '$L$' from considerations of optimum value of '$I/a$' (current per cm of anode radius) and time matching. The corresponding change, by a factor of almost 4, of the aspect ratio $a/L$, towards a 'fatter' anode leads to a further rise of conversion efficiency into plasma energy to greater than 25%. Since the scaling of the modelling is such that the temperature and density of the focussed plasma remains approximately the same [82] for the various configurations considered when each configuration is optimized it is reasonable to assume that the SXR yield will depend on the plasma energy content. Thus reduction of $L_o$ as above will lead to an increase, many-fold, of the SXR yield. Technically to achieve such a low inductance in the capacitor bank requires a system which splits the required capacitance into many small parallel capacitors with many switches also operated in parallel. Such a low-inductance system combined with high repetition rate is necessary for the high performance needed for applications as a high intensity SXR source. Our laboratory is already in the process of developing such a high performance system for SXR lithography applications.

# References


[1] A.G. Michette and C.J. Buckley, "*X-ray Science and Technology*", Institute of Physics Publishing, Bristol and Philadelphia, 35 (1993)

[2] W. Lochte-Holtgreven, *Plasma Diagnostics,* New York, 70 (1995)

[3] B. Edle`n, and A. Ericson, *Nature* **125**, 233 (1930)

[4] E. Ekefors, *Physik*. **Z. 31**, 737 (1930)

[5] V.A. Bazylev and N.K. Zhevago, *Sov. Phys. Usp.* **25**, 565 (1982)

[6] E. Cullman, T. Kunneth, W. Neff, and K.H. Stephan, *J. Vac. Sci. Technol*. **B5**(3), 638 (1987)

[7] W. Neff, J. Eberle, R. Holz, R. Lebert and F. Richter, "The Plasma Focus as Soft X-ray Source for Microscopy and Lithography", *SPIE Vol. **1140**, X-ray Instrumentation*, (1989)

[8] R. Feder, J.S. Pearmann, J.C. Riordan and J.L. Costa, *J. Microsc.* **135**, 347 (1984)

[9] W. Neff, J. Eberle, R. Holz, F. Richter and R. Lebert, in *X-ray Microscopy II*, D.Sayre, M.Howells, J.Kirz, H.Rarback, eds., Springer Series in Optical Sciences, Vol. **56**, Springer, New York, 22-39 (1988)

[10] R. Holz, J. Eberle, R. Lebert, W. Neff, F. Richter, "A source for Soft X-ray Imaging Microscopy with Nanosecond Exposure Time", *SPIE*, Vol. **1140** *X-ray Instrumentation*, (1989)

[11] Y. Kato, I. Ochiai. Y. Watanabe, and S. Murayama, *J. Vac. Sc. Technol*. **B6**(1), 195-198 (1988)

[12] A. Heuberger, *J. Vac. Sci. Technol.* **B6**(1), 107-121 (1988)

[13] A.R. Striganov, *Usp. Fiz. Nauk*. 139, 719 (1983) *(Sov. Phys. Usp.* **26**, 373 (1983))

[14] B.L. Henke, H.T. Yamada, T.J. Tanaka, *Rev. Sci. Instrum.* **54**(10), 1311 (1983)

[15] J.S. Pearlman, J.C. Riodan, *Radit. Phys. Chem*. **25**, 709 (1985)

[16] J.P. Apruzese, P.C. Kepple, K.G. Whitney, J. Davis, D. Duston, *Phys. Rev. A* **24** (2), 1001 (1980)

[17] L. Mathews, P.L. Hagelstein, M.D. Rosen, etc., *Phys. Rev. Lett.* **54** (2), 110 (1985)

[18] A. Bernard, H. Bruzzone, P. Choi, H. Chuaqui, V. Gribkov, K. Hirano, A. Krejci, S. Lee, C.M. Luo, F. Mezzetti, M. Sadowski, H. Schmidt, K. Ware, C.S. Wong, V. Zoita, *"A Concept for an International Centre for Dense Magnetized Plasmas"*, (1993)

[19] D. Elliott. *"Integrated Circuit Fabrication Technology."* McGraw-Hill, (1982)

[20] P. Burggraaf. *"Semiconductor International"*, March:52, (1992)

[21] B.J. Lin. *"Fine Line Lithography"*, North-Holland Publishing Company, (1980)

[22] L.F. Thompson, C.G. Willson, and M.J. Bowden. *"Introduction to Microlithography"*, ACS, (1983)

[23] F. Richter, J. Eberle, R. Holz, W. Neff, and R. Lebert, *AIP Conf. Proc*. **195**, 515 (1989)

[24] P.G. Burkhalter, G. Mehlman, D.A. Newman, M. Krishnan and R.R. Prasad, *Rev. Sci. Instrum.*, **63(10)**, 5052 (Oct 1992)

[25] R.R. Prasad, M. Krishnan, J. Mangano, P. A. Greene, *SPIE* Vol. **2194**/120

[26] S. Lee, *IEEE Trans. on plasma Sci.*, **19**(5), 912 (1991)

[27] J.W. Mather, *Phys. of Fluids*, **3**, 134 (1960)

[28] N.V. Filippov, T.I. Filippova, and V.P. Vinogradov, *Nucl. Fus. Suppl.*, **2**, 577 (1962)

[29] J.W. Mather, in *"Methods of Experimental Physics"*, Edited by H. Griem and R. Lovberg (Academic, New York), **9B**, 187 (1971)

[30] G. Decker and R. Wiencke. *Physics* **82C**, 155 (1976)

[31] Y.H. Chen, "Parametric Study of Focus Optimization", *Ph.D. Thesis*, University of Malaya, (1978)

[32] R.S. Rawat, "Laser Shadowgraphic Studies on Dense Plasma Focus and Plasma Processing", *Ph.D Thesis*, University of Delhi, (1993)

[33] A. Serban, "Anode Geometry and Focus Characteristics", *Ph.D Thesis*, Nanyang Technological University, (1995)

[34] V.M. Korzhavin, in *Unconventional Approach to Fusion*, edited by B. Brunelli and G. Leotta, Plenum Press, New York, 193 (1982)

[35] H. Conrads, *Nucl. Sci. and Engg.*, **106**, 299 (1990)

[36] H. Rapp, *Phys. Lett.* A, **43**, 420 (1973)

[37] J.W. Mather, in *4th Conf. on Plasma Phys. and Nucl. Fusion*, Wisconsin, USA, (1971)

[38] H.J. Kaeppeler, in *Proc. 6th Int. Conf. on Plasma and Contr. Nucl. Fusion Res.*, IAEA-CN-35E/18-1

[39] G. Decker, L. Flemming, H.J. Kaeppeler, T. Oppenländer, G. Pross, P. Schilling, H. Schmidt, M. Shakhatre and M. Trunk, *Plasma Phys.*, **22**, 245 (1980)

[40] P. Chatterton, in *Electrical Breakdown in Gases*, edited by Meek & Craggs, Wiley, (1978)

[41] A. Donges, G. Herziger, H. Krompholz, F. Ruhl and K. Schönbach, *Phys. Lett.* **76A**, 391 (1980)

[42] H. Krompholz, W. Neff, F. Ruhl, K. Schönbach and G. Herziger, *Phys. Lett.* **77A**, 246 (1980)

[43] J. Nowikowski and Z. Jankowicz, in *Proc. 9th Europ. Conf. on Contr. Fusion and Plasma Phys.*, Oxford, **2**, 542 (1979)

[44] M. Borowiecki and S. Czekaj, in *Proc. 4th Int. Workshop on Plasma Focus and Z-Pinch Res.*, Warsaw, 86 (1985)

[45] W. Kies, *Plasma Phys. and Contr. Fusion*, **28**, 1645 (1986)

[46] J.N. Feugas, *J. Appl. Phys.*, **66**, 3467 (1989)

[47] W.H. Bostick, L. Grunberger and W. Prior, in *Proc. 3rd Europ. Conf. on Contr. Fusion and Plasma Phys.*, Utrecht, **1**, 120 (1969)

[48] A. Bernard, A. Coudeville, A. Jolas, J. Launspach and J. de Mascureau, *Phys. Fluids*, **18**, 180 (1975)

[49] H. Herold, A. Juzykiewiez, M. Sadowski and H. Schmidt, *Nucl. Fusion*, **29**, 1255 (1989)

[50] Y.A. Kolesnikov, *Sov. J. Tech. Phys.*, **36**, 833 (1968)

[51] D.E. Potter, *Phys. Fluids*, **14**, 1911 (1971)

[52] S. Maxon and J. Eddelman, *Phys. Fluids*, **21**, 1856 (1978)

[53] S.V. Bazdenkov and V.V. Vikhrev, *Sov. J. Plasma Phys.*, **1**, 250 (1975)

[54] W.H. Bostick, L. Grunberger, V. Nardi and W. Prior, in *Proc. 4th Europ. Conf. on Contr. Fusion and Plasma Phys.*, Rome, **1**, 108 (1970)

[55] H. Bruzzone, R. Gratton, H. Kelly, M. Milanese and J. Pouzo, in *Proc. Int. Conf. on Energy Storage, Compression and Switching*, New York, 255 (1976)

[56] H. Krompholz, F. Ruhl, W. Schneider, K. Schönbach and G. Herziger, *Phys. Lett.* **82A**, 2 (1981)

[57] W.H. Bostick, V. Nardi, L. Grunberger, and W. Prior, in *Proc. 10th Int. Conf. Ionized Gases*, Oxford, 237 (1971)

[58] T. Oppenländer, G. Pross, G. Decker and M. Trunk, *Plasma Phys.*, **19**, 1075 (1977)

[59] T.S. Kobata, *Plasma Phys and Contr. Fusion*, **26**, 575 (1984)

[60] H. Bruzzone, C. Moreno and H. Kelly, *Meas. Sci. and Tech.*, **2**, 1195 (1991)

[61] S.P. Chow, S. Lee and B.C. Tan, *J. Plasma Phys.*, **4**, 729 (1970)

[62] K.H. Kwek, T.Y. Tou and S. Lee, *IEEE Trans. on Plasma Sci.*, **PS-18**, 826 (1990)

[63] G. Bsasque, A. Jolas and J.P. Watteau, *Phys. Fluids*, **11**, 1384 (1968)

[64] F. Gratton and M. Vargas, in *Proc. 7th Europ. Conf. on Plasma Phys. and Nucl. Phys.*, Lausanne, **1**, 64 (1975)

[65] J.C. Keck, *Phys. Fluids*, **5**, 630 (1962)

[66] P.J. Hart, *J. Appl. Phys.*, **35**, 3425 (1964)

[67] S. Lee, in *Proc. of 1984 Tropical College on Appl. Phys.: Laser and Plasma Technology*, edited by S. Lee, B.C. Tan, C.S Wong and A.C. Chew, World Scientific, Singapore, 387 (1985)

[68] S. Lee, Y.H. Chen, S.P. Chow, B.C. Tan, H.H. Tek and S.P. Thong, *Int. J. Elect.*, **33**, 85 (1972)

[69] M. Vargas, F. Gratton, J. Gratton, H. Bruzzone and H. Kelly, in *Proc. 6th Int. Conf. on Plasma Phys. and Contr. Nucl. Fusion Res.*, Berchtesgaden, **3** (IAEA), 483 (1976)

[70] K. Behler and H. Bruhns, *Phys. Fluids*, **30**, 3767 (1987)

[71] H. Schmidt, in *Proc. 2nd Latin American Workshop on Plasma Phys. and Contr. Thermonucl. Fusion*, Medellin, **12**, 1 (CIF Series, 1987)

[72] A.J. Toepfer, D.R. Smith and E.H. Beckner, *Phys. Fluids,* **14**, 52 (1971)

[73] N.J. Peacock, M.G. Hobby and P.D. Morgan, in *5th Int. Conf. on Plasma Phys. and Contr. Nucl. Fusion Res.*, IAEA-CN-28/D-3, Tokyo, (1972)

[74] A. Jeffrey and T. Taniuti, in *"Magnetohydrodynamic Stability and Thermonuclear Containment"*, (1966)

[75] Y.H. Chen and S. Lee, *Int. J. Elect.*, **35**, 341 (1973)

[76] H. Bruzzone, H. Kelly and C. Moreno, *IEEE Trans. on Plasma Sci.*, **18**, 689 (1990)

[77] M.J. Bernstein, D.A. Meskan, H.L.L. Paassen, *Phys. Fluids*, **12**, 2193 (1969)

[78] S. Lee, *Plasma Phys.*, **25**, 571 (1983)

[79] S. Lee, *J. Phys. D: Appl. Phys.*, **16**, 2463 (1983)

[80] T.Y. Tou, *PhD Thesis*, Univ. of Malaya, Malaysia, (1986)

[81] S. Lee, *J. Appl. Phys.*, **54**, 3603 (1983)

[82] S. Lee and A. Serban, *IEEE trans. on plasma phys.,* **24**(3), 1101 (1996)

[83] G.R. Neil and R.S. Post, *Plasma Phys.*, **23**, 425 (1981)

[84] A.G. Michette and C.J. Buckley, *"X-ray science and technology"*, Institute of Physics Publishing, Bristol and Philadelphia, 121 (1993)

[85] M.L. Ginter, in *"X-ray Microscopy"* (G. Schmahl and D. Rudolph, Eds.) Springer Series in Optical Sciences 42 25 (Berlin:Springer), (1984)

[86] P. Choi, A.E. Dangor and C. Deeney, *Proc. SPIE* **733,** 52 (1986)

[87] W. Neff, J. Eberle, R. Holz, R. Lebert and F. Richter, *SPIE*, **1140**, 1310 (1989)

[88] V.A. Gribkov, *Chinese Phys. Lett*, **10**, (Suppl.), 26 (1993)

[89] W.H. Bostick, V. Nardi, W. Prior and C. Cortese, in *Proc. 3rd Top. Conf. on Pulsed High-β Plasmas*, edited by D.E. Evans, **C.1.6**, 407 (1975)

[90] J.W. Mather, *Phys. Fluids*, **8**, 366 (1965)

[91] V.D. Ivanov, V.A. Kochetov, M.P. Moiseeva, A.A. Palkin, E.B. Svirskii, A.R. Terentiev, N.V. Filippov, T.I. Filippova, A.V. Gribkov, A.V. Dubrovskii, A.I. Isakov, V.M. Korzhavin, O.N. Krokhin, V.Y. Nikulin and O.G. Semenov, in *Plasma Phys. and Contr. Nucl. Fusion Res. (Proc. 8th Int. Conf.*, Brussels, 1980), *IAEA*, **2**, 175 (1981)

[92] W.H. Bostick, V. Nardi and W. Prior, *J. Plasma Phys*, **8**, 7 (1972)

[93] N.J. Peacock, M.G. Hobby and P.D. Morgan, in *Plasma Phys. and Contr. Nucl. Fusion Res. (Proc. 4th Int. Conf.*, Madison, 1971), *IAEA*, **1**, 537 (1971)

[94] P. Choi, C.S. Wong and H. Herold, *Laser and Particle Beams*, **7A**, 763 (1989)

[95] P. Choi, R. Aliaga-Rossel, C. Dumitrescu-Zoita and C. Deeney, in *Proc. 3rd Int. Conf. on Dense Z-Pinches*, London (1993)

[96] R.K. Rout and A. Shayam, *Plasma Phys. and Contr. Fusion*, **31**, 877 (1989)

[97] K. Hirano, H. Nakajima, I. Kaneko, T. Yamamoto and K. Shimoda, *Japan J. Appl. Phys.*, **29**, 779 (1990)

[98] M. Favre, S. Lee, S.P. Moo and C.S. Wong, *Plasma Sources Sci. Technol.*, 1, 122 (1992)

[99] V. Zoita, R. Presura, F. Gherendi and C. Dumitrescu-Zoita, in *Proc. 20th IEEE Int. Conf. on Plasma Sci.*, Vancouver, 584 (1993)

[100] V. Zambreanu and V. Zoita, in *Proc. of the 1992 Int. Conf. on Plasma Phys.*, Innsbruck, **16C**, 687 (1992)

[101] R. Presura and V. Zoita, in *Proc. 16th Int. Conf. on X-Ray and Inner-Shell Processes*, Debrecen, 104 (1993)

[102] M. Yokoyama, Y. Kitagawa, C. Yamanaka and K. Hirano, in *Plasma Phys. and Contr. Nucl. Fusion Res.* (*Proc. 8th Int. Conf.*, Brussels, 1980), *IAEA*, **2**, 187 (1981)

[103] R.L. Gullickson and R.H. Barlett, in *"Advances in X-Ray Analysis"*, edited by W.L. Pickles, Vol. **18**, p. 184, Plenum Press, New York, (1974)

[104] D.C. Gates, in *Proc. Int. Conf. on Energy Storage, Compression and Switching*, Vol. **2**, p. 329, Plenum Press, N.Y., (1978)

[105] S. Lee, in *"Radiation in Plasmas"*, Ed. B. McNamara, World Scientific Publishing Co., 967-977 (1984)

[106] S. Lee, in *"Radiation in Plasmas"*, Ed. B. McNamara, World Scientific Publishing Co. 978 (1984)

[107] S. Lee *et al*, in *"Laser and Plasma Technology"*. World Scientific, 387-420 (1985)

[108] S. Lee, in *"Small Plasma Experiments II"*, Eds.: S. Lee & P.H. Sakanaka, World Sci Pub Co., Singapore, 113 (1989)

[109] S. Lee, Y.H. Chen, S.P. Chow, B.C. Tan, H.H. Tek and S.P. Thong, *Int. J. Elect.*, **33**, 85 (1972)

[110] D.E. Potter, *Nucl. Fusion*, **18**, 813 (1978)

[111] S. Lee, "Technology of a Small Plasma Focus" in *Small Plasma Experiments II* Ed S. Lee & P.H. Sakanaka, World Sci Pub Co., Singapore, 113 (1989)

[112] S. Lee and A. Serban, in *Proc. Int. Conf. on Plasma Phys.*, ICPP'94, Foz Do Iguacu, Brazil, **1**, 181 (1994)

[113] S. Lee, in *Int. Conf. on Plasma Sci. Technol.* '94, ICPST '94-Chengdu, (Jun 16-20, 1994)

[114] Z.L. Xiang and C.X. Yu, *"High Temperature Plasma Diagnostic Techniques"*, Shanghai Sci. and Technol. Press, 56 (1982)

[115] A.G. Michette and C.J. Buckley, *"X-ray science and technology"*, Institute of Physics Publishing, Bristol and Philadelphia, 130 (1993)

[116] R.H. Huddlestone and S.L. Leonard (Eds.), *"Plasma Diagnostic Techniques"*, (New York: Academic press) (1965)

[117] W. Lochte-Holgreven, *"Plasma diagnostics"*, North-Holland Pub. Com., (1968)

[118] J.D. Huba (ed.), *NRL Plasma Formulary*, Naval Research Laboratory, Washington, DC. (1994)

[119] R.P. McWhirter in *"Plasma Diagnostic Techniques",* Eds. R.H. Huddlestone and S.L. Leonard (New York: Academic Press) (1965)

[120] D.R. Bates, A.E. Kingston and R.W.P. Mcwhirter, *Proc. Roy. Soc.* **A 267** 297 (1962)

[121] S. Lee, *Bul. Fizik Malaysia*, **2**, 240 (1981)

[122] S. Lee, *Aust. J. Phys.*, 36, 891-5 (1983)

[123] C.E. Moore, *"Atomic Energy Levels"*, U.S. Bureau of Standards Cir. No.467, (1949)

[124] W.H. Bennet, *Phys. Rev.* **45**, 890 (1934)

[125] K.H. Kwek, T.Y. Tou and S. Lee, *J. Fiz. Mal.*, 9, 36 (1988); *IEEE Trans. on Instrum. and Measurement*, IM-38, 103 (1989)

[126] K.H. Kwek, "Pinch Structure of a Plasma Focus", *Ph.D. Thesis*, University of Malaya (1989)

[127] G. Guderley, *Luftfahrtforschung*, **19**, 302 (1942)

[128] S. Lee, C.S. Wong, T.Y. Tou, Jalil b Ali, and A.C. Chew, in *Proc. of 1984 Tropical College on Appl. Phys.: Laser and Plasma Technology*, edited S. Lee, B.C. Tan, C.S Wong and A.C. Chew, World Scientific, Singapore, 63 (1985)

[129] S. Lee, T.Y. Tou, S.P. Moo, M.A. Eissa, A.V. Gholap, K.H. Kwek, S. Mulyodrono, A.J. Smith, *Am. J. Phys.* **56**, 62 (1988)

[130] S. Lee, *PhD Thesis*, Australian National University (1969)

[131] R. Keller, *Rev. Sci. Instrum.*, **35**, 1057 (1964)

[132] A. Serban and S. Lee, *Rev. Sci. Instrum.* **66** (10), 4958 (1995)

[133] R. Lebert, J. berle, R. Holz, W. Neff, F. Richter, "Investigation of Soft X-ray Emission from Plasma Focus", ***SPIE*** *Vol.* ***1140*** *X-ray Instrumentation*, 279-288 (1989)

[134] K. Eidmann, T. Kishimoto, P. Herrmann, J. Mizui, P. Pakula, R. Sigel and S. Witkowski, *Laser and Particle Beams*, **4(3)**, 521-536 (1986)

[135] R. Siegel, K. Eidmann, J. Mayer-ter-Vehn, G.D. Tsakiris, S. Witkowski, "Laser-generated soft X-rays", *SPIE Proceeding,* Vol. 831, (1988)

[136] Yu.M. Alexandrov, M.O. Koshevoi, V.A. Murashova, T.F. Nikitina, A.A. Rupasov, G.V. Sklizkov, M.N. Yakimenko, K. Eidmann, R. Siegel and G.D. Tsakiris, *Laser and Part. Beams*, 6(3), 561 (1988)

[137] K.G. Whitney, P.C. Kepple, *J.Quant. Spectrosc. Radiat. Transfer*, **27(3)**, 281 (1982)

[138] Robert Guenther, *Modern Optics*, John Wiley & Sons, 87 (1990)

[139] X. Feng, X.B. Hou and Z. Q. Zhang, *China J. of Laser*, **B3**, 414 (1994)

[140] H. Schnopper, *Appl. Otp.*, **16**, 1088 (1977)

[141] B.A. Bryunetkin, S.A. Pikuz, I.Y. Skobelev and A.Y. Faenov, *Laser and Particle Beams*, **10**, 849 (1992)

[142] X.F. Wang, *J. Appl. Phys.*, **69**, 2015 (1991)

[143] X. Feng, *10th VUV international conference*, 9-13 July, Paris, France, (1987)

[144] R.A. Armistead, *Rev. Sci. Instrum.*, **45** (8), 996 (1974)

[145] Yu.M. Alexandrov, K. Eidmann, *et al*, *Nucl. Instrum. and Methods in Phys. Research* **A308**, 343-346 (1991)

[146] B.L. Henke, F.G. Fujiwara, and M.A. Tester, *J. Opt. Soc, Am. B*, **1**(6), 828 (1984)

[147] C.M. Dozier, D.B. Brown, and L.S. Birks, *J. Appl. Phys.*, **47**(8), 3732 (August 1976)

[148] K. Hirano, N. hisatome, T. Yamamoto and K. Shimoda, *Rev. Sci. Instrum.*, **65(12)**, 3761 (1994)

[149] A.J. Cole, M.H. Key, A. Ridgeley, D.A. Brown, P.A. Norreys, E.R. Wooding and J.W. Barbee, *Opt. Commun.*, **62**, **1** (1987)

[150] X. Feng , X.B. Hou and Z.Q. Zhang, *China J. of Laser,* **B3**, 414 (1994)

[151] S. Lee, H. Ahmad, T.Y. Tou, K.H. Kwek and C.S. Wong, *J. Fiz. Mal.*, **6**, 23 (1985)

[152] B.L. Henke, S.L. Kwok, J.Y. Uejio, H.T. Yamada, and G.C. Young, *J. Opt. Soc. Am. B*, 1 (6), 818 (1984)

[153] D.B. Brown, J.W. Criss, and L.S. Birks, *J. Appl. Phys.*, **47** (8), 3722 (1976)

[154] A.G. Michette and C.J. Buckley, *"X-RAY Science and Technology"*, Ins. Phys. Publishing, Bristol and Philadelphia, 249 (1993)

[155] E.M. Gullikson, R. Korde, L.R. Canfield, R.E. Vest, in *Proceedings of VUV **11***, Tokyo, Japan, (August 1995)

[156] R.C. Alig, S. Bloom and C.W. Struck, *Phys. Rev.* **B 22**, 5565 (1980)

[157] G.W. Fraser, *et al*. *Nucl. Instrum. and Meth.* **A 350**, 368 (1994)

[158] M. Krumrey and E. Tegeler, *Rev. Sci. Instrum.*, **63**, 797 (1992)

[159] ***, *RS Data Library,* (1987)

[160] C.S. Wong, *Five Channel Diode X-ray Spectrometer, Instruction Manual, ICAC-UM/DXS-4,* Univ. of Malaya, Malaysia (1992)

[161] H. Kromphloz, F. Ruhl, W. Schneider and G. Herziger, *Phys. Lett.* **82A**, 82 (1981)

[162] S.P. Chow, S. Lee, and B.C. Tan, *J. Plasma. Phys.*, **8**, 21-31 (1972)

[163] K. Eidman, *Laser and Particle Beams*, **4**, 521 (1986)

[164] Y. Kato, I. Ochiai, T. Sato, S. Murayama and M. Taniguchi, *Jpn. J. Appl. Phys.*, **31**, 3695 (1992)

[165] Yoshio Takahama, Jian Du, Takeshi Yanagigaira and Katsumi Hirano, *Rev. Sci. Instrum.*, **65**, 2505 (1994)

[166] R.L. Kelly, *J. Phys. Chem. Ref. Data*, **16** Suppl. (1), (1987)

[167] J.F. Seely, *Phys. Rev. Lett.* **42**, 1606 (1979)

[168] J.C. Stewart and K.D. Pyatt, Jr., *Astrophys. J.*, **144**, 1203 (1966)

[169] C.D. Michelis, *Nuclear Fusion*, **21**, 677 (1981)